

Lightweight Cellular Concrete: Applicability of Pavement Subbase Layer Materials

by

Frank Mi-Way Ni

A thesis

presented to the University of Waterloo

in fulfillment of the

thesis requirement for the degree of

Doctor of Philosophy

in

Civil Engineering

Waterloo, Ontario, Canada, 2021

© Frank Mi-Way Ni 2021

Examining Committee Membership

The following served on the Examining Committee for this thesis. The decision of the Examining Committee is by majority vote.

External Examiner	Dr. Daman Panesar Professor Civil & Mineral Engineering University of Toronto,
Supervisor	Dr. Susan Tighe Professor Civil & Environmental Engineering University of Waterloo
Supervisor	Dr. Rebecca Saari Professor Civil & Environmental Engineering University of Waterloo
Internal Member	Dr. Hassan Baaj Professor Civil & Environmental Engineering University of Waterloo
Internal Member	Dr. Sina Varamini Professor Civil & Environmental Engineering University of Waterloo
Internal-external Member	Dr. Kaan Inal Professor Mechanical & Mechatronics Engineering University of Waterloo

Author's Declaration

This thesis consists of material all of which I authored or co-authored: see Statement of Contributions included in the thesis. This is a true copy of the thesis, including any required final revisions, as accepted by my examiners. I understand that my thesis may be made electronically available to the public.

Statement of Contributions

Chapter 5 of this thesis contains parts of a paper submitted for publication. The paper is co-authored by me, Wei Yu, Xu Liang, Abimbola Grace Oyeyi, and my supervisor (Dr. Tighe). Dr. Yu and I developed the methodology and research design of the paper, with input from Dr. Tighe, while Mr. Xu provide help on image processing. Yu completed the writing regarding the image processing parts, and I am responsible for summarize the experiment data in the paper with the help from Mrs. Oyeyi.

Abstract

Canada is the second-largest country in the world and has over 1.04 million km of roads. Residents and industries rely on the road network as it contributes significantly to quality of life. Pavement structures built over weak subgrade soil suffers from freeze-thaw and frost heave, this also leads to increased total cost of maintenance and rehabilitation and can also have an adverse environmental impact. Therefore, this research has proposed different solutions to solve these challenges, Lightweight Cellular Concrete (LCC) is one of the materials that has been applied in this type of situation which can provide technical, economic, and environmental benefits.

The use of Lightweight Cellular Concrete (LCC) in transportation infrastructure has been growing in recent years. LCC is a versatile material that contains several benefits to pavement construction, such as excellent flowability, good freeze-thaw resistance, and sustainability. As the subbase layer's quality and strength requirements are not as harsh as the base layer, LCC becomes a feasible material to be implemented to protect the weak soil roadbed. However, there is a lack of mechanical analysis and design guidelines for LCC usage in pavement design. The on-field pavement performance is also lacking with the LCC materials.

Three different densities of LCC are considered and evaluated in this research. Laboratory tests and pavement performance analysis using different evaluation methods were used in this research. Laboratory tests were performed at the Centre for Pavement and Transportation Technology (CPATT) at the University of Waterloo. The tests evaluated various properties including mechanical properties, durability, microstructure of LCC, and other LCC properties. Overall, it was found that the LCC is a stiffer material compared with unbound granular material but weaker than chemically stabilized base materials. The density of the LCC greatly influences its properties. The 475 kg/m³ and 600 kg/m³ densities were found to have a better pore structure than the 400 kg/m³ density LCC. Moreover, the 475 kg/m³ and 600 kg/m³ densities were discovered to be durable after 180 cycles of freeze and thaw cycling.

The pavement performance analysis was performed using three different methods: the failure criteria analysis, granular base equivalency method, and the Mechanistic-Empirical Pavement Design Guide (MEPDG) software. In the failure criteria analysis, LCC sections outperformed the granular subbase section in both fatigue cracking and rutting. The allowable loads of LCC sections were found to be at least 1.6 to 7 times of granular sections, showing that LCC sections' bearing capacity is greater than that of granular sections based on the testing. In the granular base equivalency method, the LCC sections could reduce their layer thickness compared to the unbound granular subbase section by 44% to 65%. MEPDG results showed that pavement with LCC as a subbase layer also demonstrated superior performance than the granular subbase section, especially in heavier traffic road class. 600 kg/m³ density LCC is suitable for major arterial roads with 7,500 Average Annual Daily Truck Traffic (AADTT). On the other hand, lower densities like 475 kg/m³ density and 400 kg/m³ density could be applied in lower-traffic road classes such as major arterial with 5,000 AADTT, minor arterial road, and collector. Therefore, the pavement design using LCC as the subbase layer should consider the road class to determine the density to be used.

The main findings from this research are (1) LCC with density above 400 kg/m³ are able to support the pavement, and the traffic could be open after three to seven days when the construction finished. (2) The pore characteristics of LCC were found to be relevant to its mechanical properties. The 475 and 600 kg/m³ densities LCC demonstrated better pore shape than the 400 kg/m³ density LCC. Even though the 475 kg/m³ density LCC had more significant results of circularity and solidity than the 600 kg/m³ density LCC, it was found that 600 kg/m³ density LCC had greater average thickness between pores, leading to a better strength than the 475 kg/m³ density LCC. (3) The 475 and 600 kg/m³ density LCC have excellent freeze-thaw resistance when it can maintain its moisture, this could benefit when LCC is applied in areas that have a higher water table. (3) According to MEPDG and Weslea results, the LCC sections have better pavement performance in rutting and fatigue cracking than granular section and could be considered in reducing the subbase thickness. (4) It was found the 600 density LCC pavement could withstand up to

7,500 AADTT major arterial road. For road classes that have lower traffic volume, lower densities of LCC could be considered. The above analysis showed that using LCC as a subbase material could provide a more durable pavement in Canada.

Acknowledgements

I would like to express my sincere gratitude to my supervisors Professor Susan Tighe for her support, encouragement, and patience throughout my PhD study.

I would like to acknowledge my Ph.D. committee members Professor Hassan Baaj, Professor Kaan Inal, Professor Rebecca Saari, Professor Sina Varamini from University of Waterloo, and my external examiner Professor Daman Panesar from University of Toronto for participating in my Ph.D. defense.

I would like to thank Brad Dolton, Jim Li, Albert Fang, and Dan Hanley from CEMATRIX (Canada) Inc. for their useful feedbacks and support on this research.

My heartfelt gratitude goes to the Civil and Environmental Engineering Department staffs, particularly Richard Morrison, Peter Volcic, Douglas Hirst, Terry Ridgway, and Victor Lewis for their professional advice and support in the laboratory.

Special thanks to PSI technologies for letting me conduct laboratory tests to finish my Ph.D. research during the pandemic, big thanks to Dr. Vimy Henderson, Dr. Dan Pickel, Mathias Cawthra, Anthony, Maddy, and Eden for their help and support.

I am very grateful to my best friend Hung-Wen Chung for his consistent encouragement and emotional support.

Further thanks to all my CPATT colleagues for their help with field and laboratory works and for their emotional support, especially Abimbola Grace Oyeyi for her countless encouragement and patience.

Last but not least, I would like to thank my parents and my siblings for their patience and understanding throughout the research period.

I would like to acknowledge the following sponsoring partners of this research project:

- The Centre for Pavement and Transportation Technology (CPATT), Norman W. McLeod Chair, University of Waterloo.
- The Natural Sciences and Engineering Research Council of Canada (NSERC)

Collaborative Research and Development Program.

- CEMATRIX (Canada) Inc.

Table of Contents

List of Figures	xv
List of Tables	xxi
Chapter 1 Introduction	1
1.1 Background	1
1.2 Research Hypothesis	3
1.3 Research Scope and Objectives	3
1.4 Research Methodology	4
1.5 Thesis Organization	5
Chapter 2: Literature Review	7
2.1 Current Practice/Materials for the subbase layer	7
2.1.1 Unbound granular pavement layer	8
2.1.2 Treated granular layer	9
2.1.3 Alternative Subbase Material	11
2.2 Lightweight Cellular Concrete	11
2.2.1 Definitions	11
2.2.2 Standards and Specifications	12
2.2.3 Constituent Materials	13
2.2.4 Mix Design and mixing method	16
2.2.5 Properties of lightweight cellular concrete	17
2.2.6 Cellular concrete concerning sustainable construction	26
2.2.7 Applications of lightweight cellular concrete	28

2.3 Performance Prediction Models.....	29
2.3.1 Unconfined Compressive Strength	29
2.3.2 Modulus of Elasticity	30
2.3.3 Modulus of Rupture	31
2.3.4 Indirect Tensile Test	32
2.3.5 Fatigue cracking.....	33
2.4 Case Studies in Canada.....	34
2.5 Classification of LCC in the Mechanistic-Empirical Pavement Design Guide (MEPDG).....	37
2.5.1 Material categories for flexible pavement design	37
2.5.2 Input characterization for the chemically stabilized materials	37
2.6 Summary of Gaps related to lightweight cellular concrete.....	41
2.6.1 Constructability	41
2.6.2 Durability.....	41
2.6.3 Sustainability	41
2.6.4 Pavement applications in Canada.....	42
2.6.5 Gaps	42
Chapter 3 Research Methodology.....	43
3.1 Laboratory Experiment	43
3.1.1 Unconfined Compressive Strength	45
3.1.2 Splitting Tensile Test.....	46
3.1.3 Modulus of Elasticity and Poisson’s Ratio.....	47
3.1.4 Modulus of rupture	49

3.1.5 Water absorption	50
3.1.6 Permeability test	52
3.1.7 Sorptivity test	53
3.1.8 Freeze-thaw resistance.....	54
3.1.9 Drying Shrinkage.....	57
3.1.10 Resonant Column test	57
3.2 Laboratory data analysis	58
3.3 Summary of Methodology	59
Chapter 4 Laboratory data analysis.....	60
4.1 The mix design and production of LCC	60
4.2 The properties of hardened concrete.....	63
4.2.1 Unconfined Compressive Strength	63
4.2.2 Modulus of Elasticity (MOE) and Poisson’s Ratio	65
4.2.3 Indirect Tensile Strength	70
4.2.4 Modulus of rupture	71
4.2.5 Drying Shrinkage.....	73
4.2.6 Damping Ratio measurement.....	74
4.3 Effect of LCC density on other properties	77
4.4 Summary and Findings	79
Chapter 5 Microstructure of ultra-low density lightweight cellular concrete.....	82
5.1 Image capturing technology.....	82
5.1.1 Industrial HD Camera System (IHDCS)	82

5.1.2 ESEM Imaging Method	84
5.2 Image Processing Methodology.....	85
5.3 Results and Analysis.....	86
5.3.1 ESEM Pore Characteristics Analysis	86
5.3.2 Pore Size and Thickness of Solid Part.....	88
5.3.3 Shape Descriptors.....	90
5.3.4 Image Processing Results Analysis of ESEM and IHDCS	91
5.3.5 Relationship with mechanical properties	94
5.4 Summary and Findings	95
Chapter 6 Freeze-thaw resistance of Lightweight Cellular Concrete	97
6.1 Scenario settings	97
6.2 Twenty-Eight days samples	97
6.2.1 Thaw in water scenario	97
6.2.2 Thaw in air scenario.....	101
6.3 One-year samples.....	102
6.3.1 Thaw in water scenario	102
6.3.2 Thaw in air scenario.....	105
6.4 Visual images of the Samples.....	107
6.5 Water absorption.....	114
6.6 Permeability	116
6.7 Sorptivity.....	117
6.8 Summary and Findings	118
Chapter 7 Optimization of application of LCC in pavement subbase	120

7.1 Pavement performance and structural analysis.....	120
7.2 Failure criteria analysis via Weslea	120
7.2.1 Model Inputs	121
7.2.2 Model Result	123
7.3 Granular Base Equivalency (GBE) of LCC.....	133
7.4 MEPDG performance criteria analysis	134
7.4.1 MEPDG Input and Scenarios.....	134
7.4.2 MEPDG Model Results.....	137
7.5 Summary and Findings	143
Chapter 8: Conclusions and Recommendations	144
8.1 Conclusions.....	144
8.2 Major Contribution	146
8.3 Recommendations.....	147
References.....	149
Appendices.....	159
Appendices A.....	160
Appendices B.....	164
Appendices C	177

List of Figures

Figure 1-1 Organization of the Thesis	6
Figure 2-1 Basic component of a typical pavement system (FHWA 2006).....	7
Figure 2-2 Examples of the instability of ultra-low density foamed concrete (a) in the laboratory; (b) on-site (Jones et al. 2016)	17
Figure 2-3 Influence of plastic density on temperature profiles of foamed concrete (Jones and McCarthy 2006)	19
Figure 2-4 Drying shrinkage of lightweight concretes with fly ash (Chindaprasirt and Rattanasak 2011).....	22
Figure 2-5 Relationship between E-value and 28-day sealed cured cube compressive strength of foamed concrete (Jones and McCarthy 2005)	24
Figure 2-6 Influence of plastic density and fly ash on the eCO ₂ of foamed concrete (Ozlutas 2015).....	27
Figure 3-1 Proposed Research Methodology.....	44
Figure 3-2 Unconfined Compressive Strength test setup	46
Figure 3-3 Splitting Tensile Strength test setup.....	47
Figure 3-4 Modulus of Elasticity and Poisson's ratio test setup.....	49
Figure 3-5 Modulus of Rupture test layout.....	50
Figure 3-6 Water absorption test layout.....	51
Figure 3-7 Permeability test layout.....	53
Figure 3-8 Sorptivity test setup.....	54
Figure 3-9 Test setup of freeze-thaw resistance test.....	56
Figure 3-10 Typical layout of the drying shrinkage test (ControlsGroup)	57
Figure 3-11 The layout of the resonant column test	58

Figure 4-1 Relationship between LCC density and Compressive strength	65
Figure 4-2 Compressive Strength over time	65
Figure 4-3 Modulus of Elasticity and LCC density	68
Figure 4-4 Poisson's ratio and LCC density	68
Figure 4-5 Modulus of Elasticity over time	69
Figure 4-6 Poisson's ratio over time	69
Figure 4-7 Splitting tensile strength and LCC density.....	70
Figure 4-8 Relationship between tensile strength and compressive strength	71
Figure 4-9 Modulus of rupture and LCC density.....	72
Figure 4-10 Relationship between modulus of rupture and compressive strength.....	73
Figure 4-11 Test results of drying shrinkage for three densities	74
Figure 4-12 Damping ratio of soft clay (Dobry and Vucetic 1987)	75
Figure 4-13 Damping ratio for kaolinite clay (Ashmawy et al. 1995).....	76
Figure 4-14 Damping ratio of sand (Delfosse-Ribay et al. 2004).....	76
Figure 4-15 Damping ratio of granular material (Sitharam and Vinod 2010).....	77
Figure 5-1 Industrial HD macro photography image capturing system	83
Figure 5-2 Images of specimens captured by IHDCS	84
Figure 5-3 Test layout of the environmental scanning electron microscope (ESEM).84	
Figure 5-4 ESEM images with different densities.....	85
Figure 5-5 Image processing procedure.....	86
Figure 5-6 Heat map of correlation coefficient result.....	87
Figure 5-7 Box chart and cumulative frequency analysis of Equivalent radius (a) Box chart of the equivalent radius (b) Cumulative frequency of pore radius	88

Figure 5-8 Average thicknesses of solid parts (a) Inverted binary image (b) Skeleton of the solid part (c) Average thickness of solid parts and area ratio as a function of specimen density89

Figure 5-9 Data of shape descriptors of specimens with different densities90

Figure 5-10 Results of pore characteristics based on IHDCS (a) Area ratio and average thickness as a function of specimen density based on IHDCS images (b) Shape descriptors of specimens with different densities based on IHDCS images.....92

Figure 5-11 Comparative analysis of physical parameter results between ESEM and IHDCS.....93

Figure 5-12 Mechanical properties of LCC (a) Unconfined compressive strength (b) Modulus of elasticity (c) Modulus of rupture (d) Splitting tensile strength94

Figure 6-1 Freeze-thaw deterioration data for 600 samples – 28 days thaw in water .98

Figure 6-2 Freeze-thaw deterioration data for 475 samples – 28days thaw in water ..98

Figure 6-3 Freeze-thaw deterioration data for 400 samples – 28days thaw in water ..99

Figure 6-4 Freeze-thaw deterioration data (average value)– 28days thaw in water ..100

Figure 6-5 Compressive strength of LCC under freeze-thaw cycling (average value)– 28days thaw in water 100

Figure 6-6 Freeze-thaw deterioration data (average value)– 28days thaw in air..... 101

Figure 6-7 Compressive strength of LCC under freeze-thaw cycling (average value)– 28days thaw in air 102

Figure 6-8 Freeze-thaw deterioration data for 600 samples – 365 days thaw in water103

Figure 6-9 Freeze-thaw deterioration data for 475 samples – 365 days thaw in water103

Figure 6-10 Freeze-thaw deterioration data for 400 samples – 365 days thaw in water104

Figure 6-11 Freeze-thaw deterioration data (average value)– 365 days thaw in water104

Figure 6-12 Compressive strength of LCC under freeze-thaw cycling (average value)– 365 days thaw in water	105
Figure 6-13 Freeze-thaw deterioration data (average value)– 365 days thaw in air..	106
Figure 6-14 Compressive strength of LCC under freeze-thaw cycling (average value)– 365 days thaw in air	106
Figure 6-15 Visual images of the 600 samples at 0 and 180 cycles – thaw in water	108
Figure 6-16 Visual images of the 475 samples at 0 and 180 cycles – thaw in water	109
Figure 6-17 Visual images of the 400 samples at 0 and 180 cycles – thaw in water	110
Figure 6-18 Visual images of the 600 samples at 0 and 180 cycles – thaw in air	111
Figure 6-19 Visual images of the 475 samples at 0 and 180 cycles – thaw in air	112
Figure 6-20 Visual images of the 400 samples at 0 and 180 cycles – thaw in air	113
Figure 6-21 Water Absorption at different density.....	114
Figure 6-22 Results of Water Absorption test (150 by 300 mm)	115
Figure 6-23 Results of Water Absorption test (75 by 150 mm)	115
Figure 6-24 Results of permeability test.....	116
Figure 6-25 Results of Sorptivity test (air dry samples).....	117
Figure 6-26 Results of Sorptivity test (oven dry samples)	118
Figure 7-1 Weslea pavement structure input window	122
Figure 7-2 Weslea traffic load input window	123
Figure 7-3 Allowable number of loads for fatigue cracking and rutting for major arterial (Avg. MOE).....	125
Figure 7-4 Allowable number of loads at different thicknesses for major arterial (Avg. MOE)	125

Figure 7-5 Allowable number of loads for fatigue cracking and rutting for minor arterial (Avg. MOE) 126

Figure 7-6 Allowable number of loads at different thicknesses for minor arterial (Avg. MOE) 126

Figure 7-7 Allowable number of loads for fatigue cracking and rutting for collector (Avg. MOE) 127

Figure 7-8 Allowable number of loads at different thicknesses for collector (Avg. MOE) 127

Figure 7-9 Vertical compressive strain at the top of the subgrade layer (Avg. MOE)128

Figure 7-10 Horizontal tensile strain at the bottom of the surface layer (Avg. MOE)128

Figure 7-11 Allowable number of loads for fatigue cracking and rutting for major arterial (Lowest MOE) 129

Figure 7-12 Allowable number of loads at different thicknesses for major arterial (Lowest MOE) 129

Figure 7-13 Allowable number of loads for fatigue cracking and rutting for minor arterial (Lowest MOE) 130

Figure 7-14 Allowable number of loads at different thicknesses for minor arterial (Lowest MOE) 130

Figure 7-15 Allowable number of loads for fatigue cracking and rutting for collector (Lowest MOE) 131

Figure 7-16 Allowable number of loads at different thicknesses for collector (Lowest MOE) 131

Figure 7-17 Vertical compressive strain at the top of the subgrade layer (Avg. MOE)132

Figure 7-18 Horizontal tensile strain at the bottom of the surface layer (Lowest MOE)132

Figure 7-19 Results of performance criteria for the major arterial road (7500 AADTT)138

Figure 7-20 Results of performance criteria for the major arterial road (5000 AADTT)139

Figure 7-21 Results of performance criteria for the minor arterial road (1000 AADTT)

..... 141

Figure 7-22 Results of performance criteria for the minor arterial road (500 AADTT)142

List of Tables

Table 2-1 Specification for foamed concrete in the United Kingdom (Ozlutas 2015)	13
Table 2-2 Foaming agent types and properties (Ozlutas 2015)	15
Table 2-3 Classification of Foam Concrete Based on Flow Time (Jones et al. 2003)	18
Table 2-4 Typical properties of foamed concrete based on British Concrete Association (BCA 1994)	20
Table 2-5 Compressive strength of cellular concrete after cycles of freezing and thawing (Tikalsky et al. 2004)	23
Table 2-6 Summary of foamed concrete applications based on density (Sari and Sani 2017)	28
Table 2-7 Empirical model for foamed concrete compressive strength determination (Amran et al. 2015)	30
Table 2-8 Empirical model for foamed concrete modulus of elasticity determination (Amran et al. 2015)	31
Table 2-9 Empirical model for foamed concrete flexural strength determination (Amran et al. 2015)	32
Table 2-10 Empirical model for foamed concrete tensile strength determination (Amran et al. 2015)	33
Table 2-11 Summary of Cases of Using LCC as a Subbase Material in Pavement Structure in Canada (Averyanov 2018)	35
Table 2-12 Minimum Compressive Strengths for Cement, Lime, and Combine Lime, Cement, Fly ash Stabilized Materials (AASHTO 2008)	38
Table 2-13 Summary of typical resilient modulus values for chemically stabilized materials (AASHTO 2008)	39

Table 2-14 Typical flexural strength (MR) values for chemically stabilized materials (AASHTO 2008).....	40
Table 2-15 Recommended ranges of Poisson’s ratios for chemically stabilized materials (AASHTO 2008).....	40
Table 4-1 Production of lightweight cellular concrete	61
Table 4-2 Chemical composition of cement and slag (%).....	62
Table 4-3 Mix design of three densities lightweight cellular concrete.....	62
Table 4-4 Test results of Unconfined Compressive Strength at 28days.....	64
Table 4-5 Test results of Modulus of Elasticity and Poisson’s ratio at 28 days	67
Table 4-6 Test results of Modulus of Rupture at 28 days.....	72
Table 4-7 Damping ratios of lightweight cellular concrete for three densities.....	74
Table 4-8 Relationship of density with mechanical properties.....	78
Table 4-9 Relationship of compressive strength with mechanical properties	78
Table 4-10 Summary of material properties of LCC and other subbase material	81
Table 5-1 Tech specs of Industrial HD Camera.....	83
Table 6-1 Results of Permeability test for three densities	116
Table 7-1 Model input for Weslea software	122
Table 7-2 Input parameter and results of GBE	134
Table 7-3 Pavement structure for different road classes.....	135
Table 7-4 MEPDG input for Major Arterial.....	136
Table 7-5 Results of performance criteria for the major arterial road at year 25	137
Table 7-6 Results of performance criteria for the major arterial road at year 25	139
Table 7-7 Results of performance criteria for the minor arterial road at year 25	140
Table 7-8 Results of performance criteria for the collector at year 25	142

Chapter 1 Introduction

1.1 Background

Canada is the second-largest country in the world, with 9.98 million km². Its road network is also top seventh globally with a total length of 1.04 million km (World Fact Book 2011). Transportation Canada mentioned that most passengers and goods in Canada rely on the road network (Transportation Canada 2016). This fact indicated that Canada relies on its road network heavily. However, since Canada is in high latitudes, the pavement structure in the most region suffers from freeze-thaw cycling and frost heave. Thawing can be very destructive to the pavement structure as it weakens the effective strength of the pavement structure (TAC 2013). Furthermore, typical pavement structure uses unbound crushed granular material to support the asphalt surface layer and protect the weak soil roadbed. However, the material's structural dead weight is a heavy burden to the roadbed. It is time consuming and expensive to excavate and haul the quarry materials to the construction site and increases the emission generated from the construction.

Lightweight Cellular Concrete (LCC) or Foamed Concrete is a cementitious material with a typical plastic density ranging from 375 to 1,600 kg/m³ (Ozlutas 2015) that contains a homogeneous air bubble structure in the mix. It was first patented in 1923 (Valore 1954) and used as a void filler material in the 1970s. There are several studies regarding the properties of LCC. For instance, mechanical properties such as compressive strength and modulus of elasticity are often investigated. Pore characteristics of LCC has also been investigated and the pore characteristics of LCC is the key factor to determine the density and the strength of LCC (Amran 2015, Jiang et al. 2016, Favaretto et al. 2017, Fu et al. 2020).

The application of LCC in construction provides several benefits: reducing earth pressure, resistance to freezing and thawing, mitigating settlement, and good thermal insulation (Maruyama and Camarini 2015, Tiwari 2017). LCC is often used in construction projects which required light material and construction workability. For instance, construction

projects such as bulk filling, trench reinstatements, floor screeds, thermally insulating foundations, and stabilizing soils (Mydin 2010, Ozlutas 2015).

LCC has been a useful backfilling material in the world. However, researchers have found that LCC could be a viable option as structural materials (McCarthy 2005). Studies have proven that LCC could be a feasible choice for structural applications such as stabilization of weak soil (Drusa 2011, Lee 2009), replacement of weak soil in the sandwich solution for foundation slabs (Hulimka 2013), industrial concrete floor (Kadela 2016).

The usage of LCC in transportation infrastructure can potentially provide numerous benefits including (Drusa 2016, Ramamurthy 2009):

1. Straightforward and quick placement – The contractor can produce and pour 400 to 600 m³ per day to reduce the construction time and cost.
2. Self-compacting – No extra compaction and leveling is required as compared to unbound granular base layer as the lightweight cellular concrete can fill all the cavities.
3. Excellent Freeze-thaw resistance – protect the weak subgrade soil beneath the lightweight cellular concrete layer.
4. Environmentally friendly – Faster construction time and material can be mixed on site and poured directly means less traffic disturbing and manipulation. Recycling and excavating is also easy and energy efficient.

Several road construction projects have been completed with the LCC due to these benefits. For instance, LCC has been used in an industrial zone in the UK as a subbase material to replace the original layer, which consists of peat (Drusa 2016). Illinois also applies LCC in their road construction to provide a solution to the soft organic underlying soil. It benefits the contractor by lowering unit cost, reduced construction time, and higher material quality (Drusa 2013). Applications of LCC are also found in Canada; Alberta used the LCC as subbase material in bus-lane construction. Ontario also applied LCC in rural roads and highways (Dolton and McIntosh 2018, Maher 2016).

Though there are several LCC applications and studies, there is still a need for a complete and thorough evaluation and guideline for the design, and construction of LCC into flexible pavement design in Canada. Mechanical properties of LCC at a specific ultra-low density (400 to 600 kg/m³) need to be adequately examined. Thus, this research aims to conduct a comprehensive analysis of the LCC as a pavement subbase material; this includes structural properties, bearing capacity, durability analysis, pore characteristics, and other properties such as drying shrinkage and dynamic property for LCC. Under this motivation to provide a viable solution for flexible pavement design over weak subgrade soils which also considers cold climate.

1.2 Research Hypothesis

The primary hypothesis of this research are as follows:

- I. The structural properties and bearing capacity of lightweight cellular concrete make it possible to be used in flexible pavement subbase.
- II. The pore characteristics of lightweight cellular concrete has significant influence on its performance as a pavement material.
- III. Lightweight cellular concrete can provide excellent resistance to the freeze-thaw effect and protect the weak subgrade soil.
- IV. The pavement performance for different road classes of the lightweight cellular concrete subbase pavement depends on the density of lightweight cellular concrete.

1.3 Research Scope and Objectives

The overall purpose of this research is to evaluate and determine the feasibility of using LCC as an alternative material for the subbase layer. For this matter, the LCC assessment is based on evaluation of structural properties, durability, pore characteristics, and performance under heavy traffic loading. The outcome of this research could provide a more in-depth assessment of how lightweight cellular concrete performs in the pavement structure. The predicted pavement performance using pavement software in this study will be based on Ontario's typical pavement design. This research involved partnering

with CEMATRIX(Canada), Inc. and Natural Sciences and Engineering Research Council (NSERC) Collaborative Research and Development program (CRD) to conduct laboratory testing to achieve these goals.

The primary objectives of this research are:

- I. Evaluate the lightweight cellular concrete's structural properties at different densities and compare them with conventional granular subbase material.
- II. Examine the relationship between pore characteristics and mechanical properties of ultra-low density lightweight cellular concrete.
- III. To assess the freeze-thaw resistance of lightweight cellular concrete in different situations.
- IV. To investigate lightweight cellular concrete subbase pavement's performance and provide suitable densities for different road classes.

1.4 Research Methodology

Based on the research scope and objectives, the evaluation plan of this research can be divided into several sections and described as follows:

1. A comprehensive review of lightweight cellular concrete is presented.
2. Laboratory testings that evaluate material properties, including mechanical properties, durability, pore characteristics and microstructure, and other properties, are performed.
3. Pavement design implemented with software and input parameters were taken from laboratory results. Comparison between the conventional pavement structure and lightweight cellular concrete subbase pavement is examined.
4. Preliminary Optimum densities of lightweight cellular concrete pavement were recommended under different traffic loading conditions.

1.5 Thesis Organization

This thesis comprises six chapters, with tables and figures supporting the main content.

Chapter one describes the background of this research and the scope and objectives. A general methodology is also explained in this chapter.

Chapter two provides the literature review of the lightweight cellular concrete, including its material properties, applications, current state-of-practice, and the current gaps.

Chapter three outlines the methodology followed in this research, covering the laboratory testing and numerical model analysis.

Chapter four presents the laboratory results of this study. Properties such as mechanical property, durability, and dynamic property are provided.

Chapter five investigates the pore characteristics by examining the microstructure of the lightweight cellular concrete.

Chapter six describes the freeze-thaw resistance of lightweight cellular concrete, and other properties related to water penetration were also presented.

Chapter seven discusses lightweight cellular concrete's applicability as a pavement subbase material. This involved using pavement analysis software including the MEPDG and Weslea.

Chapter eight summarizes the conclusions and recommendations and describes for future opportunities for research, it also summarizes the major contribution of this research.

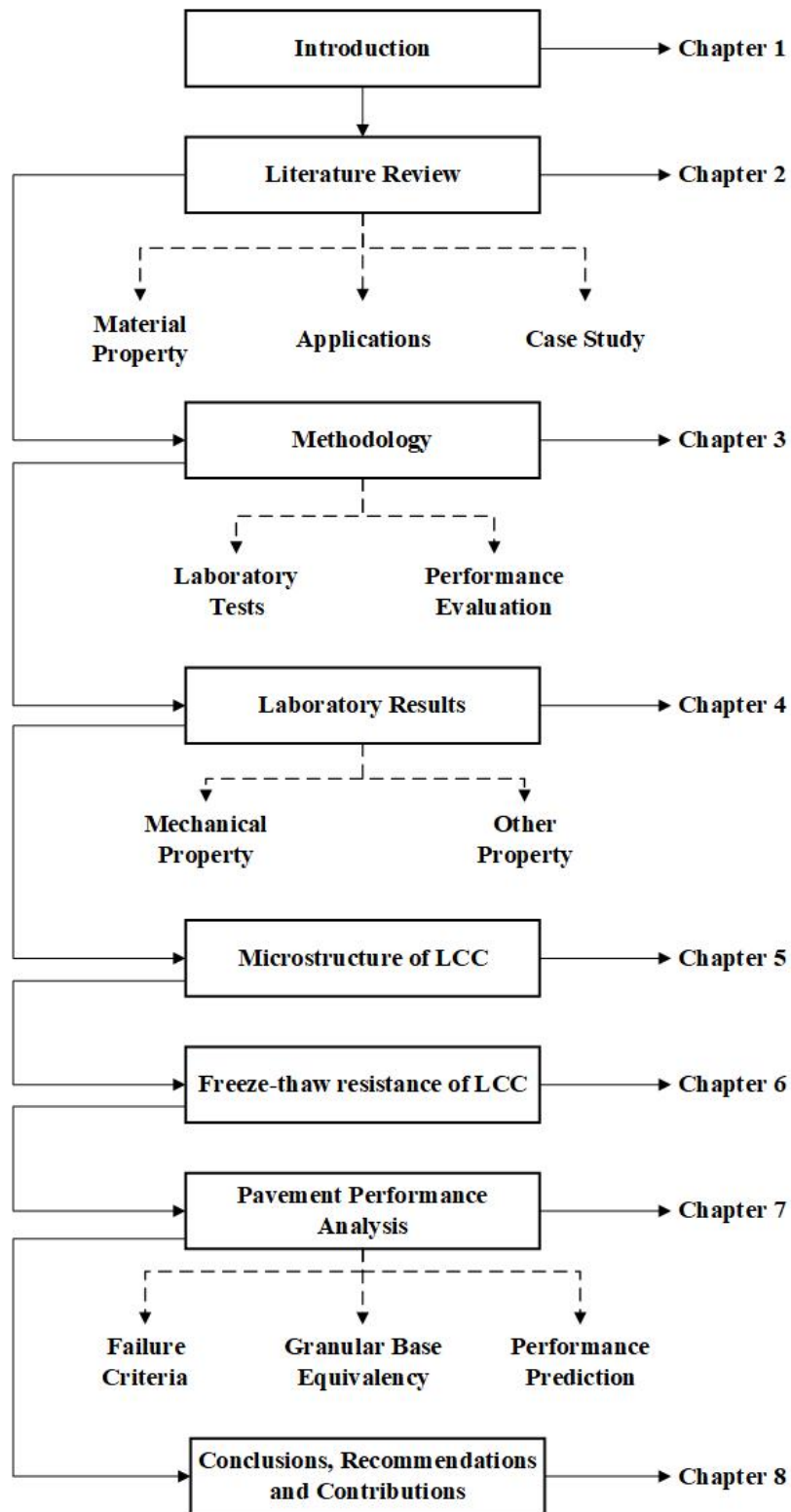


Figure 1-1 Organization of the Thesis

Chapter 2: Literature Review

2.1 Current Practice/Materials for the subbase layer

The typical flexible pavement structure in Canada contains one or more asphalt layers, granular base, and granular subbase layer over the subgrade soil (TAC 2013). The surface and base layer is designed mainly to carry and distribute the traffic loading homogeneously along with the layer. In contrast, the subbase layer is constructed to impose the loads from the overlying layer to the subgrade soil or embankment. The subbase layer should have good drainage properties to provide a non-frost susceptible layer over the subgrade soil. The quality of the subbase layer is usually lower than the base layer (FHWA 2006). A typical pavement structure is shown in Figure 2-1.

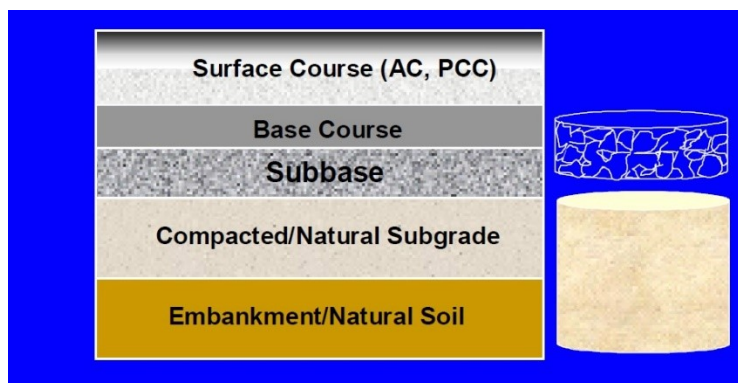


Figure 2-1 Basic component of a typical pavement system (FHWA 2006)

The subbase layer usually consists of a compacted treated or untreated granular material or a layer treated with suitable admixture. Subbase material specification is less strict than base material for strength, plasticity, and gradation (AASHTO 1993). Apart from contributing to the structural capability to the pavement system, the subbase layer provides additional functions such as (FHWA 2006, AASHTO 1993):

1. Protect the base layer from the intrusion of fine-grained subgrade soil.
2. Reduce the damaging effects of frost action. A subbase layer provides an insulation layer on top of the frost-susceptible subgrade soil and, in some cases, increases the

height of the pavement surface above the groundwater table.

3. Prevent free water from entering the pavement system.
4. Provide a work platform for the construction equipment where the roadbed soil is too weak and cannot provide support to the operation.

2.1.1 Unbound granular pavement layer

The unbound granular layer is a common type of base and subbase layer material in flexible pavement and rigid pavement. Low quality of aggregate significantly reduces the pavement life and therefore increases the maintenance costs. Flexible pavements that used low-quality granular layers can lead to failures such as rutting, cracking, depressions, corrugations, and frost heave. On the other hand, the rigid pavement will encounter pumping, faulting, cracking, corner breaks, and fatigue cracking (Saeed 2001).

Factors related to the poor performance of the unbound layer that causes distress in both flexible and rigid pavement are:

1. Shear strength
2. Density
3. Gradation
4. Fines content
5. Moisture level
6. Particle angularity and surface texture
7. Degradation during construction and under repeated loads
8. Freeze-thaw cycling
9. Drainability

Regarding the aggregate properties, elements that are affecting the performance of unbound granular base and subbase layer are (Tutumluer 2013):

1. Shear strength

2. Frost susceptibility
3. Durability
4. Stiffness
5. Toughness

2.1.2 Treated granular layer

The granular base material can be treated or stabilized by adding different additives. The purpose is to enhance the strength and durability of the layer under traffic loading. These treatments are applied in areas that lack the suitable quality of granular materials. The two significant groups of stabilizer for granular materials are (MTO, TAC 2013):

1. Bituminous Stabilization Systems
2. Cementitious Stabilization Systems

Bituminous Stabilization Systems

Bituminous materials are applied not only to improve the stability and strength of the granular materials. The two standard treatments are Emulsion Stabilized Base and Expanded asphalt Stabilization.

A. Emulsion Stabilized Base

Emulsion Stabilized Base can be produced via a central plant or mix-in-place. A slow to medium setting emulsified asphalt is mixed with the granular material. The construction will involve various equipment, including traveling or portable plants, pulvimixers, windrow mixing machines, and Midland paver (TAC 2013).

The Emulsified Stabilized Base is considered flexible as it provides fatigue resistance to the pavement structure. Though, there are a few weaknesses of the Emulsified Stabilized Base. First, it takes a longer curing time for the treatment to reach its full strength. Second, the moisture content of the layer might go beyond the designed moisture content as the existing layer's moisture level might be high and result in an unstable structure.

Third, the emulsion asphalt cost is more expensive than cement and foamed asphalt (Kearney and Huffman 1999).

B. Expanded Asphalt Stabilization

The Ministry of Transportation of Ontario (MTO) has used Expanded Asphalt Stabilization since 2001. It mainly uses foam asphalt as a stabilizing agent. The asphalt starts foaming by adding a small amount of cold water into the hot asphalt cement (typically 2-2.5% by mass) in the controlled expansion chamber. The cold water will turn into steam and expand the volume of asphalt cement 10 to 15 times to its original form. The foamed asphalt will then mix with the granular materials and be paved (MTO 2013).

One of the advantages of Expanded Asphalt Stabilization is its ability to gain strength rapidly and thus could open the traffic faster. The cost is also lower than the emulsified asphalt. The limitations of the foamed asphalt are based on two aspects (Kearney and Huffman 1999):

1. The temperature of the asphalt cement is set to be around 180°C.
2. The materials that are being stabilized needs to have 5 to 15 percent passing the 75-micron sieve (No. 200).

Cementitious Stabilization Base

The primary type of treatment in Cementitious Stabilization Base is the Cement Treated Base. The purpose of adding Portland cement into the mix is to improve granular materials' stability and strength (TAC 2013).

Cement Treated Base is constructed by adding Portland cement (typically 2 to 5 percent) and water to granular material and mix to achieve the optimum moisture content. The treatment provides good early strength and resistance to moisture damage and is stronger than the unstabilized base. The treatment application reduced the possibility of cracking related to the base and subgrade layer. However, the primary problem of the treatment is the drying shrinkage of the cement-treated base. If the shrinkage cracks are too broad, they may reflect through the surface layer and generate cracks (Abaska 2004).

Another drawback of the cement-treated base is the time interval between mixing, and the compaction process is limited to approximately 2 to 4 hours. Wind and heat may also affect the available working time (FHWA 2017). In this case, it is not possible to delay the compaction in Cement Treated Base.

The emulsified and foamed asphalt can be enhanced by adding Portland cement into the mixture. The addition of the cement could prevent the previously dried aggregate stripped from the binder (Oruc 2007). The cement also provides early strength to reduce curing time and water resistance to the mixture (Schmidt 1973). However, adding cement into the asphalt mixture is considered to be expensive (Kearney and Huffman 1999).

2.1.3 Alternative Subbase Material

Other alternative materials had been considered to replace the traditional granular material for use in the subbase layer. For instance, polystyrene, lightweight treated soil, recycled waste glass blended with crushed rock, crushed brick, and lightweight cellular aggregate were proposed as they provide various benefits. These benefits, such as reduced waste, good workability, excellent insulation properties, and cost savings (Baaj et al. 2020, Viet Vo and Park 2016, Arulrajah et al. 2014, Kim, Jeon and Lee 2012). These materials, based on circumstances, provide a more viable solution compared to traditional granular material.

2.2 Lightweight Cellular Concrete

2.2.1 Definitions

The term “cellular concrete.” or “foamed concrete” can be referred to as a type of lightweight concrete that contains a stable air bubble or gas cell distributed homogeneously in the cement mix (ACI 523). Unlike the traditional Portland cement concrete, LCC does not contain any coarse aggregate in the mix (Maruyama and Camarini 2015). ASTM C796 gives a more detailed definition of the LCC as:

“A lightweight product consisting of portland cement, cement-silica, cement-pozzolan, lime-pozzolan, or lime-silica pastes, or pastes containing blends of these ingredients and

having a homogeneous void or cell structure, attained with gas-forming chemicals or foaming agents (for cellular concretes containing binder ingredients other than, or in addition to Portland cement, autoclave curing is usually employed)”

Another definition that has been widely cited noted that the foamed concrete is:

“A cementitious material having a minimum of 20 percent by volume of mechanically entrained foam in the plastic mortar or grout.”

This definition further narrows down the type of foamed concrete since air-entrained concrete has lower entrained air (3-8%), and aerated concrete is formed chemically. (Barnes 2009).

Both mentioned that cellular concrete or foamed concrete is a cementitious material that contains air bubbles or foam in the mix. Since this research is mainly using material from Canada, it would be better to follow the definition from ASTM and ACI.

2.2.2 Standards and Specifications

Currently, there are no test standards for cellular concrete in Canada. American Concrete Institute (ACI) published two guides for the cellular concrete with unit weight above 800 kg/m³ (ACI 523.3R) and less than 800 kg/m³ (ACI 523.1R). The two guides provide a general concept of cellular concrete, such as concrete properties, mixing procedures, and applications. It is noted that the application mentioned in ACI 523.1R is for the roof deck application. American Society for Testing and Materials (ASTM) issued two standards for the foaming agent (ASTM C796 and ASTM C869) and ASTM C495 for the compressive strength test of lightweight cellular concrete. The Portland Cement Association (PCA) also published a guide for lightweight cellular concrete providing detailed information on the material properties, design, processing, and applications of lightweight cellular concrete (LCC) for geotechnical applications (PCA 2021).

Ozlutas (2015) arranged a list of foamed concrete specifications in the UK (Table 2-1). These specifications provide guidelines regarding the properties, advantages, and application of the foamed concrete.

Table 2-1 Specification for foamed concrete in the United Kingdom (Ozlutas 2015)

Publishing body	Title of the specification	Contents
BCA (1991)	Foamed concrete – a Dutch view	Definition, properties, advantages, and potential applications
BCA (1994)	Foamed concrete – composition and properties	
UKWIR (1995)	Specification of foamed concrete	General requirements for foamed concrete as an alternative reinstatement material
HAUC(2010) 1 st & 2 nd publications in 1992 and 2002	Specification for the reinstatement of openings in highways	General requirements for foamed concrete as an alternative reinstatement material
TRL- Brady et al. (2001) with contributions of University of Dundee	TRL Report AG39 – Specification for foamed concrete	Constituents, production, properties, uses, guideline for specifications, uses and quality control
Jones et al. (2004), CTU, University of Dundee	Development of foamed concrete insulating foundations for buildings and pilot demonstration project	Specification and quality control test framework for use in thermally insulating foundations and ground slabs
WRAP (2005)	Recycled and secondary aggregates in foamed concrete	Specification on the use of recycled and secondary aggregates in production
WRAP (2007)	Specification and quality control of foamed concrete incorporating RSA	Constituent materials, requirements, production control, transport, formwork pressure and end-of-life and recycling of RSA foamed concrete
Barnes (2009)	Good Concrete Guide 7 – Foamed concrete: application & specification	Case studies, practicalities, properties, quality control

2.2.3 Constituent Materials

Lightweight cellular concrete's typical composition contains Portland cement, Pozzolan materials, fine aggregate, water, and foam.

A. Portland cement

Typically Type GU Portland cement or Type I Portland cement, blast furnace slag cement, and portland pozzolan cement can be used as the base mix. Type III and IIIA cement are also used if the mixture requires high early strength (ACI 523.1R). The total cement contents are usually around 300 to 400 kg/m³. The cement density can be adjusted depending on the strength requirements or the design density of the mix (Jones, 2000).

B. Pozzolan materials

The Pozzolan material is a finely divided material that is rich in silica or alumina. Pozzolanic by-products such as fly ash and blast furnace slag could benefit the contractor by reducing the cost, maintaining consistency, and increasing strength in long-term performance (Kearsley 2001). Jones et al. (2017) stated that replacing Portland cement with fly ash up to 40% could significantly reduce the embodied carbon dioxide by 65% compared to the 100% Portland cement mix while having a similar 28 d strengths (0.25 MPa compared to 0.31MPa). However, the drawbacks of using fly ash are the slow rate of strength gain, and it might cause foam instability as the water demand might increase (Ozlutas 2015).

C. Fine aggregate

Fine sand is the typical fine aggregate used to produce high-density cellular concrete (Wang et al. 2020). It is found that sand with a maximum size of 2 mm yields higher strength than 5 mm sand. BCA (1994) suggested replacing fine sand with coarse fly ash in mixes with a plastic density below 600 kg/m³.

D. Water

The water to cement ratio plays a vital role in cellular concrete. The w/c ratio needs to be determined based on the constituents' materials to provide and maintain the mix's suitable workability. The typical range of the w/c ratio is from 0.40 to 1.25 (Ramamurthy 2009). Insufficient water in the mix may lead to the mix's collapse, while excess water could increase drying shrinkage (Nambiar and Ramurthy et al., 2006). Bad quality water may

affect the preformed foam, setting time, and lightweight cellular concrete strength. It is recommended in ACI 523.1R that the mix's compressive strength should be tested when mixed with adequate water.

E. Foam

Pre-formed foam is essential in cellular concrete as it can control the plastic density of the mix (Wee et al. 2006). It consists of a foaming agent and compressed air to help produce foam (BCA 1994). The foam should have a homogeneous bubble structure to provide concrete with reasonable strength (Brady 2001). The structure should be capable of resisting the pressure of the base mix until the initial setting time is reached, as the air bubbles will be surrounded by a strong skeleton of concrete (Ramamurthy et al. 2009).

The purpose of using a foaming agent is to decrease the high surface tension of the water and create foam (Ozlutas 2015). Several types of foaming agents are resin-based, synthetic, protein-based, composite, and synthetic surfactant. The most commonly used are synthetic and protein-based (Wang et al. 2020). Panesar (2013) conducted testing on cellular concrete using protein-based and synthetic foaming agents and found out that the type of agent may affect the sorptivity and thermal conductivity of the cellular concrete but less of an effect on the mechanical property. Table 2-2 shows the comparison between synthetic and protein-based foaming agents.

Table 2-2 Foaming agent types and properties (Ozlutas 2015)

Type	Example composition	Properties	Characteristics of foam produced	Application areas in foamed concrete
Protein	Hydrolyzed animal proteins & keratin	Variable, highly refined & stabilized	Stable, relatively low drainage, strong & firm texture, closed-cell bubbles	In low-density FCs and when high strength or waterproofing is required
Synthetic	Alkyl Sulfates	Stable, easy to formulate & consistent	Larger & more open cells due to higher expansion, lower strength	In higher density FCs, useful for large, fast placing

2.2.4 Mix Design and mixing method

Brady et al. (2001) stated that there is no standard method to calculate the mix proportions of cellular concrete. Jones and McCarthy (2005) mentioned that it is difficult to design for the target dry density due to the desorption (50 to 200 kg/m³) of cellular concrete. Therefore, the design criterion of cellular concrete is the target plastic density. According to the mix design approach which is developed at the University of Dundee (Dhir et al. 1999; Brady et al. 2001), the target plastic density is assumed to be the sum of solids and water mix:

$$D = C + W + F \quad 2.1$$

where:

D= target plastic density, kg/m³

C= cement content, kg/m³

W= water content, kg/m³

F=fine aggregate content, kg/m³

Lightweight cellular concrete's mixing procedure can be classified into two methods: the prefoaming and mix-foaming methods. The prefoaming method generates foam separately and then added into the base mix. On the other hand, the mix-foaming method mixes the foaming agent or Surfactants into the base mix, producing a foam structure (Wang et al. 2020). There are two ways of generating bubbles, dry and wet procedures. The wet procedure sprays the foaming agent to fine mesh to create a 2 to 5 mm size bubble and is less stable. The dry procedure forces the foaming agent through high-density restriction and uses compressive air to generate bubbles. The dry procedure produces bubbles that are more stable than the wet procedure. The bubble size could be smaller than 1 mm and make it easy to blend into the base mix (Ramamurthy et al. 2009).

2.2.5 Properties of lightweight cellular concrete

A. Fresh state

Cellular concrete is free-flowing, self-leveling, and self-compacting in its fresh state. These characteristics mean that cellular concrete is a highly workable material (Barnes, 2009). The two properties to evaluate the fresh state of the cellular concrete is consistency (flow behavior) and stability (volumetric stability), which depends on the water content in the mix and the amount of foam added (Ramamurthy 2008). The cellular concrete is thixotropic (BCA 1994), and it can be difficult to restart the construction once the concrete is starting to harden (Barnes, 2009).

i. Stability

Nambiar and Ramamurthy (2007) defined stability of LCC as: “*the state of stability in cellular concrete as the unity of design and measured density (i.e., measured density is within the acceptance limits of $\pm 50 \text{ kg/m}^3$)*”. If the cellular concrete is unstable, the separation of solids and air phases might cause segregation during the fresh state. This leads to a complete loss of air content and leaves only the base mix. Figure 2-2 shows the example of unstable cellular concrete (Jones et al. 2016).

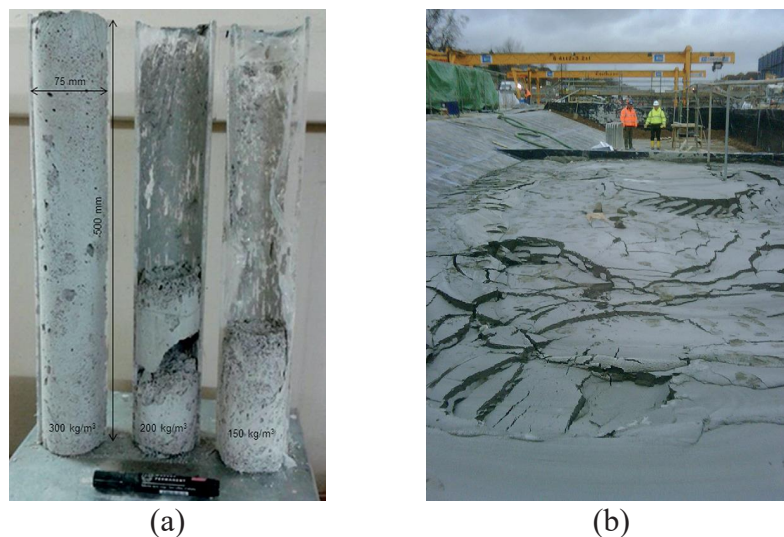


Figure 2-2 Examples of the instability of ultra-low density foamed concrete (a) in the laboratory; (b) on-site (Jones et al. 2016)

The factors that could affect the stability of cellular concrete including environmental conditions (winds, evaporation, vibration, and temperature), materials used (foaming agent, the proportion of the constituent), construction quality, and the instability of the foam itself (quality and volume) (Brady 2001, Jones et al. 2016).

ii. Consistency

The consistency of cellular concrete depends on its spreadability and flowability (Jones and McCarthy 2005). The spreadability can be measured using the Brewer spread test and slump flow test (Jones et al. 2003, Mostert 2005). The flowability is determined by measuring the time taken for paste flow through the Marsh cone with a small opening. The faster the flow time, means better flowability. Jones et al.(2003) present a table for cellular concrete classification based on flow time (Table 2-3).

Table 2-3 Classification of Foam Concrete Based on Flow Time (Jones et al. 2003)

Main Class		Sub Class	
Number	Description	Name	Description
1	1 L in < 1 min	A ^a	Constant flow
2	1 min < efflux < 2 min	B ^a	Interrupted flow
3	0.5 L < efflux < 1 L	C	Completion of flow after tamping gently
4	Efflux < 0.5 L		
5	No flow		

^a Used in Main Class 1 and 2 only

The consistency of cellular concrete is affected by the level of density. It was reported that the flowability of cellular concrete reduces with decreasing density (where the volume of foam is more significant compared to solids). The stiffness of the mix increased as the adhesion between the bubbles and solid particles increase (Nambiar and Ramamurthy 2006). Mohammad (2011) stated that the flow times of 600 kg/m³ cellular concrete is longer than the 1,000 kg/m³ mix. Moreover, blending 30 percent (by mass) of fly ash improves the flowability.

B. Early Stage

i. Heat of hydration

Due to its cellular structure, cellular concrete is considered to have good thermal insulation, which generates more heat of hydration that lasts longer compared to normal concrete. The hydration of cellular concrete is influenced by the volume of the pour, the cement content, the density of the concrete, the amount, type, and characteristics of the cement/filler/aggregate used (Brady 2001, Jones and McCarthy, 2006, Tarasov et al. 2010). Jones and McCarthy (2006) found that the peak temperature reduced by 40% as the cement content decreased from 600 to 300 kg/m³. Moreover, the peak temperature could decrease when replacing 30% of the cement content with fly ash, as shown in Figure 2-3.

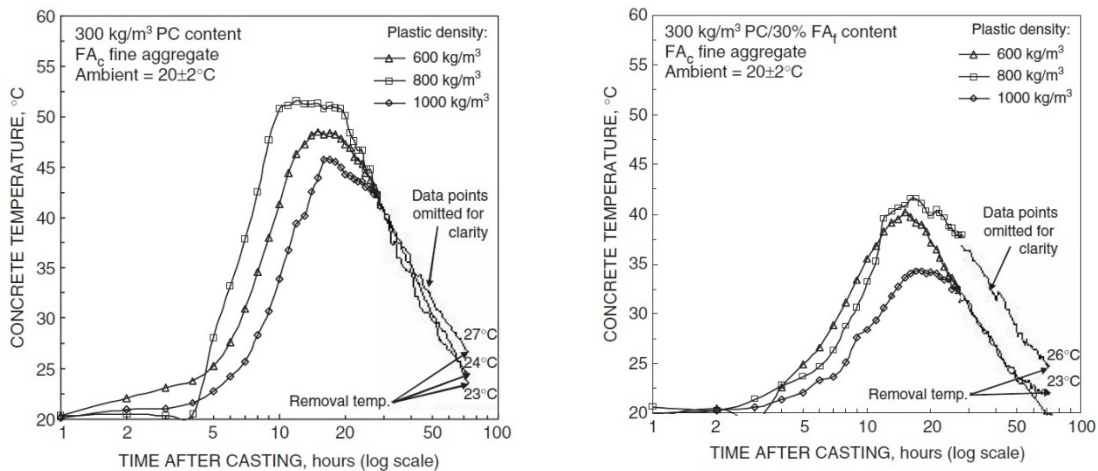


Figure 2-3 Influence of plastic density on temperature profiles of foamed concrete (Jones and McCarthy 2006)

ii. Rate of hardening

The setting time of cellular concrete is crucial as it influences the construction time. Despite there is no standard test method for determining the setting time of cellular concrete, the test method for cement mentioned in ASTM C266 may be suitable to test

the setting time of cellular concrete (Brady et al. 2001). Dhir et al. (1999) and Jones (2000) indicated that the stiffening of cellular concrete occurs after 5 hours since it was cast at 20 °C. Brady et al. (2001) stated that cellular concrete's typical setting time is between 12 and 24 hours.

C. Hardened state properties

i. Compressive Strength

The compressive strength represents the capacity of a material or structure to resist loads. The typical compressive strength of cellular concrete with dry density from 400 kg/m³ to 1600 kg/m³ is demonstrated in Table 2-4. It showed that the compressive strength of cellular concrete decreased as the density reduced. Ramamurthy (2009) stated that the factors that affect cellular concrete's compressive strength are the size and shape of specimens, water content, the direction of loading, age, type of ingredient used, the method of curing, and the type of foaming agents.

Table 2-4 Typical properties of foamed concrete based on British Concrete Association (BCA 1994)

Dry Density (kg/m³)	Compressive Strength (MPa)	Drying Shrinkage (%)	Modulus of Elasticity (MPa)	Thermal Conductivity (W/mK)
400	0.5-1.0	0.30-0.35	800-1,000	0.10
600	1.0-1.5	0.22-0.25	1,000-1,500	0.11
800	1.5-2.0	0.20-0.22	2,000-2,500	0.17-0.23
1000	2.5-3.0	0.15-0.18	2,500-3,000	0.23-0.30
1200	4.5-5.5	0.09-0.11	3,500-4,000	0.38-0.42
1400	6.0-8.0	0.07-0.09	5,000-6,000	0.50-0.55
1600	7.5-10.0	0.06-0.07	10,000-12,000	0.62-0.66

Jones and McCarthy (2006) reported that a small change of w/c ratio does not influence the strength of cellular concrete. On the other hand, The long-term (180 days) compressive strength of cellular concrete with 30% of cement replaced by fly ash is not significantly different from ordinary cellular concrete (Jones et al. 2003). Furthermore, The amount of cement replaced by fly ash could up to 75% without significantly impacting the strength (Kearsley and Wainwright 2001).

ii. Porosity and Permeability

The cellular concrete porosity is related to strength properties such as compressive strength and flexural strength. The porosity of cellular concrete is influenced by its pore diameter, distribution, continuity, tortuosity, and type of foam agent. The most effective method for measuring the porosity of the cellular concrete is the total vacuum saturation method as it is reported to have 66% and 13% greater accuracy than the apparent and mercury intrusion porosimetry method. The permeability of cellular concrete is a measure that expresses the level of water flowing under pressure in a saturated porous medium. The permeability is related to the water absorption of the cellular concrete. The permeability of cellular concrete is found to be almost twice as normal concrete (Kearsley and Wainwright 2001). ACI 523.1R reported the permeability values for lightweight cellular concrete ranging from 1×10^{-4} to 1×10^{-5} mm/s.

iii. Sorptivity

Sorptivity describes the water absorption and movement in material via capillary action (Amran et al. 2015). Lightweight cellular concrete's sorptivity relies on pore structure, filler type, permeation mechanism, foam agent, and curing conditions (Ramamurthy et al. 2009). The sorptivity of lightweight cellular concrete is increased when its foam volume increased. The addition of fly ash into the mixes in place of sand also raises its sorptivity (Jones and McCarthy 2005).

iv. Drying Shrinkage

It is reported that the lack of aggregate causes cellular concrete to generate ten times of drying shrinkage than normal-weight concrete (Ramamurthy 2009). Ramamurthy (2009) stated that the drying shrinkage of cellular concrete decreased as the density reduced the amount of shrinkage cement paste decreased as well. On the contrary, BCA (1994), McCarthy (2004), and Concrete Society (2009) mentioned that the drying shrinkage would increase when the density is reduced. Table 4 demonstrated the amount of drying shrinkage at different densities.

Jones (2003) reported reducing drying shrinkage by replacing cement content with fine fly ash by up to 30%. Chindaprasirt and Rattanasak (2011) also mentioned reducing drying shrinkage by replacing 30% of fly ash, which is shown in Figure 2-4. Fly ash plays a role as the shrinkage reducer due to its pozzolanic property. The fine particles of fly ash added into the cement paste help the pore refinement. It generated the segmentation of large pores and create nucleation sites for the precipitation of hydration products. Moreover, in ACI 523.1R, lightweight cellular concrete's drying shrinkage is not considered critical when used for geotechnical applications. This is because the bearing capacity does not reduce when any shrinkage cracking occurs.

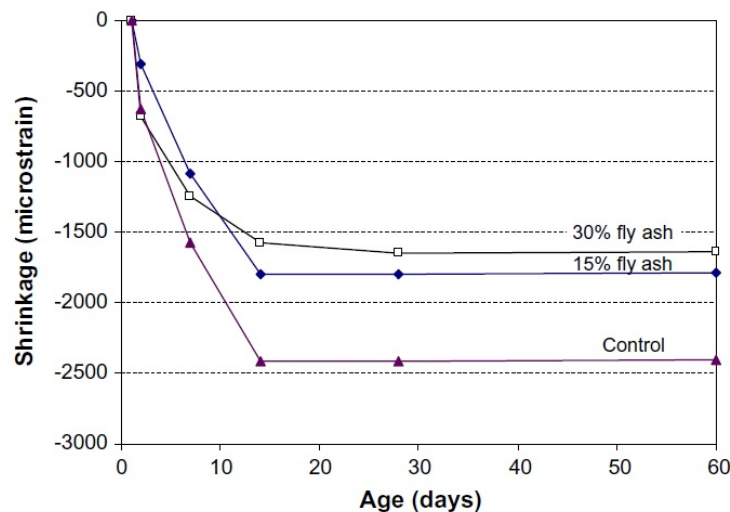


Figure 2-4 Drying shrinkage of lightweight concretes with fly ash (Chindaprasirt and Rattanasak 2011)

v. Freeze-Thaw Resistance

Cellular concrete is considered to have excellent freeze-thaw resistance due to the hollow voids which hold the expansive forces resulting from the freeze water (Brady 2001). It was found that the strength, depth of initial penetration, absorption, and absorption rate of the cellular concrete at low density provide good freeze-thaw resistance. Tikalsky et al. (2004) reported the compressive strength of the four specimens with different densities (M1: 629 kg/m³, M2: 631 kg/m³, M3: 497 kg/m³, M6:678 kg/m³) after cycles of freeze-thaw exposures. The mixture was shown to have a compressive strength higher than 1 MPa is durable to freeze-thaw cycles, as shown in Table 2-5. The study also stated that if the air voids in cellular concrete are not saturated with water, then the material's deterioration is impossible. ACI 523.1R stated that the lightweight cellular concrete might require a longer thawing time, and a minimum of 120 cycles should be performed.

Table 2-5 Compressive strength of cellular concrete after cycles of freezing and thawing (Tikalsky et al. 2004)

Cycles	Low-Density Cellular Concrete (MPa)			
	M1	M2	M3	M6
0	1.77	2.07	1.09	0.73
10	1.76	1.98	1.07	0.80
30	1.54	2.17	1.43	0.85
50	1.91	2.05	1.50	0.85
70	1.55	2.10	1.43	0.84
90	1.90	1.92	1.44	1.09
150	1.82	1.96	1.36	1.22

vi. Modulus of Elasticity

The modulus of elasticity in pavement design represents how much the concrete will compress under load (TAC 2013). The modulus of elasticity of the lightweight cellular concrete is considered to be lower than normal-weight concrete. Table 4 showed the typical E-values of cellular concrete ranging from 800 to 12,000 MPa for dry density ranging from 400 to 1,600 kg/m³. The lower E-value of cellular concrete may be attributed to the mix's lack of coarse aggregate (Brady et al . 2001). Jones and McCarthy (2005) compared the modulus of elasticity of cellular concrete with different fine aggregate (Sand and Fly ash) to normal-weight concrete and lightweight aggregate concrete, as shown in Figure 2-5. It is noted that cellular concrete with sand as fine aggregate has a higher E-value than cellular concrete with fly ash. This is due to the lack of small particles to provide an interlocking effect in the structure.

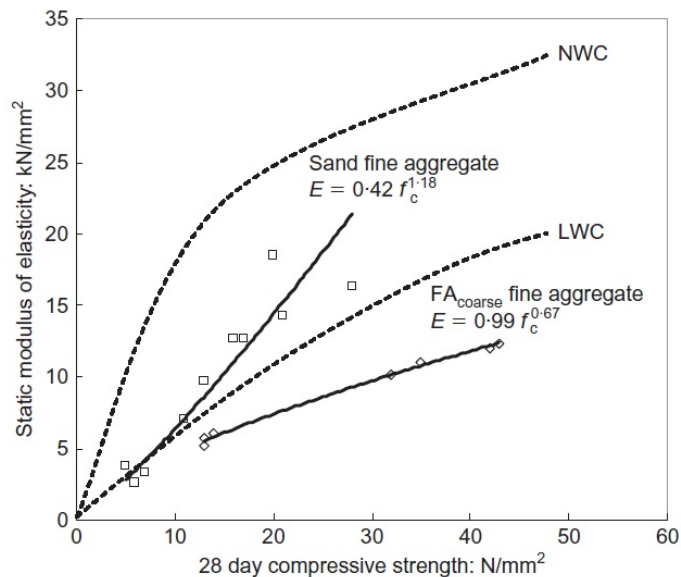


Figure 2-5 Relationship between E-value and 28-day sealed cured cube compressive strength of foamed concrete (Jones and McCarthy 2005)

vii. Flexural Strength

The concrete flexural strength (or modulus of rupture) is the maximum value of allowable stress before the concrete fractured in pavement design (TAC 2013). It is necessary to understand the material's flexural strength before applying it in the pavement layer (Hajek et al. 2016). The flexural strength of low-density cellular concrete is reported to reduce with increasing w/c ratio (De Rose and Morris 1999). The typical range for the ratio of flexural strength to the compressive strength of cellular concrete is 0.25 to 0.35 (Valore 1954). Also, Narayanan and Ramamurthy (2000) reported that the ratio of flexural strength to compressive strength is almost zero when the cellular concrete is produced at a density below 300 kg/m³.

viii. Indirect Tensile Strength

The indirect tensile strength of cellular concrete has a similar trend to compressive strength as it increases with increasing density of the mix (Brady 2001). Kearsley and Mostert (1997) reported that the addition of fiber could increase the tensile strength of cellular concrete. The indirect tensile strength of cellular concrete is lower than the normal-weight concrete and lightweight aggregate concrete, yet the strength value of cellular concrete with sand is higher than those with fly ash. This is due to the interlocking between sand and paste as the shear capacity increased (Ramamurthy et al. 2009). Typically, the tensile strength to the compressive strength ratio of cellular concrete is reported in the range between 0.2 and 0.4, whereas the ratio of normal-weight concrete is between 0.08 and 0.11 (Amran et al. 2015).

ix. Poisson's Ratio

Poisson's ratio is one of the factors to calculate the stress, strain, and displacement within the pavement structure (TAC 2013). Poisson's ratio stands for the ratio of transverse strain to the axial strain. The typical range of Poisson's ratio for normal weight concrete is 0.15 to 0.22 (Neville 2011). Lee et al. (2004) reported the Poisson's ratio of cellular concrete with densities 1,000kg/m³ and 1,400kg/m³, which is 0.13 to 0.16 and 0.18 to 0.19. For density below 1,000 kg/ m³, Ozlutas (2015) stated that the Poisson's ratio for

300, 600, and 1,000 kg/m³ cellular concrete were found to be 0.14, 0.19, and 0.08. Breg (2020) reported the Poisson's ratio of approximate 0.15 to 0.33 for 600 to 2,000 kg/m³ densities with various cellular concrete compositions.

x. Pore Characteristics

Several research studies have been conducted to investigate the pore characteristics of lightweight cellular concrete. The pore structure inside the cellular concrete are a combination of interlayer pores/spaces, gel pores, capillary pores, and air voids. The sizes of the pores varying from nanoscale scale to millimeter scale (Zang and Wang 2016). Chung et al. (2017) evaluated the relationship between the pore characteristics of lightweight cellular concrete with its mechanical properties via the use of Scanning Electron Microscope (SEM) and X-Ray Computed Tomography scan (Micro-CT) technology. The Pore characteristics, such as pore sizes, distributions, shapes and cell thickness are strongly affecting its physical properties and strength (Nambiar and Ramamurthy 2007, Batool and Bindiganavile 2017, Nguyen et al. 2019).

xi. Dynamic property

When constructed on soft soil, geotechnical applications often face challenges such as settlement issues, low shear strength, and bearing capacity. Those issues worsen when the soft soil is located in a seismic area, leading to higher structural requirements. Tiwari et al. (2018) evaluated lightweight cellular concrete's dynamic behavior for possible geotechnical applications such as earth retaining walls. It was found that lightweight cellular concrete showed a decreasing damping ratio trend as the shear strain increased. Moreover, the damping ratios of different densities of lightweight cellular concrete at any effective normal stress did not vary when shear strain is 0.5%.

2.2.6 Cellular concrete concerning sustainable construction

Cellular concrete is a lightweight construction material that can contain up to 80 to 90 percent of the air void at low densities. The high air void content significantly reduced the number of ingredients used and wasted produced (Ozlutas 2015). Jones and

McCarthy (2005) noted that cellular concrete's self-flowing ability excludes the need for compaction, which saves the energy from placement. Furthermore, it is easy to excavate and remove from the site due to its low strength (Concrete Society 2009).

Cellular concrete reduces the use of non-renewable primary sources such as coarse aggregate and fine aggregate at densities below 600 kg/m³ (BCA 1994). Alternatively, Jones et al. (2012) stated that recycled (demolition fines) and industry by-product (fly ash) can be used in cellular concrete as filler. Fine fly ash could also provide several benefits, such as reducing embodied carbon dioxide (eCO₂) and drying shrinkage strains. Ozlutas (2015) demonstrated the influence of replacing Portland cement with fly ash up to 40% in Figure 2-6.

In pavement construction, cellular concrete provides a sustainable solution to soft soil base. This is due to its good constructibility, such as short install time, reducing excavation time, self-compacting, and being placed in winter (Maher 2016).

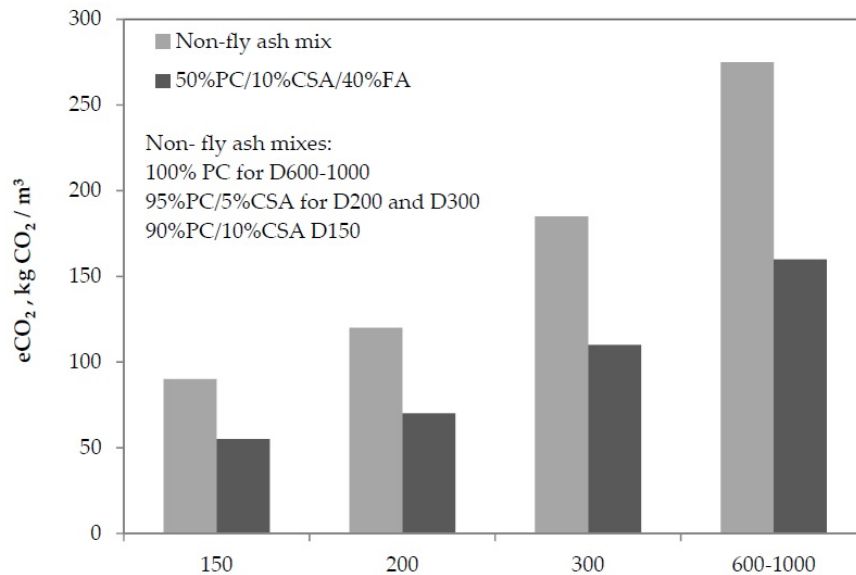


Figure 2-6 Influence of plastic density and fly ash on the eCO₂ of foamed concrete (Ozlutas 2015)

2.2.7 Applications of lightweight cellular concrete

Lightweight cellular concrete has been widely used in civil and structural engineering areas due to its distinctive properties such as reduced density, low thermal conductivity, excellent flowability, self-compaction ability, and relative cost-effectiveness (Amran and Farzadnia, 2015). Sari and Sani (2017) summarized the cellular concrete applications with different densities, as shown in Table 2-6. The typical densities of cellular concrete in the application are between 1,000 kg/m³ to 1,500 kg/m³, mainly used for cast-in-place walls, prefabrication, and housing applications. Densities between 300 kg/m³ to 600 kg/m³ are related to pavement construction as it provides soil stabilization and road construction functions.

Table 2-6 Summary of foamed concrete applications based on density (Sari and Sani 2017)

Density (kg/m³)	Application
300-600	Replacement of existing soil, soil stabilization, raft foundation.
500-600	Currently being used to stabilize a redundant, geotechnical rehabilitation and soil settlement. Road construction.
600-800	Widely used in void filling, as an alternative to granular fill. Some such applications include filling of old sewerage pipes, wells, basement, and subways.
800-900	Primarily used in production of blocks and other non-load bearing building element such as balcony railing, partitions, parapets, etc.
1,100-1,400	Used in prefabrication and cast-in-place wall, either load bearing or non-load bearing and floor screeds.
1,100-1,500	Housing applications.
1,600-1,800	Recommended for slabs and other load-bearing building element where higher strength required.

The application of lightweight cellular concrete has become popular in the world. For instance, it has been a solution for the southern US regions suffering from the housing shortage or adverse weather such as hurricanes and earthquakes. The lightweight cellular concrete were also considered as an impact-resistant materials which had been used as an aircraft captured material in the U.S.A (Clark and Lange 2021). In Canada, lightweight cellular concrete is used as a filler for tunnel annulus grouting, flowable fills, and geotechnical applications. The annual market size of lightweight cellular concrete in the UK is estimated to be 250,000 to 300,000 m³ annually, including an extensive mine stabilization project. This is the same market size in Korea while used as an essential component in a floor heating system. Lightweight cellular concrete was used as subbase material in Holland due to the low traffic loading and considered cost-effectiveness at the times of repair and rehabilitation. The lightweight cellular concrete also provides resistance to the freeze-thaw cycle and frost heave in concrete paving (Amran and Farzadnia 2015, Mindess 2019).

2.3 Performance Prediction Models

Unconfined compressive strength (UCS), modulus of elasticity (E), modulus of rupture (MR), and indirect tensile test (IDT) are the primary characters to determine the strength of the cellular concrete (Hajek et al. 2016, Jones and McCarthy 2005). Several empirical models regarding these properties with different proportions of constituent and density have been conducted by researchers and described as follows.

2.3.1 Unconfined Compressive Strength

Several studies have been conducted on the prediction model for the unconfined compressive strength of cellular concrete. Amran et al. (2015) listed some of the empirical equations in Table 2-7 that demonstrate a significant relationship between compressive strength and other parameters such as porosity and w/c ratio.

**Table 2-7 Empirical model for foamed concrete compressive strength determination
(Amran et al. 2015)**

Equations	Remarks
$f_c = K \left[\frac{1}{\left(1 + \frac{w}{c}\right) + \left(\frac{a}{c}\right)} \right]^n$	K = empirical constants n = strength to gel-space ratio
$f_c = K_s \ln \left[\frac{P_{cr}}{P} \right]$	P_{cr} = the critical porosity corresponding to zero strength Ks = a constant, “Schiller’s equation.”
$f_c = K g^n$	K = the intrinsic strength of the gel g = the gel-space ratio (Power’s gel-space ratio)
$f_c = P_o(1 - P)^n$	P_o = the strength at zero porosity n = a constant (Balshin’s expression)
$f_c = 1.27f_{c7} + 2.57$	f_{c7} = 7 days compressive strength
$f_c = 1.5e_{con}^{5\gamma}$	When using $w/c = 0.5$ and $s/c = 0$ and using polymer foam agent

2.3.2 Modulus of Elasticity

The modulus of elasticity is related to the density of cellular concrete. Table 2-8 demonstrates the relationship between compressive strength, modulus of elasticity, and density. The empirical equation shows that higher compressive strength and density result in higher modulus of elasticity.

**Table 2-8 Empirical model for foamed concrete modulus of elasticity determination
(Amran et al. 2015)**

Equations	Remarks
$E = 33W^{1.5}(f_c)^{0.5}$	It used Pauw's equation
$E = 0.99(f_c)^{0.67}$	Used when fly ash utilized as fine aggregate
$E = 0.42(f_c)^{1.18}$	Used when sand is utilized as fine aggregate
$E = 5.31 \times W - 853$	Density is ranged between 200 and 800 kg/m ³
$E = 6326(\gamma_{con})^{1.5}(f_c)$	γ_{con} = unit weight of concrete f_c = compressive strength of concrete where average Poisson's ratio = 0.2, and using polymer foam agent
$E = 57,000(f_c)^{0.5}$	Density of normal concrete limited between 2,200 and 2,400 kg/m ³ substituting with 80 kg/m ³ for steel
$E = 9.10(f_c)^{0.33}$	f_c = compressive strength of concrete
$E_c = 1.70 \times 10^{-6}P^2(f_c)^{0.33}$	P = plastic density (kg/m ³)

2.3.3 Modulus of Rupture

Hu et al. (1997) proposed empirical relationships between compressive strength and flexural strength of cellular concrete with a dry density of 500 kg/m³ to 840 kg/m³.

$$F = 0.22 + 0.162C \text{ (Correlation coefficient } r^2 = 0.85) \quad 2.2$$

where:

F=Flexural strength (MPa)

C=Compressive strength (MPa)

Table 2-9 list the empirical equation of flexural strength of cellular concrete. The mix is reinforced with polypropylene fibers and fly ash.

Table 2-9 Empirical model for foamed concrete flexural strength determination (Amran et al. 2015)

Equations	Remarks
$f_{crT} = f_{cr}(-0.00526T + 1.01052)$	20 C < T < 400 C
$f_{crT} = f_{cr}(-0.025T + 1.8)$	400 C < T < 600 C
$f_{crT} = f_{cr}(-0.0005T + 0.6)$	600 C < T < 1000 C
	$f_{cr T}$ = flexural strength of foamed concrete at high temperature, f_{cr} = at ambient temperature

2.3.4 Indirect Tensile Test

The indirect tensile test of cellular concrete can be conducted by ASTM C496. Table 2-10 present the developed equations showing the significant relationship between tensile strength and compressive strength. It is clear that the factors have the same effect on tensile strength as on compressive strength.

**Table 2-10 Empirical model for foamed concrete tensile strength determination
(Amran et al. 2015)**

Equations	Remarks
$f_t = 0.20(f_c)^{0.70}$	For density between 1400 and 1800 kg/m ³
$f_t = 0.23(f_c)^{0.67}$	fc = 28 days compressive strength, N/mm ²
$f_t = 1.03(f_c)^{0.5}$	When w/c = 0.5 and fc = 28 days compressive strength, N/mm ²

2.3.5 Fatigue cracking

The performance model for a chemically stabilized material in MEPDG is the Fatigue cracking model. It is stated in MEPDG that the reflective crack to the HMA layer may be minimized or eliminated if a crack relief layer is placed between the HMA and chemically stabilized material layer (AASHTO 2008). The fatigue model in MEPDG is:

$$\log N_f = \frac{0.972\beta_{c1} - \left(\frac{\sigma_t}{MR}\right)}{0.0825 \times \beta_{c2}} \quad 2.3$$

where:

N_f = number of repetitions to fatigue cracking of the CSM layer.

σ_t = maximum traffic induced tensile stress at the bottom of the CSM layer(psi)

MR = 28-day Modulus of Rupture (Flexural Strength) (psi)

β_{c1},β_{c2} = field calibration factors

2.4 Case Studies in Canada

As mentioned in section 2.2.6, lightweight cellular concrete could be used in pavement applications. Averyanov (2018) summarized a list of case studies in Canada that used lightweight cellular concrete as pavement subbase material in Table 2-11. It should be noted that visual field inspection indicated that these roads perform well in their current state, and significant crackings or severe ruttings were merely found. Griffiths and Popik (2013) mentioned that the structural coefficient of lightweight cellular concrete is approximately 0.2. This is back-calculated using the results from the Falling Weight Deflectometer (FWD) test, and the structural coefficient of the asphalt concrete layer and the granular base layer is 0.38 and 0.12, respectively. The composite elastic modulus of lightweight concrete sections ranged from 714 to 737 MPa. This is at least 3.5 times greater than unbound Granular B material, which typically has a modulus of 200 MPa (Applied Research Associate 2015).

Table 2-11 Summary of Cases of Using LCC as a Subbase Material in Pavement Structure in Canada (Averyanov 2018)

	Dixie Road. Region of Peel, Ontario	Highway 9, Holland Marsh, Ontario	View and Vancouver Streets, City of Victoria, British Columbia	Brentwood Light Rail Transit (LRT) Bus-Lane. Calgary, Alberta	Winston Churchill Boulevard, Brampton. Ontario
Cause of Reconstruction	Settlement. Length-120m Peat/marl deposits were located from the depth of 2.1 m to 5.4 m below the existing pavement surface	Settlement. Length-100m Underlain with organic materials (peat) and inorganic (soft to firm clayey silt to silty clay or compact silt and sand)	Settlement. Length 430m on View Street and 137m on Vancouver Street. Excessive decay and consolidation of the underlying peat	Length-60m. Severe frost heave and subsequent spring thaw weakening of the frost susceptible soils.	Settlement. Length300m. Underlain with peat
Year of Construction	2009	2014	2007	2000	2016
Road Type	Rural Highway	Highway	Urban	Urban	Rural

Table 2-11 Summary of Cases of Using LCC as a Subbase Material in Pavement Structure in Canada (Averyanov 2018), Continued

	Dixie Road, Region of Peel, Ontario	Highway 9, Holland Marsh, Ontario	View and Vancouver Streets, City of Victoria, British Columbia	Brentwood Light Rail Transit (LRT) Bus-Lane. Calgary, Alberta	Winston Churchill Boulevard, Brampton. Ontario
Material Composition	CEMATRIX CMEF-475. “Dry” mix	CEMATRIX-475. “Wet” mix	CEMATRIX-475. “Wet” mix	CEMATRIX CMRI-475.	CEMATRI X-475. “Dry” mix
Pavement Structure	AC-140mm; Granular ‘A’- 150mm; LCC–650mm	AC-200mm; Granular “O” base layer-200mm; LCC-1100mm; Biaxial geogrid (300m from the top of LCC layer)	AC-75mm; Crushed Granular base course 150mm; LCC-500mm; (Tensar BX1100 geogrid was placed between the LCC layers)	AC-125mm; Granular base course-150mm; LCC-200mm; drainage rock- 50mm; Geotextile fabric (at the bottom of LCC layer)	AC-120mm; Granular base course 240mm; LCC-550mm; geogrid reinforce fiber glass
Performance Evaluation	Visual inspection, FWD, Benkelman Beam test	Visual inspection	FWD, Benkelman Beam test	Visual inspection, Benkelman Beam test	Visual inspection

2.5 Classification of LCC in the Mechanistic-Empirical Pavement Design Guide (MEPDG)

2.5.1 Material categories for flexible pavement design

In the Mechanistic-Empirical Pavement Design Guide (MEPDG), the primary material category for flexible pavement design includes the following (AASHTO 2008):

1. Hot-mix asphalt
2. Asphalt stabilized base
3. Cement stabilized base
4. Other chemically treated materials (e.g., lime-fly ash, soil cement, lime-stabilized soils, etc.)
5. Unbound aggregate base/subbase
6. Subgrade soils

Since the definition of LCC mentioned it is a cementitious material, it may be suitable to categorize it as a cement stabilized base or chemically treated material in MEPDG. It is noted that the cement-treated and other pozzolanic stabilized materials should be treated as a separate layer when used as a base layer for structural support. The layer could be considered an unbound material with constant layer modulus if it is not designed to provide long-term strength and durability. Alternatively, these treated or stabilized layers could be classified as a chemically stabilized structural layer if they can provide structural support.

2.5.2 Input characterization for the chemically stabilized materials

In MEPDG, the necessary strength and modulus properties of chemically stabilized materials are the modulus of elasticity (MOE) or resilient modulus (M_r), minimum modulus of elasticity (MOE), or resilient modulus (M_r) after damage from traffic, flexural

strength, and Poisson’s ratio. On the other hand, the required thermal properties are thermal conductivity and heat capacity.

A. Compressive Strength

Table 2-12 demonstrated the minimum requirement of compressive strength for the chemically stabilized material used as the base, subbase, and subgrade layers in the rigid or flexible pavement. Compared to the typical compressive strength of LCC at different densities in Table 1, it is found that LCC with a density lower than 600 kg/m³ does not meet the MEPDG requirement for minimum compressive strength in the subbase.

In addition to minimum compressive strength satisfaction, it should also ensure that the chemically stabilized materials satisfy the durability (e.g., freeze-thaw resistance) requirement.

Table 2-12 Minimum Compressive Strengths for Cement, Lime, and Combine Lime, Cement, Fly ash Stabilized Materials (AASHTO 2008)

Stabilized Layer	Minimum Unconfined Compressive Strength MPa (psi) ^{1,2}	
	Rigid Pavement	Flexible Pavement
Base Course	3.45 (500)	5.17 (750)
Subbase, Select Material, or Subgrade	1.38 (200)	1.72 (250)

1. Compressive strength determined at 7-days for cement stabilization and 28-days for lime and lime-cement-fly ash stabilization.
2. These values shown in the table should be modified as needed by the local agency for specific site conditions.

B. Modulus of Elasticity

The typical value of modulus of elasticity and resilient modulus used in MEPDG are listed in Table 2-13. It shows a significant difference when comparing the typical E-value of LCC to the MEPDG inputs.

Table 2-13 Summary of typical resilient modulus values for chemically stabilized materials (AASHTO 2008)

Chemically Stabilized Material	MOE or Mr Range (MPa)	MOE or Mr Typical (MPa)
Lean concrete	10,342 to 17,236	13,790
Cement stabilized aggregate	4,826 to 10,342	6,895
Open graded cement stabilized aggregate	-	5,171
Soil cement	345 to 6,895	3,447
Lime-cement-fly ash	3,447 to 13,790	10,342
Lime stabilized soils	207 to 414	310

C. Flexural Strength

The typical ratio of flexural strength (MR) to compressive strength in MEPDG for cement-treated aggregate is 0.20. The typical range of flexural strength to compressive strength for cellular concrete is 0.25 to 0.35. The standard input of flexural strength is listed in Table 2-14.

**Table 2-14 Typical flexural strength (MR) values for chemically stabilized materials
(AASHTO 2008)**

Chemically Stabilized Material	Typical MR (MPa)
Lean concrete	3.10
Cement stabilized aggregate	1.38
Open-graded cement stabilized aggregate	1.38
Soil cement	0.69
Lime-cement-fly ash	1.03
Lime stabilized soils	0.17

D. Poisson’s Ratio

Poisson’s Ratio is an essential factor for structural analysis. The recommended range of Poisson’s Ratio is shown in Table 2-15.

**Table 2-15 Recommended ranges of Poisson’s ratios for chemically stabilized
materials (AASHTO 2008)**

Material	Poisson’s Ratio
Cement Stabilized Aggregate	0.1 to 0.2
Soil Cement	0.15 to 0.35
Lime-Fly Ash Materials	0.1 to 0.15
Lime-Stabilized Soil	0.15 to 0.2

Although the LCC is considered a chemically stabilized material, it is evident that its specific engineering properties differ from the characteristic value of chemically stabilized materials in MEPDG. This indicates the need to develop new models and inputs for the LCC to integrate into the MEPDG.

2.6 Summary of Gaps related to lightweight cellular concrete

The previous studies mentioned several properties of lightweight cellular concrete. These properties may positively or negatively influence the pavement construction of lightweight cellular concrete. To further describe these effects, they can be categorized into few aspects: constructability, durability, and sustainability.

2.6.1 Constructability

The low density, lightweight, good flowability, and self-compacting ability benefit the lightweight cellular concrete in its constructability. Therefore, the material can be installed quickly, which minimizes the excavation time. Furthermore, it can be placed in winter and does not require compaction and associated testing.

2.6.2 Durability

The strength of the lightweight cellular concrete is highly dependent on its pore characteristics and structure. Pore size, distribution, shapes and cell thickness are the key factors that relevant to its strength. The typical compressive strength of the lightweight cellular concrete at the density of 400 kg/m³ to 600 kg/m³ ranges from 0.5 MPa to 1.5 MPa, which is considered sufficient to support the traffic loads. Furthermore, the lightweight cellular concrete is found to resist the freeze-thaw and frost heave. This makes it a trustable material for the pavement subbase layer to protect the weak subgrade soil.

2.6.3 Sustainability

The lightweight cellular concrete is considered to be a sustainable material due to several reasons. First, it reduces the need to excavate natural aggregate as it does not contain coarse aggregate. Moreover, sand can be replaced by industrial by-products such as fly ash in low density lightweight cellular concrete. As it provides good freeze-thaw resistance and strength to protect the subgrade soil, reducing the times of repair and

rehabilitation of the pavement. Finally, the good constructability simplified the traffic staging, thus reducing traffic interruption.

2.6.4 Pavement applications in Canada

A few pavement applications use lightweight cellular concrete as subbase material in Canada. Visual field inspection indicated that these roads perform well in their current state. However, performance evaluations among these cases are limited. Only Dixie road had a structural evaluation using the FWD test, which gave an approximate structural coefficient of 0.2 for lightweight cellular concrete.

2.6.5 Gaps

Some applications are using lightweight cellular concrete as pavement layer materials. However, some gaps need to be identified about lightweight cellular concrete in pavement construction.

First, it has been stated that lightweight cellular concrete has excellent freeze-thaw resistance. This material is not expected to fail if it is not saturated with water. However, past research does not consider situations like the pavement structure, where the material could be fully saturated with water.

Second, there is a lack of standards, specifications, and guidelines for using lightweight cellular concrete in the current pavement design method. A complete assessment of how to determine the layer thickness when using lightweight cellular concrete is needed.

Third, pavement application involves a multi-layer structure affected by traffic loading and the environment. Even though some pavement applications use lightweight cellular concrete, the structural and bearing capacity under traffic loading of lightweight cellular concrete is yet to be evaluated in the pavement structure.

Chapter 3 Research Methodology

This research investigates the applicability of using lightweight cellular concrete as a subbase layer in pavement design. Therefore, two core aspects are considered: lightweight cellular concrete's structural capacity and durability. Lightweight cellular concrete's structural capacity is directly related to its strength, such as compressive strength, flexural strength, and modulus of elasticity. Lightweight cellular concrete's durability is linked to its water absorption, permeability, sorptivity, and freeze-thaw resistance. It is essential to understand its bearing capacity with different densities and constituent composition under traffic loading. Moreover, the pore characteristics of lightweight cellular concrete is found to be related to its strength. Therefore, the microstructure of lightweight cellular concrete is examined to determine its pore characteristics.

Furthermore, drying shrinkage and dynamic property should also be considered as supplementary data. The laboratory results will be used as the input parameters for the pavement performance analysis. The analysis will be performed through pavement performance software such as Weslea 3.0 and MEPDG software. Performance comparison between the LCC with different densities will be done. Figure 3-1 outlines the laboratory tests and field works for this research. The detailed description of each task is explained in the following sections.

3.1 Laboratory Experiment

The lightweight cellular concrete at three different plastic densities is used in this study. The samples will be provided by CEMATRIX (Canada). The sample densities are 400 kg/m³, 475 kg/m³, and 600 kg/m³. These are the common densities been specified in past research for pavement construction and used in Canada in the past. The properties such as w/c ratio, air content, and constituent materials are obtained during the mix's production. The following sections discussed the laboratory tests planned to perform on the materials: Structural tests, Durability tests, and other property tests.

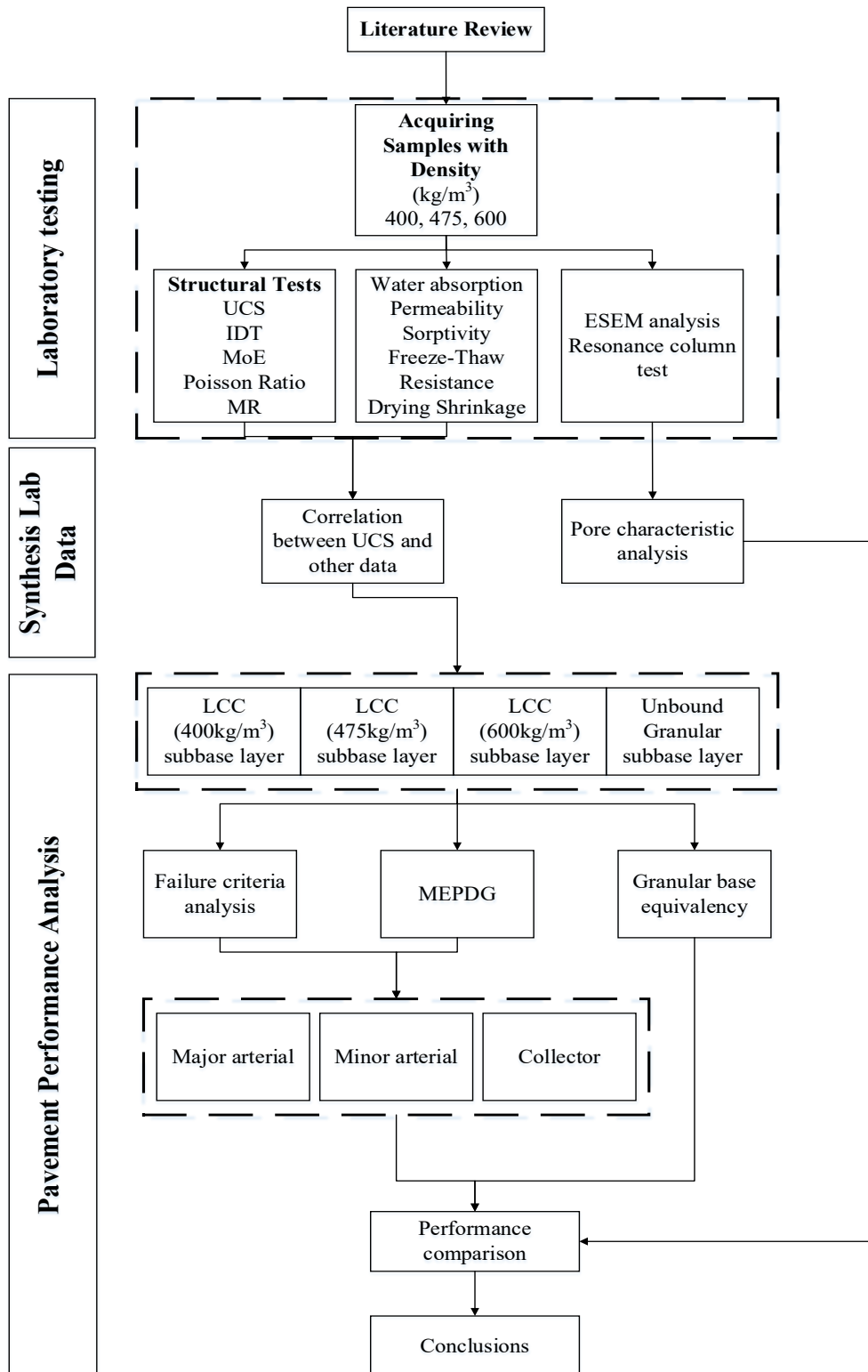


Figure 3-1 Proposed Research Methodology

3.1.1 Unconfined Compressive Strength

The test method of unconfined compressive strength of cellular concrete is described in ASTM C 495. Figure 3-2 demonstrates the test setup. The test specimen is specified to be a 75 by 150 mm cylinder. For each density, a total of four specimens should be applied in the test (ASTM C 796). The specimen should be cured at a temperature of 21 ± 6 °C in the first 24 hours after demolded. Place the specimens in a moist condition at a temperature of 23 ± 2.0 °C after it was cured after 24 ± 2 hours from day 2 to day 25. After that, dry the specimens at a temperature of 21 ± 6 °C with a relative humidity of $50 \pm 10\%$ for three days. During testing, ensure that the load is applied at a constant rate and the maximum load should be reached in 65 ± 15 seconds. The following equation calculates the UCS of the specimen.

$$\text{UCS} = \frac{P}{A} \quad 3.1$$

Where:

UCS = unconfined compressive strength, MPa

P = maximum load recorded, kN

A = the cross-sectional area of the specimen, mm²

The curing times for the UCS test are 1,3,7,14,28 days. The purpose of testing the specimens at 1 and 3 days is to determine the strength growth in the early stage as the construction of the base and surface layer may begin after one day of curing. Therefore, it is essential to understand whether the material has enough strength for the construction equipment.

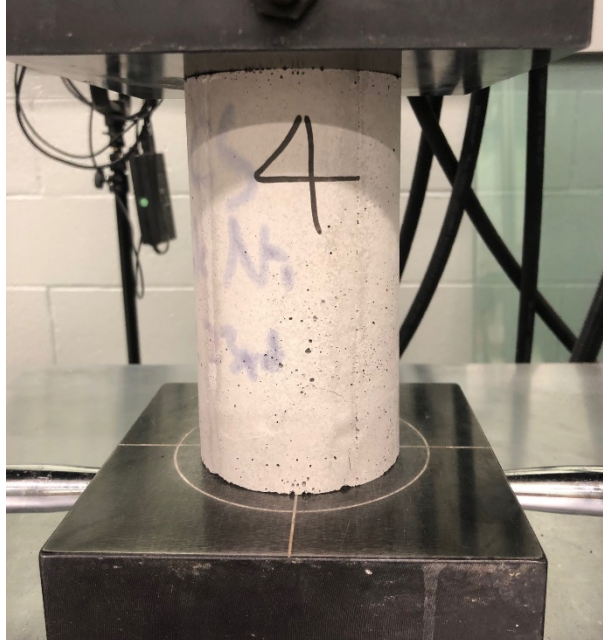


Figure 3-2 Unconfined Compressive Strength test setup

3.1.2 Splitting Tensile Test

The test method of splitting tensile test should conform to ASTM C 496. The test specimen is a cylinder sample with a diameter of 150 mm and a length of 300 mm. Like the UCS test, a total of four specimens should be applied in the test for each density (ASTM C 796). It is noted that the specimens should be placed in an air-dry condition at a temperature of 23 ± 6 °C and 50 ± 5 % relative humidity for 21 days after seven days of moist cure. The specimen should be positioned using an aligning jig before testing, as shown in Figure 3-3. The constant load rate should be in the range of 0.7 to 1.4 MPa. The splitting tensile strength can be calculated with the following equation:

$$T = \frac{2P}{\pi ld} \quad 3.2$$

Where:

T = splitting tensile strength, .MPa

P = maximum applied load indicated by the testing machine, N

l = length, mm

d = diameter, mm

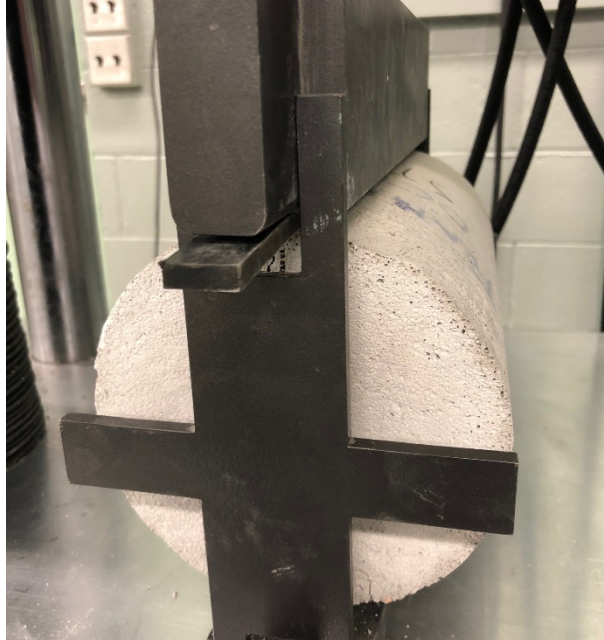


Figure 3-3 Splitting Tensile Strength test setup

3.1.3 Modulus of Elasticity and Poisson's Ratio

The test method for determining the modulus of elasticity and Poisson's ratio is in accordance with ASTM C 469. The dimension of the specimen is 150 mm by 300 mm for each cellular concrete density. At least two specimens should be tested for each density to determine the compressive strength. The 40% of the maximum load determined in the trial test is the maximum load for the elasticity test. The use of compressometer and extensometer is necessary to measure the modulus of elasticity and Poisson's ratio as they provide readings for longitudinal strain and lateral strain. The configuration of the test apparatus is shown in Figure 3-4. The calculation of the two parameters are described as follow:

For Modulus of Elasticity

$$E = \frac{(S_2 - S_1)}{(\varepsilon_2 - 0.000050)} \quad 3.3$$

Where:

E = chord modulus of elasticity, MPa

S₂ = stress corresponding to 40% of ultimate load, MPa

S₁ = stress corresponding to a longitudinal strain, ε₁, of 50 millionths, MPa

ε₂ = longitudinal strain produced by stress S₂

For Poisson's ratio:

$$\mu = \frac{(\varepsilon_{t2} - \varepsilon_{t1})}{(\varepsilon_2 - 0.000050)} \quad 3.4$$

Where:

μ = Poisson's ratio

ε_{t2} = transverse strain at midheight of the specimen produced by stress S₂

ε_{t1} = transverse strain at midheight of the specimen produced by stress S₁

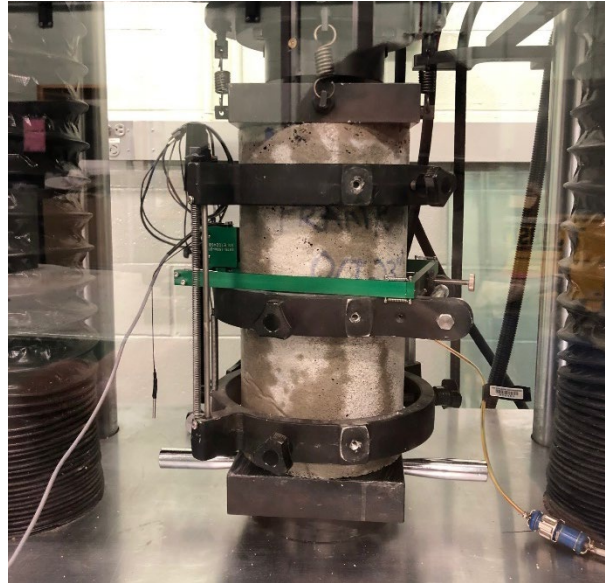


Figure 3-4 Modulus of Elasticity and Poisson's ratio test setup

3.1.4 Modulus of rupture

The flexural strength of lightweight cellular concrete will be determined through the test method conforming to ASTM C78. The test specimen is a beam that is 100 mm wide, 100 mm thick, and 400 mm long. The test is planned to conduct seven days and 28 days specimen to simulate the early stage and saturate phase of the lightweight cellular concrete. The example of the test layout is demonstrated in Figure 3-5. The modulus of rupture could be calculated with the following equation if the fracture of the specimen initiates at the middle third position.

$$R = \frac{PL}{bd^2} \quad 3.5$$

Where:

R = modulus of rupture, MPa

P = maximum applied load indicated by the testing machine, N

L = specimen length, mm

b = average width of the specimen, mm, at the fracture

d = average thickness of the specimen, mm, at the fracture

If the fracture was found outside of the middle third of the specimen length no more than 5% of the span length, use the following equation to calculate the modulus of rupture instead.

$$R = \frac{3Pa}{bd^2} \quad 3.6$$

Where:

a = average distance between the line of fracture and the nearest support measured on the tension surface of the beam, mm



Figure 3-5 Modulus of Rupture test layout

3.1.5 Water absorption

The water absorption could be used to assess the permeability of cellular concrete. Two different lightweight cellular concrete dimensions were tested, which are 75 by 150 mm cylinder and 150 by 300 mm cylinder. The test setup is shown in Figure 3-6. The

conditioning method was modified to simulate field conditions, in which the specimens were cured in the sealed mold for 28 days and immersed in the water right after demolded and trimmed. Initial weight was measured before it was immersed in water, and the following measurement was recorded after immersed in water for 1, 3, 7, 14, 28, 56, and 90 days. Before recording the wet mass of the specimen, immersing it into a 23.0 ± 2.0 °C water and wait 30 seconds for the excess water to run off after removing it from the tank. The water absorption could be calculated by the equation (ASTM C769):

$$\text{Absorption, \% by volume} = 100 \frac{V_w}{V_c} \quad 3.7$$

Where:

V_w = volume of water absorbed by test specimen in 24 h, m^3

V_c = volume of test specimen (cylinder), m^3

The oven-dried samples' water absorption was also measured by putting the sample into the oven at 110 °C for 24 hours and record the mass.



Figure 3-6 Water absorption test layout

3.1.6 Permeability test

The permeability test was performed using the Gilson NCAT Asphalt Field Permeameter Kit (AP-1B). The test procedure was developed by the National Center for Asphalt Technology (NCAT). The test is based on the falling head principle of permeability. The water level change from the beginning to the end of the test is observed, and the time was recorded. The coefficient of permeability is calculated as follows:

$$K = \left(\frac{aL}{At}\right) \ln\left(\frac{h_1}{h_2}\right) \quad 3.8$$

Where:

K = coefficient of permeability.

a = inside cross-sectional area of standpipe, cm²

(Varies depending on tier used for testing; see listed values in Calculation section.)

L = length of the sample, cm (thickness of the asphalt mat)

A = cross-sectional area of permeameter through which water can penetrate the pavement (test area), cm².

t = Elapsed time between h₁ and h₂.

h₁ = Initial head, cm.

h₂ = Final head, cm.



Figure 3-7 Permeability test layout

3.1.7 Sorptivity test

The sorptivity stands for the rate of water absorption, which is a measure that determines the capacity of the medium to absorb liquid by capillarity. The sorptivity test was performed by a modified method in accordance with ASTM C 1585. The specimens were cast in 150 mm by 300 mm cylinder molds for 21 days. The specimens were then put into the humidity chamber at 21 ± 6 °C with a relative humidity of $50 \pm 10\%$. Within 28 days, the specimens were demolded and cut to three 150 mm by 75 mm cylinders. Before performing the test, the samples were cured in the air at room temperature and oven at 50 °C for one day. To prevent the water from infiltrating from the side of the sample, the side was sealed by duct tape. The top of the sample was covered by wrap to prevent water vapor. Sealed samples were then placed into the container with a support stand underneath. The containers were filled with water. The water level is controlled to a range of 1 to 3 mm. The weight of the samples was measured at a certain time and use the following equation to calculate the absorption.

$$I = \frac{m_t}{a \times d} \quad 3.9$$

Where:

I = the absorption,

m_t = the change in specimen mass in grams, at the time t ,

a = the exposed area of the specimen, in mm^2 , and

d = the density of the water in g/mm^3 .

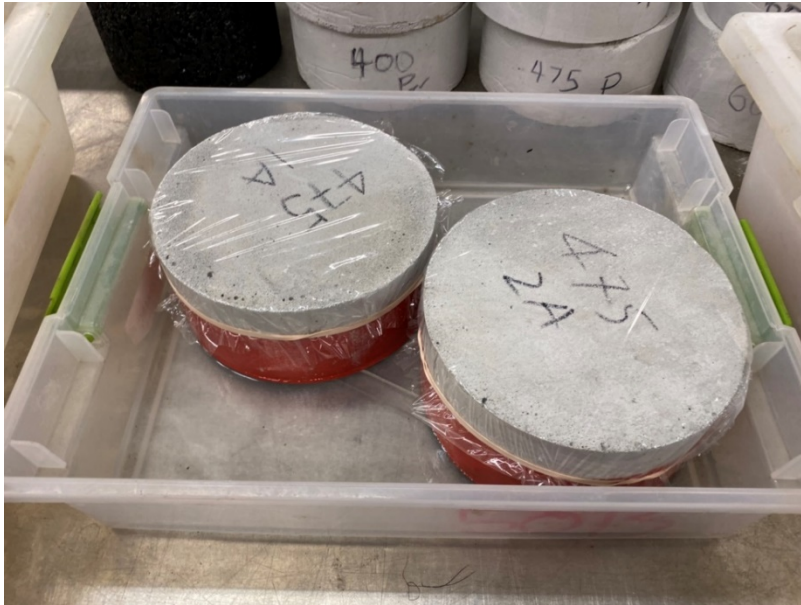


Figure 3-8 Sorptivity test setup

3.1.8 Freeze-thaw resistance

The test method for assessing the freeze-thaw resistance of normal weight concrete is described in ASTM C 666. The mass loss and natural frequency of the specimen are monitored after cycles of freezing and thawing. The target freezing temperature is $-18 \pm 2^\circ\text{C}$ and the target thawing temperature is $4 \pm 2^\circ\text{C}$. The standard provides two procedures to perform the freeze-thaw test. Procedure A tests the specimen consists of freezing and thawing the specimens in the water, while Procedure B freezes the specimen in air and thaws the specimens in the water. Procedure A was considered to be a more aggressive way for freeze and thaw cycling. Therefore, this research used Procedure B with a modified freeze and thaw cycling time to perform the test. According to Tikalsky (2004),

the cellular concrete has good freeze and thaw resistance and will not be damaged when the samples are not saturated. The cellular concrete also has excellent insulation properties which lower the speed at which the target freezing temperature is reached. The freezing time for cellular concrete is between eight to ten hours while thawing to target temperature takes one to two hours. Therefore, this research adopted the same freezing and thawing conditions to Tikalsky's research. However, considering that pavement is not always saturated. This research also performed thaw in air scenario, which the samples were freeze in air and also thawed in air. The curing and pre-conditioning followed with the thaw in water scenario.

The test specimens that were used to perform the test in this research is 76 by 102 by 406 mm beams, which is within the range of the requirement. Total of four specimen per densities were tested in this research. The general testing procedures are listed as follow:

- I. Cured the specimens for at least 28 days before testing.
- II. Saturate the specimen in water for 28 days or the change of weight is less than 1% in two days.
- III. Measure the fundamental transverse frequency, mass, and average value of the specimen's length and dimension after bringing down the temperature to -1 °C and 2 °C.
- IV. Place the specimen in the thawing water/air to start the freeze-thaw cycle. measure the fundamental transverse frequency, dimension, and mass of each specimen every 15 cycles. Put the specimens back to the apparatus after the measurement.
- V. The freezing time is between 8 to 10 hours, while thawing take one to two hours to complete for both water and air.
- VI. Repeat the procedure until 180 cycles are reached, or the relative dynamic modulus reaches 70% of the initial figures.

The relative dynamic modulus of elasticity can be calculated with the following equation:

$$P_c = \left(\frac{n_1^2}{n^2} \right) \times 100 \quad 3.10$$

Where:

P_c = relative dynamic modulus of elasticity, after c cycles of freezing and thawing, percent

n = fundamental transverse frequency at 0 cycles of freezing and thawing

n_1 = fundamental transverse frequency after c cycles of freezing and thawing

The Durability factor can be calculated with the formula:

$$DF = \frac{PN}{M} \quad 3.11$$

where:

DF = durability factor

P = relative dynamic modulus of elasticity at N cycles, %

N = number of cycles at which P reaches the specified minimum value for discontinuing the test or the specified number of cycles at which the exposure is to be terminated

M = specified number of cycles at which the exposure is to be terminated

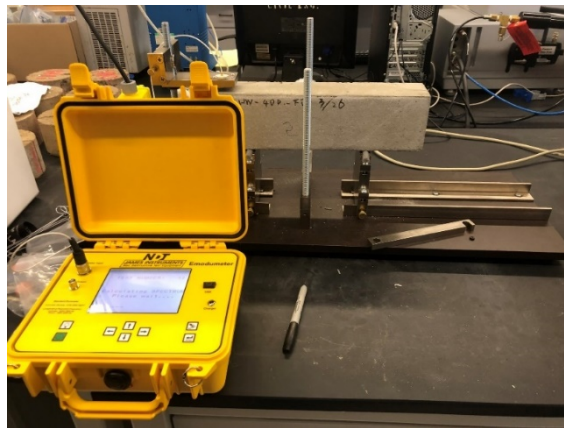


Figure 3-9 Test setup of freeze-thaw resistance test

3.1.9 Drying Shrinkage

The evaluation of drying shrinkage was carried out following ASTM C157. The dimension of the specimens was 100 by 100mm for cross-section area and a length of 285mm. A total of four specimens were tested for each density. It should be noted that it took seven days for curing before demolding the specimens for this test. The demolded specimens were immersed in lime-saturated water for 21 days. The specimens were kept in the air storage method with a relative humidity of $50 \pm 4\%$ and room temperature of 23 ± 2 °C for twenty-eight days. Initial readings were taken using the length comparator after the specimens were demolded and immersed in water for twenty-four hours. The second readings were taken after the specimens completed fifty-six days of being immersed in water (twenty-one days) and been air stored (twenty-eight days). The length change of the specimens was then reported.

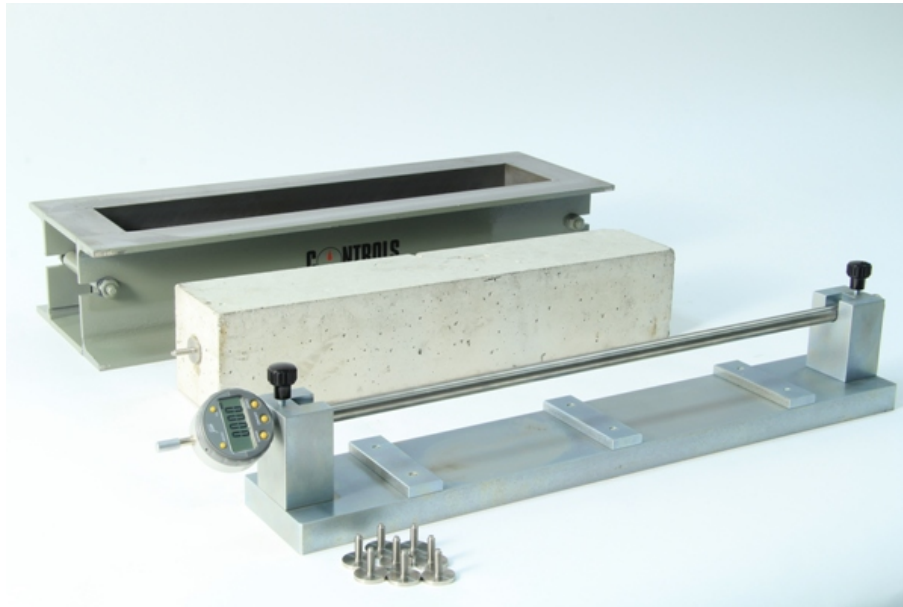


Figure 3-10 Typical layout of the drying shrinkage test (ControlsGroup)

3.1.10 Resonant Column test

The resonant column test was performed in accordance with ASTM D 4015. Two samples of each density were tested at 120 days. The dimension is 75 by 150 mm

cylindrical for all the samples. Torsional sinusoidal vibrations were applied to the samples during testing to obtain the equivalent elastic shear modulus and damping capacity. According to the standard, the amplitude of vibration (related to shear strain) varies to determine the variation of modulus and damping as a function of shear strain. Figure 3-10 demonstrates the test layout and measurement chart.

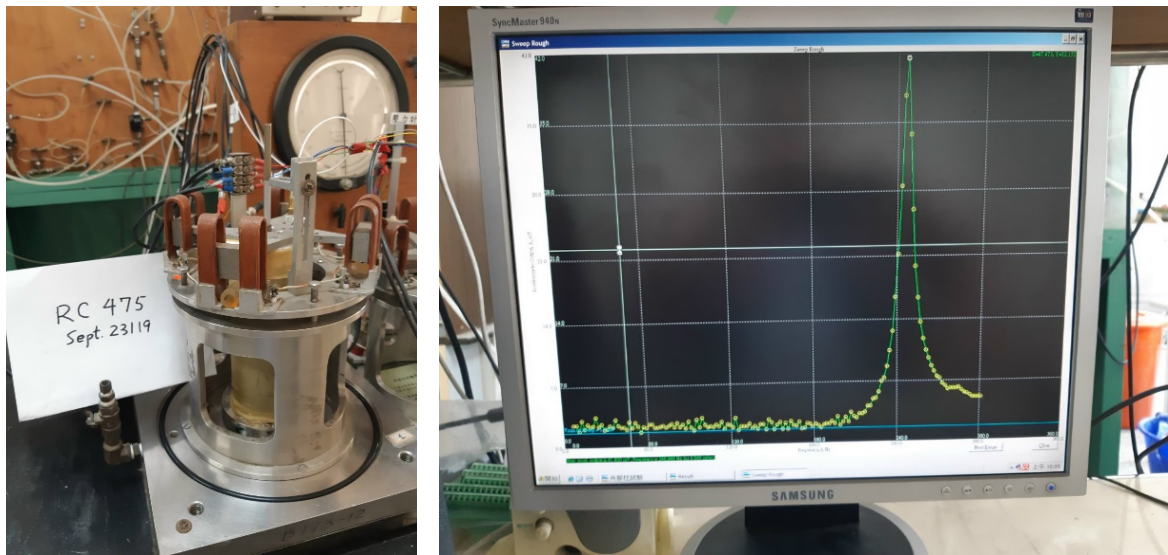


Figure 3-11 The layout of the resonant column test

3.2 Laboratory data analysis

In this section, the laboratory test results will be used to discover the relationship between structural properties and physical properties. The strength of the lightweight cellular concrete is influenced greatly by porosity and density. Therefore, UCS results will be used to examine the relationship between the concrete's density and porosity. Other relationships between the UCS and other factors are also planned to seek, such as the indirect tensile strength, modulus of elasticity, flexural strength. The reason for choosing UCS as the main factor is its accessibility as it is easy to conduct the UCS test than other tests.

The freeze-thaw test results are planned to validate the hypothesis of the lightweight cellular concrete as it is assumed to have excellent freeze-thaw resistance. Porosity, water

absorption, Permeability, Sorptivity, and drying shrinkage are factors for evaluating the potential risk of water penetrating the subgrade soil for lightweight cellular concrete.

3.3 Summary of Methodology

This section described the flow of methodology for this research and most of the laboratory tests of this research. The laboratory tests were related to mechanical properties and other properties such as permeability, water absorption, drying shrinkage, sorptivity, and dynamic property. Other tests like microstructure and freeze and thaw test were explained in Chapter 5 and 6. The above tests results were key element in this research. The details presented in this chapter may benefit other researchers who wish to conduct laboratory testing for the lightweight cellular concrete.

Chapter 4 Laboratory data analysis

4.1 The mix design and production of LCC

Table 4-1 outlined the production of lightweight cellular concrete. Three different densities (400, 475, and 600 kg/m³) of lightweight cellular concrete were cast and studied in this research. Cement, slag, and water were used in the base mixture. The mixture used 80% of General Use Portland cement and 20% of grade 80 Newcem blast furnace slag. The material properties of the cement and slag are reported in Tables 4-2 and 4-3. The water to cementitious material ratio was 0.5 for all mixes. The target density of the cement slurry was 1,823 kg/m³. Once the target density was reached, the pre-foamed foam was added into the slurry to bring down the plastic density to 400, 475, and 600 kg/m³.

The lightweight cellular concrete was mixed in a laboratory drum mixer. Portland cement, slag, and water were first blended for ten minutes. To ensure the quality of the slurry, plastic density and the slurry temperature were checked after the blend. Furthermore, a marsh cone test was conducted to confirm the mix met the desired requirement. According to industrial experience, it was found that 45 to 90 seconds could provide a stable and quality cement slurry. Once the slurry is completed, the pre-foamed foam was added to the base mix. The pre-foamed foam was made by mixing a protein-based foaming agent with the water and created by using compressed air.

The plastic density of cellular concrete was continuously checked to ensure the target plastic density was reached. The mixing procedure generally conformed to ASTM C192 (ASTM 2016), except that, there was no consolidating and vibrating during the molding process since it might harm the bubble structure of the mix. The mixing of the LCC was completed by CEMATRIX, Inc, Canada Lab in Alberta, Canada. All specimens were cured at room temperature instead of placing them into the curing before sending the samples to CPATT Lab. Once the samples were delivered to CPATT Lab, the curing and

demolding of the specimens varied for different tests. The following sections discussed the laboratory tests that were planned and performed on the materials.

Table 4-1 Production of lightweight cellular concrete





Step No.	Descriptions	Photos
1	Cement, slag, and water were mixed to produce the base slurry mix.	
2	Marsh cone test to ensure the quality of base slurry mix.	
3	Foaming agent was used to generate foam.	
4	Adding foam into the base slurry mix.	

Table 4-1 Production of lightweight cellular concrete, Continued



Step No.	Descriptions	Photos
5	Density was continuously checked to meet target density.	
6	Preparation of molds and example of samples	

Table 4-2 Chemical composition of cement and slag (%)

Material	SiO ₂	Al ₂ O ₃	Fe ₂ O ₃	CaO	MgO	SO ₃
Cement	20.2	3.7	4.3	62	4.2	2.5
Slag	34.8	10.6	0.8	39.3	11	-

Table 4-3 Mix design of three densities lightweight cellular concrete

Material	600	475	400
	kg/m ³		
Cement	311	247	208
Slag	78	62	52
Water	195	154	130
Foam	16	13	11

4.2 The properties of hardened concrete

4.2.1 Unconfined Compressive Strength

The unconfined compressive strength of low density lightweight cellular concrete was investigated in this research. Strength is considered the most important property of concrete (Neville 2011). The compressive strength of lightweight cellular concrete had been investigated at low and high density, which 1,000 kg/m³ density is high and 600 to 1,000 kg/m³ density is low. Data for densities below 600 kg/m³ is considered ultra-low, and its compressive strength range is insufficient (Ramamurthy et al. 2009, Ozlutas 2015).

Two batches of lightweight cellular concrete had been tested for unconfined compressive strength (UCS) in 2018 and 2019. The test results are shown in Table 4-4. Compressive strength results showed consistency with past works as it ranged between 0.5 and 1.0 for 400 kg/m³ and 1.0 to 1.5 for 600 kg/m³ (BCA, 1994). The results also showed a strong relationship between density and compressive strength as its coefficient of determination (R^2) is 0.84, as shown in Figure 4-1. T-test had been performed for three densities between two batches, and results had shown no significant differences between the two batches as all the results (p) exceeds 0.05.

With a compressive strength over 0.5 MPa, the lightweight cellular concrete has sufficient strength to support the pavement used as subbase material (Maher and Hagan 2016). Compressive strength was found to increase with the number of days, as illustrated in Figure 4-2. The results showed a consistent increase across days with no outlier data observed. 2018 batch has slightly higher compressive strength than the 2019 batch at 28 days, and the differences are between 0.12 to 0.17 MPa. All three densities samples exceed 0.5 MPa at seven days, while 475 and 600 kg/m³ samples already have 0.53 and 1.02 MPa at three days.

Table 4-4 Test results of Unconfined Compressive Strength at 28days

Produce Date	Plastic density (kg/m ³)	Test Density (kg/m ³)	Compressive Strength (MPa)	Mean	Standard deviation	T-test (p)
2018/3/21	400	374	0.97	0.89	0.08	0.44
		359	0.91			
		360	0.97			
		363	0.97			
2019/9/23	400	366	0.86	0.89	0.08	0.44
		370	0.72			
		375	0.84			
2018/3/21	475	372	0.88	1.30	0.13	0.49
		441	1.39			
		429	1.46			
		447	1.26			
2019/9/23	475	435	1.51	1.30	0.13	0.49
		456	1.27			
		463	1.25			
2018/3/21	600	459	1.11	2.02	0.20	0.50
		458	1.20			
		544	2.23			
		556	1.86			
2019/9/23	600	566	2.16	2.02	0.20	0.50
		556	2.07			
		590	2.16			
2019/9/23	600	586	2.05	2.02	0.20	0.50
		599	2.03			
		606	1.57			

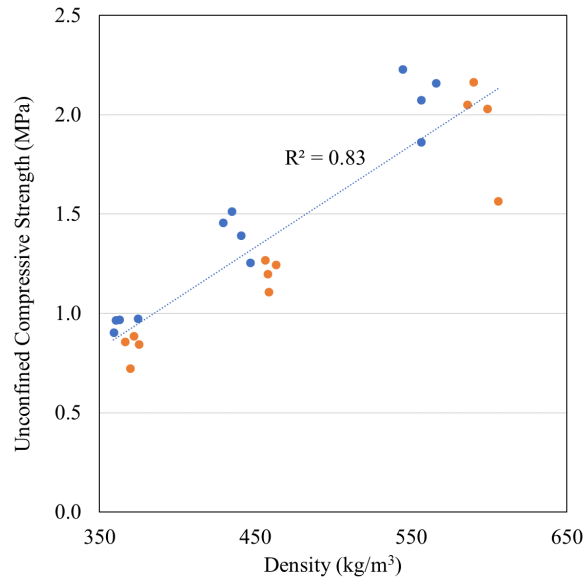


Figure 4-1 Relationship between LCC density and Compressive strength

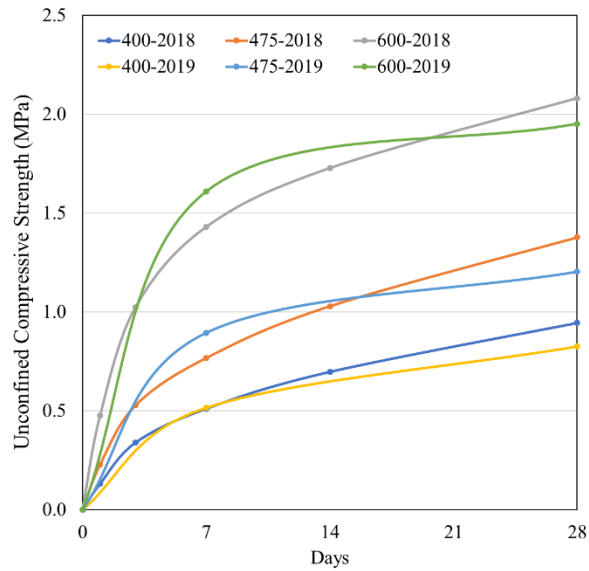


Figure 4-2 Compressive Strength over time

4.2.2 Modulus of Elasticity (MOE) and Poisson's Ratio

Pavement responses such as stress, strain, and deformation are commonly determined in a multi-layered system via the use of elastic modulus, thickness, and Poisson's ratio (TAC

2013). Therefore, it is important to understand the modulus of elasticity and Poisson's ratio of lightweight cellular concrete at ultra-low densities. Table 4-5 summarized the test results of the modulus of elasticity (MOE) and Poisson's ratio (PR) in this research. The 2018 samples were tested using a traditional frame which screws into the samples, while 2019 samples used circumstantial extensometer to measure the lateral deformation.

The compressive strength was evaluated using two batches of samples produced and tested in 2018 and 2019. It was found that the 2019 samples have higher standard deviation and average values for both MOE and PR compared to 2018 samples. Generally, the MOE increased as densities increased. However, Poisson's ratio does not follow the trend as the densities increase. Figures 4-3 and 4-4 demonstrated the MOE and PR trend to the densities, where MOE has a coefficient of determination (R^2) of 0.88 and PR has a coefficient of determination (R^2) of 0.08 to densities.

The average modulus of elasticity ranged from 700 to 1,613 MPa. Values of 400 kg/m³ density are lower than other reported values for similar densities in past research, such as BCA (1994), ranging from 800 to 1,000 MPa. However, 600 kg/m³ samples have higher values than the BCA report, ranging from 1,000 to 1,500 MPa. The MOE of ultra-low densities lightweight cellular concrete is at least three times greater than the unbound granular material such as Granular A and Granular B, a typical modulus of 250 MPa and 200 MPa (Applied Research Associate 2015).

The past research on Poisson's ratio of lightweight cellular concrete is limited (Ozlutas 2015). Reported values vary on different densities and compositions. Lee et. al (2004) mentioned that densities range from 1,000 to 1,400 kg/m³ has a PR range from 0.13 to 0.16 and 0.18 to 0.19. Ozlutas (2015) reported values of 0.14, 0.19, and 0.08 for 300, 600, and 1,000 kg/m³ densities. The test results of PR in this research compared to above values are higher, which 400 kg/m³ range from 0.15 to 0.25, 475 kg/m³ range from 0.21 to 0.27, 600 kg/m³ range from 0.20 to 0.26.

Figure 4-5 and 4-6 shows the 2019 test results of modulus of elasticity and Poisson's ratio at a different age. The average modulus of elasticity for the three densities ranged

from 757 to 1,613 MPa, increasing as density increased. The modulus of elasticity also increased at 58 days and 90 days. Compared to the first phase of samples done in 2018, the modulus of elasticity of the 2019 samples are higher, especially 475 kg/m³ and 600 kg/m³ LCC samples. Poisson's ratio ranges between 0.25 and 0.27 at 28 days. However, Figure 4-6 indicates that the Poisson's ratio decreased at 58 days and 90 days, showing the lateral deformation decreases. The Poisson's ratio of 2019 samples at 28 days are greater than 2018 samples, which could be due to the different test frames as the traditional frame uses screws which could be loosen during the tension-compression movement and thus measuring less lateral displacement. Though, the 56-days and 90-days values were closer to the 2018 samples, meaning in longer periods the movement in lateral direction of the samples could be reduced.

Table 4-5 Test results of Modulus of Elasticity and Poisson's ratio at 28 days

Produce Date	Plastic density (kg/m ³)	Test density (kg/m ³)	MOE (Mpa)	Mean (Mpa)	Standard deviation (Mpa)	PR	Mean	Standard deviation
2018/3/26	400	406	729	700	44	0.16	0.15	0.01
		411	637			0.14		
		408	733			0.16		
2019/9/24	400	407	778	757	66	0.28	0.25	0.04
		405	667			0.19		
		408	824			0.27		
2018/3/23	475	475	794	843	36	0.21	0.21	0.02
		469	879			0.24		
		463	855			0.19		
2019/9/24	475	488	1,024	1,160	105	0.22	0.27	0.04
		487	1,279			0.31		
		489	1,178			0.27		
2018/3/22	600	595	1,310	1,368	42	0.18	0.20	0.03
		581	1,409			0.19		
		580	1,384			0.24		
2019/9/24	600	615	1,422	1,613	137	0.22	0.26	0.03
		617	1,679			0.30		
		615	1,738			0.28		

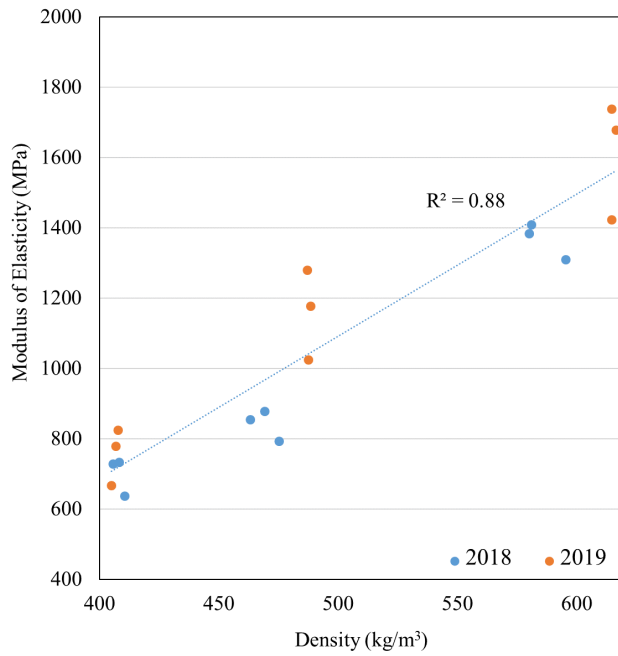


Figure 4-3 Modulus of Elasticity and LCC density

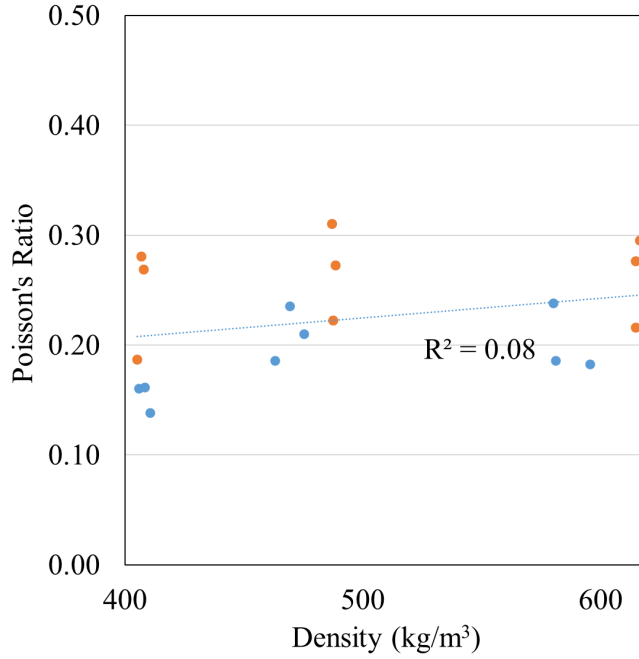


Figure 4-4 Poisson's ratio and LCC density

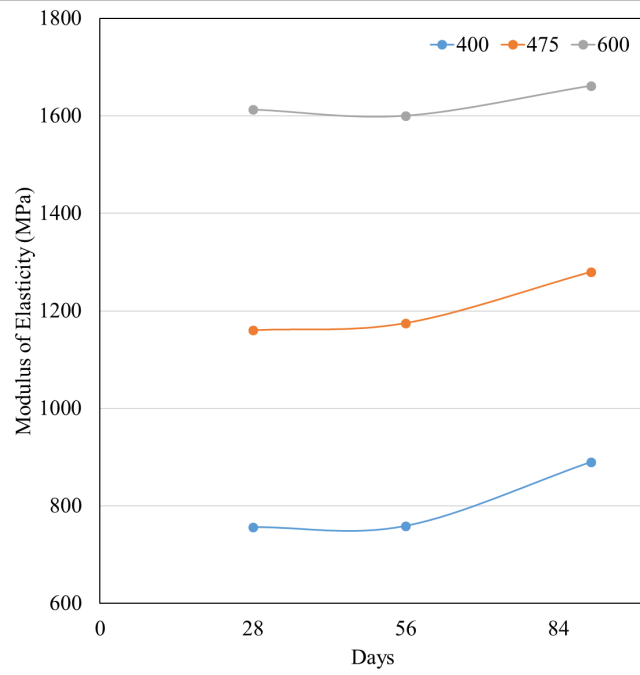


Figure 4-5 Modulus of Elasticity over time

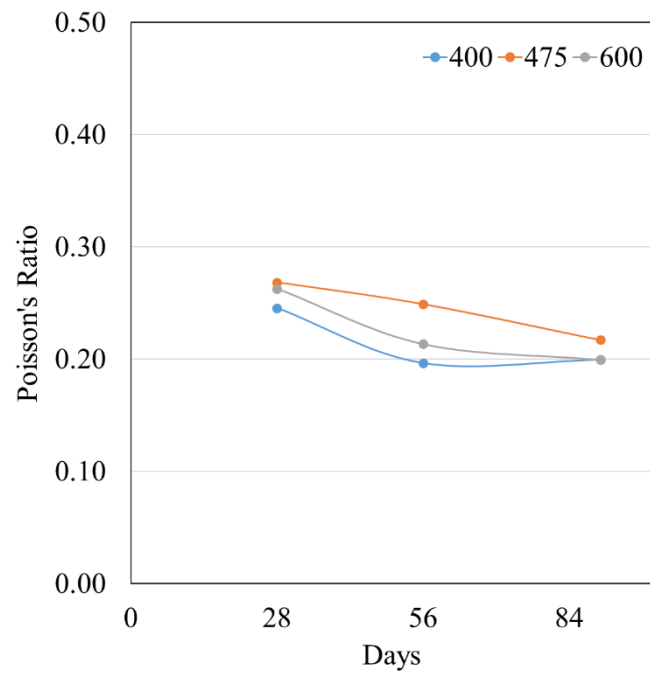


Figure 4-6 Poisson's ratio over time

4.2.3 Indirect Tensile Strength

A splitting tensile test was performed on three densities and was shown in Figure 4-7. Split tensile strength has a positive correlation with density ($R^2=0.93$). The average tensile strength of the lightweight cellular concrete is 0.16 Mpa for 400 kg/m³ density, 0.20 for 475 kg/m³ density, and 0.30 for the 600 kg/m³ density. Past research indicates that the tensile strength of LCC is within 15 to 35% of its compressive strength (Narayanan and Ramamurthy 2000). The 400 kg/m³ density results were found to be 18%, while 475 and 600 densities were around 14% of their respective compressive strength. The correlation between tensile strength and compressive strength is presented in Figure 4-8. The results demonstrate a positive relationship between the compressive strength and tensile strength with an R^2 of 0.93. This provides a possibility of using UCS in explaining the tensile strength of LCC.

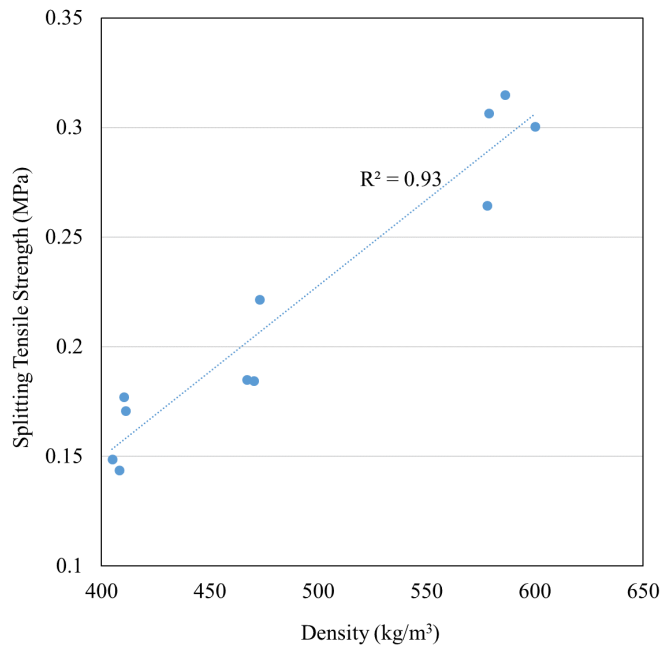


Figure 4-7 Splitting tensile strength and LCC density

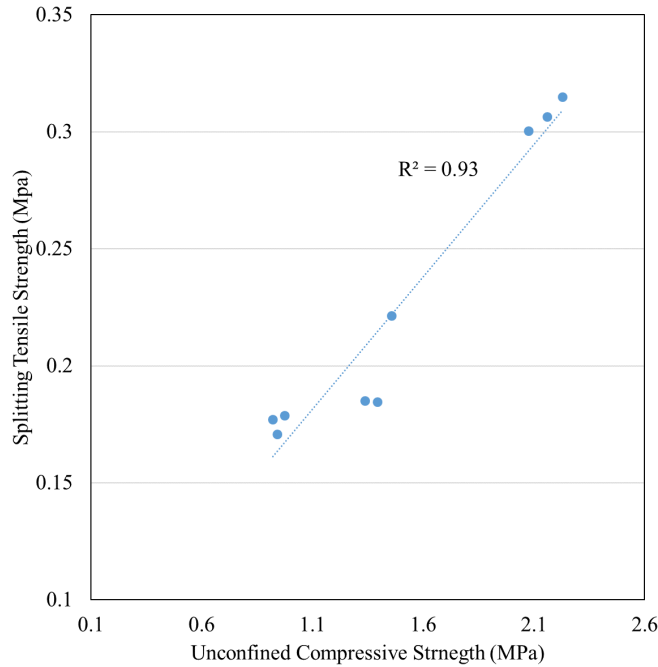


Figure 4-8 Relationship between tensile strength and compressive strength

4.2.4 Modulus of rupture

The modulus of rupture of the lightweight cellular concrete is shown in Table 4-6. The results indicated that higher densities result in a higher modulus of rupture. The modulus of rupture for the 400 kg/m³ density ranges from 0.21 to 0.25, 0.27 to 0.28 for 475 kg/m³ density), and 0.37 to 0.45 for 600 kg/m³ density. The average modulus of rupture is 0.22 for 400 kg/m³, 0.28 for 475 kg/m³, and 0.39 for 600 kg/m³ density. The modulus of rupture is 19% to 25% to its compressive strength. The typical range of the ratio is 15 to 35 % (Narayanan and Ramamurthy 2000). Figure 4-9 illustrates the modulus of rupture's test results for each density. The test results show that density strongly correlates with the Modulus of Rupture ($R^2=0.92$). Figure 4-10 indicates the relationship between the modulus of rupture and compressive strength. These results illustrate that the compressive strength of LCC has a strong relationship with the modulus of rupture ($R^2=0.93$).

Table 4-6 Test results of Modulus of Rupture at 28 days

Density (kg/m ³)	No.	Breaking Load (KN)	MR (Mpa)	Average (MPa)
400	1	0.69	0.21	0.22
	2	0.71	0.21	
	3	0.66	0.20	
	4	0.82	0.25	
475	1	0.91	0.27	0.28
	2	0.91	0.27	
	3	0.94	0.28	
	4	0.96	0.29	
600	1	1.49	0.45	0.39
	2	1.24	0.37	
	3	1.24	0.37	
	4	1.26	0.38	

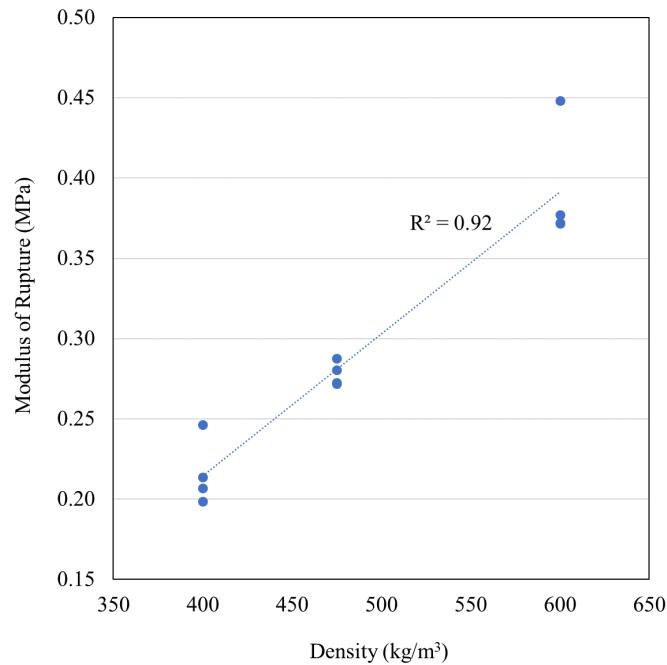


Figure 4-9 Modulus of rupture and LCC density

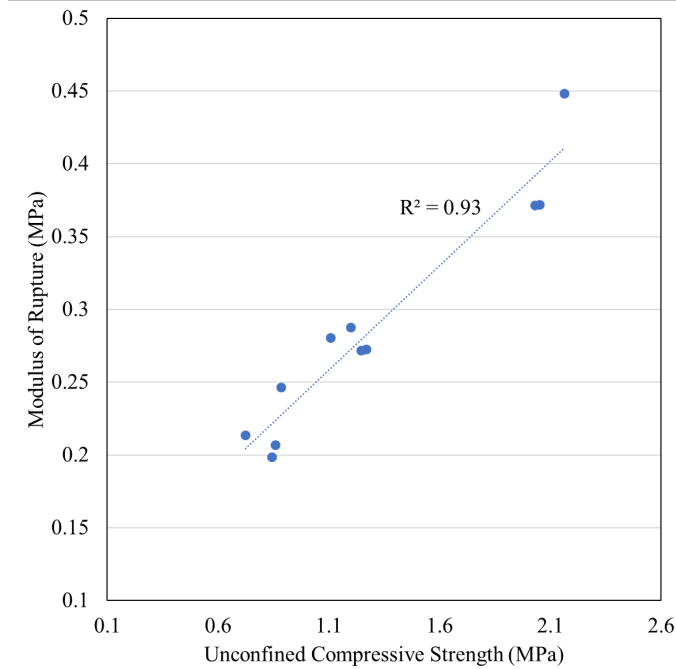


Figure 4-10 Relationship between modulus of rupture and compressive strength

4.2.5 Drying Shrinkage

Figure 4-17 demonstrated the test results of drying shrinkage for the three densities of lightweight cellular concrete. The drying shrinkage of lightweight cellular concrete decreases as density increases. The drying shrinkage strain range from 0.08 to 0.09% (800 to 900 microstrain) for 600 kg/m³ density samples, 0.11 to 0.13% (1,100 to 1,300 microstrain) for 475 kg/m³ density samples, and 0.16 to 0.2% (1,600 to 2,000 microstrain) for 400 kg/m³ density samples. The shrinkage was lower than the typical drying shrinkage of cellular concrete from BCA and Concrete Society, which are 0.3 % to 0.35 % (3,000 to 3,500 microstrain) for 400 kg/m³ density samples and 0.22 % to 0.25 % (2,200 to 2,500 microstrain) for 600 kg/m³ density samples.

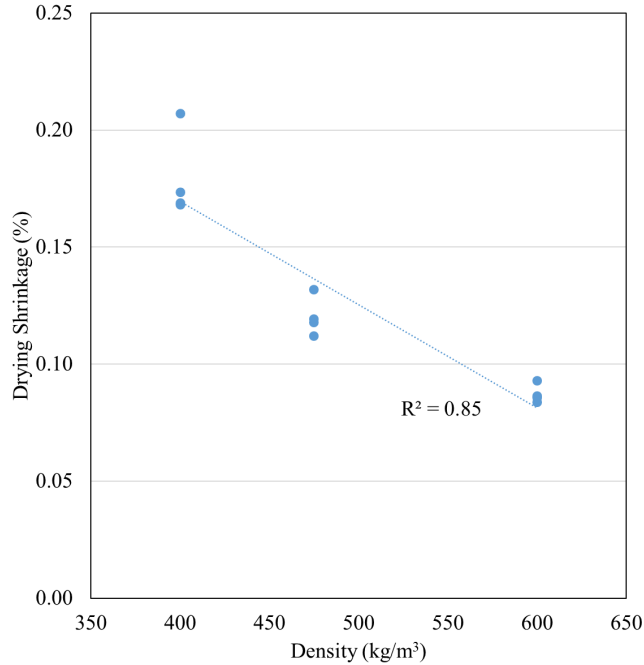


Figure 4-11 Test results of drying shrinkage for three densities

4.2.6 Damping Ratio measurement

Table 4-8 showed the damping ratios of lightweight cellular concrete for the three densities attained from the resonant column test using the Free vibration decay curve (FVDC) and Half-bandwidth method (HPBW). Test results specified that lightweight cellular concrete with densities from 400 to 600 kg/m³ has a minimum material damping ratio between 1.35% to 3.2%. These values are similar to soft clay and other soil material such as sand and granular material (Figure 4-18 to 4-21), which typically has a damping ratio of 1.5% and up to 5% at a very small shearing strain.

Table 4-7 Damping ratios of lightweight cellular concrete for three densities

Density (kg/m ³)	Shear Strain (%)	Damping Ratio (%)	
		FVDC	HPBW
400	2.763 x 10 ⁻⁵	1.434	1.353
400	1.652 x 10 ⁻⁵	1.904	1.902
475	2.542 x 10 ⁻⁵	2.763	2.669
475	1.841 x 10 ⁻⁵	3.116	3.203

Table 4-7 Damping ratios of lightweight cellular concrete for three densities, Continued

Density (kg/m ³)	Shear Strain (%)	Damping Ratio (%)	
		FVDC	HPBW
475	4.621 x 10 ⁻⁴	2.519	1.581
600	3.749 x 10 ⁻⁵	1.971	1.915
600	1.213 x 10 ⁻⁵	1.831	1.612
600	1.727 x 10 ⁻⁴	2.264	-

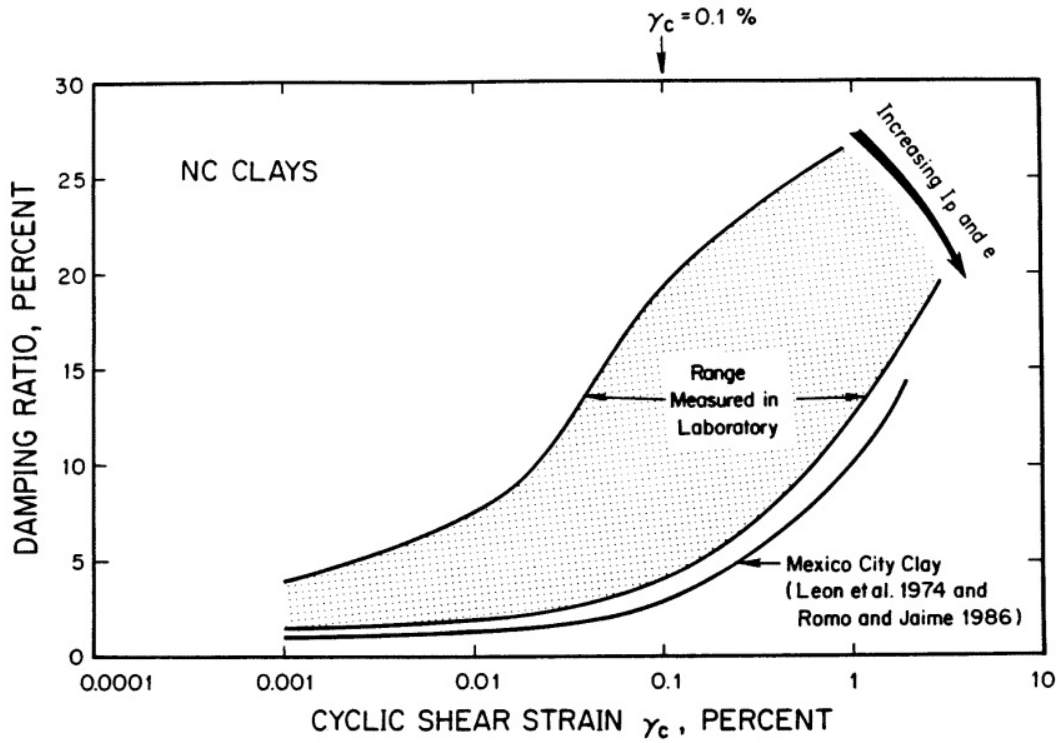


Figure 4-12 Damping ratio of soft clay (Dobry and Vucetic 1987)

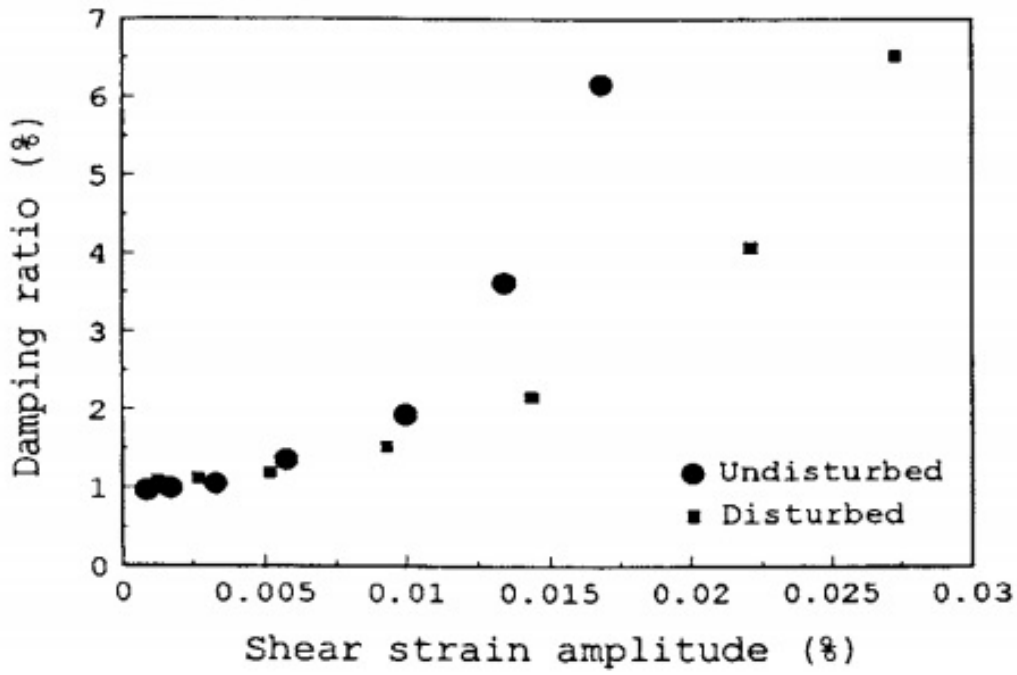


Figure 4-13 Damping ratio for kaolinite clay (Ashmawy et al. 1995)

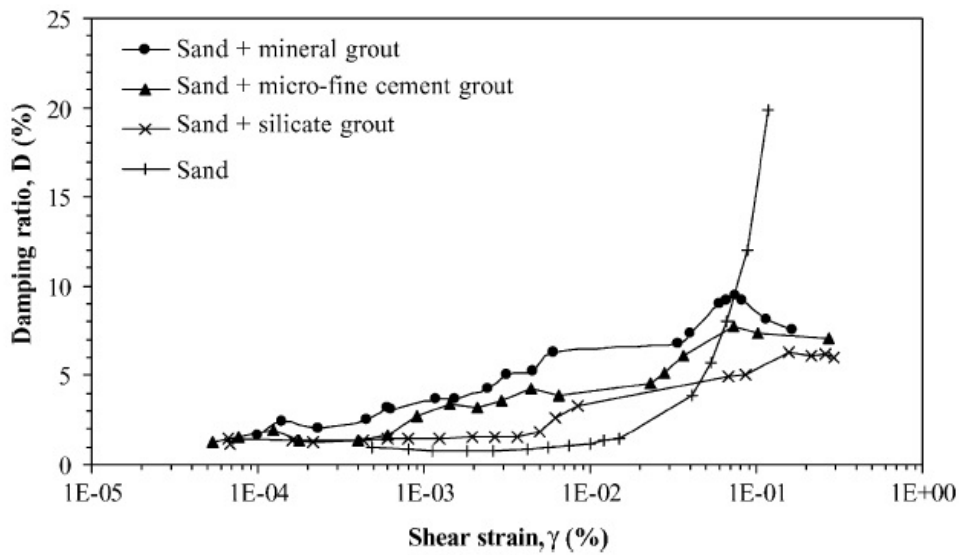


Figure 4-14 Damping ratio of sand (Delfosse-Ribay et al. 2004)

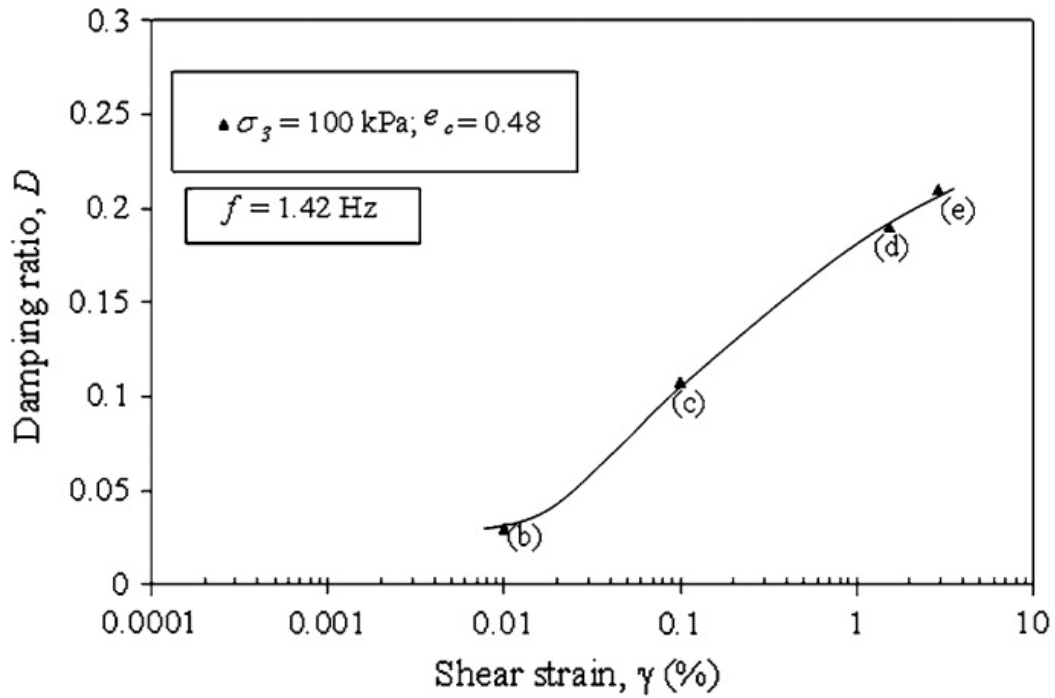


Figure 4-15 Damping ratio of granular material (Sitharam and Vinod 2010)

4.3 Effect of LCC density on other properties

Past research found that density has a positive relationship to lightweight cellular concrete's mechanical properties and is the most important factor controlling its strength. In this section, the specimens' density has been correlated to the mechanical properties results conducted in this research. Their relationships can be summarized in Table 4-9. Additionally, the density of lightweight cellular concrete has been found to impact other properties such as water absorption, permeability, sorptivity, and drying shrinkage. As a result, density could be used as the primary control factor when determining the specific applications.

Table 4-8 Relationship of density with mechanical properties

Mechanical Property	Equation	Coefficient of determination (R^2)
Compressive Strength	$D = 0.0051*UCS - 0.9728$	0.83
Modulus of Elasticity	$D = 4.04*MOE - 930.09$	0.88
Splitting Tensile Strength	$D = 0.0008*ST - 0.1635$	0.93
Modulus of Rupture	$D = 0.0009*MR - 0.1386$	0.92

Identical to density, compressive strength also has been found to correlate with other mechanical properties. Table 4-10 reviewed the relationship of compressive strength with other mechanical properties in this research. Those relationships provide a possibility of using compressive strength to predict lightweight cellular concrete's other mechanical properties.

Table 4-9 Relationship of compressive strength with mechanical properties

Mechanical Property	Equation	Coefficient of determination (R^2)
Modulus of Elasticity	$MOE = 677.43*UCS + 122.16$	0.99
Splitting Tensile Strength	$ST = 0.11*UCS + 0.06$	0.93
Modulus of Rupture	$MR = 0.14*UCS + 0.10$	0.93

4.4 Summary and Findings

The mechanical properties of ultra-low density lightweight cellular concrete obtained in this are summarized in Table 4-10. Properties of other typical pavement subbase materials such as Granular B and chemically stabilized materials are also included in the table.

The following are the main findings concerning the ultra-low density lightweight cellular concrete:

1. The density of lightweight cellular concrete has a positive correlation with the mechanical properties; other properties such as drying shrinkage also have a strong relationship with density. Therefore, it is reliable to use the density to estimate the mechanical properties of lightweight cellular concrete. Moreover, using compressive strength to predict other mechanical properties is viable since the compressive strength test is simpler to perform.
2. The ultra-low density lightweight cellular concrete has sufficient strength to support the pavement when its compressive strength exceeds 0.5 MPa. It was found that all the densities exceed 0.5 MPa at seven days, while 475 and 600 kg/m³ samples satisfied the requirement at three days. Meaning that the traffic can be open to public after the construction is complete after three days for 475 and 600 kg/m³ densities and seven days for 400 kg/m³ density when applied in pavement.
3. The modulus of elasticity of ultra-low densities lightweight cellular concrete is considered three to four times stiffer than the unbound granular material such as Granular A and Granular B. Compared to chemically stabilized materials, which often placed directly below the asphalt surface layer, ultra-low lightweight cellular concrete has a weaker modulus of elasticity except for the lime stabilized soils.
4. The modulus of rupture of ultra-low density lightweight cellular concrete is about 19 to 25% of its compressive strength. The results are considered weaker compared to cement stabilized materials, which have a range between 0.69 to 3.10 MPa, except

lime stabilized soils, which only has 0.17 MPa.

5. The drying shrinkage of lightweight cellular concrete decreases as density increases. The shrinkage was lower than the typical drying shrinkage of cellular concrete from past research, which could be due to the pozzolan material in the mix.
6. Ultra-low lightweight cellular concrete has a similar damping ratio to other geotechnical materials such as sand and granular materials at a very small strain, meaning the lightweight cellular concrete has a similar reaction to these geotechnical materials when small level of vibration happened.

Table 4-10 Summary of material properties of LCC and other subbase material

	LCC-400	LCC-475	LCC-600	Granular B	Lean concrete	Cement stabilized aggregate	Soil cement	Lime stabilized soils
Gradation Requirement	N	N	N	Y	N	N	N	N
Compressive Strength (MPa)	0.7 – 1.0	1.1 – 1.5	1.5 – 2.2	–	1.72	1.72	1.72	1.72
MOE (MPa)	600 – 850	800 – 1,300	1,300 – 1,700	250MPa	13,790	6,895	3,447	310
Poisson's Ratio	0.14 – 0.28	0.19 – 0.31	0.18 – 0.30	0.35	0.15	0.1 – 0.2	0.15 – 0.35	0.15 – 0.2
Tensile Strength (MPa)	0.16	0.20	0.30	–	–	–	–	–
Modulus of Rupture (MPa)	0.20 – 0.25	0.27 – 0.30	0.37 – 0.45	–	3.10	1.38	0.69	0.17

Chapter 5 Microstructure of ultra-low density lightweight cellular concrete

This chapter investigated the microstructure of lightweight cellular concrete. The microstructure of lightweight cellular concrete is evaluated using the Scanning electron microscope (SEM) located in the Waterloo Advanced Technology Laboratory (WATL) at the University of Waterloo and the industrial HD Camera System (IHDCS). Furthermore, captured images were processed using image processing software and packages to obtain better image segmentation.

5.1 Image capturing technology

5.1.1 Industrial HD Camera System (IHDCS)

SEM can capture clear photos of pores at microscopic scales to analyze the pore characteristics. However, the sample size could be limited due to the machine setup, typically 1 cm to 5 microns in width. This sometimes is not large enough for analysis. Therefore, the Industrial HD Camera System (IHDCS) had been put into use in this study for macro photography. The IHDCS is a convenient and fast capture camera system that consists of a capturing module (industrial HD macro photography camera module), an illumination part (LED light), a transmission part (connection cables), and a control component (Laptop). Table 5-1 presented the tech specs of the IHDCS. Test layout was demonstrated in Figure 5-1. Pore images of the three densities samples captured by the IHDCS are shown in Figure 5-2. It was found that the pore sizes of the 600 kg/m³ sample are more consistent than the 475 kg/m³ and 400 kg/m³ samples. Smaller bubbles adjacent to each other could form into larger bubbles.

Table 5-1 Tech specs of Industrial HD Camera

Name	Description	Name	Description
Module Size	38 × 38 × 6 mm	Sensitivity	TBD
Focus	AF	F/NO	2.5
Object Distance	5 cm-infinity	EFL	4.16 mm
Power	USB bus power	BFL	3.4 mm
Sensor Type	IMX179	FOV	80°
Active Array Size	3264 × 2448	TV distortion	<1.2%
Pixel Size	1.4 μm × 1.4 μm	IR filter	650 ± 10 nm
Maximum Image Transfer Rate	3264 × 2448, 2592 × 1944, 15 fps; 1920 × 1080, 1280 × 720, 30 fps	Fixed pattern noise	<0.03%

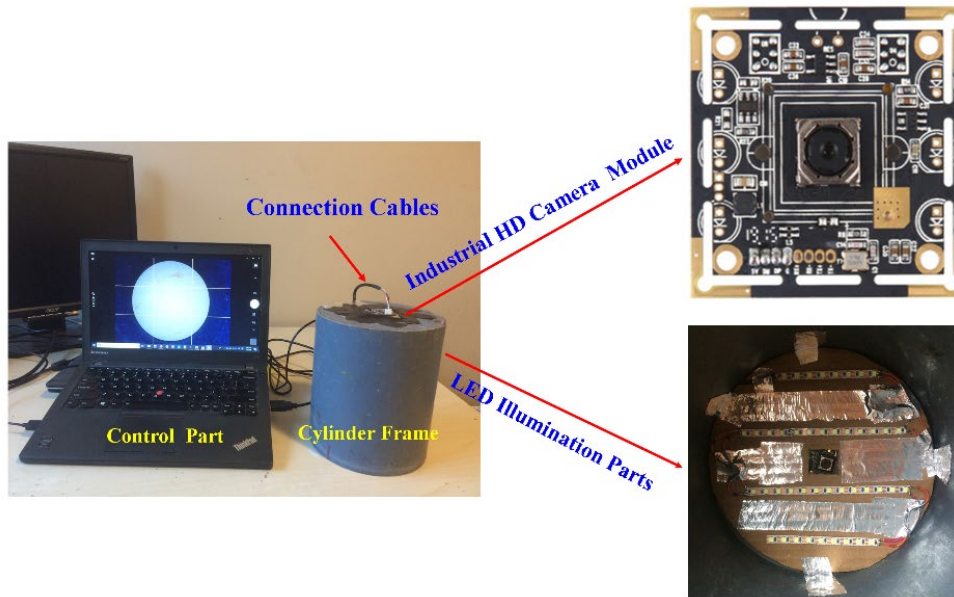


Figure 5-1 Industrial HD macro photography image capturing system

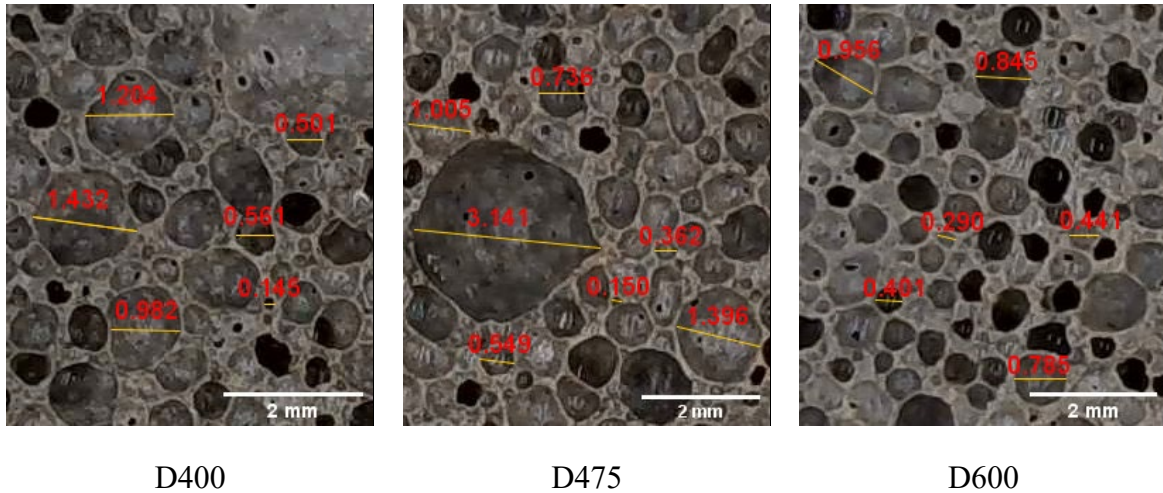


Figure 5-2 Images of specimens captured by IHDCS

5.1.2 ESEM Imaging Method

In order to understand the pore characteristics of the LCC samples at a more detailed scale, the Environmental Scanning Electron Microscope (ESEM) was used to perform the task and examine the pore sizes and pore distribution of the LCC samples. The test layout of the ESEM test is displayed in Figure 5-3. A total of six 1 cm cubes, two per each density, were prepared for the test. Figure 5-4 illustrated the secondary electron images of the LCC samples. Like IHDCS images, the 600 kg/m³ density LCC sample has a more stable and consistent bubble structure than 475 kg/m³ and 400 kg/m³ densities LCC samples. For the 400 kg/m³ density LCC sample, it was found that lots of bubbles were connected to form irregular bubbles.

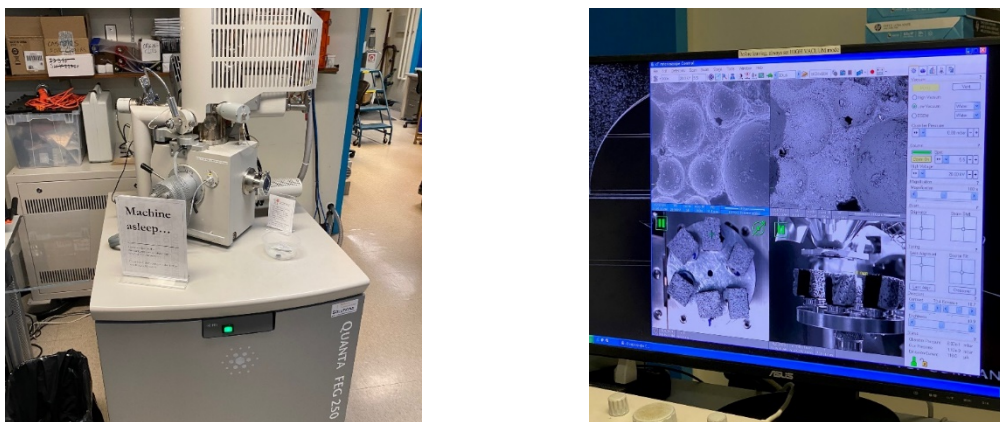


Figure 5-3 Test layout of the environmental scanning electron microscope (ESEM)

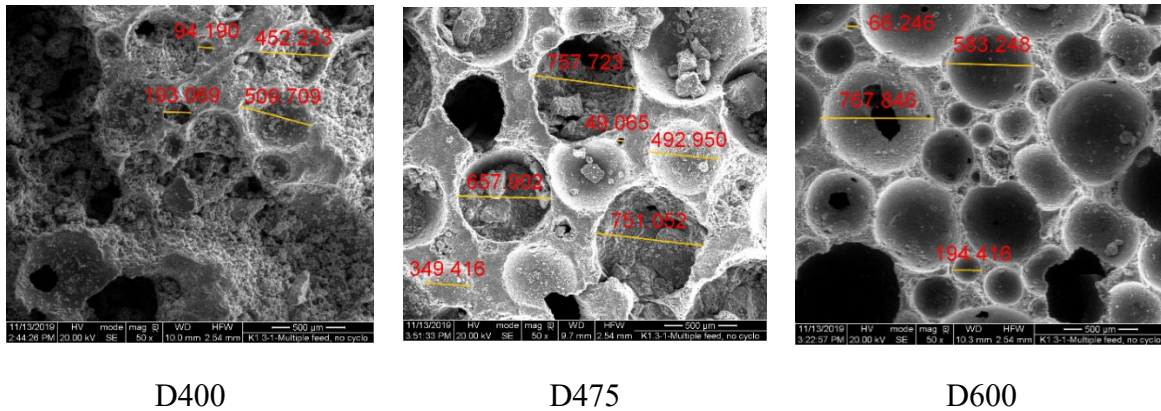


Figure 5-4 ESEM images with different densities

5.2 Image Processing Methodology

This research used FiJi ImageJ software (ImageJ 2019) to process the LCC images from IHDCS and ESEM test. FiJi is generally the ImageJ software with extra packages included, which help perform the scientific image analysis. Trainable Weka Segmentation (TWS) plugin was utilized to divide LCC's pore structure into several segments. FiJi ImageJ and TWS are both open-source programs, and TWS combines different sets of machine learning algorithms with features that allow users to produce pixel-based segmentations. The image processing procedure is exhibited in Figure 5-5. The procedure can be clarified as follows:

1. The LCC sample's pores and substantial area were selected separately, used for training to get a suitable classifier.
2. The classifier was applied to categorize the pore and substantial area and produce the TWS segmentation result, an 8-bit color image.
3. A threshold value was selected based on the Otsu method (Otsu 1979) to convert the image into a binary image.
4. In the binary image, the voids or pores are presented in black, and the substantial parts are displayed in white color. Additionally, the watershed segmentation method was utilized to improve the image segmentation quality. Thus, the contacting pores could be effectively segmented.

- The composite images of the original and watershed segmentation result were used to validate the effect of segmentation (detailed information shown in Figure 5-5). The subsequent analysis's pore characteristics is obtained through the watershed segmentation result.

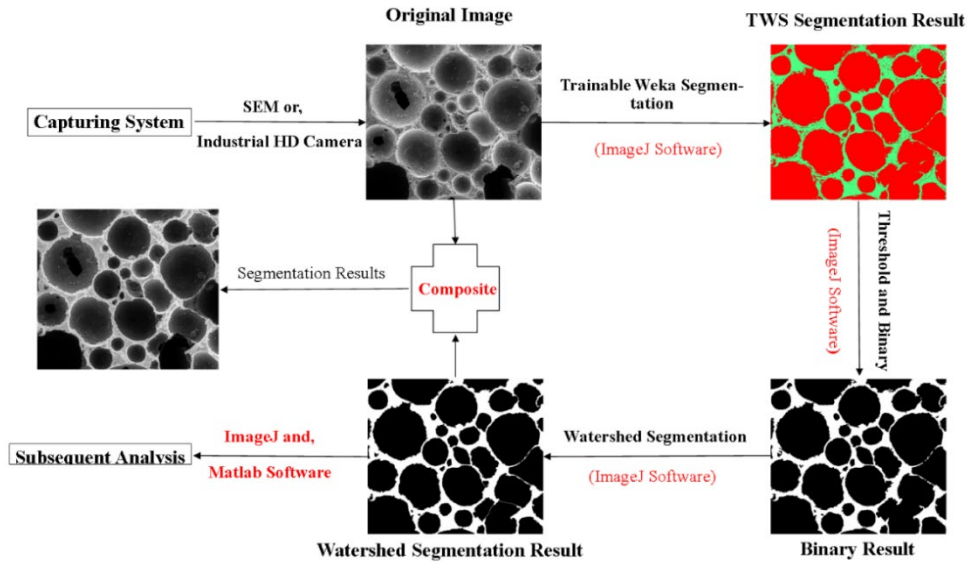


Figure 5-5 Image processing procedure

5.3 Results and Analysis

5.3.1 ESEM Pore Characteristics Analysis

Through ImageJ software, LCC's pore characteristics, including area, perimeter, primary axis, and the secondary axis of the best fitting ellipse and shape descriptors such as circularity, roundness, and solidity, are acquired. Figure 5-6 presented the heatmap, which showcases the relationship between every two parameters.

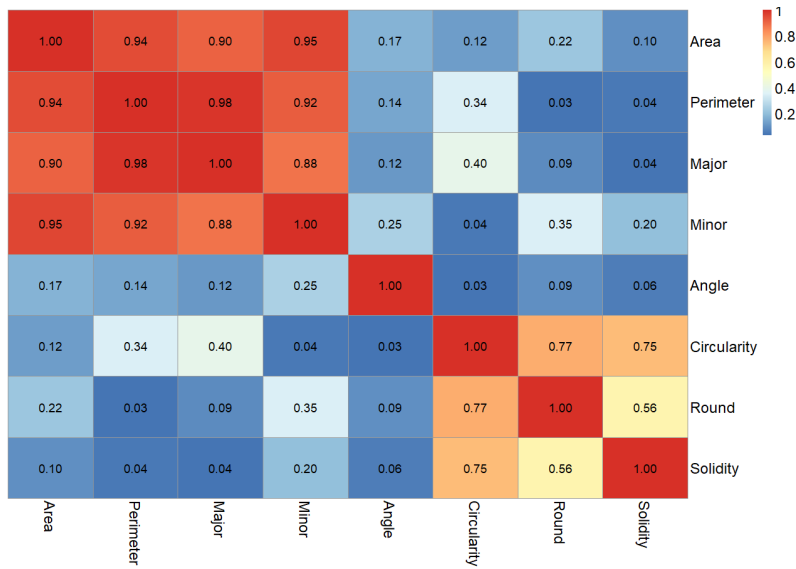


Figure 5-6 Heat map of correlation coefficient result

The heatmap could show the variance across multiple variables and provide a clear view of their relationship. The correlation coefficient of each two parameters was presented in each cell. The value ranged from -1.0 to 1.0, showing the correlation level. If the correlation equals 1.0, it is a perfect positive relationship. On the other hand, -1.0 means it is a perfect negative relationship. Parameters strongly correlate with each other regardless of the perfect negative or positive correlation. However, if the correlation is equal to 0, there is no relationship between the parameters. In this research, all the correlation results were converted into non-negative values to reflect the correlation among different parameters. Figure 5-6 showed 475 kg/m³ density LCC as an example since the results of different samples have a consistent trend. The color gradient presents the level of correlation from blue the weakest to red the most substantial relationship. Pore area, perimeter, major and minor axis has a strong relationship with each other as the lowest correlation coefficient is 0.88, meaning that the pore area, perimeter, major, and minor axis trends are highly consistent. It is suitable to assume the pore area's moving trend to characterize those of the other three parameters. The shape descriptors (circularity, roundness, and solidity) also show a high correlation trend. However, the maximum correlation value is less than 0.8. This means that the changing trend of shape descriptors has specific differences and should be considered separately. Thus, pore area, circularity, roundness, and solidity were used in the following analysis.

5.3.2 Pore Size and Thickness of Solid Part

Figure 5-7 illustrates the pore size of the LCC samples. It is clear that the samples of 400 kg/m³ and 475 kg/m³ densities are similar, while 600 kg/m³ density samples showing different distribution. 400 kg/m³ and 475 kg/m³ have twice the pore number than 600 kg/m³ density LCC. 400 kg/m³ density LCC has the highest pore number, following by 475 kg/m³ and 600 kg/m³ density LCC. However, most of the pores in the 400 kg/m³ and 475 kg/m³ densities LCC are small. As shown in Figure 5-7 (b), more than 70% of pores in 400 kg/m³ and 475 kg/m³ densities LCC have a radius less than 200 μm, while 600 kg/m³ density LCC only has 36%. Also, many pores bigger than 200 μm in 400 kg/m³ and 475 kg/m³ densities LCC. The number is similar to that in 600 kg/m³ density samples. Therefore, the pore size of 400 kg/m³ and 475 kg/m³ densities are considered to have more variations than 600 kg/m³ density samples.

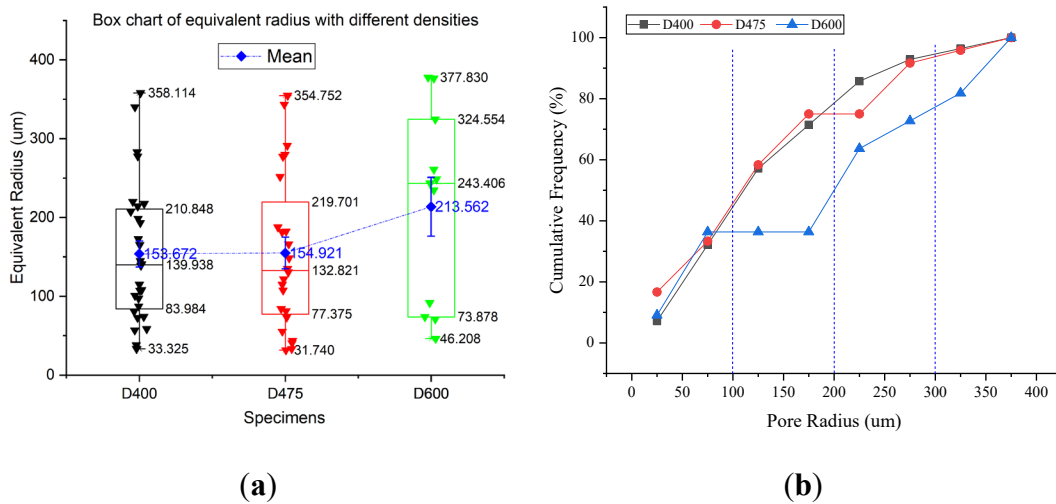
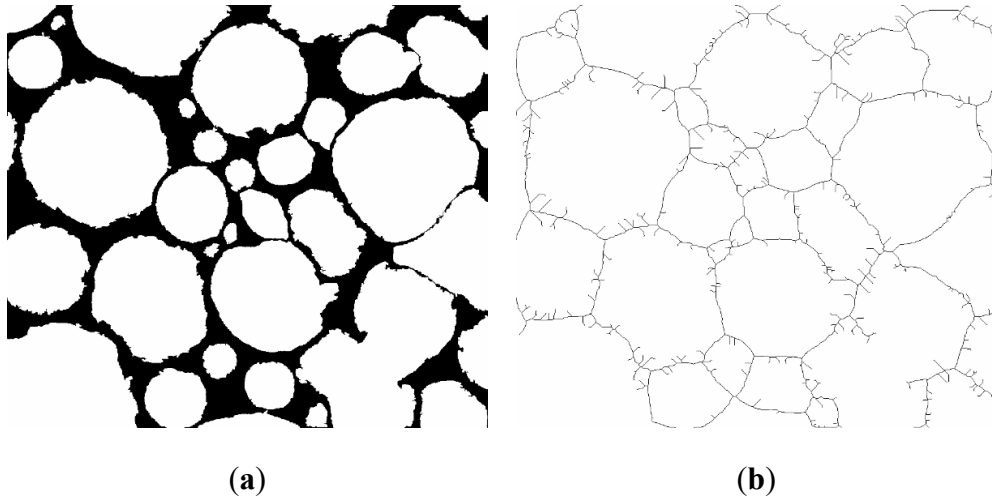


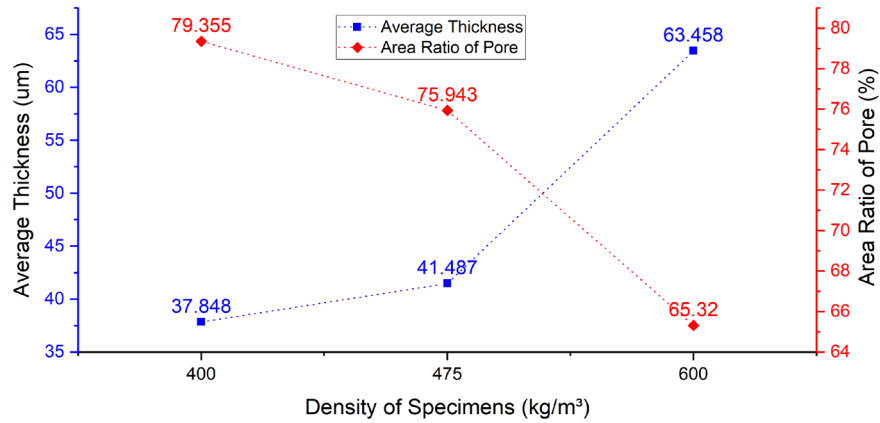
Figure 5-7 Box chart and cumulative frequency analysis of Equivalent radius (a) Box chart of the equivalent radius (b) Cumulative frequency of pore radius

Figure 5-8 showcases the average thickness of the solid part in the samples. There are a few steps to calculate the solid part's average thickness of LCC. First, the watershed segmentation binary images were inverted to show the pores as white and solid parts as black areas in Figure 5-8 (a). The total area of solid parts was then calculated. Second, The inverted image was skeletonized, as shown in Figure 5-8 (b). The solid part's skeleton can be obtained and is considered nearly

equal to the solid part's length. The average thickness of LCC was calculated after the total area, and the length of the solid part was obtained. The results are demonstrated in Figure 5-8 (c).



Average thicknesses of solid parts and area ratio as a function of specimen density



(c)

Figure 5-8 Average thicknesses of solid parts (a) Inverted binary image (b) Skeleton of the solid part (c) Average thickness of solid parts and area ratio as a function of specimen density

As shown in Figure 5-8 (c), the average thickness of solid parts in LCC increases as density increases, which means the solid part in higher density is thicker than the LCC's low densities. The solid part's average thickness in lower densities was 40% less than the higher density LCC,

which means the lower densities LCC have a more significant pore area. The pore area ratio negatively correlates with density, showing that higher density LCC has less pore than lower densities LCC.

5.3.3 Shape Descriptors

The shape descriptors included in this research are circularity, roundness, and solidity. Circularity is a measure that describes how close the pore should be to a mathematically perfect circle. It is the ratio of the object area to the area of a circle with the same perimeter. Roundness is identical to circularity. However, roundness does not reflect the local irregularities and is described as the ratio of an object's area to the area of a circle with the major axis. Solidity is a measure that defines the density of the pore. It is the ratio of an object's area to the area of a convex hull of the object. The results of the three shape descriptors for the three densities were shown in Figure 5-9.

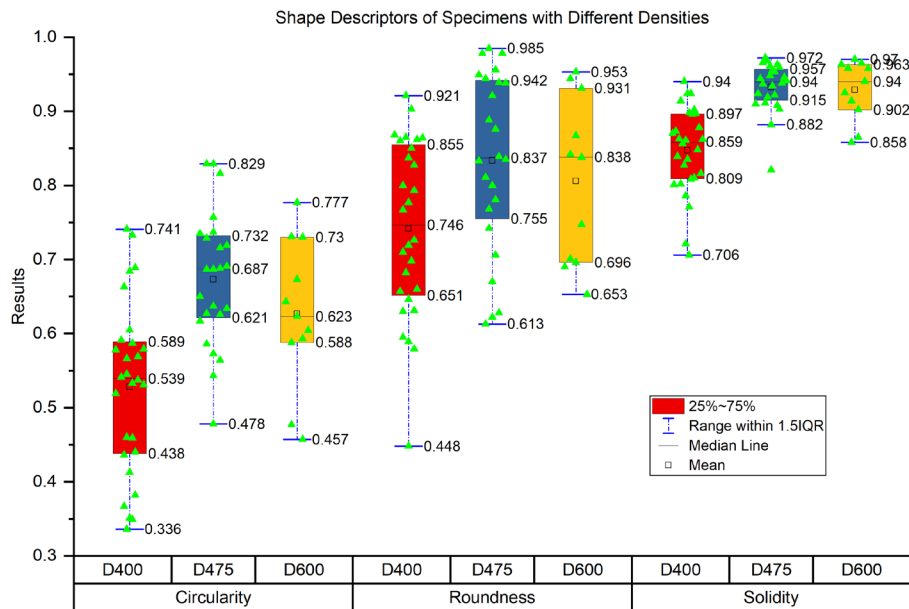


Figure 5-9 Data of shape descriptors of specimens with different densities

The data points presented in Figure 5-9 represents the pore of the samples. 475 kg/m³ density LCC has the best distribution of shape descriptors, followed by 600 kg/m³ and 400 kg/m³ density being the worst. The circularity value explains whether the pore is closed to a true circle. It was

found that half the pores in 475 kg/m³ density LCC have circularity values between 0.621 and 0.732, while 600 kg/m³ density LCC is between 0.588 to 0.73 and 400 kg/m³ density LCC range from 0.438 to 0.589. The results showed that 475 kg/m³ density LCC has a better bubble structure, beneficial for its mechanical properties.

LCC's roundness shows a similar trend to the circularity results, except that the roundness values are more significant than the circularity values. The reason is that roundness ignores the effect of local irregularities of the pore. Thus, circularity contains more shape information of the pore used to evaluate the pore's circle shape.

Solidity is a measure to evaluate the touching pores. As the pore becomes solid, the pore and convex hull areas approach each other, resulting in a solidity value of 1.0. Results showed that 475 kg/m³ and 600 kg/m³ densities LCC are more significant than 400 kg/m³ density LCC. This means that the pores in 475 kg/m³ and 600 kg/m³ densities LCC are closer to the true circle. Larger solidity values indicate fewer touching pores in the sample, consistent with the specimen's photos shown in Figure 5-4.

5.3.4 Image Processing Results Analysis of ESEM and IHDCS

Figure 5-10 illustrates the pore characteristics obtain by IHDCS on six samples of each density. It was found that the area ratio and average thickness of solid parts are significantly correlated with LCC's density, as shown in Figure 5-10 (a). The area ratio is negatively correlated with density, while the average thickness is positively correlated with density. The linear relationship for the area ratio and the average thickness is also observed with R² of 0.89 and 0.90.

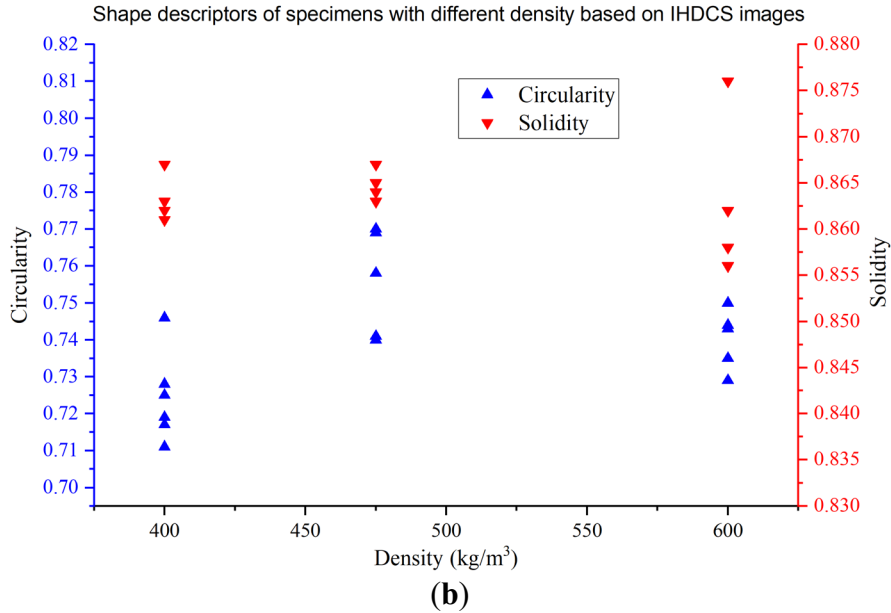
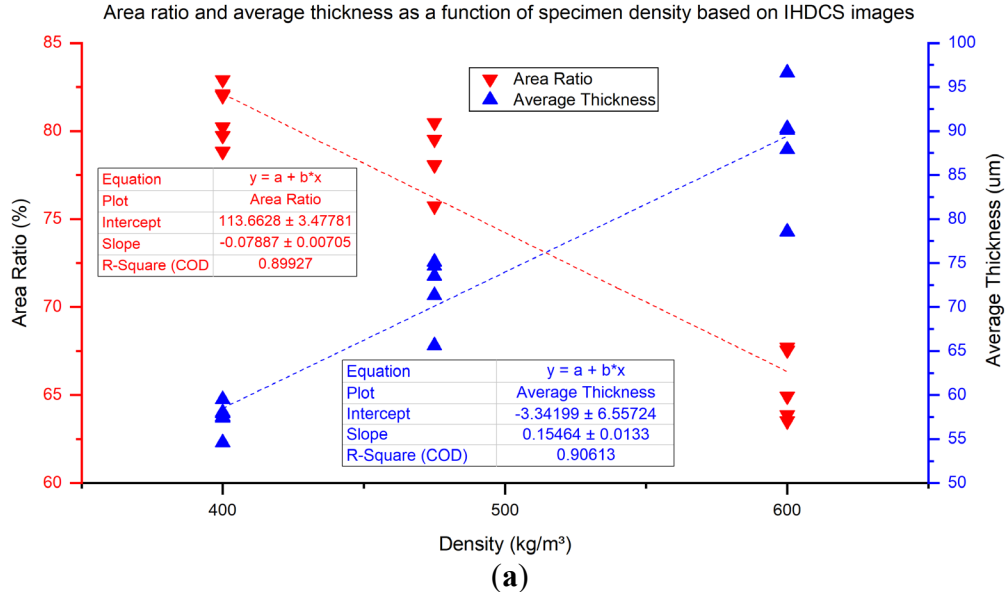


Figure 5-10 Results of pore characteristics based on IHDCS (a) Area ratio and average thickness as a function of specimen density based on IHDCS images (b) Shape descriptors of specimens with different densities based on IHDCS images

The circularity and solidity of LCC are demonstrated in Figure 5-10 (b). 475 kg/m³ density LCC has the best results. This means that the pores' shape in 475 kg/m³ density LCC is closer to a true circle. Moreover, 475 kg/m³ density LCC has less touching pores than the other two densities. On the contrary, 400 kg/m³ density LCC showing the worst results. This could be due to the

increased bubble content, which reduced the spacing between bubbles, meaning adjacent pores are more likely to touch each other. Therefore, irregular pores are created and lead to a drop in circularity and solidity values.

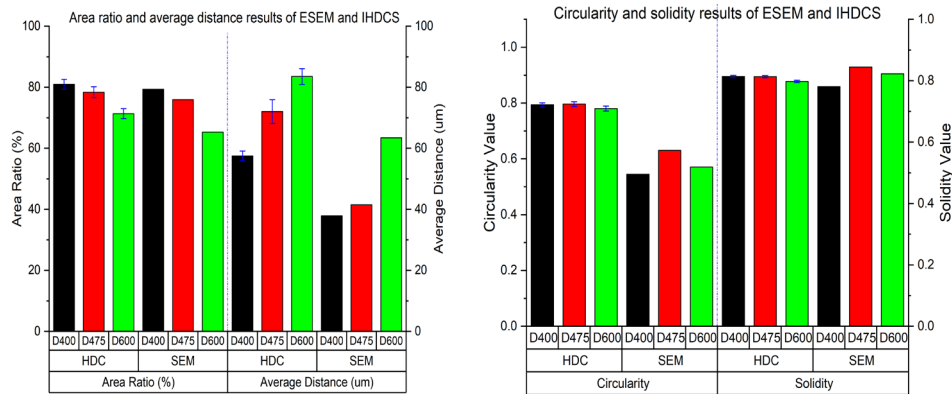


Figure 5-11 Comparative analysis of physical parameter results between ESEM and IHDCS

Figure 5-11 illustrates the comparison results of ESEM and IHDCS. The results of IHDCS and ESEM have similar values concerning the pore's area ratio and solidity. Therefore, IHDCS could be a feasible method of analyzing the pore's area ratio of LCC and the touching pores' condition. Alternatively, the difference between IHDCS and ESEM on the average distance and circularity of LCC is more considerable, even though the variation is the same. The results acquired from IHDCS are more excellent than ESEM, and the standard deviation of average distance and circularity ranged from 19.65 to 30.58 and 0.126 to 0.179.

The differences in the results of the average distance and circularity could be since: Comparing to ESEM, IHDCS attains images at a lower resolution, so the edge of the pores would be identified to be smoother, which results in higher circularity. Moreover, IHDCS obtained more pore samples than ESEM since IHDCS captured a more extensive range of images than the ESEM, and a total of six samples were used in this research. This could cause the average thickness difference between IHDCS and ESEM since IHDCS considered more LCC samples.

5.3.5 Relationship with mechanical properties

The relationship between the pore characteristics and LCC mechanical properties were examined in this section. Figure 5-12 illustrated the mechanical properties of LCC tested in this research. The mechanical properties are unconfined compressive strength (UCS), modulus of elasticity (MOE), modulus of rupture (MR), and splitting tensile strength (STS). The results of mechanical properties demonstrate a positive correlation with LCC density. 400 kg/m³ density LCC showing the lowest mechanical properties results, which reflect that lower density has weaker foam structure. In contrast, higher density LCC has a stronger foam structure.

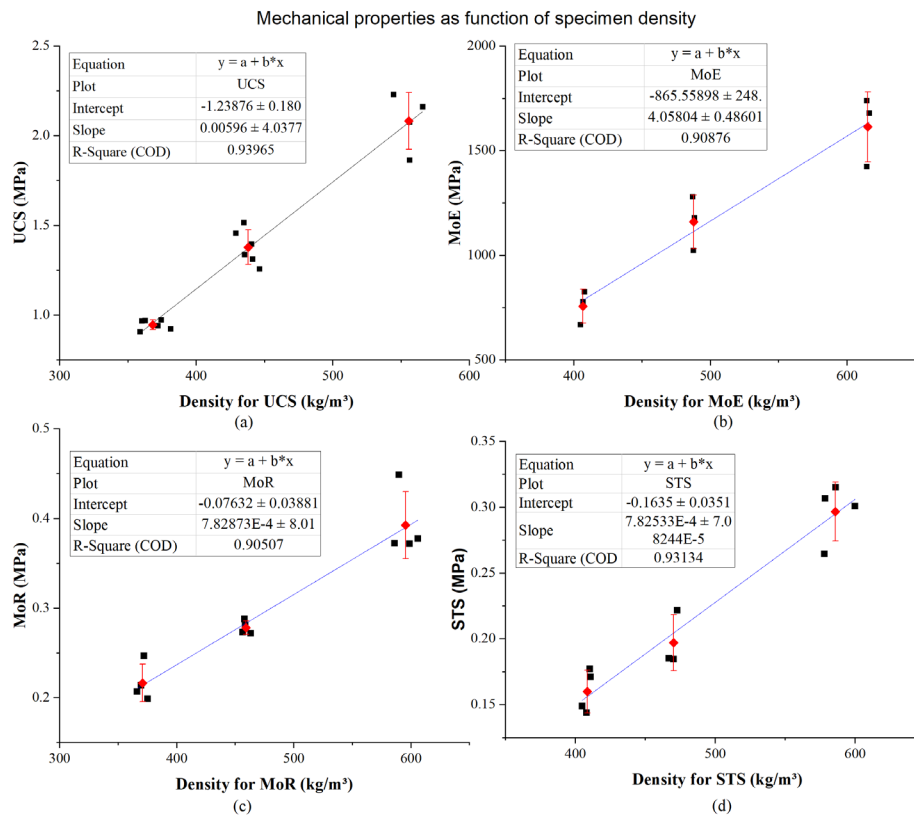


Figure 5-12 Mechanical properties of LCC (a) Unconfined compressive strength (b) Modulus of elasticity (c) Modulus of rupture (d) Splitting tensile strength

Three factors from pore characteristics obtained from IHDCS and ESEM might affect the LCC's mechanical properties. First, the pore area ratio is a significant factor since it is highly negatively correlated with LCC density. Thus, there is a highly negative correlation between area ratio and

mechanical properties. Samples with a large pore area ratio have a less solid part in the cross-section, meaning that the average thickness between pores is small. This results in a lower strength of the structure to bear the load. The second factor is the pore's shape. It had been noticed that the circularity and solidity of the 475 kg/m³ and 600 kg/m³ density LCC are higher than 400 kg/m³ density LCC, meaning that the shape of the pores in the 475 kg/m³ and 600 kg/m³ density LCC are closer to the true circle. Less touching pores were observed in the 475 kg/m³ and 600 kg/m³ density LCC. The steady shape of pores and less touching pores improve LCC's mechanical properties, which is why 475 kg/m³ and 600 kg/m³ density LCC show better strength than the 400 kg/m³ density LCC.

Despite that, the circularity and solidity of 475 kg/m³ density LCC are more significant than 600 kg/m³ density LCC. The 600 kg/m³ density LCC still shows better strength than the 475 kg/m³ density LCC. This is because the 600 kg/m³ density LCC has a higher average thickness between pores, which enhanced the strength. Moreover, the pore size variations in 600 kg/m³ density LCC are more consistent than the 475 kg/m³ density LCC, which is beneficial to its mechanical properties.

5.4 Summary and Findings

This chapter has described the pore characteristics of LCC through image processing technology and laboratory experiment results. It was found that the IHDCS can acquire similar results such as pore area ratio and solidity consistent with ESEM. IHDCS also captured a more extensive range of images than ESEM.

There are strong correlations between the pore area, perimeter, the major and minor axis for pore characteristics. Shape descriptors also have a strong correlation, but the values are lower than pore characteristic ones. The average thickness between the pores was calculated. It was found that higher densities have a greater average thickness. Moreover, the average thickness of 600 kg/m³ density LCC is 1.5 times more than lower densities LCC. The pores' area ratio showed the opposite trend, which lower densities LCC have higher pore area ratio.

The relationship between the pore characteristics and the mechanical properties were also discussed in this chapter. The pore area ratio, average thickness between pores, circularity, and solidity demonstrated a strong correlation with the mechanical properties of LCC, which could be beneficial to be used as parameters when estimating the mechanical behavior of LCC.

Chapter 6 Freeze-thaw resistance of Lightweight Cellular Concrete

6.1 Scenario settings

The freeze and thaw cycling test in this research is divided into two scenarios. Both scenarios involves saturating the samples in water before testing. The first scenario follows Tikalsky's (2004) research, where the samples are frozen in the air and thawed in water. The second scenario, however, freezes the sample in the air and also thaws them in the air at room temperature. This is to observe how the samples degrade in the air since the pavement will not always be saturated. Both scenarios prepared tests on two different ages of the lightweight cellular concrete, which are 28 days and 365 days. The rationale for different ages is to monitor the effect of curing time on their freeze and thaw resistance. All the scenarios were applied to the three densities of lightweight cellular concrete.

6.2 Twenty-Eight days samples

6.2.1 Thaw in water scenario

Figure 6-1 shown the relative values of the 600 kg/m³ lightweight cellular concrete correspond to its dynamic modulus of elasticity and weight changes. The relative dynamic modulus of elasticity will be presented as 600-1-ft for instance, while the weight of the 600 samples is represent as 600-1-mass. The relative dynamic modulus of elasticity of the 600 kg/m³ samples demonstrated an increasing trend, showing that the 600 kg/m³ samples does not get damaged by the freeze and thaw cycling but increased their strength instead. The trend is similar to one of the high-density samples in Tikalsky's research, in which the mix also has highest compressive strength compared with other higher density mixes. The weight loss of the 600 kg/m³ samples dropped to below 70% of its originated value.

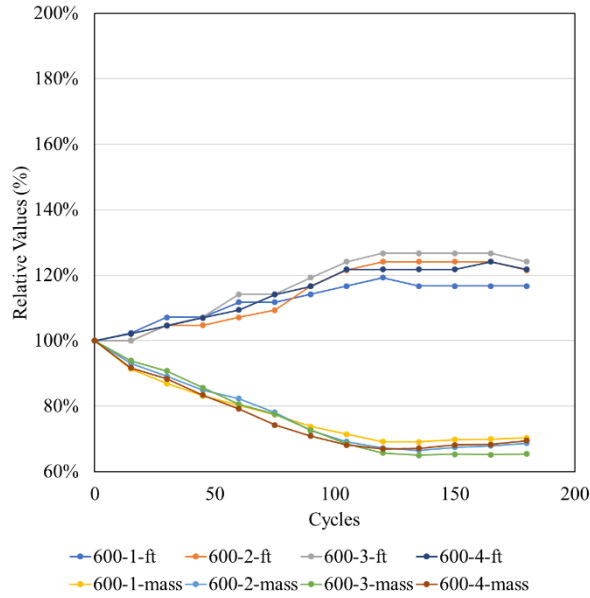


Figure 6-1 Freeze-thaw deterioration data for 600 kg/m³ samples – 28 days thaw in water

The freeze-thaw deterioration data of the 475 kg/m³ samples were illustrated in Figure 6-2. The 475 kg/m³ samples demonstrated a different trend from 600 kg/m³ samples. The relative dynamic modulus of elasticity of 475 kg/m³ samples was maintained at around 100%. The weight of the 475 kg/m³ samples dropped to 80 to 90 % before 135 cycles, but then went back to 100% at 180 cycles.

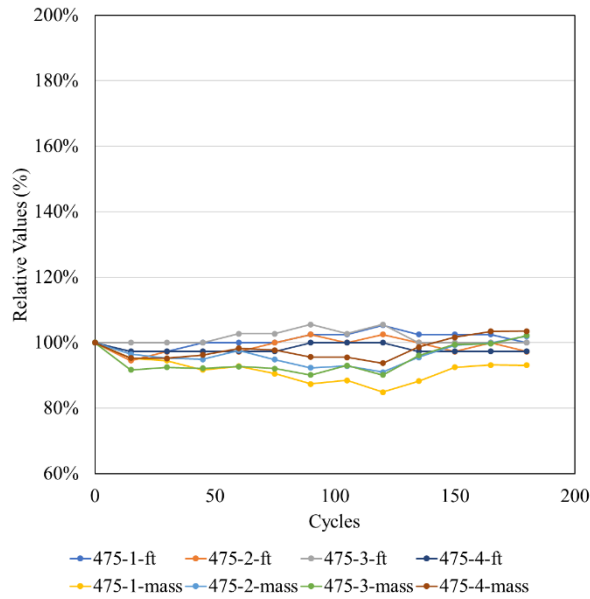


Figure 6-2 Freeze-thaw deterioration data for 475 kg/m³ samples – 28days thaw in water

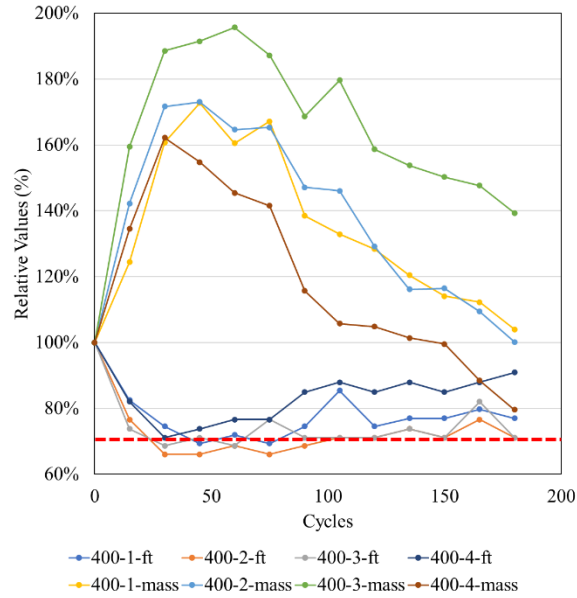


Figure 6-3 Freeze-thaw deterioration data for 400 kg/m³ samples – 28days thaw in water

The freeze-thaw deterioration data for the 400 kg/m³ samples were shown in Figure 6-3. The relative dynamic modulus of elasticity of 400 kg/m³ samples decreased significantly throughout the freeze-thaw cycling. Three out of four samples from the 400 kg/m³ density dropped below 70%, which is the threshold value from the ACI guideline. This shows that the 400 kg/m³ samples did not meet the requirement. The weight of the 400 kg/m³ samples also increases dramatically to a maximum of 190% of its original weight.

Figure 6-4 illustrated the average value of the three densities of lightweight cellular concrete. In general, The 475 and 600 kg/m³ samples were not significantly affected by the freeze-thaw cycling. However, the 400 kg/m³ samples were damaged and degraded dramatically after 15 cycles. The above results show that the 475 and 600 kg/m³ lightweight cellular concrete were more durable than the 400 kg/m³ lightweight cellular concrete.

The compressive strength of lightweight cellular concrete under freeze-thaw cycling was illustrated in Figure 6-5. The coefficient of determination (R^2) of the three densities did not exceed 0.7, showing that the compressive strength of lightweight cellular concrete did not get affected by the freeze-thaw cycling. These results also correspond to the summary from

Tikal'sky's research that the compressive strength of cellular concrete is not likely to get affected by freeze-thaw cycling.

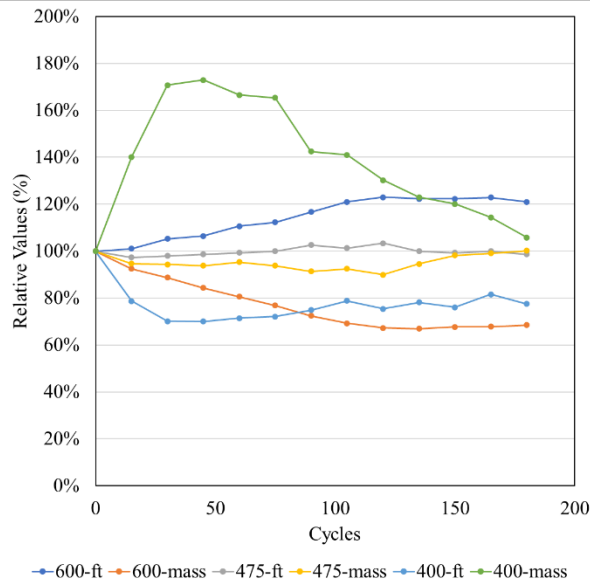


Figure 6-4 Freeze-thaw deterioration data (average value)– 28days thaw in water

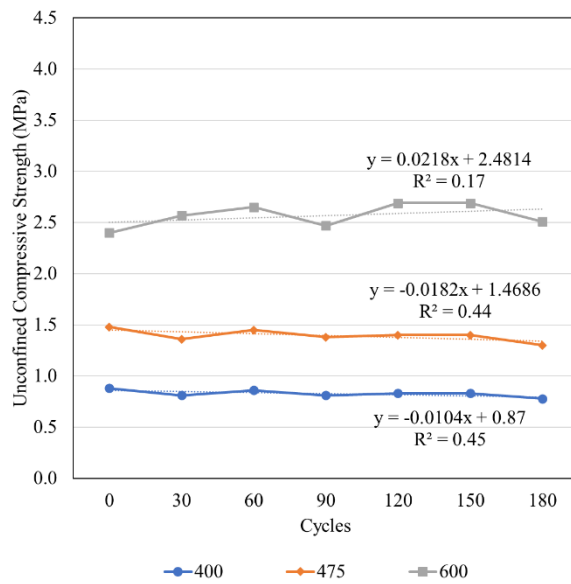


Figure 6-5 Compressive strength of LCC under freeze-thaw cycling (average value)– 28days thaw in water

6.2.2 Thaw in air scenario

The freeze-thaw deterioration data for the three densities of lightweight cellular concrete was shown in Figure 6-6. The relative dynamic modulus of elasticity for all the densities was variate between 87% to 131% and was not showing an increase nor decrease, meaning the samples were not affected by the freeze-thaw cycling.

Regarding the weight loss, it was found that the weight of the samples decreased to around 84% for 400 kg/m³ sample and 94% for 475 kg/m³ and 600 kg/m³ samples until 90 cycles, but then increased to a maximum of 138%. This shows that the samples still maintain their moisture and water within the structure, which could help prevent the drying shrinkage and thus maintain their stiffness.

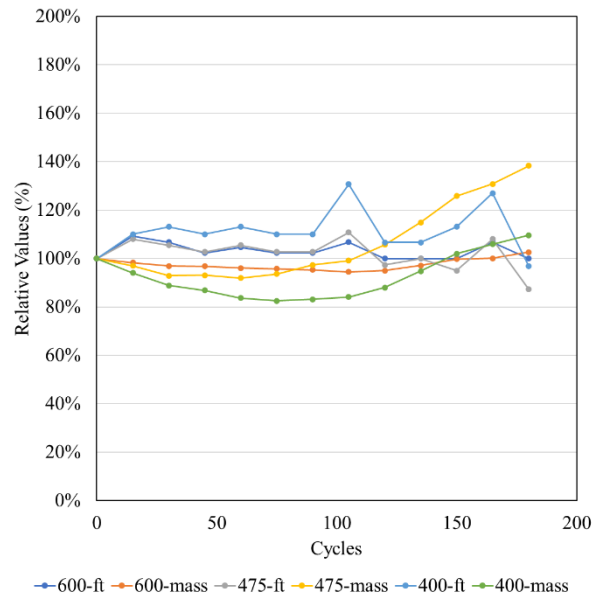
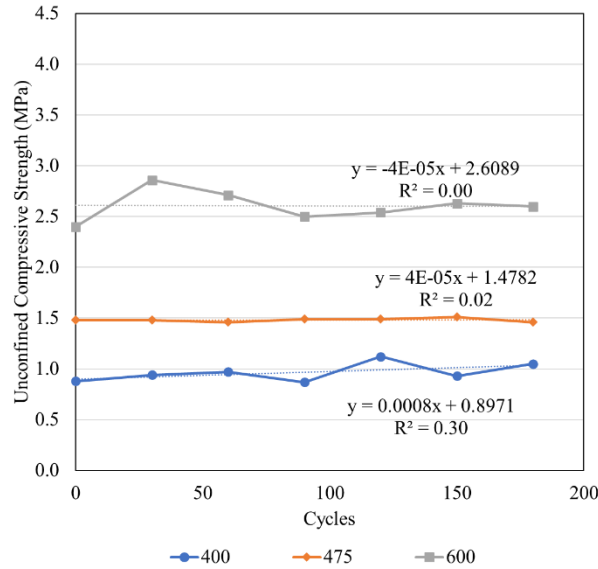


Figure 6-6 Freeze-thaw deterioration data (average value)– 28days thaw in air

Figure 6-7 demonstrated the compressive strength of lightweight cellular concrete under freeze-thaw cycling for a thaw in air condition. It was found that the coefficient of determination (R^2) for three densities also did not exceed 0.7, meaning that the compressive strength of lightweight cellular concrete did not affect the freeze-thaw cycling by thawing in air.



**Figure 6-7 Compressive strength of LCC under freeze-thaw cycling (average value)–
28days thaw in air**

6.3 One-year samples

6.3.1 Thaw in water scenario

Figure 6-8 to Figure 6-10 noted the freeze-thaw deterioration data for the lightweight cellular concrete. It was found that the relative dynamic of modulus for all densities shown an increasing trend. The relative dynamic modulus of elasticity of the 600 kg/m³ samples increased steadily to 110%, while 475 kg/m³ and 400 kg/m³ samples went up to 119% and 124%. The relative dynamic of elasticity for all densities became stable after 100 cycles. This indicated that all the densities not only didn't get affected by freeze-thaw cycling but also gained strength steadily. The weight of all the densities samples dropped approximately two to three percent per 15 cycles. Compared to the 28 days samples, the 365 samples seem to be more stable than 28 days sample in terms of the amplitude of variation.

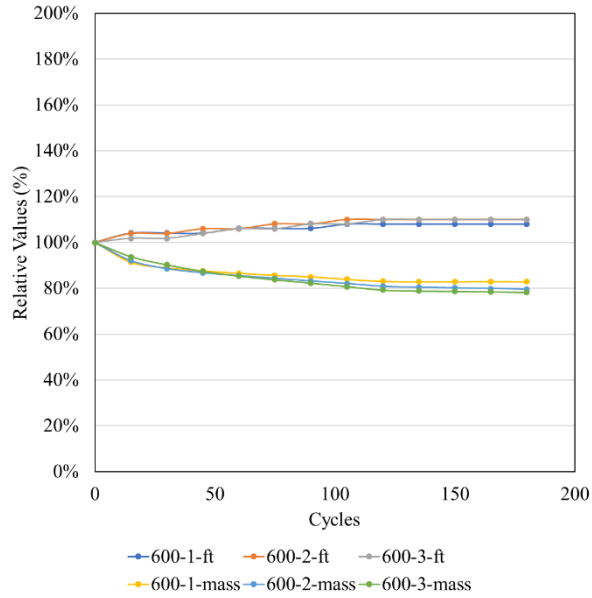


Figure 6-8 Freeze-thaw deterioration data for 600 samples – 365 days thaw in water

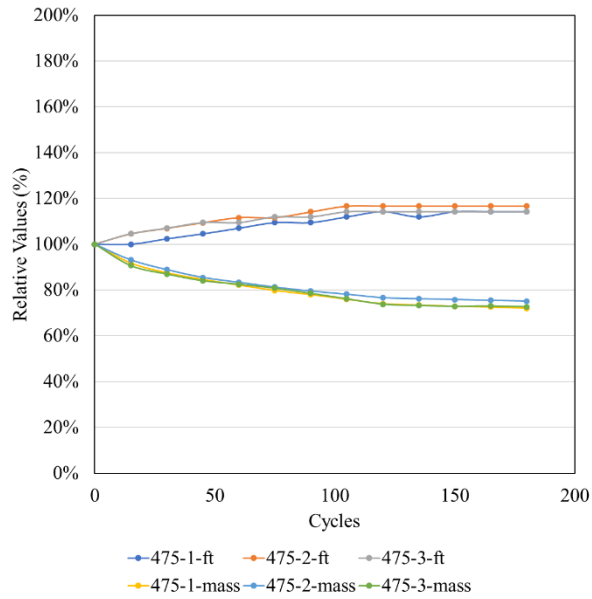


Figure 6-9 Freeze-thaw deterioration data for 475 samples – 365 days thaw in water

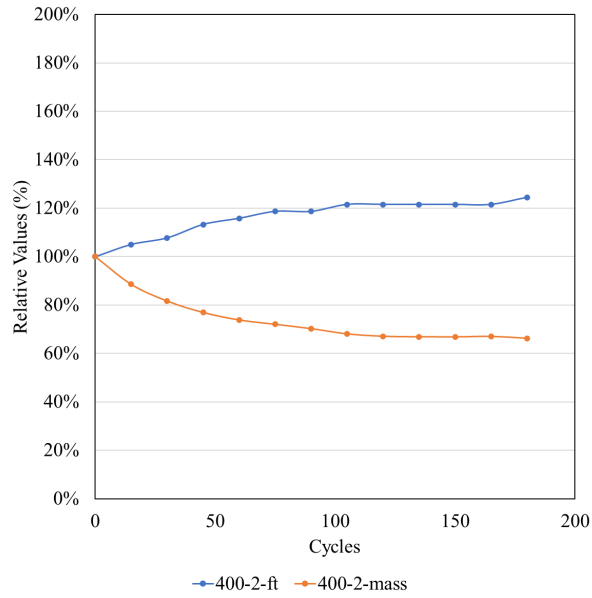


Figure 6-10 Freeze-thaw deterioration data for 400 samples – 365 days thaw in water

The average relative values of the freeze-thaw deterioration data for three densities were shown in Figure 6-11. The 400 kg/m³ samples had the highest relative dynamic modulus of elasticity but also shown a faster rate of losing weight, followed by 475 kg/m³ and 600 kg/m³ samples. The weight loss could be due to the lost of moisture and the damaged surface.

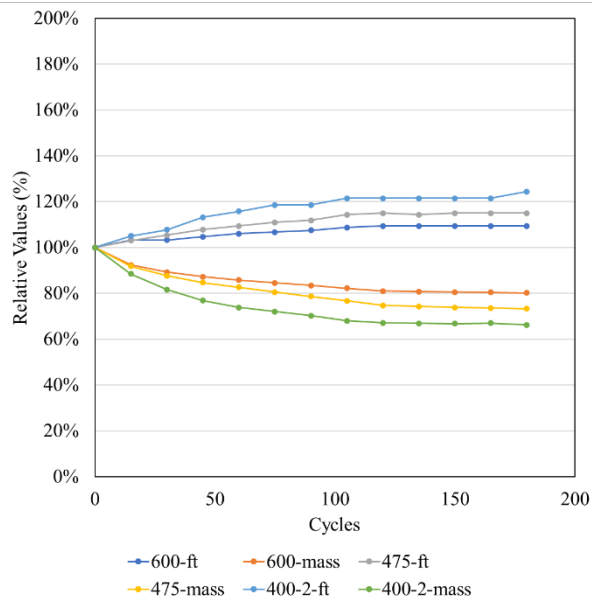


Figure 6-11 Freeze-thaw deterioration data (average value)– 365 days thaw in water

Figure 6-12 illustrated the compressive strength of lightweight cellular concrete for one year samples. Similar to the 28-days samples, the coefficient of determination (R^2) for three densities did not exceed 0.7, showing that the compressive strength for all the densities was not affected by freeze-thaw cycling, this also matched Tikalsky's research that cellular concrete with over 1 MPa has good freeze-thaw resistance.

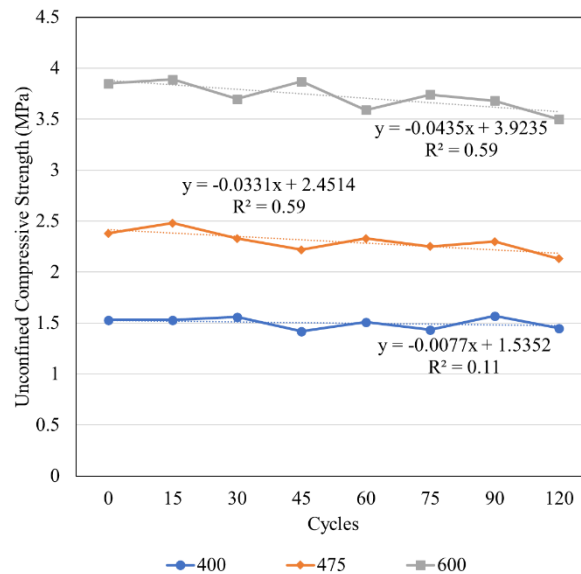


Figure 6-12 Compressive strength of LCC under freeze-thaw cycling (average value)– 365 days thaw in water

6.3.2 Thaw in air scenario

Figure 6-13 illustrated the freeze-thaw deterioration data for the 365 days samples thaw in air scenario. The relative dynamic modulus of elasticity of all densities had the increasing trend as the thaw in water scenario initially. However, all the densities began to degrade after 45 cycles. The 600 kg/m³ samples degraded faster than 475 kg/m³ and 400 kg/m³ densities, respectively. The values fell below 70% after 105 cycles for 600 kg/m³ and 475 kg/m³ samples, 150 cycles for 400 kg/m³ samples. The thaw in water scenario showed a similar trend. The 400 samples had the fastest rate of deterioration, followed by the 475 kg/m³ samples, and 600 kg/m³ samples. Nevertheless, the compressive strength for all the densities was not affected by freeze-thaw cycling, which is similar to the thaw in water scenario, as shown in Figure 6-14.

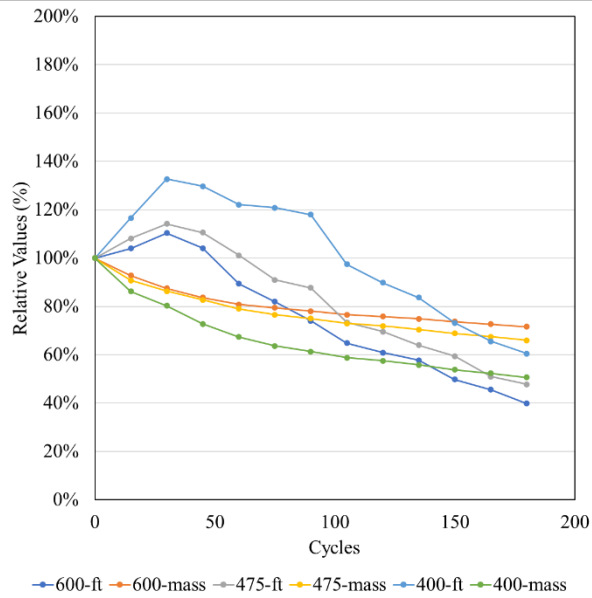


Figure 6-13 Freeze-thaw deterioration data (average value)– 365 days thaw in air

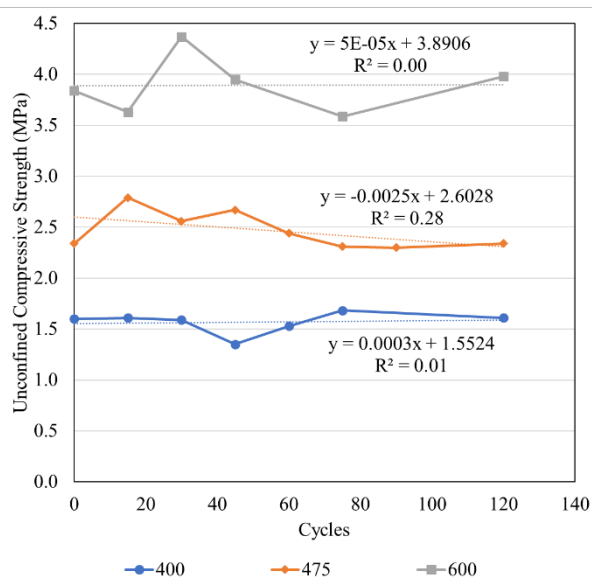


Figure 6-14 Compressive strength of LCC under freeze-thaw cycling (average value)– 365 days thaw in air

6.4 Visual images of the Samples

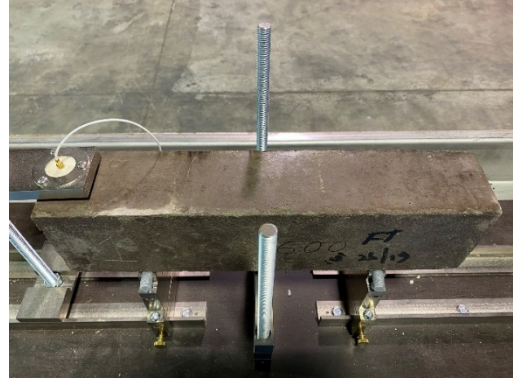
The visual images of the samples for the freeze-thaw test are presented in this section. Figure 6-15 to Figure 6-17 demonstrated the images for the thaw in water scenario at 0 and 180 cycles. The 600 kg/m³ samples for 28 days didn't have significant damages after 180 cycles. 365 days sample were found to have some parts of the surface got peeled off. However, these surface damages did not affect their relative modulus of elasticity. The 475 kg/m³ samples also showed similar results with the 600 kg/m³ samples. There were few damages found on the surface of the 475 kg/m³ samples. Nevertheless, these damages were not affecting the relative dynamic modulus of elasticity on the 475 kg/m³ samples. On the contrary, the 28 days 400 kg/m³ samples were seriously damaged after 180 cycles of freeze-thaw cycling. This explained their decreasing relative dynamic modulus of elasticity trend. Moreover, The weight of the samples increased significantly in the first 60 cycles but then decreased after 75 cycles. This could be explained by the fact that the samples absorb more water which increased their weight through the damaged surface at the start of the test. But, then dropped later due to more parts of the sample that collapsed during the test. The 365 days 400 kg/m³ samples, though, did not have significant deterioration. The relative dynamic modulus of elasticity results showed the same trend as the 365 days 475 kg/m³ and 600 kg/m³ samples.

28 days



0 cycle

365 days



0 cycle



180 cycles



180 cycles

Figure 6-15 Visual images of the 600 samples at 0 and 180 cycles – thaw in water

28 days

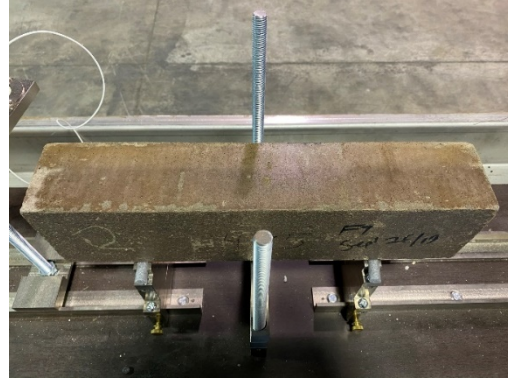


0 cycle

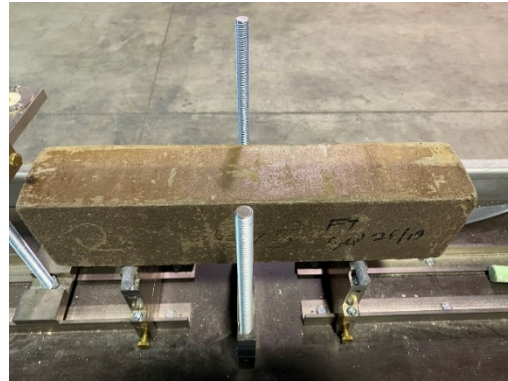


180 cycles

365 days



0 cycle



180 cycles

Figure 6-16 Visual images of the 475 samples at 0 and 180 cycles – thaw in water

28 days



0 cycle

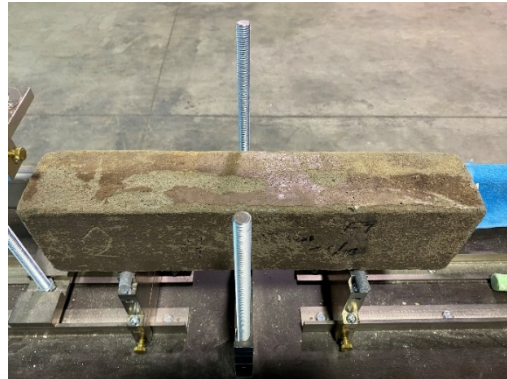
365 days



0 cycle



180 cycles



180 cycles

Figure 6-17 Visual images of the 400 samples at 0 and 180 cycles – thaw in water

Figure 6-18 to Figure 6-20 illustrated the images for the thaw in air scenario at 0 and 180 cycles. For 28 days samples, it was found that there were minimal damages to appear on the 475 kg/m³ and 600 kg/m³ samples. Some damages happened on the edge of the 400 kg/m³ samples. However, the relative dynamic modulus of elasticity results showed that the 400 kg/m³ samples did not degrade due to these damages. The weight of all the samples decreased in the first 105 cycles for 475 kg/m³ and 135 cycles for 400 kg/m³ and 600 kg/m³ samples but then increased to 110% for 400 samples, 138 for 475 kg/m³ samples, and 103% for 600 samples. This could be because of the water condensation that keeps the samples moist and absorbed the surface water. The 365 days samples were not damaged for all the densities. However, their relative dynamic modulus of elasticity degraded after 45 cycles. Furthermore, the weight of all samples decreased steadily during the freeze-thaw cycling, leading to the decreasing trend of the relative dynamic modulus of elasticity that the samples were dried and could have drying shrinkage cracks during the cycling.

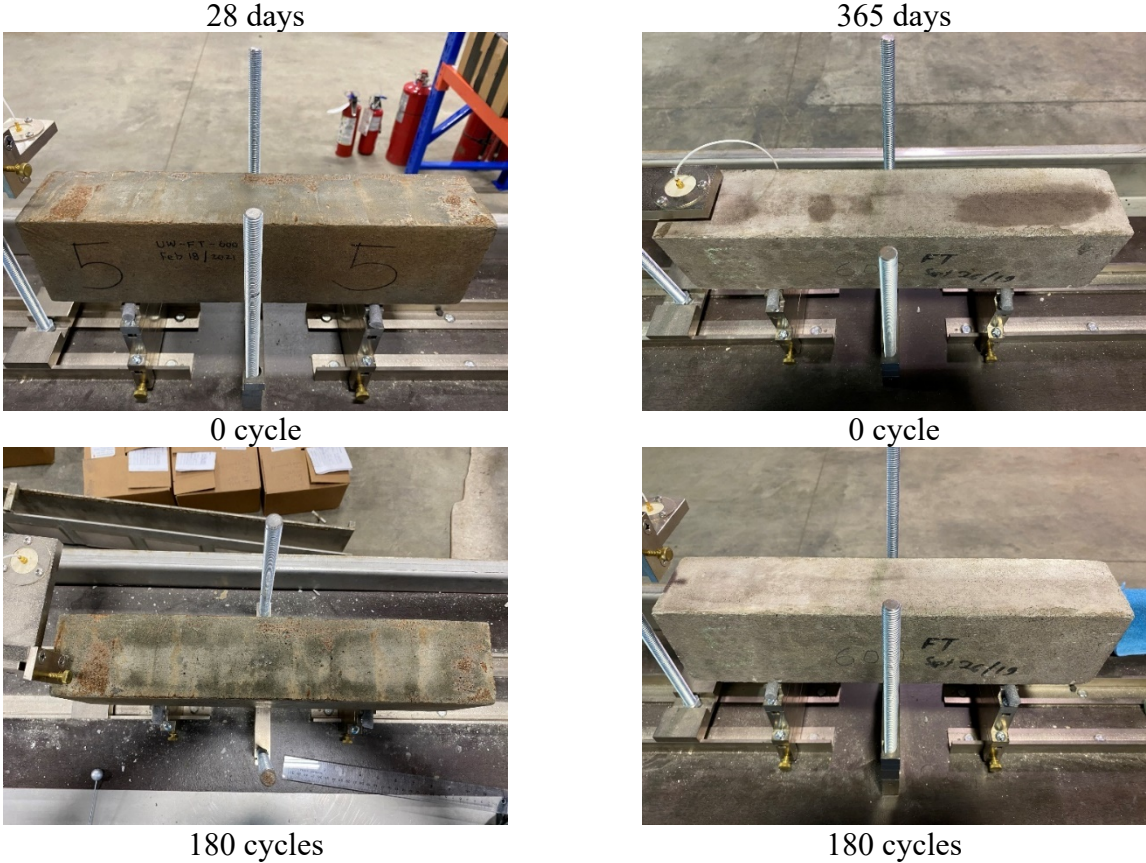
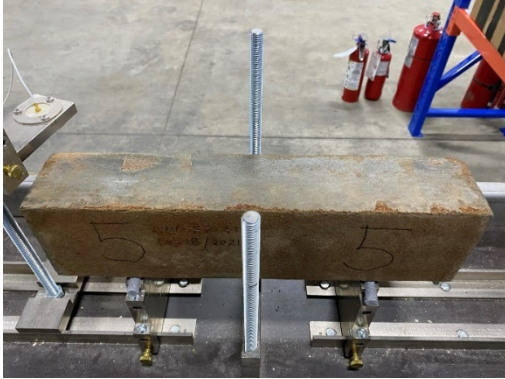


Figure 6-18 Visual images of the 600 samples at 0 and 180 cycles – thaw in air

28 days



0 cycle

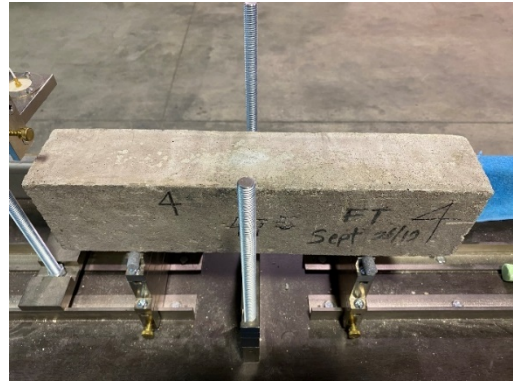


180 cycles

365 days



0 cycle



180 cycles

Figure 6-19 Visual images of the 475 samples at 0 and 180 cycles – thaw in air

28 days

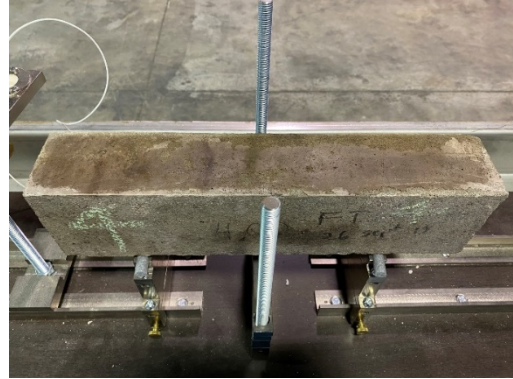


0 cycle



180 cycles

365 days



0 cycle



180 cycles

Figure 6-20 Visual images of the 400 samples at 0 and 180 cycles – thaw in air

6.5 Water absorption

Figure 6-21 demonstrated the average water absorption values of the oven-dried sample. The water absorption of the three densities ranges from 24.5% to 33%. 400 kg/m³ density has the highest water absorption while 600 kg/m³ density showing the lowest water absorption. This indicates that the density impacts the water absorption of lightweight cellular concrete ($R^2=0.99$). Another water absorption test scenario without oven-drying the samples was performed in this research. The samples were cured and put into water without oven-drying them. The results are shown in Figure 6-22 and Figure 6-23. The water absorption increased with the number of days immersed in water increased. Results also indicated that 400 kg/m³ had the highest water absorption, while 600 kg/m³ had the lowest values. The results are reasonable since the porosity of lower densities lightweight cellular concrete is higher (Kearsley and Wainwright 2002) and could absorb more water (Kearsley and Wainwright 2001). The water absorption of the three densities was considered saturated as the difference from 56 days to 90 days is below one percent. Moreover, the 150 by 300 mm samples' water absorption has lower values than 75 by 150 mm samples.

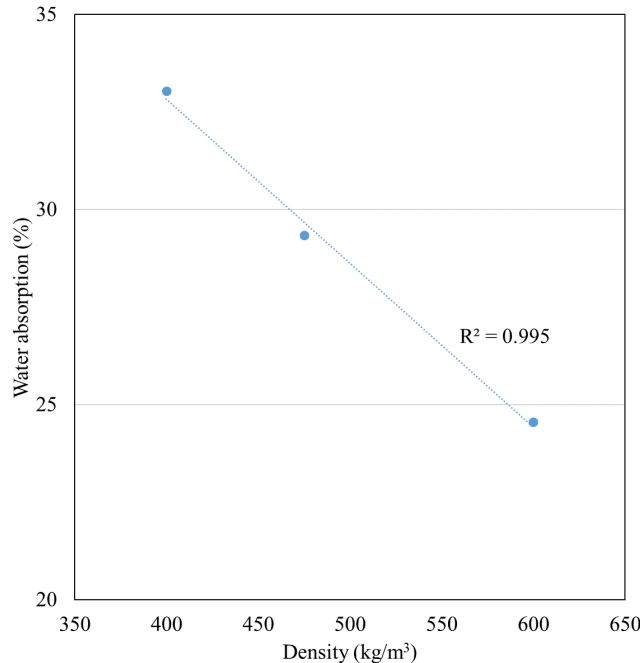


Figure 6-21 Water Absorption at different density

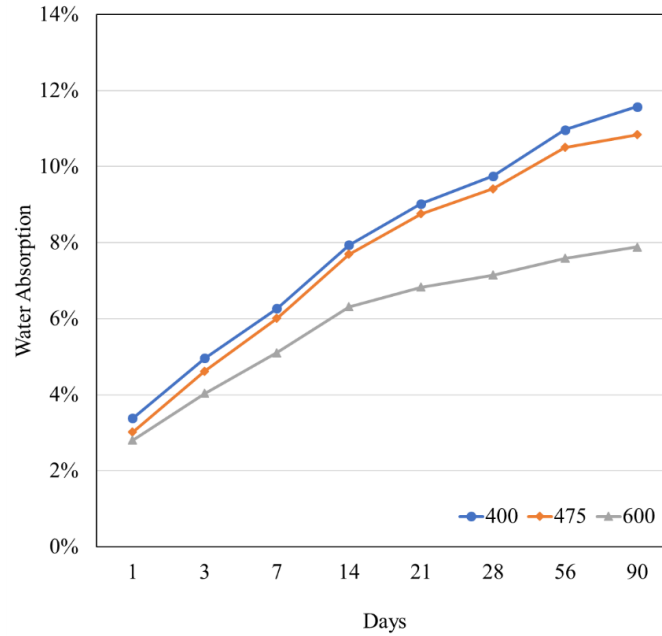


Figure 6-22 Results of Water Absorption test (150 by 300 mm)

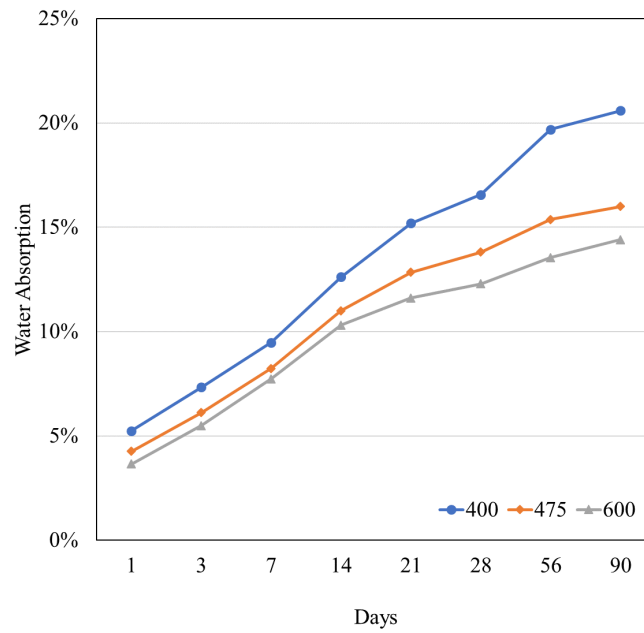


Figure 6-23 Results of Water Absorption test (75 by 150 mm)

6.6 Permeability

The results of the permeability test for three densities were shown in Table 6-1 and Figure 6-24. The results demonstrated that 600 kg/m³ density samples have no permeability with the coefficient of permeability (K) equal to 0, while 475 kg/m³ and 400 kg/m³ at 0.011 and 0.035. This mean that the running water can barely penetrate the lightweight cellular concrete in a short amount of time.

Table 6-1 Results of Permeability test for three densities

Density (kg/m ³)	1st head (mm)	2nd head (mm)	L (cm)	Time (min)	A (cm ²)	a (cm ²)	K
400	59.0	58.7	7.5	5	15.52	2.85	0.035
475	58.9	58.8	7.5	5			0.012
600	58.0	58.0	7.5	5			0

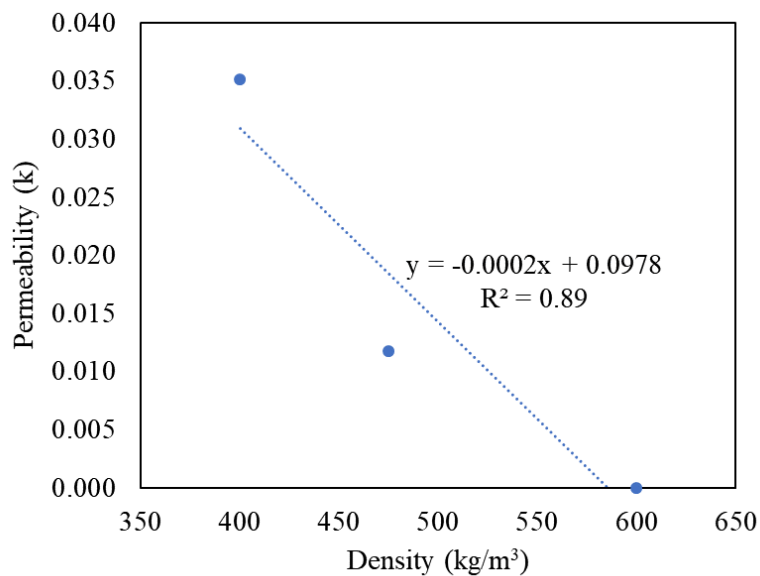


Figure 6-24 Results of permeability test

6.7 Sorptivity

Figures 6-25 and 6-26 illustrated the lightweight cellular concrete's sorptivity test results under two scenarios. The results indicated that 600 kg/m³ density had the lowest sorptivity than the 475 kg/m³ and 400 kg/m³ density samples. The air-dry scenario found that 475 kg/m³ density has higher values than 400 kg/m³. This could be because 400 kg/m³ has a broader range of standard deviation than the other two densities, which is 0.1 to 0.6 compared to the 0 to 0.1 for 475 kg/m³ and 600 kg/m³ density. However, a different trend was found in the oven-dry scenario; while 600 kg/m³ density remains to have the lowest sorptivity, the 475 kg/m³ and 400 kg/m³ have similar sorptivity results. The above results indicated that the lightweight cellular concrete may still get penetrated by water in the long term through capillary pore even though the permeability is low.

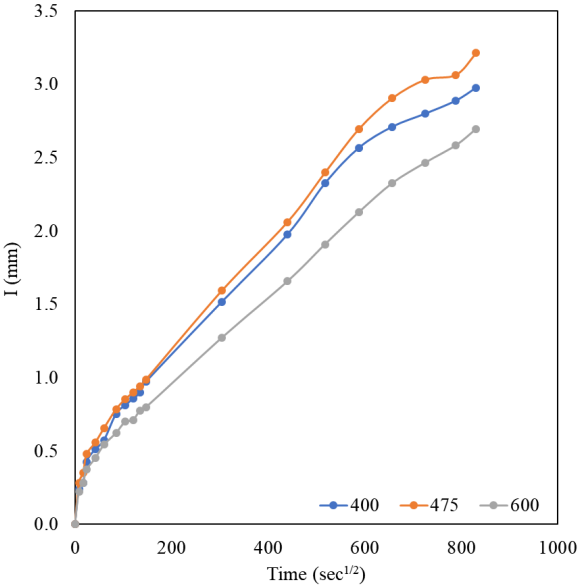


Figure 6-25 Results of Sorptivity test (air dry samples)

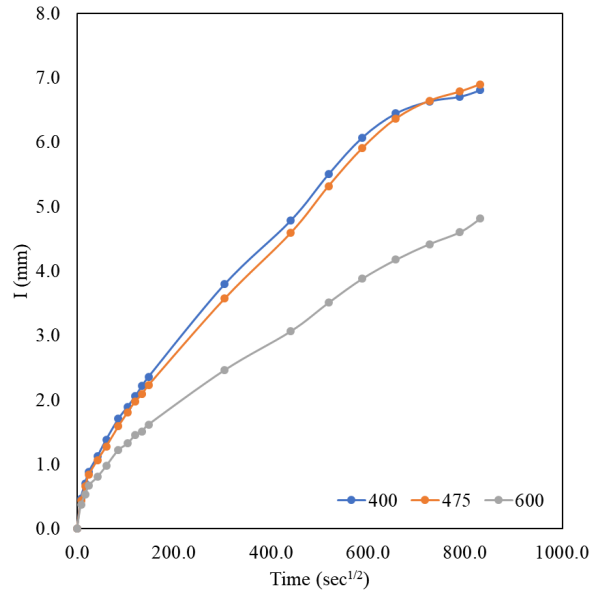


Figure 6-26 Results of Sorptivity test (oven dry samples)

6.8 Summary and Findings

This chapter described the freeze-thaw resistance of lightweight cellular concrete, along with other properties related to water penetration. The freeze-thaw test involved two different scenarios based on the cured life of the lightweight cellular concrete. Each scenario was divided into two different testing procedures. Both procedures freeze the samples until their temperature reached $-18 \pm 2^\circ\text{C}$. However, the first procedure thawed the sample in water until they got to the thawing temperature, the second procedure thawed the samples in the air instead. Other properties related to water penetration were evaluated in this chapter.

For the thawing in water procedure, the 28 days 475 kg/m^3 and 600 kg/m^3 samples were not damaged by the freeze-thaw cycling but instead increased their stiffness. However, 400 kg/m^3 samples deteriorated after 15 cycles and fall below the 70% threshold after 30 and 45 cycles. On the other hand, all the 365 days samples were not degraded but instead increased their stiffness after 180 cycles. This showed that the effect of curing time on the lightweight cellular concrete's freeze-thaw resistance.

The thaw in air procedure for both 28 days and 365 days samples was conducted in this research. The 28 days samples did not significantly get affected by the freeze-thaw cycling. However, the 365 days samples degraded after 45 cycles. The difference between the 28 days and 365 days samples' results could be due to the loss of moisture. As the 28 days, samples still maintained their weight while the 365 days samples lost 30 to 50 % of the weight. The compressive strength for both procedures was also examined. It was found that freeze-thaw cycling does not have a major effect on lightweight cellular concrete.

Other properties related to water penetration were also investigated in this research. Lower densities of lightweight cellular concrete were showing to have a higher value of water absorption. Even though the lightweight cellular concrete was found to have low permeability so running water may not penetrate the material in a short amount of time. However, the results of sorptivity indicated that the lower densities were more prompted to absorb the water through capillary pores. Nevertheless, saturated lightweight cellular concrete at 475 and 600 kg/m³ densities still appeared to be durable after 180 cycles of freeze-thaw cycling.

Chapter 7 Optimization of application of LCC in pavement subbase

7.1 Pavement performance and structural analysis

It is important to understand if the design is viable under certain traffic and environmental conditions during flexible pavement design. As the structure design is complicated in pavement design, there are different methods to evaluate pavement performance. For instance, pavement structural evaluation software such as Weslea and Mechanistic-Empirical Pavement Design Guide (MEPDG) was used to perform the task. Weslea is a mechanistic pavement analysis program that calculates pavement responses such as stress, strain, and displacement to applied tire loads. The program can also perform pavement failure criteria analysis concerning fatigue cracking and rutting. The MEPDG translates pavement responses to different performance criteria through performance models. In this study, the performance criteria considered in MEPDG are AC bottom-up fatigue cracking, permanent deformation (rutting), and International Roughness Index (IRI).

7.2 Failure criteria analysis via Weslea

In mechanistic-empirical pavement design methods, the failure criteria directed to specific types of distress are established (Huang, 1993). In flexible pavement, fatigue cracking and rutting are the two important failure criteria. The fatigue cracking of flexible pavement is based on the horizontal tensile strain at the bottom of the asphalt concrete surface layer. Simultaneously, rutting depends on the vertical compressive strain on the top of the subgrade. The Weslea for windows 3.0 software can predict the stress, strain, and displacement value generated from applied tire load. The predicted strain values can compute the allowable number of loads for fatigue cracking and rutting. The equations are listed below:

$$N_{fc} = 2.83 \times 10^{-6} \left(\frac{10^6}{\epsilon_t} \right)^{3.148} \quad 7.1$$

Where:

N_{fc} = Allowable number of load repetition before fatigue cracking

ϵ_t = Tensile strain at the bottom of the surface layer

$$N_{fr} = 1.0 \times 10^{16} \left(\frac{1}{\epsilon_v} \right)^{3.87} \quad 7.2$$

Where:

N_{fr} = Allowable number of load repetition before rutting

ϵ_v = Compressive strain at the top of the subgrade layer

7.2.1 Model Inputs

To perform the failure criteria analysis, it is essential to provide model inputs to the software. The inputs include pavement thickness, layer properties, and load configuration. The inputs are demonstrated in Table 7-1 and Figure 7-1. Three different pavement structures correspond to three different road classes were chosen to perform the failure criteria analysis. The three road classes are major arterial, minor arterial, and collector roadways. The major arterial road is assumed to have two lanes per direction, with 80 percent of the commercial truck traffic in the design lane. The minor arterial road and collector have one lane for each direction. The traffic volume for major arterial is 7,500 Average Annual Daily Truck Traffic (AADTT), 1,000 AADTT for minor arterial roads, and 500 for the collector. The three road classes' thickness design was taken from representative pavement designs for Ontario Municipalities (ARA, 2015).

It should be noted that the average and lowest modulus of elasticity LCC were used in the analysis. The material properties of the surface, base, and subgrade layers are assumed based on literature (ARA, 2015), and only the properties of the subbase layer are varying. The load location, magnitude, and tire pressure were assumed to be the software's default values, as shown in Figure 7-2. The purpose of the above assumption is to examine and compare LCC's performance to granular subbase material.

Table 7-1 Model input for Weslea software

	Surface	Base	Subbase			Subgrade	
	Hot-mix asphalt concrete	Granular A	Granular B	LCC			Soil
				600	475	400	
Average E (MPa)	3,445	250	200	1,490	1,001	728	30
Lowest E (MPa)	3,445	250	200	1,172	647	634	30
Poisson's Ratio	0.35	0.35	0.35	0.2	0.21	0.25	0.45
Major arterial	17	15	60	60	60	60	-
Minor arterial	13	15	45	45	45	45	-
Collector	12	15	40	40	40	40	-

Structural Information (F1 for Help)

Number of Layers: 2 3 4 5

	Layer 1	Layer 2	Layer 3	Layer 4	Layer 5
Material Type	AC	GB	GB	Soil	Soil
Min Modulus, MPa	551.6	34.5	34.5	20.7	20.7
Layer Modulus, MPa	3447.4	250	200	30	30
Max Modulus, MPa	13789.5	344.7	344.7	206.8	206.8
Poisson's Ratio	0.35	0.35	0.35	0.45	0.45
Min - Max	0.15 - 0.4	0.3 - 0.45	0.3 - 0.45	0.2 - 0.5	0.2 - 0.5
Thickness, cm	17	15	60	2537.46	Infinite
Slip (0 or 1)		1	1	1	1

Slip (0 or 1)
1 = Full Adhesion
0 = Full Slip

OK Cancel

Figure 7-1 Weslea pavement structure input window

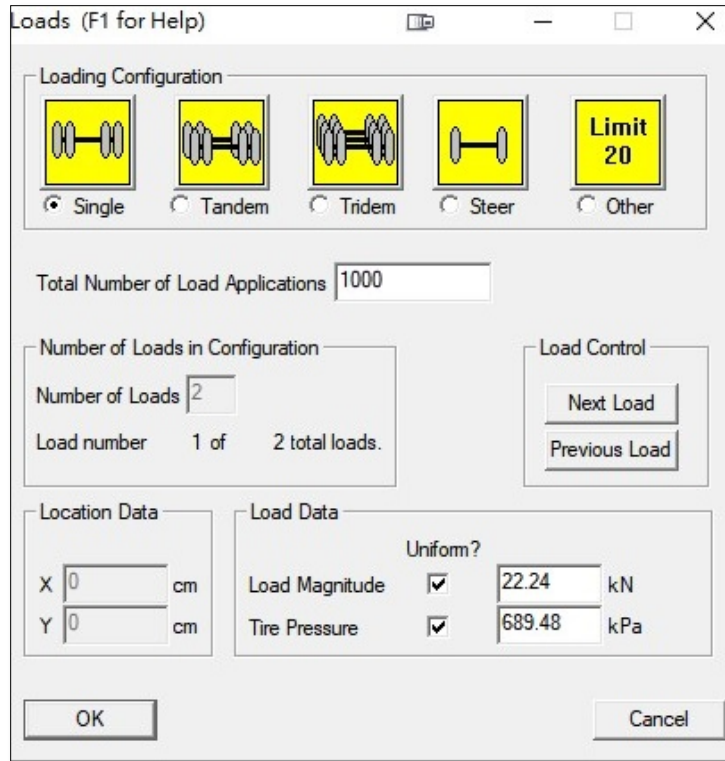


Figure 7-2 Weslea traffic load input window

7.2.2 Model Result

The failure criteria analysis results are shown in Figures 7-3 to 18. Figures 7-3 to 7-10 demonstrate the allowable number of load repetitions before fatigue cracking and rutting happen for the three road classes when using the average modulus of elasticity (MOE) of LCC to perform analysis. Figures 7-11 to 7-18 explain the results using the lowest modulus of elasticity of LCC.

When running with average MOE, it is clear that the pavement with the LCC subbase is more durable than the pavement with the Granular B layer at the same thickness since the allowable number of load repetitions for fatigue cracking and rutting are higher, as shown in Figure 7-3, 7-5, and 7-7. LCC with 600 kg/m^3 density has the highest allowable number of load repetitions for both failure criteria, following by 475 kg/m^3 , 400 kg/m^3 , and Granular B. It was found that LCC pavement has at least 70% more load repetitions than the Granular B pavement for fatigue cracking in all three road classes. As for rutting, the differences become more significant as the

allowable number of load repetitions of LCC pavement is at least seven times larger than Granular B pavement, showing that LCC has excellent rutting resistance than conventional unbound granular material. Figure 7-4, 7-6, and 7-8 demonstrate the allowable number of loads at different thicknesses for the three road classes using the average MOE of LCC. The results indicated that the pavement thickness using LCC as subbase material could be thinner than the conventional unbound granular pavement, which reduced the excavation depth during the construction and saves more time. Figures 6-9 and 6-10 illustrate the vertical compressive strain at the top of the subgrade layer and the horizontal tensile strain at the bottom of the surface layer for the three road classes. It shows that traffic load generates smaller strain values for the LCC pavement than the conventional unbound granular pavement at the same thickness for the three road classes, which explains the significant difference between the allowable number of load repetitions of LCC and granular pavement.

Figures 7-11, 7-13, and 7-15 showed the allowable number of loads for fatigue cracking and rutting using the lowest MOE of LCC. It was found that the LCC pavement outperforms granular subbase pavement, the same as the average MOE LCC results. However, the 475 kg/m³ density has similar results as the 400 kg/m³ density LCC. This is due to the comparable MOE values of the two densities. Nevertheless, the LCC pavement still has at least 65% more load repetitions for both failure criteria than the granular subbase pavement.

Figures 7-12, 7-14, and 7-16 demonstrate the allowable number of load repetitions at different thicknesses for the three road classes. Even though the differences between the Granular B and LCC pavement become smaller at the thinner thickness, the LCC still has at least 1.6 times the allowable loads than granular subbase pavement at minimum thickness. Figures 6-17 and 6-18 illustrate the vertical compressive strain at the top of the subgrade layer and the horizontal tensile strain at the bottom of the surface layer for the three road classes. Results showed that the LCC pavement has fewer strain values than granular pavement at the same thickness for the three road classes, even using the lowest MOE. The results above show that using lightweight cellular concrete as subbase layer material could be practical and possible. However, the software does not consider the environmental impact such as temperature and moisture. An in-situ field inspection is needed to evaluate the pavement's environmental effect using lightweight cellular concrete as a subbase layer.

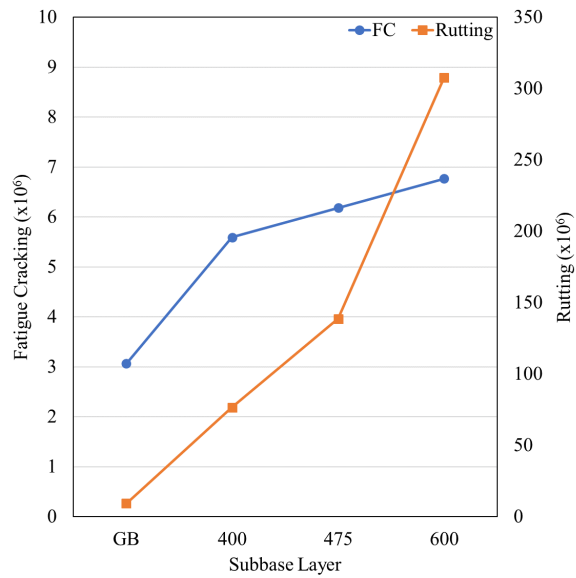
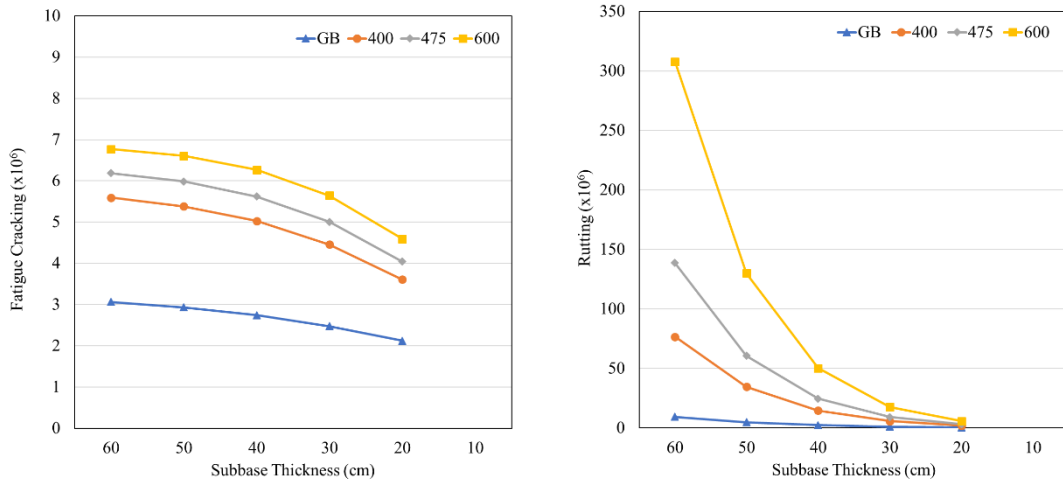


Figure 7-3 Allowable number of loads for fatigue cracking and rutting for major arterial (Avg. MOE)



(a) Fatigue cracking

(b) Rutting

Figure 7-4 Allowable number of loads at different thicknesses for major arterial (Avg. MOE)

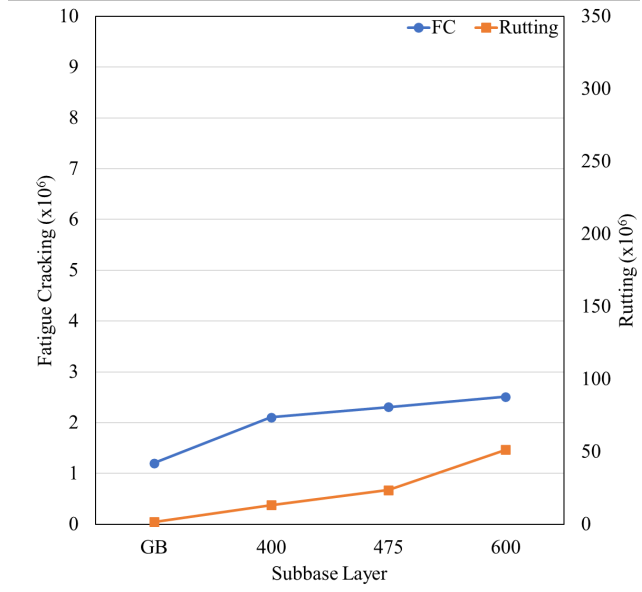
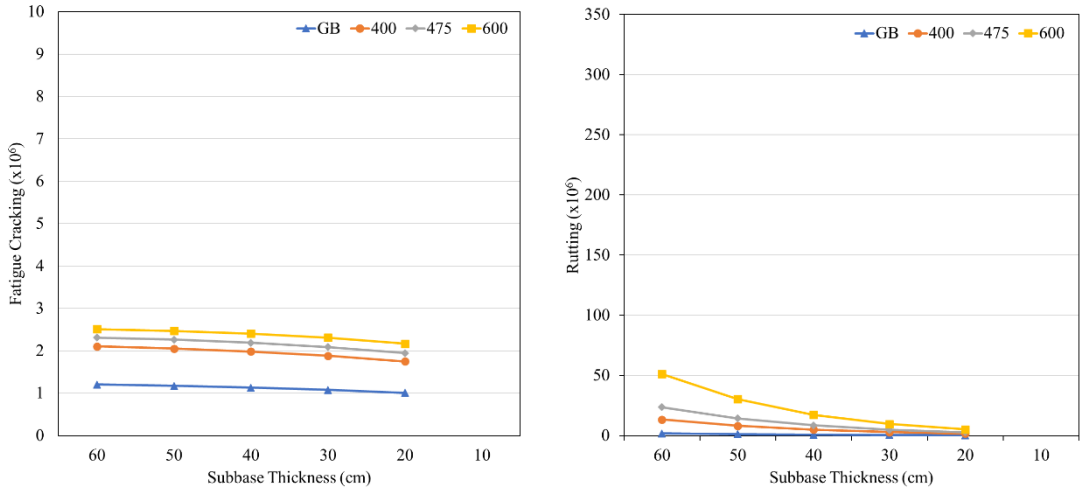


Figure 7-5 Allowable number of loads for fatigue cracking and rutting for minor arterial (Avg. MOE)



(a) Fatigue cracking

(b) Rutting

Figure 7-6 Allowable number of loads at different thicknesses for minor arterial (Avg. MOE)

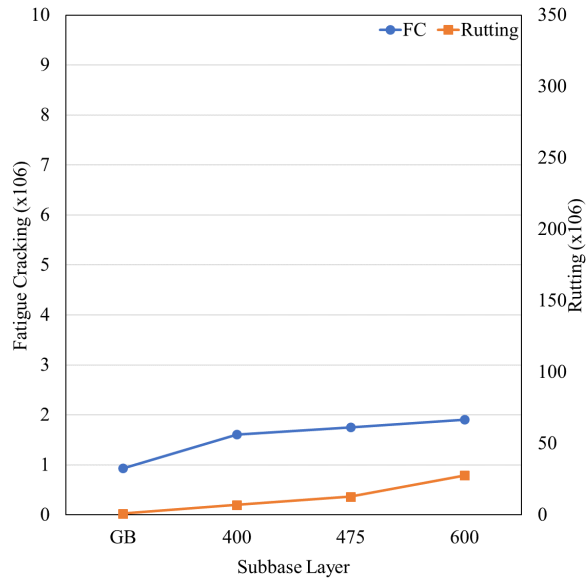
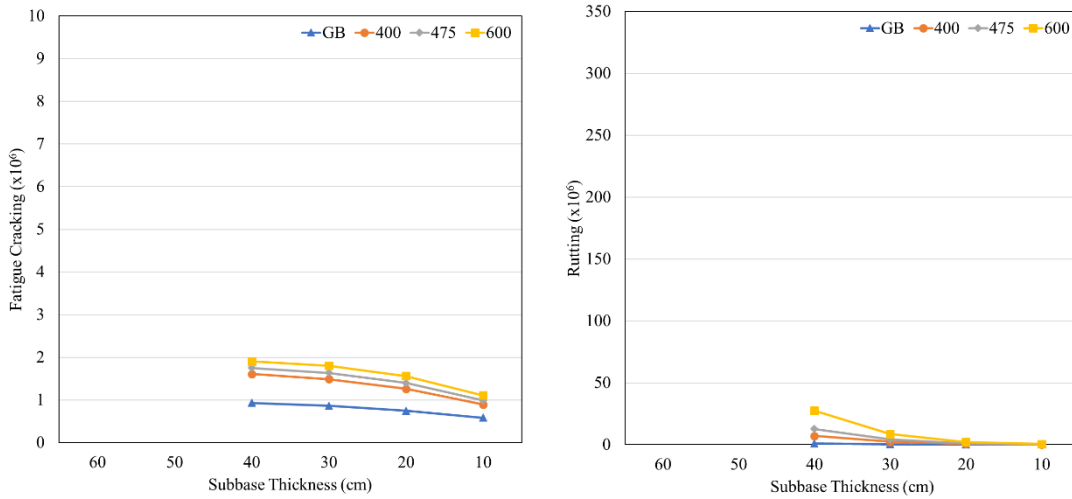


Figure 7-7 Allowable number of loads for fatigue cracking and rutting for collector (Avg. MOE)



(a) Fatigue cracking

(b) Rutting

Figure 7-8 Allowable number of loads at different thicknesses for collector (Avg. MOE)

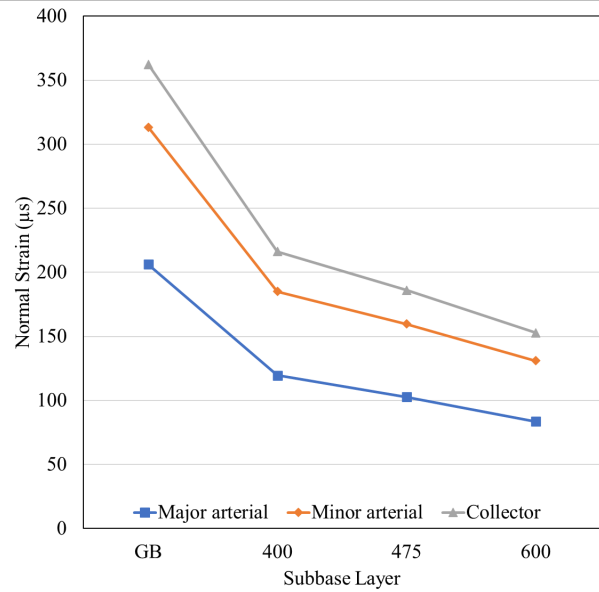


Figure 7-9 Vertical compressive strain at the top of the subgrade layer (Avg. MOE)

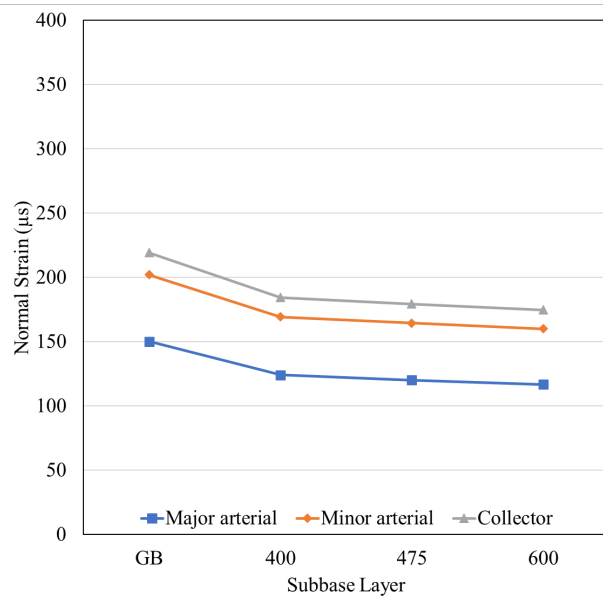


Figure 7-10 Horizontal tensile strain at the bottom of the surface layer (Avg. MOE)

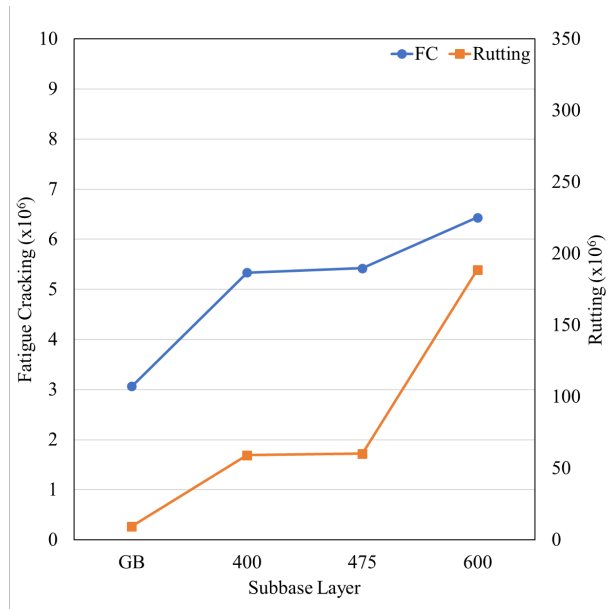
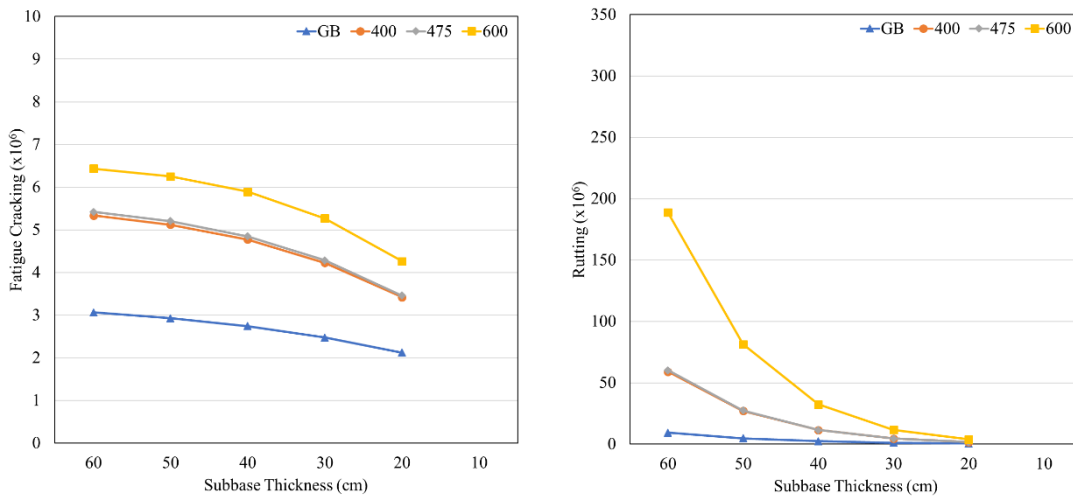


Figure 7-11 Allowable number of loads for fatigue cracking and rutting for major arterial (Lowest MOE)



(a) Fatigue cracking

(b) Rutting

Figure 7-12 Allowable number of loads at different thicknesses for major arterial (Lowest MOE)

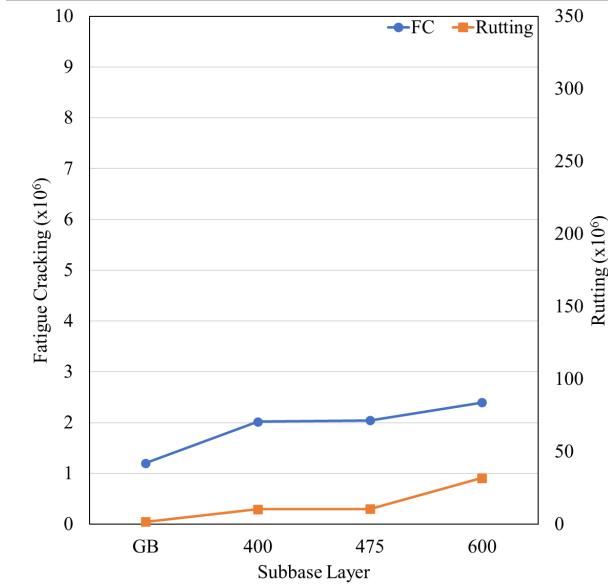
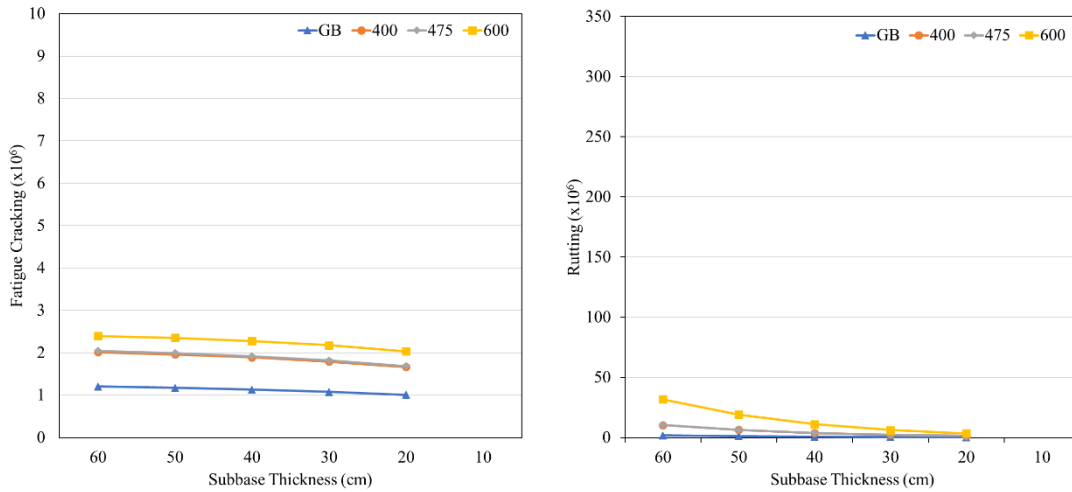


Figure 7-13 Allowable number of loads for fatigue cracking and rutting for minor arterial (Lowest MOE)



(a) Fatigue cracking

(b) Rutting

Figure 7-14 Allowable number of loads at different thicknesses for minor arterial (Lowest MOE)

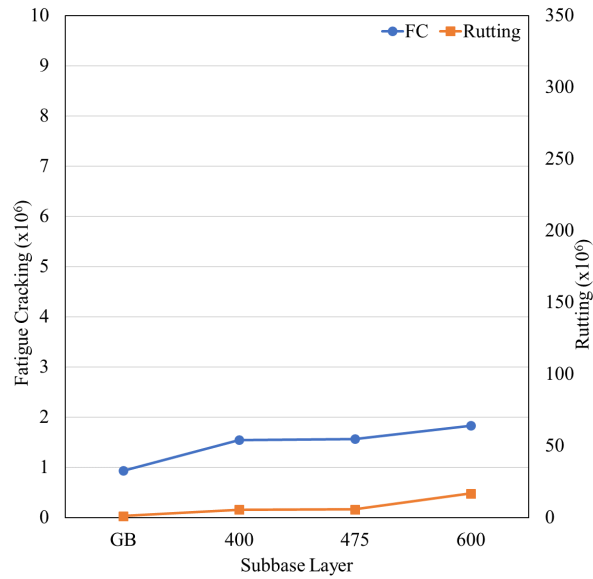
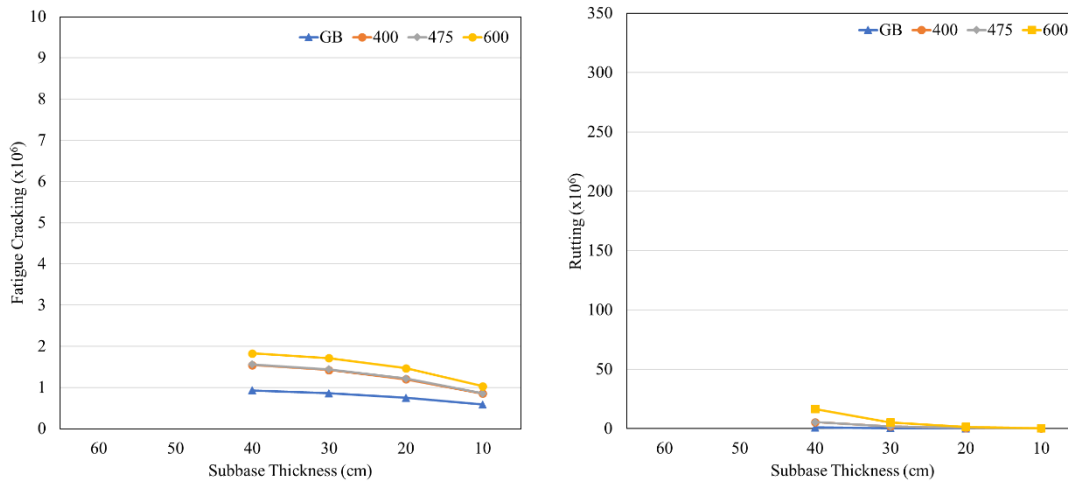


Figure 7-15 Allowable number of loads for fatigue cracking and rutting for collector (Lowest MOE)



(a) Fatigue cracking

(b) Rutting

Figure 7-16 Allowable number of loads at different thicknesses for collector (Lowest MOE)

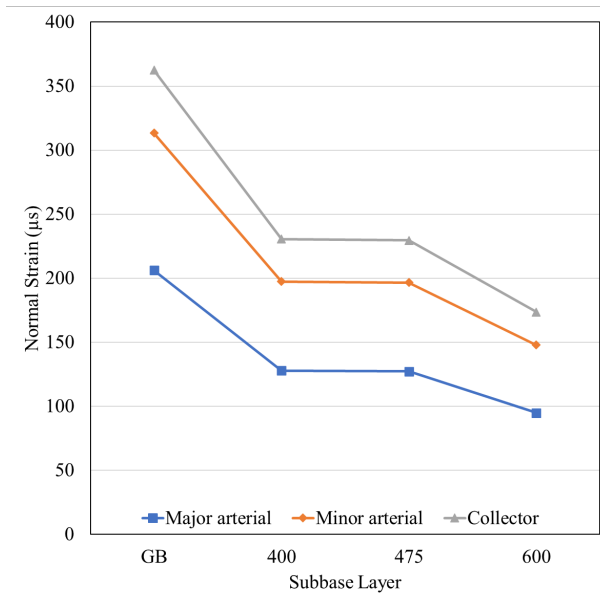


Figure 7-17 Vertical compressive strain at the top of the subgrade layer (Lowest MOE)

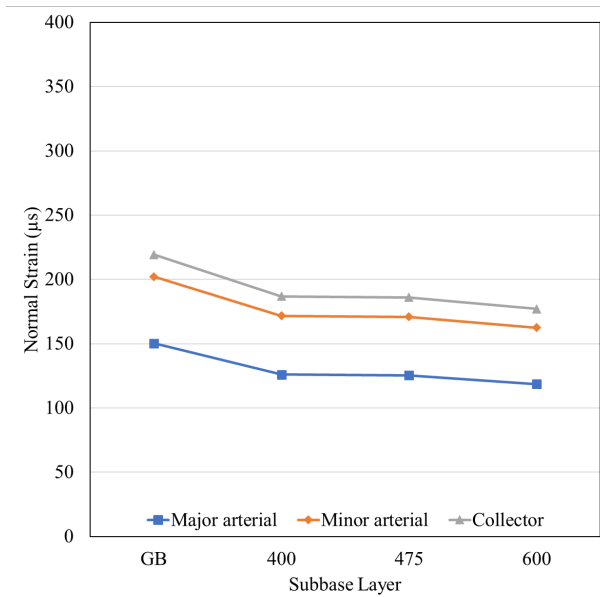


Figure 7-18 Horizontal tensile strain at the bottom of the surface layer (Lowest MOE)

7.3 Granular Base Equivalency (GBE) of LCC

The Granular Base Equivalency (GBE) is a method that expresses each pavement layer's structural contribution by converting their thickness into the equivalent thickness of the granular base. Granular Base Equivalency (GBE) equates the pavement materials' strength in terms of their thicknesses. “The GBE thickness is the required overall structural pavement thickness expressed in terms of an equivalent thickness of Granular A” (MTO, 2013). GBE is usually calculated as follows:

$$\text{GBE (He)} = a_1h_1 + a_2h_2 + a_3h_3 \quad 7.3$$

Where:

He = the equivalent granular thickness.

a_1, a_2, a_3 = strength coefficients of the asphalt layer, base layer, and subbase layer.

h_1, h_2, h_3 = the actual thicknesses of the asphalt layer, base layer, and subbase layer.

The typical strength coefficients (equivalency factors) for the control section consisting of the asphalt layer, granular A for the base layer, and Granular B for the subbase layer are obtained from the OPAC 2000 specifications. The thickness for these layers has been obtained from ARA's typical values for the required traffic level and subgrade condition. Typical values for Poisson's ratio and Modulus of Elasticity for each layer are also used for the control section.

For the LCC sections, to calculate the required baseline pavement thickness that would produce the same GBE value as the control section, the Weslea software is used. The microstrain values produced at the bottom of the subbase layers for various thicknesses are determined to achieve this. Laboratory results for Modulus of Elasticity and Poisson's ratio are utilized. The simulated values for strain and corresponding thickness for the Control and LCC sections were interpolated to determine thicknesses that would provide the same strain level. The strength coefficient for the LCC layers using the GBE formula was obtained. For weak subgrade with the resilient modulus less than 30MPa, the GBE expert value for the design traffic should not be less than 800 for 15 years according to OPAC 2000 values by MTO. The layer thickness was adjusted to

obtain a GBE expert value of 800 for all sections. The Input values and Strength Coefficient obtained for each layer are presented in Table 7-2. The GBE for LCC is calculated to be 1.22 for 400 kg/m³, 1.46 for 475 kg/m³, and 1.91 for 600 kg/m³. The results showed that LCC has a higher strength coefficient than Granular B, which results in a thinner subbase layer compared to the granular subbase layer.

Table 7-2 Input parameter and results of GBE

	Surface	Base		Subbase			Subgrade
	Hot-mix asphalt concrete	Granular A	Granular B	LCC			Soil
				600	475	400	
Average E (MPa)	3,445	250	200	1,490	1,001	728	30
Poisson's Ratio	0.35	0.35	0.35	0.2	0.21	0.25	0.45
Thickness(cm)	15	15	52	18	24	29	-
GBE strength coefficient	2	1	0.67	1.22	1.46	1.91	-

7.4 MEPDG performance criteria analysis

7.4.1 MEPDG Input and Scenarios

The MEPDG scenario follows the typical Ontario pavement design for different road classes (ARA, 2015). The scenario is set to be a newly constructed flexible pavement. The service period is 25 years. The road classes are major arterial, minor arterial, and collector. The traffic volume of major arterial is 7,500 annual average daily truck traffic (AADTT). The roadway is a four-lane highway with two lanes per direction. 80% of the commercial vehicles are running on the design lane. The minor arterial and collector have an AADTT of 1,000 and 500. Each road is a two-lane roadway with one lane per direction. Table 7-3 and Table 7-4 presented the pavement structure and layer material properties for the MEPDG input. In general, the pavement structure for all the road classes is consists of five layers. The five layers include an asphalt concrete

friction course, an asphalt concrete layer, an unbound granular base layer, a subbase layer, and a subgrade layer. The surface, base, and subgrade layer's material properties were taken from past research (ARA 2015, MTO 2019). However, the subbase layer's inputs were taken from past research and the LCC lab results. Though, in MEPDG, the LCC layer is assumed to be an unbound granular layer with a constant modulus. Climate input follows the Waterloo local weather station.

Table 7-3 Pavement structure for different road classes

		Road class		
		Major arterial	Minor arterial	Collector
Traffic volume (AADTT)		7,500	1,000	500
Layer	1	40 mm SP 12.5 FC1	40 mm SP 12.5 FC1	40 mm SP 12.5 FC1
	2	130 mm SP 19	90 mm SP 19	80 mm SP 19
	3	150 mm Granular A	150 mm Granular A	150 mm Granular A
	4	600 mm Granular B	450 mm Granular B	400 mm Granular B

Table 7-4 MEPDG input for Major Arterial

Major arterial			
7,500 AADTT			
Layer 1 SP 12.5 FC1		Layer 2 SP 19	
Thickness (mm)	40	Thickness (mm)	130
PG	PG 64-28	PG	PG 58-28
Effective Binder Content - by Volume (%)	11.8	Effective Binder Content - by Volume (%)	11.2
Air voids (%):	7	Air voids (%):	7
Poisson's Ratio	0.35	Poisson's Ratio	0.35
Total unit weight (kgf/m ³):	2390	Total unit weight (kgf/m ³):	2460
Layer 3 Granular A		Layer 4 Granular B	
Thickness (mm)	150	Thickness (mm)	600
Maximum dry unit weight (kgf/m ³)	2038.2	Maximum dry unit weight (kgf/m ³)	2022.2
Specific gravity of solids	2.7	Specific gravity of solids	2.7
Saturated hydraulic conductivity (m/hr)	0.02376	Saturated hydraulic conductivity (m/hr)	0.06073
Water content (%)	5.7	Water content (%)	7.3
Liquid Limit	6	Liquid Limit	11
Plasticity Index	0	Plasticity Index	0
Modulus (MPa)	250	Modulus (MPa)	200
Poisson's Ratio	0.35	Poisson's Ratio	0.35
Coefficient of Lateral Pressure (k ₀)	0.5	Coefficient of Lateral Pressure (k ₀)	0.5
Layer 5 Subgrade soil			
Thickness (mm)	Semi-infinite		
Maximum dry unit weight (kgf/m ³)	1748.5		
Specific gravity of solids	2.7		
Saturated hydraulic conductivity (m/hr)	8.13E-06		
Water content (%)	16.8		
Liquid Limit	26		
Plasticity Index	12		
Modulus (MPa)	30		
Poisson's Ratio	0.45		
Coefficient of Lateral Pressure (k ₀)	0.5		

7.4.2 MEPDG Model Results

This section presents the results of the MEPDG. According to the user inputs, the MEPDG software predicted pavement performance. This research's main performance criteria are the International Roughness Index (IRI), Permanent deformation, and bottom-up fatigue cracking. Table 7-5 to Table 7-7 demonstrated the predicted pavement performance criteria for three road classes at year 25. In general, most of the LCC sections' performance criteria outperform the Granular B section.

A. Major Arterial Roads

The MEPDG results for Major arterial roads at year 25 are demonstrated in Table 7-5. It was found that the terminal IRI and bottom-up fatigue cracking in the Granular B section exceed the threshold value. For the LCC section, 400 and 475 kg/m³ density LCC section also did not pass the bottom-up fatigue cracking standard. However, the values are 63% and 77% less than the Granular B section. Figure 7-19 illustrated the performance criteria for all the sections in the major arterial road. It was evident that the Granular B section exceeds the IRI and bottom-up fatigue cracking limit at year 23 and year 12, while 400 and 475 kg/m³ density LCC sections exceed the bottom-up fatigue cracking threshold value at year 22 and year 25. This showed that the LCC section could last longer than the Granular B section before pavement maintenance. It was found that the permanent deformation of the LCC section in the asphalt concrete layer is higher than in the granular section. However, the Granular B section is still higher than the LCC section when comparing the total layer's permanent deformation, even though all the sections pass the standard.

Table 7-5 Results of performance criteria for the major arterial road at year 25

Performance criteria	Target	Granular B	400	475	600
Terminal IRI (m/km)	3	3.22	2.99	2.97	2.96
Permanent deformation - total pavement (mm)	10	8.69	7.35	7.10	6.85
AC bottom-up fatigue cracking (%)	10	47.55	17.60	11.00	6.52
Permanent deformation - AC only (mm)	6	3.10	3.35	3.41	3.48

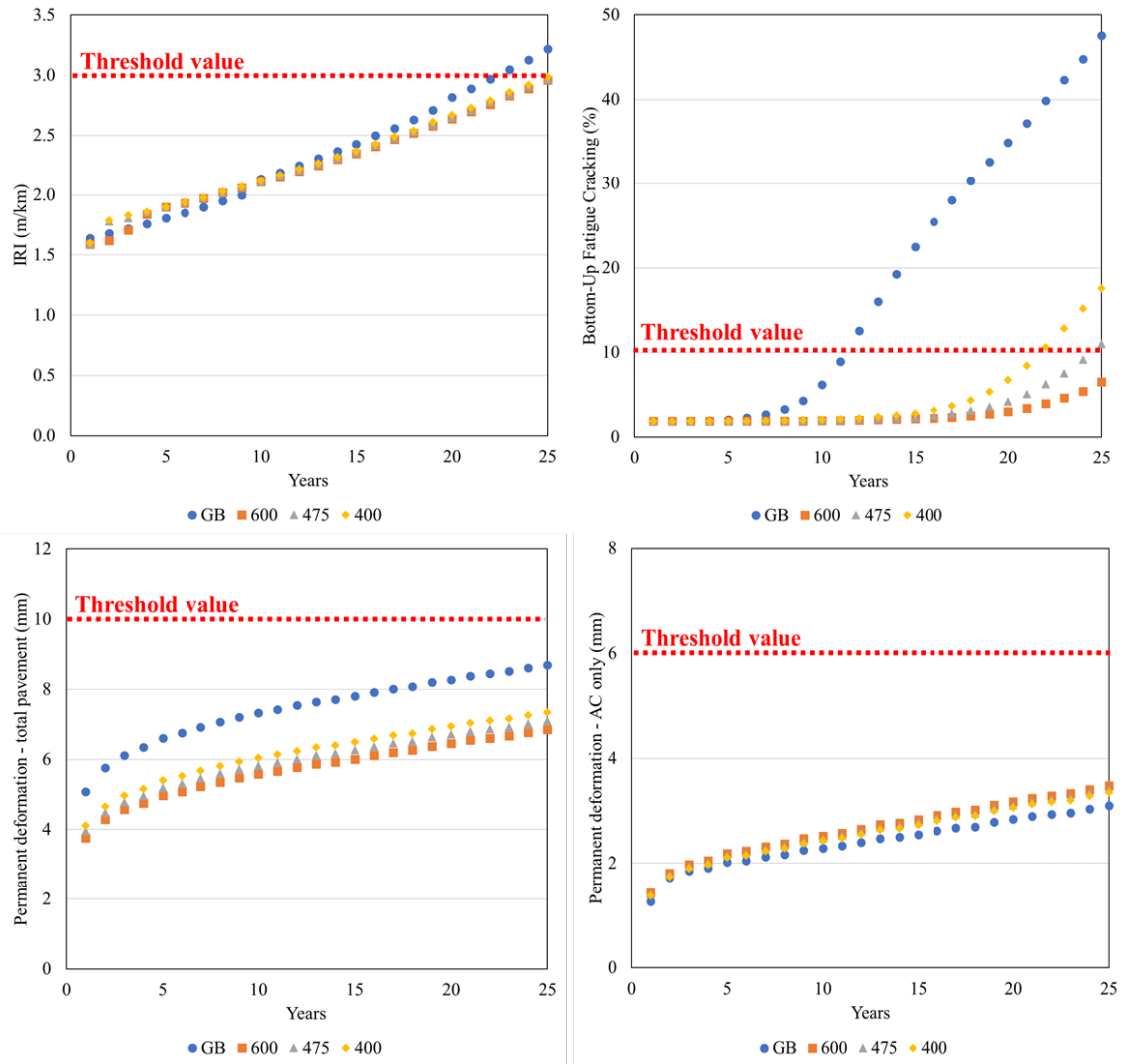


Figure 7-19 Results of performance criteria for the major arterial road (7500 AADTT)

An additional scenario for the major arterial road targeting lower traffic levels is analyzed. The traffic level is 5,000 AADTT. The MEPDG results are shown in Table 7-6 and Figure 7-20. All the LCC sections pass the standard in 5,000 AADTT major arterial scenarios, while the Granular B section still fails to meet the IRI standard and bottom-up fatigue cracking.

Table 7-6 Results of performance criteria for the major arterial road at year 25

Performance criteria	Target	Granular B	400	475	600
Terminal IRI (m/km)	3	3.08	2.93	2.94	2.93
Permanent deformation - total pavement (mm)	10	8.18	6.82	6.57	6.31
AC bottom-up fatigue cracking (percent)	10	32.19	6.25	3.97	2.91
Permanent deformation - AC only (mm)	6	2.64	2.87	2.92	2.98

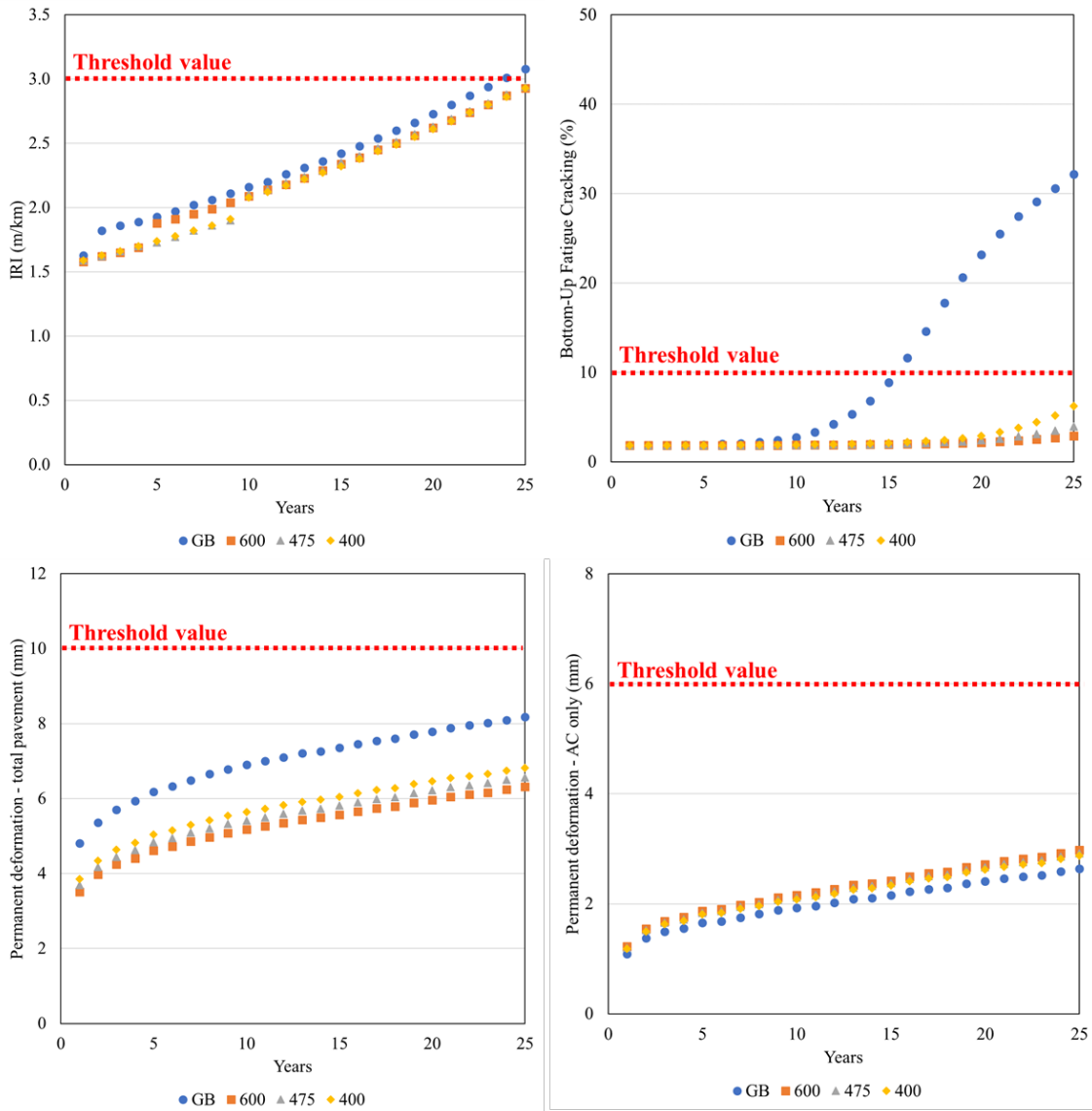


Figure 7-20 Results of performance criteria for the major arterial road (5000 AADTT)

B. Minor Arterial Roads

Table 7-7 showed the minor arterial road's performance criteria at year 25. Unlike the major arterial scenario, all the sections pass the threshold value. For IRI and bottom-up fatigue cracking, the 600 kg/m³ density LCC section holds the best performance, followed by the 475 kg/m³ density LCC section, 400 kg/m³ density LCC sections. Granular B section showing the worst performance results. It should be noted that even though the Granular B section passes the bottom-up fatigue cracking limit, it still degrades faster than the LCC section, as shown in Figure 7-21. The permanent deformation results show that the 400 kg/m³ density LCC section has the highest values. This was due to an increase in the asphalt concrete layer's deformation. The overall trend in permanent deformation shows that LCC sections have superior performance than the Granular B section.

Table 7-7 Results of performance criteria for the minor arterial road at year 25

Performance criteria	Target	Granular B	400	475	600
Terminal IRI (m/km)	3	2.93	2.98	2.90	2.89
Permanent deformation - total pavement (mm)	10	7.60	8.00	6.19	5.89
AC bottom-up fatigue cracking (%)	10	2.21	1.94	1.92	1.90
Permanent deformation - AC only (mm)	6	1.74	3.94	2.13	2.13

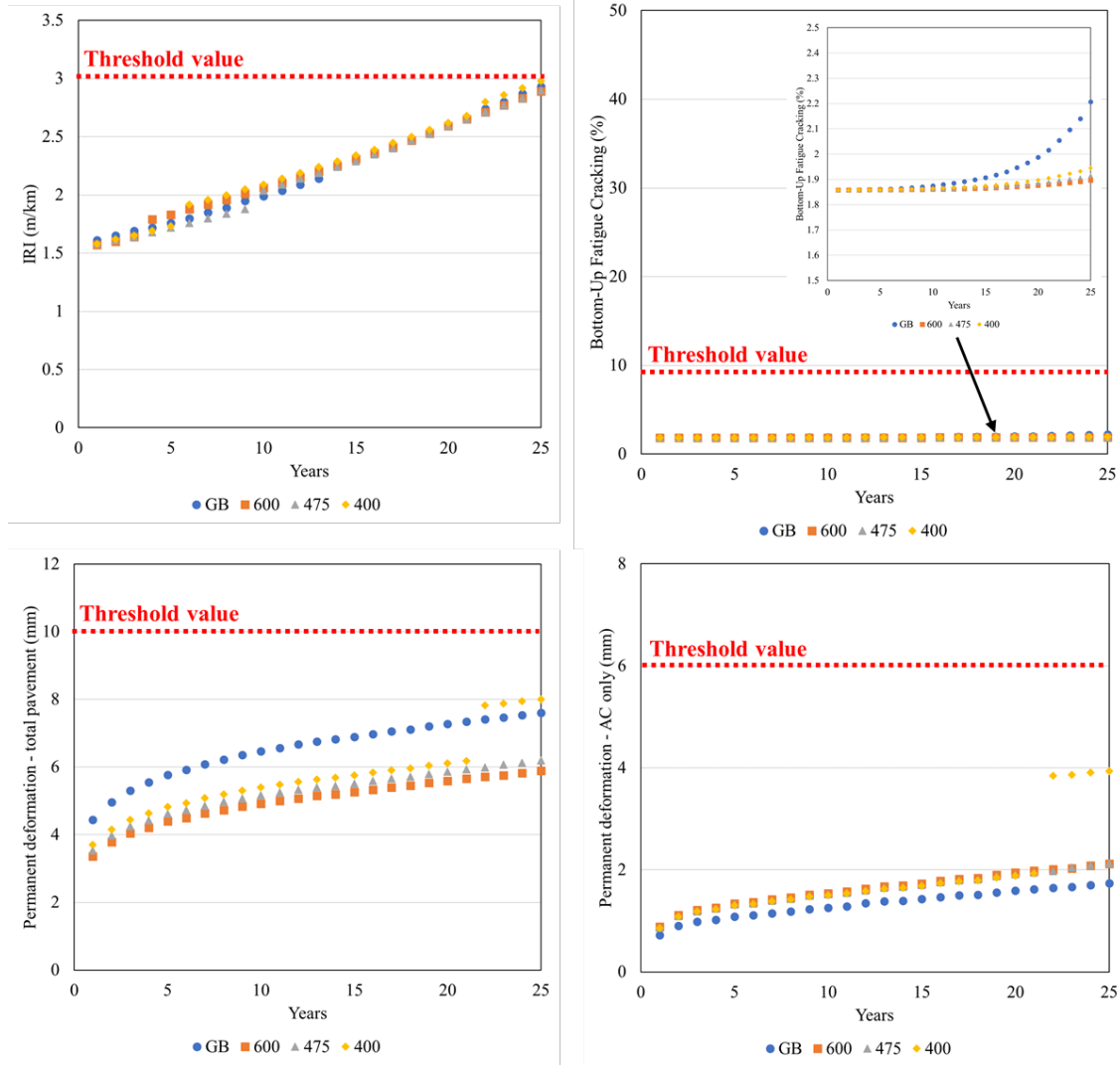


Figure 7-21 Results of performance criteria for the minor arterial road (1000 AADTT)

C. Collector Roads

The results of performance criteria predicted by MEPDG software for the collector scenario are shown in Table 7-8 and Figure 7-22. LCC sections perform better than the Granular B section concerning permanent deformation and bottom-up fatigue cracking, with an improvement of 16% to 24% for permanent deformation and 2.6% to 3.0%. However, 400 kg/m³ density LCC and 475 kg/m³ density LCC sections have 1.7% to 2.0% greater IRI values than the Granular B section. The LCC and Granular B section's performance difference becomes smaller in lower-traffic-level road classes.

Table 7-8 Results of performance criteria for the collector at year 25

Performance criteria	Target	Granular B	400	475	600
Terminal IRI (m/km)	3	2.85	2.91	2.90	2.84
Permanent deformation - total pavement (mm)	10	6.93	5.85	5.51	5.26
AC bottom-up fatigue cracking (%)	10	1.92	1.87	1.87	1.86
Permanent deformation - AC only (mm)	6	1.51	1.72	1.61	1.63

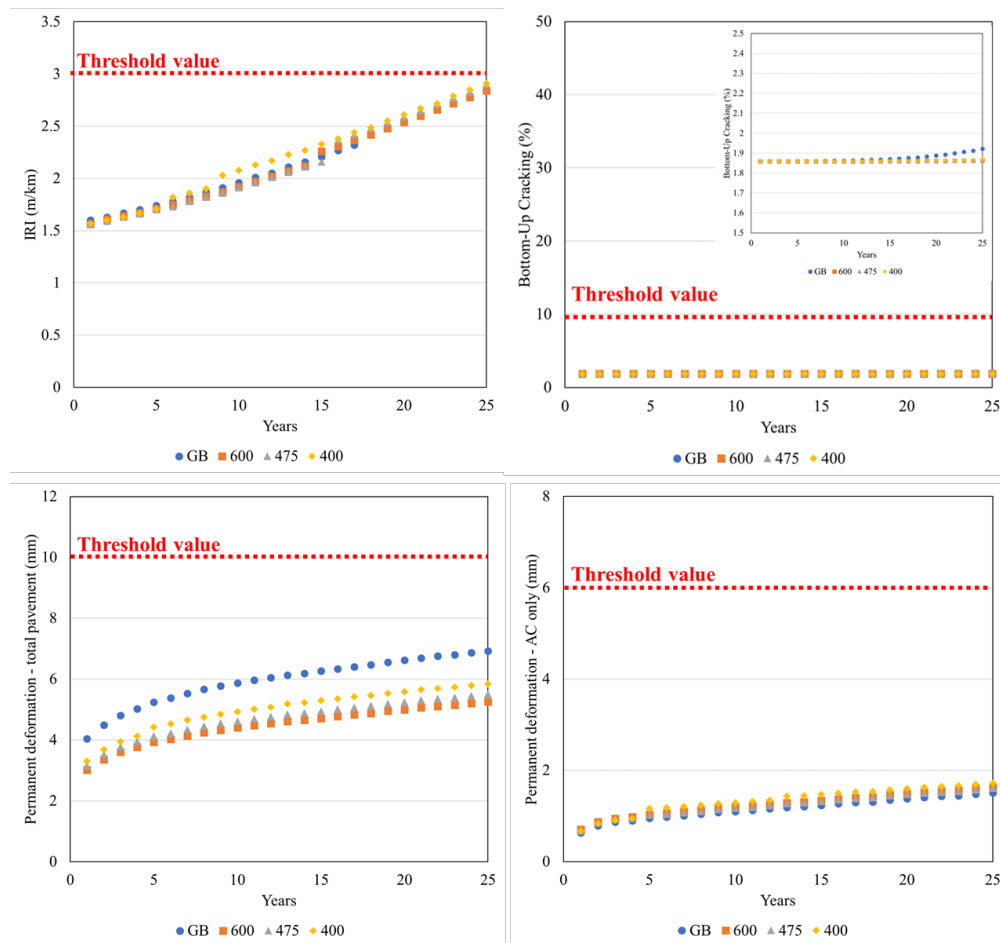


Figure 7-22 Results of performance criteria for the minor arterial road (500 AADTT)

7.5 Summary and Findings

This chapter described LCC's pavement performance as subbase material through different evaluation methods. The methods applied in this chapter are Weslea, Granular Base Equivalency (GBE), and MEPDG software. The summary of how LCC sections performed and the comparison with the Granular B section are presented.

In the Weslea analysis, three different pavement structures representing three road classes were chosen for the analysis. It was found that LCC sections outperform the Granular B section in failure criteria analysis. LCC sections have 70% more allowable number of load repetition for fatigue cracking than the Granular B section, the gap increases as the LCC density increases. The rutting results also showed that LCC sections have superior performance compared to the Granular B section, with seven allowable load repetitions. Analysis regarding different subbase thicknesses was also performed. Results showed that LCC sections could reduce their subbase thickness while still perform better than the Granular B section.

In the GBE method, the three densities LCC's GBE strength coefficient was computed. The LCC values were found to be at least 1.82 times the Granular B values, which could reduce subbase thickness by 230 mm to 340 mm while remaining the same GBE as the Granular B section.

The MEPDG software predicted the LCC and Granular B section's pavement performance for three road classes. This research's performance criteria are the International Roughness Index (IRI), AC bottom-up fatigue cracking, and permanent deformation of the pavement. Results showed that LCC sections perform better for all the road classes. For major arterial roads, only 600 kg/m³ density LCC section passes all the performance criteria at 7,500 AADTT. However, all the LCC sections fulfill the requirement at 5,000 AADTT major arterial road scenarios, while the Granular B section still fails to meet the standard. All the sections pass the standard for minor arterial roads and collectors. It was found that LCC has superior performance on permanent deformation and bottom-up fatigue cracking than Granular B, meaning LCC sections are more durable and reduce the frequency for pavement maintenance. The above analysis showed that LCC as a subbase material could provide better pavement performance than the conventional unbound granular subbase.

Chapter 8: Conclusions and Recommendations

8.1 Conclusions

This thesis included different aspects of evaluation on the lightweight cellular concrete: laboratory testing, the microstructure of the lightweight cellular concrete, and pavement performance between lightweight cellular concrete subbase and Granular B subbase. The results are summarized in the conclusion of the thesis. Analysis that supports the following conclusion and recommendations were demonstrated in previous chapters.

The laboratory testing regarding mechanical properties, durability, and other properties are presented as follows:

1. The density of lightweight cellular concrete strongly correlates with its mechanical properties and other properties such as water absorption, permeability, sorptivity, and drying.
2. The ultra-low density lightweight cellular concrete has sufficient strength to support the pavement when its compressive strength exceeds 0.5 MPa. 475 and 600 kg/m³ samples satisfied the requirement at three days while it took 400 kg/m³ density seven days to reach the condition. This could influence the timing of open-up traffic.
3. The ultra-low densities lightweight cellular concrete is a stiffer material compared to unbound granular material. Its modulus of elasticity is at least two to eight times greater than the granular material; The modulus of elasticity of the ultra-low densities lightweight cellular concrete is highly correlated to its compressive strength.
4. The modulus of rupture of ultra-low density lightweight cellular concrete is about 19 to 25% of its compressive strength. The results are considered weaker than cement stabilized materials, which range between 0.69 to 3.10 MPa, except lime stabilized soils, which only have 0.17 MPa.
5. The sorptivity of 600 kg/m³ density has the lowest results, while 400 kg/m³ and 475 kg/m³ density samples have comparable values.
6. The permeability test indicated that ultra-low density lightweight cellular concrete has very

low permeability.

7. Ultra-low lightweight cellular concrete has a similar damping ratio to other geotechnical materials such as sand and granular materials at a very small strain.
8. The 475 kg/m³ and 600 kg/m³ density lightweight cellular concrete appeared to have excellent freeze-thaw resistance. However, the 400 kg/m³ density lightweight cellular concrete deteriorated in the first 15 cycles.
9. The curing time of the lightweight cellular concrete affects its freeze-thaw resistance. The 365 days 400 kg/m³ density samples were shown to have better freeze-thaw resistance than the 28 days 400 kg/m³ density samples.

The microstructure evaluation of the lightweight cellular concrete using two different image capturing systems are concluded below:

1. The IHDCS can acquire similar results such as pore area ratio and solidity consistent with ESEM. IHDCS also captured a more extensive range of images than ESEM.
2. There are strong correlations between the pore area, perimeter, the major and minor axis for pore characteristics. Shape descriptors also have a strong correlation, but the values are lower than pore characteristic ones.
3. The average thickness between the pores was found that higher densities have a greater average thickness. Moreover, the average thickness of 600 kg/m³ density LCC is 1.5 times more than lower densities LCC. The pores' area ratio showed the opposite trend, which lower densities LCC have higher pore area ratio.
4. The pore area ratio, average thickness between pores, circularity, and solidity demonstrated a strong correlation with the mechanical properties of LCC, which could be beneficial to be used as parameters when estimating the mechanical behavior of LCC.
5. Comparing to 400 kg/m³ density LCC, 475 and 600 kg/m³ density LCC have a better pore structure and pore shape, which benefit their strength.

The conclusion from the pavement performance analysis can be summarized as follow:

1. The fatigue criteria analysis found that LCC sections outperform Granular B section as LCC sections have 70% more allowable loads for fatigue cracking than the Granular B section. The gap increases as the LCC density increases. The rutting results also showed that LCC sections have superior performance than the Granular B section, with seven times the allowable load repetitions. LCC sections could also reduce their subbase thickness while still performing better than the Granular B section regarding fatigue cracking and rutting.
2. The granular base equivalency's strength coefficient of the three densities LCC was at least 1.82 times the Granular B values. Using LCC as a subbase material could reduce the subbase layer thickness by 230 mm to 340 mm while remaining the same granular base equivalency as the Granular B section.
3. MEPDG results showed that LCC sections perform better for all the road classes than the Granular B section. Only 600 kg/m³ density LCC section passes all the performance criteria for 7,500 AADTT major arterial roads. All the sections pass the standard for minor arterial roads and collectors. However, LCC sections still have better performance than the Granular B section.
4. It was found that LCC has superior performance on permanent deformation and bottom-up fatigue cracking than Granular B, meaning LCC sections could last longer and reduce the need for pavement maintenance.

All the analyses showed that LCC as a subbase material could provide better pavement performance than the conventional unbound granular subbase.

8.2 Major Contribution

The following points presented the contribution to science from this research.

1. Investigated the mechanical properties of ultra-low density LCC and demonstrated the LCC satisfies the required strength level for a pavement subbase layer.
2. The pore characteristics of LCC were evaluated using a new image capture system (IHDCS)

and compared to ESEM. Results shown that the new system (IHDCS) could provide a more accessible way to assess the pore characteristics of LCC.

3. Assessed freeze-thaw characteristics of ultra-low density lightweight cellular concrete in two different scenarios and compared their durability for pavement subbase application.
4. Computed the granular base equivalency strength coefficient to use lightweight cellular concrete in the flexible pavement structure.
5. Developed possible usage of various lightweight cellular concrete densities on differing road types.
6. Possible thickness savings for incorporating lightweight cellular concrete in pavement design and construction were proposed.
7. The LCC sections' predicted pavement performance is completed via the use of the current pavement evaluation methods.

8.3 Recommendations

The thesis provides a full evaluation of how lightweight cellular concrete can be designed into a flexible pavement structure. The following points summarized the recommendations from this research and other future research recommendations.

1. The granular base equivalency strength coefficient for the ultra-low lightweight cellular concrete is recommended to be 1.22 for 400 kg/m³ density, 1.46 for 475 kg/m³ density, and 1.91 for 600 kg/m³ density.
2. When designing the ultra-low lightweight cellular concrete, the subbase thickness for flexible pavement using ultra-low lightweight cellular concrete as subbase material could be reduced by 44% to 65% comparing to unbound granular subbase.
3. For major arterial roads or higher traffic road class, 600 kg/m³ density lightweight cellular concrete is more recommended to be used. However, for lower-traffic road classes such as minor arterial road and collector roads, lower density lightweight cellular concrete such as

400 kg/m³ and 475 kg/m³ densities could be considered instead.

4. Considering the growth of strength, microstructure, and other properties, 475 kg/m³ is more recommended to be used over 400 kg/m³ density as it has a more stable pore structure, strength, and freeze-thaw resistance.
5. The recommended time for opening traffic after road construction is three days for 475 kg/m³ density and 600 kg/m³ density, while 400 kg/m³ density is seven days.
6. The Regression model of the compressive strength and modulus of elasticity could be taken as a reference to estimate the strength and stiffness of the lightweight cellular concrete in the field.

Future work:

1. The current pavement performance analysis did not consider the freeze-thaw benefit of the Lightweight cellular concrete.
2. Field evaluation concerning the performance of ultra-low density lightweight cellular concrete used as a subbase should be conducted.
3. The Life-Cycle Cost Analysis and Life Cycle Assessment of ultra-low density lightweight cellular concrete subbase pavement needs to be performed.
4. Construction benefits such as time-saving and the production rate of using LCC should be considered and evaluated.
5. Performance prediction models adapting the lightweight cellular concrete coefficient need to be investigated.

References

- Abd, A.M. and Abd, S.M., 2017. Modelling the strength of lightweight foamed concrete using support vector machine (SVM). *Case studies in construction materials*, 6, pp.8-15.
- Adaska, W. S., & Luhr, D. R., 2004. Control of reflective cracking in cement stabilized pavements. *In Proceedings of 5th International RILEM Conference on Cracking in Pavements* , pp. 309-316.
- American Association of State Highway, & Transportation Officials, 1993. AASHTO Guide for Design of Pavement Structures, 1993 (Vol. 1). AASHTO.
- American Association of State Highway, & Transportation Officials, 2008. *Guide for Mechanistic-Empirical Design of New and Rehabilitated Pavement Structures*. (NCHRP 1-37A). Washington, DC. United States.
- American Concrete Institute, 2014. *ACI 523.3R-14: Guide for Cellular Concretes above 50lb/ft³*. ACI, Farmington Hills, Michigan, United States.
- American Concrete Institute, 2006. *ACI 523.1R-06: Guide for Cast-in-Place Low Density Cellular Concrete*. ACI, Farmington Hills, Michigan, United States.
- Amran, Y.M., Farzadnia, N. and Ali, A.A., 2015. Properties and applications of foamed concrete; a review. *Construction and Building Materials*, 101, pp.990-1005.
- Applied Research Associates, 2015. Methodology for the Development of Equivalent Pavement Structural Design Matrix for Municipal Roadways: Including Maintenance and Rehabilitation Schedules and Life Cycle Cost Analysis.
- Ashmawy, A.K., Salgado, R., Guha, S. and Drnevich, V.P., 1995, April. Soil damping and its use in dynamic analyses. *In International conferences on recent advances in geotechnical earthquake engineering and soil dynamics* (Vol. 9).
- American Society for Testing and Materials, 2012. *Standard Test Method for Foaming Agents for Use in Producing Cellular Concrete Using Preformed Foam*. ASTM C796/C796M. ASTM International. West Conshohocken, PA, USA.

American Society for Testing and Materials, 2012. *Standard Test Method for Compressive Strength of Lightweight Insulating Concrete*. ASTM C495/C495M. ASTM International. West Conshohocken, PA, USA.

American Society for Testing and Materials, 2014. *Standard Test Method for Static Modulus of Elasticity and Poisson's Ratio of Concrete in Compression*. ASTM C469/469M. ASTM International. West Conshohocken, PA, USA.

American Society for Testing and Materials, 2015. *Standard Test Method for Resistance of Concrete to Rapid Freezing and Thawing*. ASTM C666/666M. ASTM International. West Conshohocken, PA, USA.

American Society for Testing and Materials, 2015. *Standard Test Methods for Modulus and Damping of Soils by Fixed-Base Resonant Column Devices*. ASTM C4015. ASTM International. West Conshohocken, PA, USA.

American Society for Testing and Materials, 2016. *Standard Specification for Foaming Agents Used in Making Preformed Foam for Cellular Concrete*. ASTM C869/869M. ASTM International. West Conshohocken, PA, USA.

American Society for Testing and Materials, 2017. *Standard Test Method for Length Change of Hardened Hydraulic-Cement Mortar and Concrete*. ASTM C157/157M. ASTM International. West Conshohocken, PA, USA.

American Society for Testing and Materials, 2017. *Standard Test Method for Splitting Tensile Strength of Cylindrical Concrete Specimens*. ASTM C496/496M. ASTM International. West Conshohocken, PA, USA.

American Society for Testing and Materials, 2018. *Standard Test Method for Time of Setting of Hydraulic-Cement Paste by Gillmore Needles*. ASTM C266. ASTM International. West Conshohocken, PA, USA, 2018.

American Society for Testing and Materials, 2019. *Standard Practice for Making and Curing Concrete Test Specimens in the Laboratory*. ASTM C192/192M. ASTM International. West Conshohocken, PA, USA.

- American Society for Testing and Materials, 2020. *Standard Test Method for Measurement of Rate of Absorption of Water by Hydraulic-Cement Concretes*. ASTM C1585. ASTM International. West Conshohocken, PA, USA.
- American Society for Testing and Materials, 2021. *Standard Test Method for Flexural Strength of Concrete (Using Simple Beam with Third-Point Loading)*. ASTM C78/78M. ASTM International. West Conshohocken, PA, USA.
- Arulrajah, A., Disfani, M.M., Horpibulsuk, S., Suksiripattanapong, C. and Prongmanee, N., 2014. Physical properties and shear strength responses of recycled construction and demolition materials in unbound pavement base/subbase applications. *Construction and Building Materials*, 58, pp.245-257.
- Averyanov, S., 2018. *Analysis of construction experience of using lightweight cellular concrete as a subbase material* (Master's thesis, University of Waterloo).
- Baaj, H., Tavassoti, P., Dias, G. and Lorena, G., 2020. Innovative Lightweight High-Performance Concrete (LHPC) Material for Flexible Pavements' Insulation. Technical Report. InnovAct Consulting Inc. Kitchener, Ontario, Canada.
- Barnes, R.A., 2008. Foamed concrete: Application and specification. *In Excellence in Concrete Construction through Innovation* (pp. 19-26). CRC Press.
- Batool, F. and Bindiganavile, V., 2017. Air-void size distribution of cement-based foam and its effect on thermal conductivity. *Construction and Building Materials*, 149, pp.17-28.
- British Cement Association, 1994. *Foamed Concrete; Composition and Properties*, Report Ref. 46.042, BCA, Slough, Berkshire, England.
- Brady, K.C., Watts, G.R.A. and Jones, M.R., 2001. *Specification for foamed concrete*. Crowthorne, UK: TRL Limited.
- Clark, J.V. and Lange, D.A., 2021. Optimization of Cellular Concrete Microstructure for Improved Impact Resistance. *Transportation Research Record*, doi: 10.1177/03611981211026308.

- Chindaprasirt, P. and Rattanasak, U., 2011. Shrinkage behavior of structural foam lightweight concrete containing glycol compounds and fly ash. *Materials & Design*, 32(2), pp.723-727.
- Chung, S.Y., Lehmann, C., Abd Elrahman, M. and Stephan, D., 2017. Pore characteristics and their effects on the material properties of foamed concrete evaluated using micro-CT images and numerical approaches. *Applied Sciences*, 7(6), p.550.
- Decký, M., Drusa, M., Zgútová, K., Blaško, M., Hájek, M. and Scherfel, W., 2016. Foam concrete as new material in road constructions. *Procedia engineering*, 161, pp.428-433.
- Delfosse-Ribay, E., Djeran-Maigre, I., Cabrillac, R. and Gouvenot, D., 2004. Shear modulus and damping ratio of grouted sand. *Soil Dynamics and Earthquake Engineering*, 24(6), pp.461-471.
- De Rose, L. and Morris, J., 1999. *The influence of mix design on the properties of microcellular concrete* (pp. 185-197). Thomas Telford: London, UK.
- Dhir, R., Jones, M. and Nicol, L., 1999. Development of structural grade foamed concrete. *Final Report, DETR Research Contract*, 39(3), p.385.
- Dobry, R., 1987. Dynamic properties and seismic response of soft clay deposits. *In Proc. of the Int. Symp. on Geotech. Engrg. of Soft Soils* (Vol. 2, pp. 51-86). Sociedad Mexicana de Mecanica de suelos.
- Drusa, M., Fedorowicz, L., Kadela, M., & Scherfel, W. (2011). Application of geotechnical models in the description of composite foamed concrete used in contact layer with the subsoil. *Zbornik*, 1, 644-652.
- Drusa, M., Fedorowicz, L., Kadela, M. and Scherfel, W., 2011. Application of geotechnical models in the description of composite foamed concrete used in contact layer with the subsoil. *In Proceedings of the 10th Slovak Geotechnical Conference "Geotechnical problems of engineering constructions*.
- Drusa, M. and Decky, M., 2013. Designing and Quality Control of Earth Structures on Transport Constructions. *Edis Uniza*, 522.

- Federal Highway Administration, 2006. *Geotechnical aspects of pavements* (No. FHWA-NHI-05-037). Washington, DC, United States.
- Federal Highway Administration, 2017. *Bases and Subbases for Concrete Pavements*. (No. FHWA-HIF-16-005). Washington, DC, United States.
- Favaretto, P., Hidalgo, G.E.N., Sampaio, C.H., Silva, R.D.A. and Lermen, R.T., 2017. Characterization and use of construction and demolition waste from south of Brazil in the production of foamed concrete blocks. *Applied Sciences*, 7(10), p.1090.
- Fu, Y., Wang, X., Wang, L. and Li, Y., 2020. Foam concrete: A state-of-the-art and state-of-the-practice review. *Advances in Materials Science and Engineering*, 2020.
- Griffiths F. and Popik, M. (2013). Pavement Evaluation - CEMATRIX Site Dixie Road, Caledon, Ontario. *Thurber Engineering Ltd.*
- Hajek, M., Decky, M., Drusa, M., Orininová, L. and Scherfel, W., 2016, October. Elasticity modulus and flexural strength assessment of foam concrete layer of Poroflow. *In IOP conference series: Earth and environmental science* (Vol. 44, No. 2, p. 022021). IOP Publishing.
- Hájek, M. and Decký, M., 2017. Homomorphic model pavement with subbase layer of foam concrete. *Procedia engineering*, 192, pp.283-288.
- Harvey, J., Meijer, J., Ozer, H., Al-Qadi, I.L., Saboori, A. and Kendall, A., 2016. *Pavement life cycle assessment framework* (No. FHWA-HIF-16-014). United States. Federal Highway Administration.
- United States. Federal Highway Administration, Tyson, S., Hein, D.K., Rao, S.P., Tayabji, S.D. and Lee, H., 2017. *Bases and Subbases for Concrete Pavements*. Federal Highway Administration.
- <http://www.provoton.com/downloads/route141.1.pdf> [22.03.2016]
- Hu, W., Neufeld, R.D., Vallejo, L.E., Kelly, C. and Latona, M., 1997. Strength properties of autoclaved cellular concrete with high volume fly ash. *Journal of energy engineering*, 123(2), pp.44-54.

- Huang, Y. H., 1993. *Pavement analysis and design*. Englewood Cliffs, N.J., Prentice Hall.
- Hulimka, J., Knoppik-Wróbel, A., Krzywoń, R. and Rudišin, R., 2013. Possibilities of the structural use of foamed concrete on the example of slab foundation. *In Proceedings of the 9th Central European Congress on Concrete Engineering*, Vol. 67, p. 74.
- ImageJ. Available online: <https://imagej.net/Fiji> (accessed on 6 October 2019).
- Jiang, J., Lu, Z., Niu, Y., Li, J. and Zhang, Y., 2016. Study on the preparation and properties of high-porosity foamed concretes based on ordinary Portland cement. *Materials & Design*, 92, pp.949-959.
- Jones, M. R., 2001. Foamed concrete for structural use. *In Proceedings of one day seminar on foamed concrete: properties. Applications and latest technological developments*, Loughborough University , Vol. 3, pp. 27-60.
- Jones, M.R., McCarthy, M.J. and McCarthy, A., 2003. Moving fly ash utilisation in concrete forward: A UK perspective. *In Proceedings of the 2003 International Ash Utilization Symposium* (pp. 20-22). University Press of Kentucky.
- Jones, M.R. and McCarthy, A., 2005. Preliminary views on the potential of foamed concrete as a structural material. *Magazine of concrete research*, 57(1), pp.21-31.
- Jones, M.R. and McCarthy, A., 2006. Heat of hydration in foamed concrete: Effect of mix constituents and plastic density. *Cement and concrete research*, 36(6), pp.1032-1041.
- Jones, M.R., Ozlutas, K. and Zheng, L., 2016. Stability and instability of foamed concrete. *Magazine of Concrete Research*, 68(11), pp.542-549.
- Jones, M.R., Ozlutas, K. and Zheng, L., 2017. High-volume, ultra-low-density fly ash foamed concrete. *Magazine of Concrete Research*, 69(22), pp.1146-1156.
- Jones, R., Zheng, L., Yerramala, A. and Rao, K.S., 2012. Use of recycled and secondary aggregates in foamed concretes. *Magazine of concrete research*, 64(6), pp.513-525.
- Kadela, M. and Kozłowski, M., 2016. Foamed concrete layer as sub-structure of industrial concrete floor. *Procedia Engineering*, 161, pp.468-476.

- Kadela, M., Kozłowski, M. and Kukielka, A., 2017. Application of foamed concrete in road pavement–weak soil system. *Procedia Engineering*, 193, pp.439-446.
- Kearsley, E.P. and Mostert, H.F., 1999. The use of foamcrete in Southern Africa. *In Proceedings of ACI International Conference on high performance concrete: Special Publication*, 172, pp.919-934.
- Kearsley, E.P. and Wainwright, P.J., 2001. The effect of high fly ash content on the compressive strength of foamed concrete. *Cement and concrete research*, 31(1), pp.105-112.
- Kearsley, E.P. and Wainwright, P.J., 2001. Porosity and permeability of foamed concrete. *Cement and concrete research*, 31(5), pp.805-812.
- Kearsley, E.P. and Wainwright, P.J., 2002. The effect of porosity on the strength of foamed concrete. *Cement and concrete research*, 32(2), pp.233-239.
- Kearsley, E.P. and Mostert, H.F., 2005. Designing mix composition of foamed concrete with high fly ash contents. *In Use of Foamed Concrete in Construction: Proceedings of the International Conference held at the University of Dundee, Scotland, UK on 5 July 2005* (pp. 29-36). Thomas Telford Publishing.
- Kim, H.K., Jeon, J.H. and Lee, H.K., 2012. Workability, and mechanical, acoustic and thermal properties of lightweight aggregate concrete with a high volume of entrained air. *Construction and Building Materials*, 29, pp.193-200.
- Kunhanandan Nambiar, E.K. and Ramamurthy, K., 2008. Fresh state characteristics of foam concrete. *Journal of materials in civil engineering*, 20(2), pp.111-117.
- Lee, Y. L., Goh, K. S., Koh, H. B., & Bakar, I., 2009. Foamed aggregate pervious concrete—an option for road on peat. *In Proceedings of MUCEET2009*. Pahang, Malaysia.
- Maher, M.L. and Hagan, J.B., 2016. MAT-758: Constructability Benefits of the Use of Lightweight Foamed Concrete Fill (LFCF) in Pavement Applications. *In Proceedings of 2016 CSCE Annual Conference*. London, Ontario, Canada.
- Maruyama, R.C. and Camarini, G., 2015. Properties of cellular concrete for filters. *International Journal of Engineering and Technology*, 7(3), p.223.

- Mohammad, M., 2011. *Development of foamed concrete: enabling and supporting design* (Doctoral dissertation, University of Dundee).
- Mindess, S. ed., 2019. *Developments in the Formulation and Reinforcement of Concrete*. Woodhead Publishing.
- Ministry of Transportation of Ontario, 2013. *Pavement Design and Rehabilitation Manual*. Materials Engineering and Research Office. Second Edition. Ontario. Canada.
- Ministry of Transportation of Ontario, 2019. *Ontario's Default Parameters for AASHTOWare Pavement ME Design Interim Report*, MTO, Material Engineering and Research Office, Downsview, Ontario, Canada.
- Mydin, M.A.O., 2014. Models for Prediction the Strength and Stiffness of Foamed Concrete at Ambient Temperature. *European researcher. Series A, 1*(67), p.124.
- Narayanan, N. and Ramamurthy, K., 2000. Structure and properties of aerated concrete: a review. *Cement and Concrete composites, 22*(5), pp.321-329.
- Nambiar, E.K. and Ramamurthy, K., 2006. Influence of filler type on the properties of foam concrete. *Cement and concrete composites, 28*(5), pp.475-480.
- Neville, A. M., 2011. *Properties of concrete* . 5th edition, Pearson Education Ltd.
- Nguyen, T.T., Bui, H.H., Ngo, T.D., Nguyen, G.D., Kreher, M.U. and Darve, F., 2019. A micromechanical investigation for the effects of pore size and its distribution on geopolymer foam concrete under uniaxial compression. *Engineering Fracture Mechanics, 209*, pp.228-244.
- Oruc, S., Celik, F. and Akpınar, M.V., 2007. Effect of cement on emulsified asphalt mixtures. *Journal of materials engineering and performance, 16*(5), pp.578-583.
- Otsu, N., 1979. A threshold selection method from gray-level histograms. *IEEE transactions on systems, man, and cybernetics, 9*(1), pp.62-66.
- Ozlutas, K., 2015. *Behaviour of ultra-low density foamed concrete* (Doctoral dissertation, University of Dundee).

- Panesar, D.K., 2013. Cellular concrete properties and the effect of synthetic and protein foaming agents. *Construction and building materials*, 44, pp.575-584.
- Portland Cement Association, 2021. *Guide to Lightweight Cellular Concrete for Geotechnical Applications*. PCA Special Report SR1008P. Washington, DC, United States.
- Ramamurthy, K., Nambiar, E.K. and Ranjani, G.I.S., 2009. A classification of studies on properties of foam concrete. *Cement and concrete composites*, 31(6), pp.388-396.
- Saeed, A., Hall Jr, J.W. and Barker, W., 2001. *Performance-related tests of aggregates for use in unbound pavement layer* (No. Project D4-23 FY'96). National Cooperative Highway Research Program (NCHRP 453), Transportation Research Board (TRB), National Research Council, Washington, D.C. USA.
- Sari, K.A.M. and Sani, A.R.M., 2017. Applications of foamed lightweight concrete. In *MATEC Web of Conferences* (Vol. 97, p. 01097). EDP Sciences.
- Schmidt, R.J., Santucci, L.E. and Coyne, L.D., 1973. Performance characteristics of cement-modified asphalt emulsion mixes. In *Association of Asphalt Paving Technologists Proc* (Vol. 42).
- Sitharam, T.G. and Vinod, J.S., 2010. Evaluation of shear modulus and damping ratio of granular materials using discrete element approach. *Geotechnical and Geological Engineering*, 28(5), pp.591-601.
- Tarasov, A.S., Kearsley, E.P., Kolomatskiy, A.S. and Mostert, H.F., 2010. Heat evolution due to cement hydration in foamed concrete. *Magazine of concrete research*, 62(12), pp.895-906.
- Tikalsky, P.J., Pospisil, J. and MacDonald, W., 2004. A method for assessment of the freeze-thaw resistance of preformed foam cellular concrete. *Cement and concrete research*, 34(5), pp.889-893.
- Tiwari, B., Ajmera, B., Maw, R., Cole, R., Villegas, D. and Palmerson, P., 2017. Mechanical properties of lightweight cellular concrete for geotechnical applications. *Journal of Materials in Civil Engineering*, 29(7), p.06017007.

- Tiwari, B., Ajmera, B. and Villegas, D., 2018. Dynamic properties of lightweight cellular concrete for geotechnical applications. *Journal of Materials in Civil Engineering*, 30(2), p.04017271.
- Tutumluer, E., 2013. *Practices for unbound aggregate pavement layers* (No. Project 20-05, Topic 43-03). National Cooperative Highway Research Program (NCHRP 445), Transportation Research Board (TRB), National Research Council, Washington, D.C. USA.
- Valore, R. C., 1954. Cellular Concretes: Composition and Method of Preparation. *Journal of American Concrete Institute*, 2, 773-795.
- Viet Vo, H. and Park, D.W., 2016. Lightweight treated soil as a potential sustainable pavement material. *Journal of Performance of Constructed Facilities*, 30(1), p.C4014009.
- Wee, T.H., Babu, D.S., Tamilselvan, T. and Lim, H.S., 2006. Air-void system of foamed concrete and its effect on mechanical properties. *ACI materials journal*, 103(1), p.45.
- Zhang, Z. and Wang, H., 2016. The pore characteristics of geopolymer foam concrete and their impact on the compressive strength and modulus. *Frontiers in Materials*, 3, p.38.

Appendices

Appendices A
Environmental Scanning Electron Microscopy Images

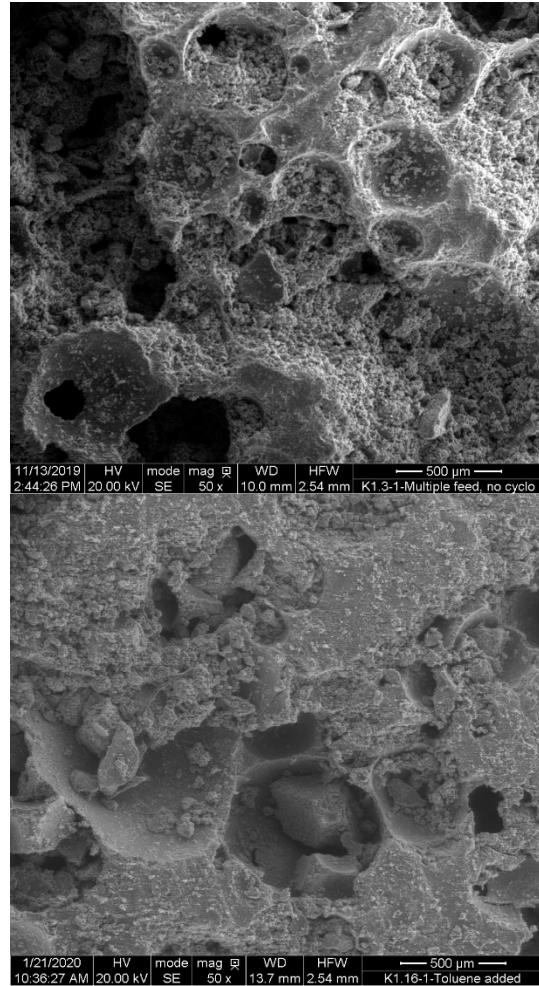
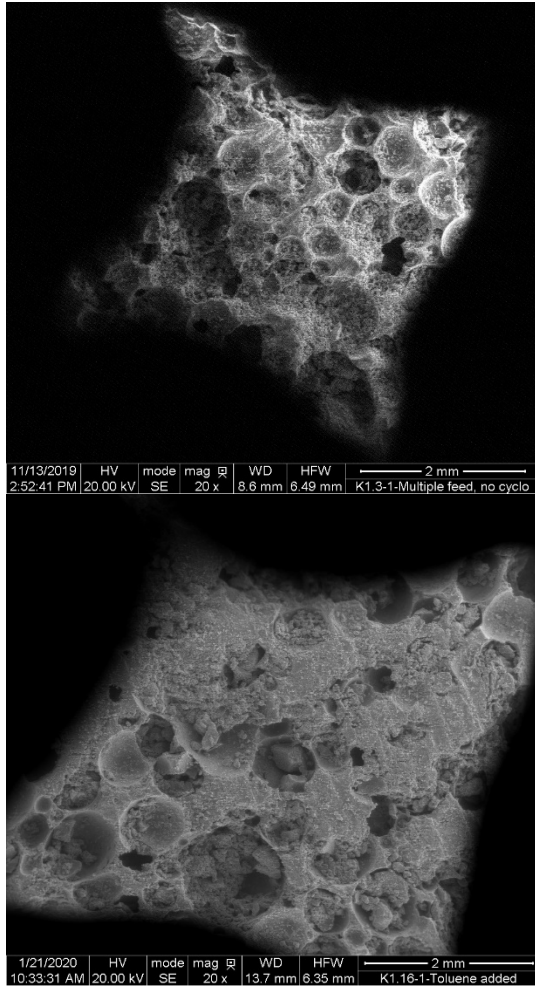


Figure A-1 Microstructure of 400 kg/m³ lightweight cellular concretes

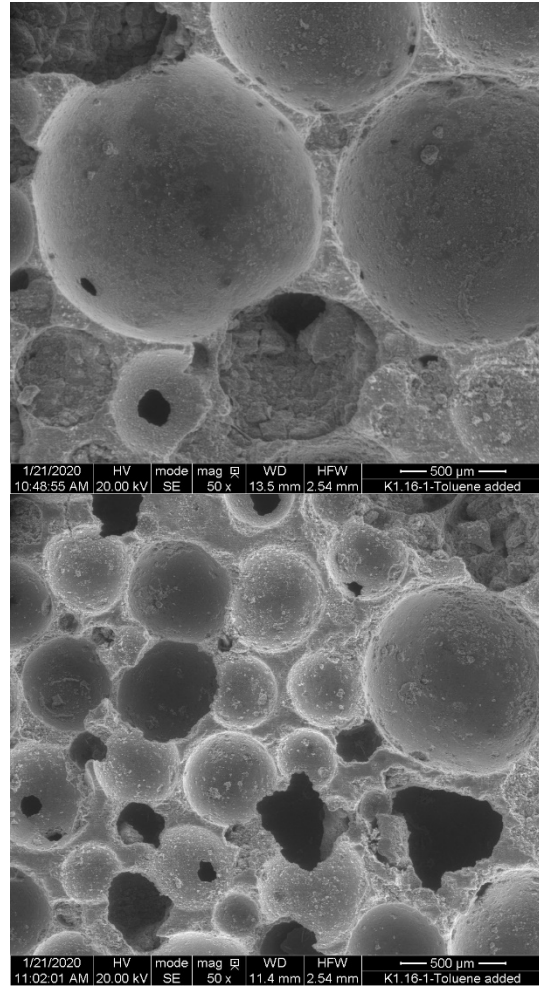
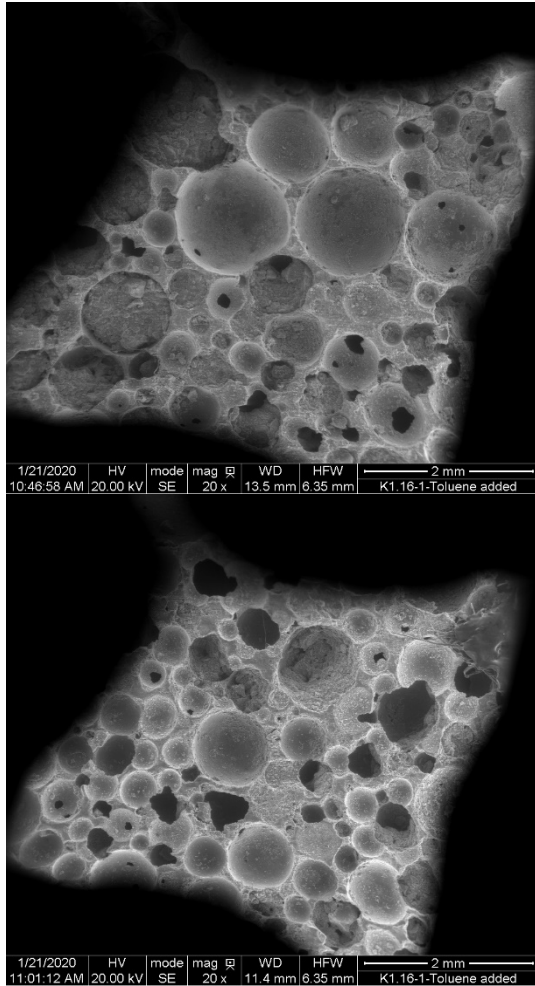


Figure A-2 Microstructure of 475 kg/m³ lightweight cellular concretes

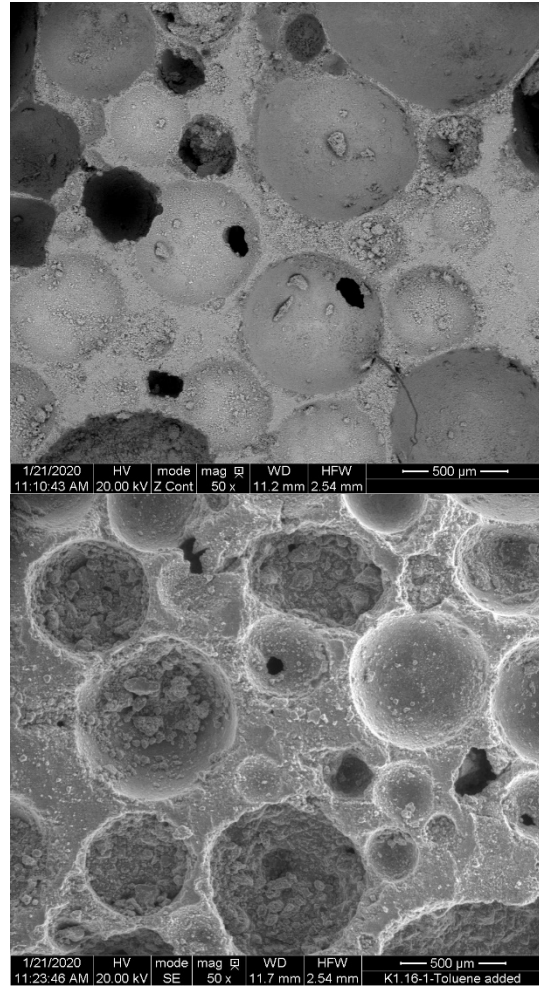
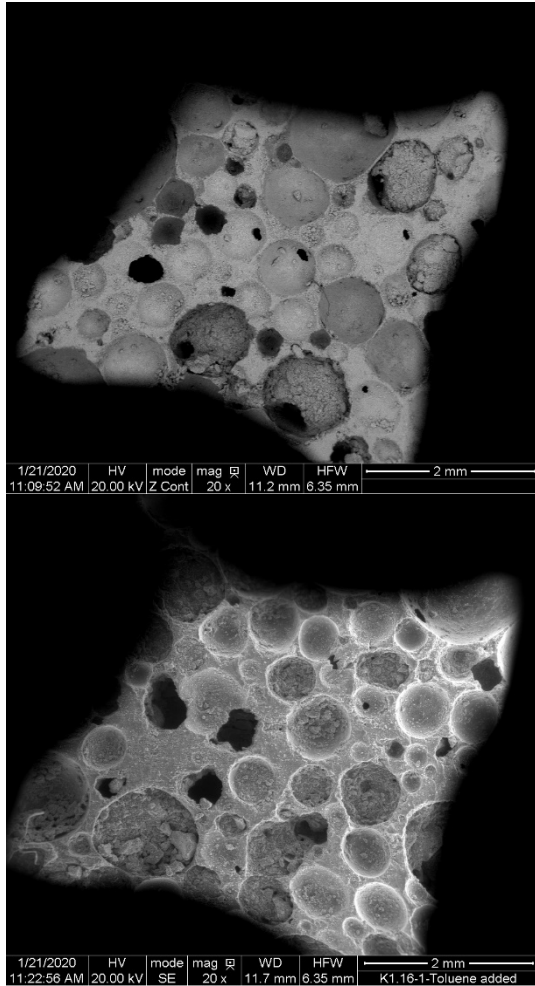


Figure A-3 Microstructure of 600 kg/m³ lightweight cellular concretes

Appendices B
Freeze and Thaw test Sample Images

Figure B-1 Visual images of the 600 samples at every 45 cycles – thaw in water

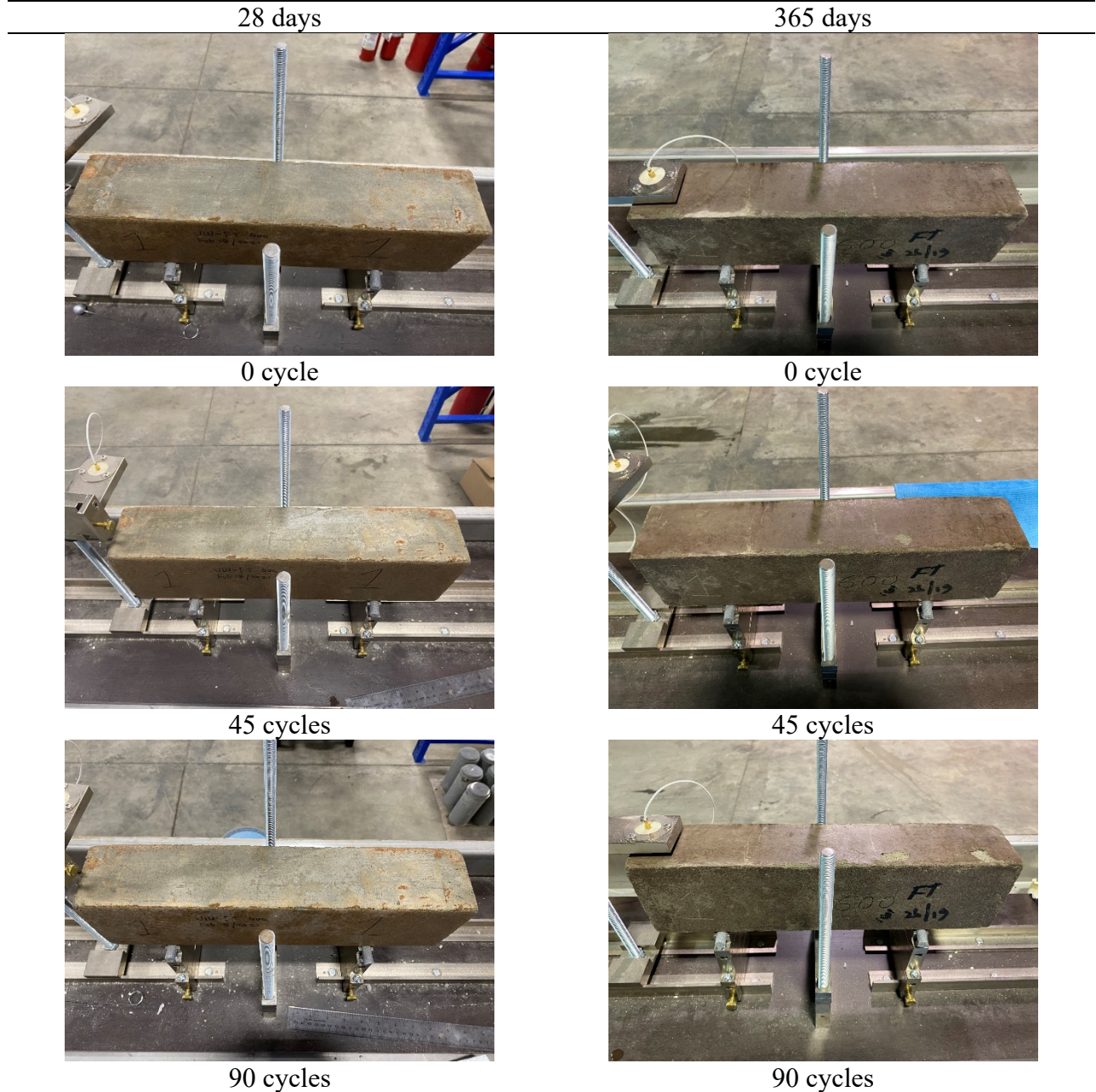


Figure B-1 Visual images of the 600 samples at every 45 cycles – thaw in water (Continued)



135 cycles



135 cycles



180 cycles



180 cycles

Table B-2 Visual images of the 475 samples at every 45 cycles – thaw in water




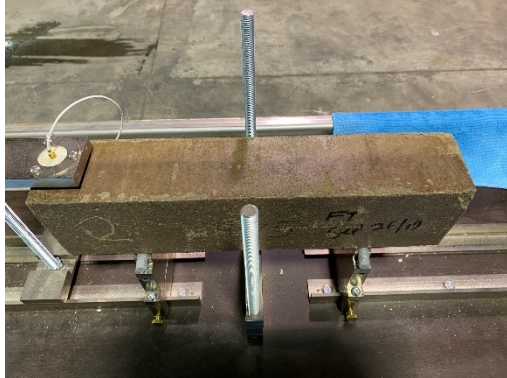

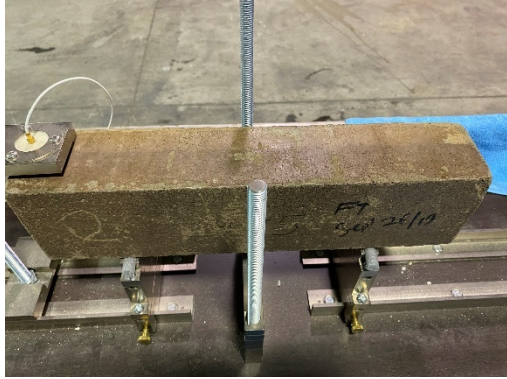
28 days	365 days
 <p>A rectangular concrete sample is mounted on a metal test rig. The sample is light brown and shows some surface texture. It is held in place by a central vertical threaded rod and two side supports. The rig is on a concrete floor.</p>	 <p>A rectangular concrete sample is mounted on a metal test rig. The sample is dark brown and appears more weathered than the 28-day sample. It is held in place by a central vertical threaded rod and two side supports. The rig is on a concrete floor.</p>
0 cycle	0 cycle
 <p>A rectangular concrete sample is mounted on a metal test rig. The sample is light brown and shows some surface texture. It is held in place by a central vertical threaded rod and two side supports. The rig is on a concrete floor.</p>	 <p>A rectangular concrete sample is mounted on a metal test rig. The sample is dark brown and appears more weathered than the 28-day sample. It is held in place by a central vertical threaded rod and two side supports. The rig is on a concrete floor.</p>
45 cycles	45 cycles
 <p>A rectangular concrete sample is mounted on a metal test rig. The sample is light brown and shows some surface texture. It is held in place by a central vertical threaded rod and two side supports. The rig is on a concrete floor.</p>	 <p>A rectangular concrete sample is mounted on a metal test rig. The sample is dark brown and appears more weathered than the 28-day sample. It is held in place by a central vertical threaded rod and two side supports. The rig is on a concrete floor.</p>
90 cycles	90 cycles

Table B-2 Visual images of the 475 samples at every 45 cycles – thaw in water (Continued)



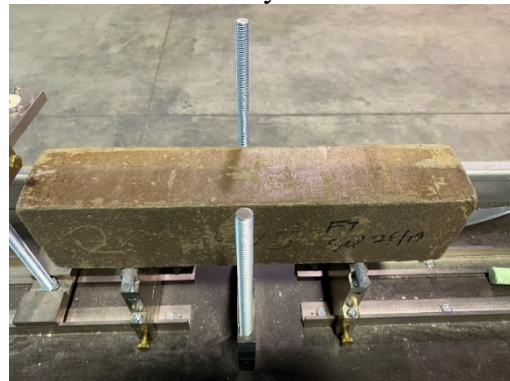
135 cycles



135 cycles



180 cycles



180 cycles

Table B-3 Visual images of the 400 samples at every 45 cycles – thaw in water




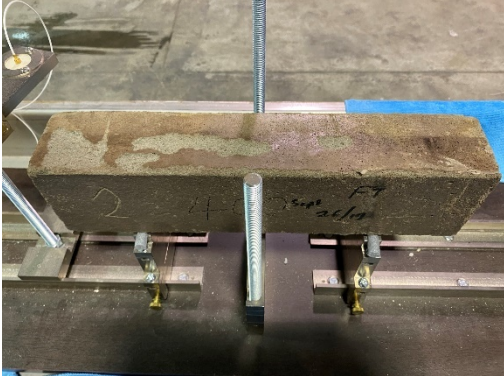

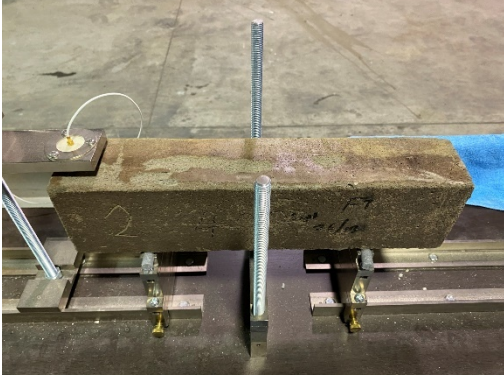
28 days	365 days
 <p>A rectangular concrete sample is mounted on a metal testing frame. The surface is relatively smooth and light-colored.</p>	 <p>A rectangular concrete sample is mounted on a metal testing frame. The surface is darker and shows some staining. Handwritten markings '2 40' and 'F7' are visible on the top surface.</p>
0 cycle	0 cycle
 <p>A rectangular concrete sample is mounted on a metal testing frame. The surface shows some darkening and minor surface wear.</p>	 <p>A rectangular concrete sample is mounted on a metal testing frame. The surface is significantly darker and shows more pronounced staining and surface texture.</p>
45 cycles	45 cycles
 <p>A rectangular concrete sample is mounted on a metal testing frame. The surface is dark and shows signs of surface erosion and staining.</p>	 <p>A rectangular concrete sample is mounted on a metal testing frame. The surface is very dark and shows significant surface degradation and staining.</p>
90 cycles	90 cycles

Table B-3 Visual images of the 400 samples at every 45 cycles – thaw in water (Continued)



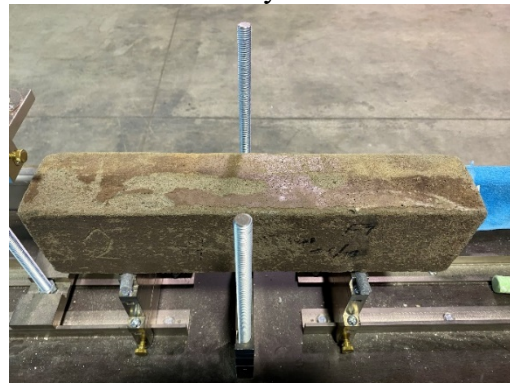
135 cycles



135 cycles



180 cycles



180 cycles

Table B-4 Visual images of the 600 samples at every 45 cycles – thaw in air




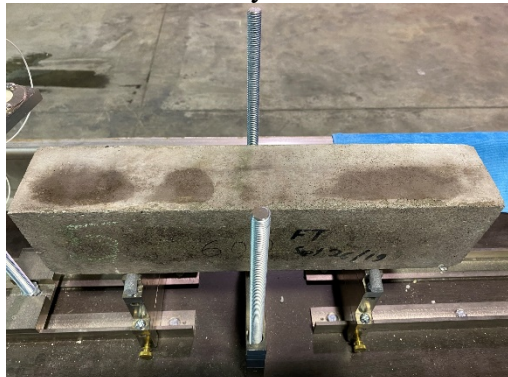

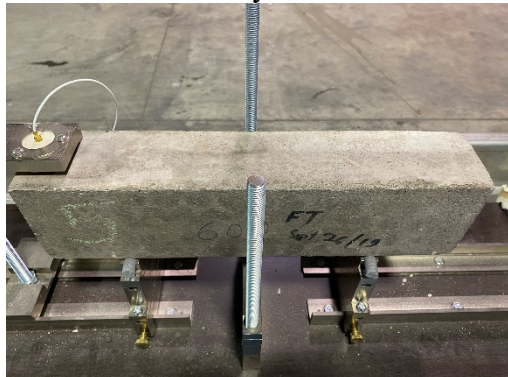
28 days	365 days
 <p>Concrete sample 5, 28 days, 0 cycles. The sample is a rectangular block with '5' and 'UW-FT-600 Feb 18/2021' written on it. It is mounted on a metal test rig.</p>	 <p>Concrete sample 600, 365 days, 0 cycles. The sample is a rectangular block with '600' and 'FT 6/22/19' written on it. It is mounted on a metal test rig.</p>
0 cycle	0 cycle
 <p>Concrete sample 5, 28 days, 45 cycles. The sample shows some surface discoloration and is mounted on a metal test rig.</p>	 <p>Concrete sample 600, 365 days, 45 cycles. The sample shows some surface discoloration and is mounted on a metal test rig.</p>
45 cycles	45 cycles
 <p>Concrete sample 5, 28 days, 90 cycles. The sample shows some surface discoloration and is mounted on a metal test rig.</p>	 <p>Concrete sample 600, 365 days, 90 cycles. The sample shows some surface discoloration and is mounted on a metal test rig.</p>
90 cycles	90 cycles

Table B-4 Visual images of the 600 samples at every 45 cycles – thaw in air (Continued)



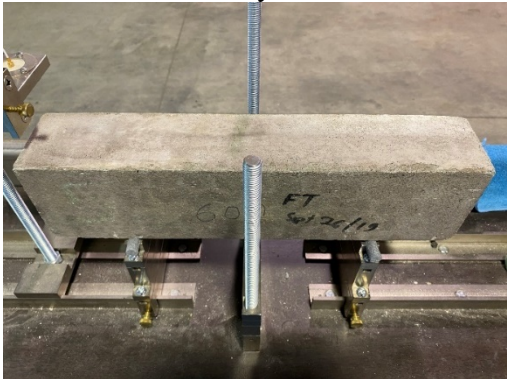
135 cycles



135 cycles



180 cycles



180 cycles

Table B-5 Visual images of the 475 samples at every 45 cycles – thaw in air

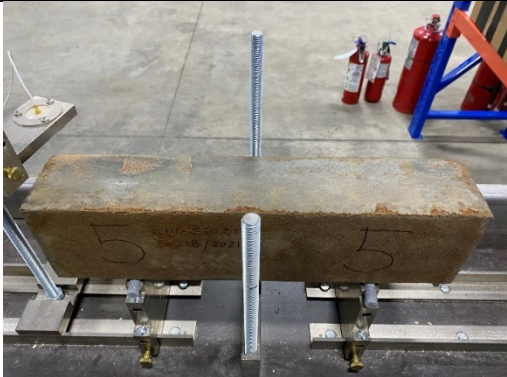


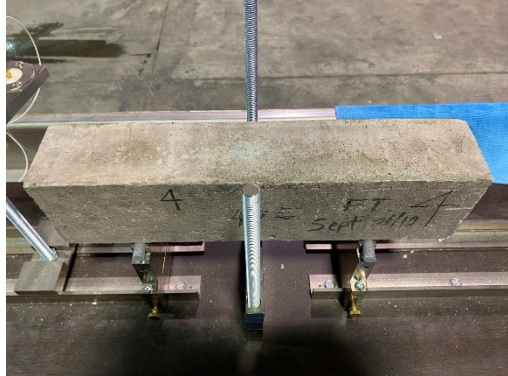

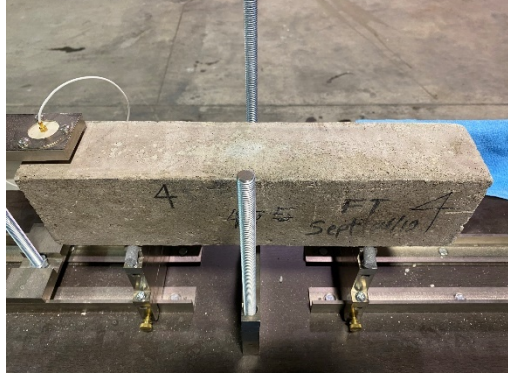
28 days	365 days
 <p>A rectangular concrete sample with a weathered, greyish-brown surface. It is mounted on a metal test fixture with a vertical threaded rod passing through its center. The number '5' is handwritten on both ends of the sample.</p>	 <p>A rectangular concrete sample with a weathered, greyish-brown surface. It is mounted on a metal test fixture with a vertical threaded rod passing through its center. The number '4' is handwritten on both ends, and 'FT 4' and 'Sept 2010' are written on the right end.</p>
0 cycle	0 cycle
 <p>A rectangular concrete sample with a weathered, greyish-brown surface. It is mounted on a metal test fixture with a vertical threaded rod passing through its center. The number '5' is handwritten on both ends.</p>	 <p>A rectangular concrete sample with a weathered, greyish-brown surface. It is mounted on a metal test fixture with a vertical threaded rod passing through its center. The number '4' is handwritten on both ends, and 'FT 4' and 'Sept 2010' are written on the right end.</p>
45 cycles	45 cycles
 <p>A rectangular concrete sample with a weathered, greyish-brown surface. It is mounted on a metal test fixture with a vertical threaded rod passing through its center. The number '5' is handwritten on both ends.</p>	 <p>A rectangular concrete sample with a weathered, greyish-brown surface. It is mounted on a metal test fixture with a vertical threaded rod passing through its center. The number '4' is handwritten on both ends, and 'FT 4' and 'Sept 2010' are written on the right end.</p>
90 cycles	90 cycles

Table B-5 Visual images of the 475 samples at every 45 cycles – thaw in air (Continued)



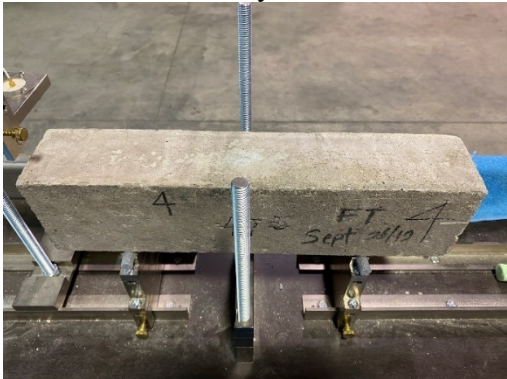
135 cycles



135 cycles



180 cycles



180 cycles

Table B-6 Visual images of the 400 samples at every 45 cycles – thaw in air







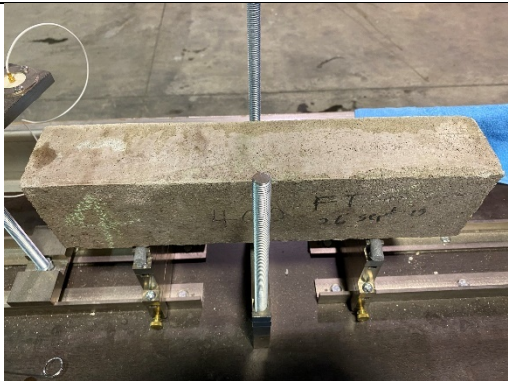
28 days	365 days
 A rectangular concrete sample, approximately 10x4x2 inches, is mounted on a metal test fixture. The sample is light brown and shows some surface texture. It is held in place by a central vertical threaded rod and two side rods. The number '5' is handwritten on the front face.	 A rectangular concrete sample, similar in size to the one on the left, is mounted on a metal test fixture. The sample is a darker, more weathered brown color. It is held in place by a central vertical threaded rod and two side rods. The letters 'FT' and some numbers are handwritten on the front face.
0 cycle	0 cycle
 A rectangular concrete sample, similar to the one at 0 cycles, is mounted on a metal test fixture. The surface appears slightly more weathered. It is held in place by a central vertical threaded rod and two side rods. The number '5' is handwritten on the front face.	 A rectangular concrete sample, similar to the one at 0 cycles, is mounted on a metal test fixture. The surface shows more significant weathering and discoloration. It is held in place by a central vertical threaded rod and two side rods. The letters 'FT' and some numbers are handwritten on the front face.
45 cycles	45 cycles
 A rectangular concrete sample, similar to the one at 45 cycles, is mounted on a metal test fixture. The surface shows further weathering. It is held in place by a central vertical threaded rod and two side rods. The number '5' is handwritten on the front face.	 A rectangular concrete sample, similar to the one at 45 cycles, is mounted on a metal test fixture. The surface shows significant weathering and discoloration. It is held in place by a central vertical threaded rod and two side rods. The letters 'FT' and some numbers are handwritten on the front face.
90 cycles	90 cycles

Table B-6 Visual images of the 400 samples at every 45 cycles – thaw in air (Continued)



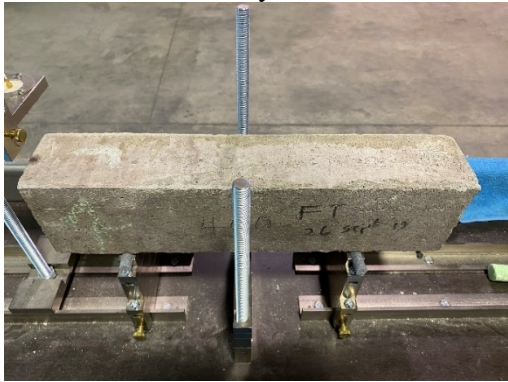
135 cycles



135 cycles



180 cycles



180 cycles

Appendices C
Sample AASHTOWare Pavement ME Outputs



GB Section Major Arterial 7500AADTT

File Name: C:\Users\admin\Desktop\Frank Ni\Major Arterial\7500 AADTT\GB Section Major Arterial 7500AADTT.dgpx



Design Inputs

Design Life: **25 years** Base construction: **May, 2021** Climate Data: **43.5, -80.625**
 Design Type: **FLEXIBLE** Pavement construction: **June, 2022** Sources (Lat/Lon)
 Traffic opening: **September, 2022**

Design Structure

Layer type	Material Type	Thickness(mm)
Flexible	Default asphalt concrete	40.0
Flexible	Default asphalt concrete	130.0
NonStabilized	A-1-a	150.0
NonStabilized	A-1-b	600.0
Subgrade	A-1-a	Semi-infinite

Volumetric at Construction:

Effective binder content (%)	11.8
Air voids (%)	7.0

Traffic

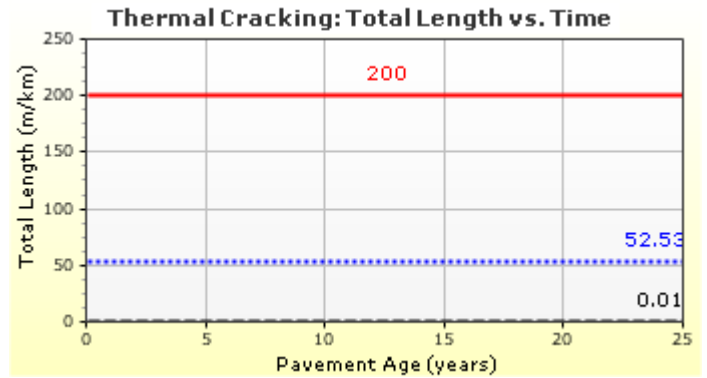
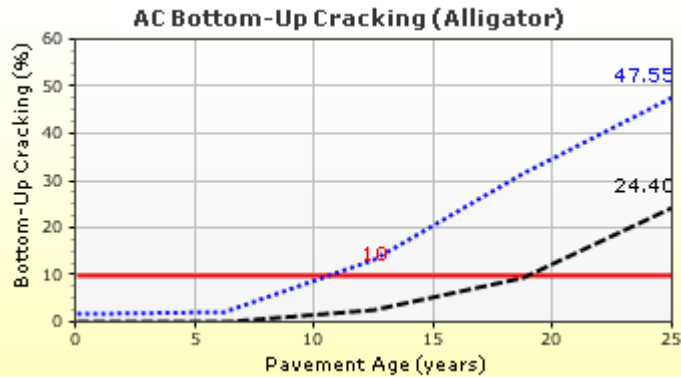
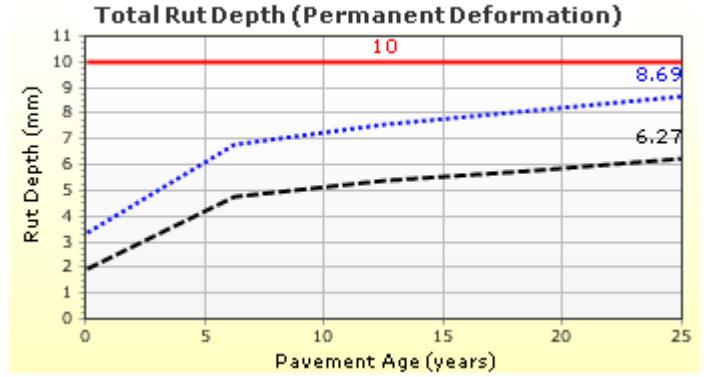
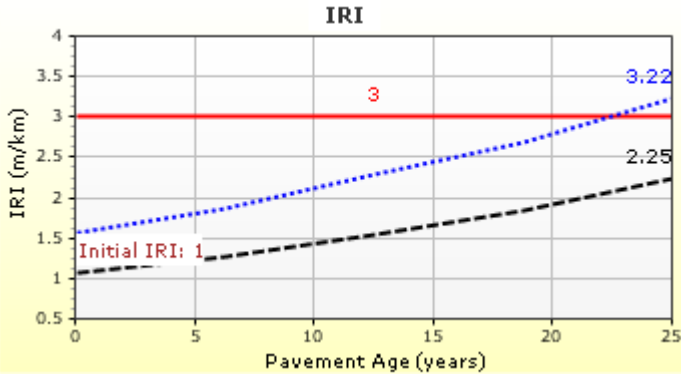
Age (year)	Heavy Trucks (cumulative)
2022 (initial)	7,500
2034 (12 years)	16,063,700
2047 (25 years)	37,255,500

Design Outputs

Distress Prediction Summary

Distress Type	Distress @ Specified Reliability		Reliability (%)		Criterion Satisfied?
	Target	Predicted	Target	Achieved	
Terminal IRI (m/km)	3.00	3.22	95.00	89.85	Fail
Permanent deformation - total pavement (mm)	10.00	8.69	95.00	99.45	Pass
AC bottom-up fatigue cracking (percent)	10.00	47.55	95.00	15.31	Fail
AC thermal cracking (m/km)	200.00	52.53	95.00	100.00	Pass
AC top-down fatigue cracking (m/km)	378.80	2746.63	95.00	0.04	Fail
Permanent deformation - AC only (mm)	6.00	3.10	95.00	100.00	Pass

Distress Charts

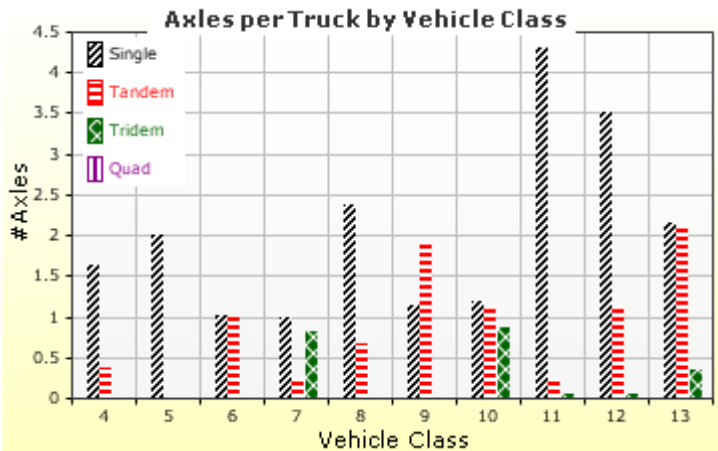
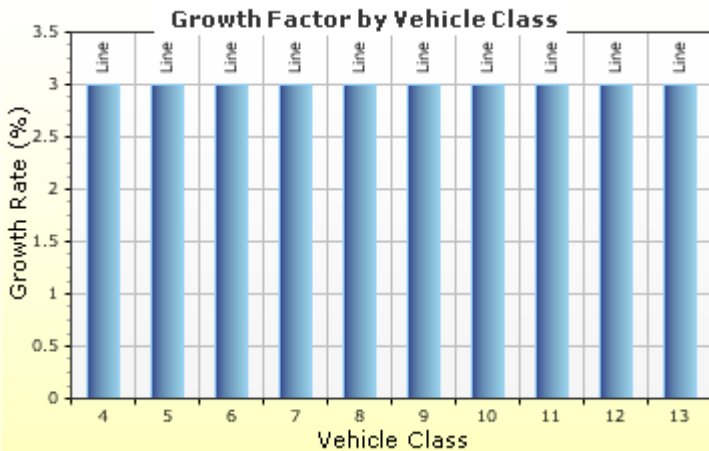
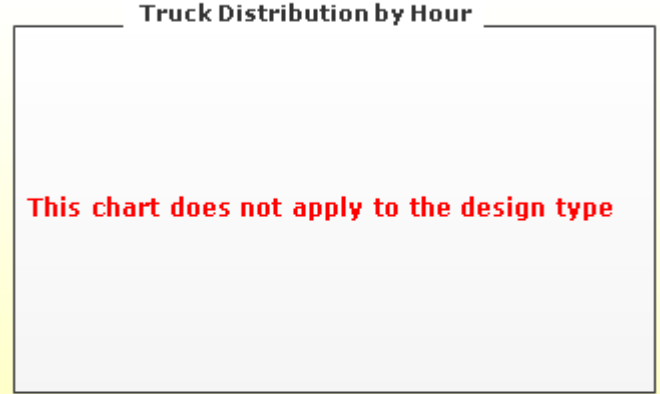
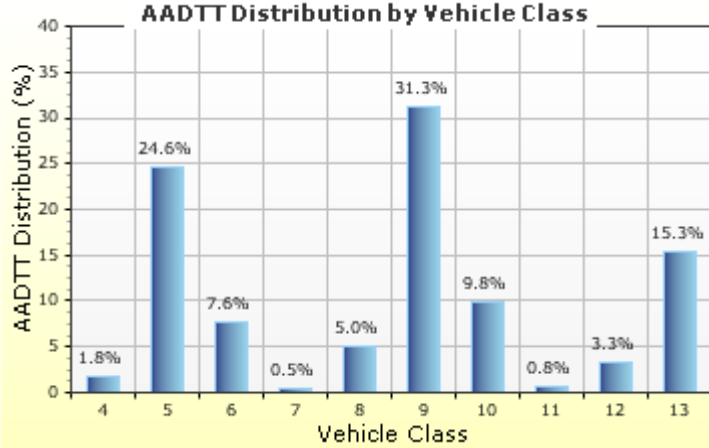


Traffic Inputs

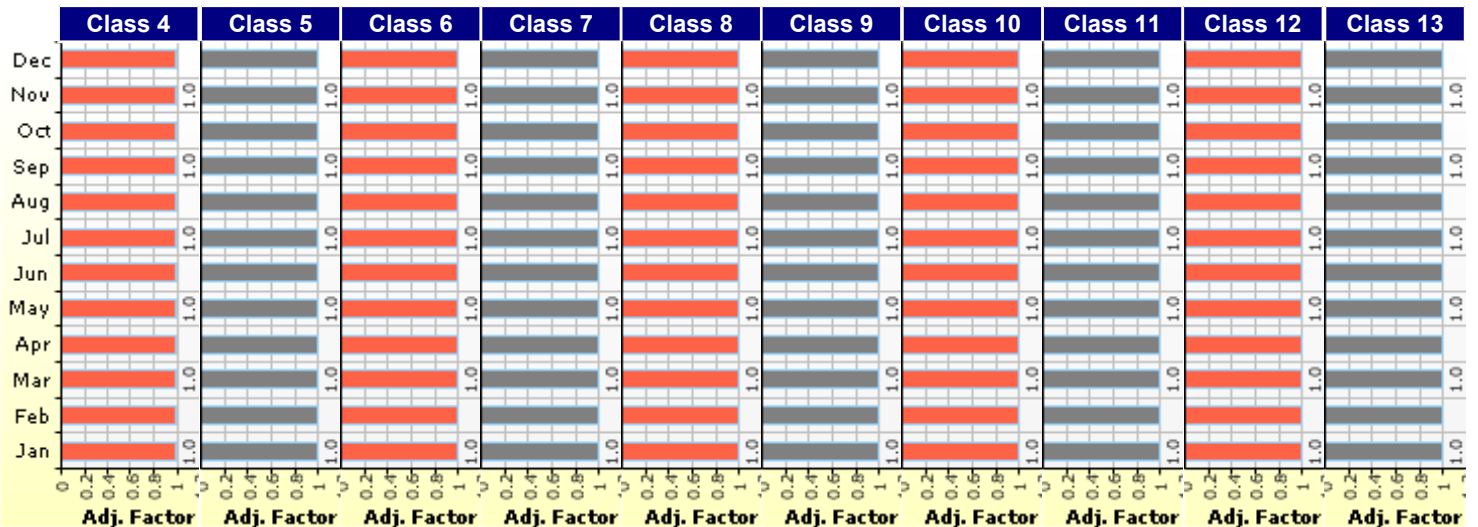
Graphical Representation of Traffic Inputs

Initial two-way AADTT: **7,500**
 Number of lanes in design direction: **2**

Percent of trucks in design direction (%): **50.0**
 Percent of trucks in design lane (%): **80.0**
 Operational speed (kph): **100.0**



Traffic Volume Monthly Adjustment Factors



Tabular Representation of Traffic Inputs

Volume Monthly Adjustment Factors Level 3: Default MAF

Month	Vehicle Class									
	4	5	6	7	8	9	10	11	12	13
January	1.0	1.0	1.0	1.0	1.0	1.0	1.0	1.0	1.0	1.0
February	1.0	1.0	1.0	1.0	1.0	1.0	1.0	1.0	1.0	1.0
March	1.0	1.0	1.0	1.0	1.0	1.0	1.0	1.0	1.0	1.0
April	1.0	1.0	1.0	1.0	1.0	1.0	1.0	1.0	1.0	1.0
May	1.0	1.0	1.0	1.0	1.0	1.0	1.0	1.0	1.0	1.0
June	1.0	1.0	1.0	1.0	1.0	1.0	1.0	1.0	1.0	1.0
July	1.0	1.0	1.0	1.0	1.0	1.0	1.0	1.0	1.0	1.0
August	1.0	1.0	1.0	1.0	1.0	1.0	1.0	1.0	1.0	1.0
September	1.0	1.0	1.0	1.0	1.0	1.0	1.0	1.0	1.0	1.0
October	1.0	1.0	1.0	1.0	1.0	1.0	1.0	1.0	1.0	1.0
November	1.0	1.0	1.0	1.0	1.0	1.0	1.0	1.0	1.0	1.0
December	1.0	1.0	1.0	1.0	1.0	1.0	1.0	1.0	1.0	1.0

Distributions by Vehicle Class

Vehicle Class	AADTT Distribution (%) (Level 3)	Growth Factor	
		Rate (%)	Function
Class 4	1.8%	3%	Linear
Class 5	24.6%	3%	Linear
Class 6	7.6%	3%	Linear
Class 7	0.5%	3%	Linear
Class 8	5%	3%	Linear
Class 9	31.3%	3%	Linear
Class 10	9.8%	3%	Linear
Class 11	0.8%	3%	Linear
Class 12	3.3%	3%	Linear
Class 13	15.3%	3%	Linear

Truck Distribution by Hour does not apply

Axle Configuration

Traffic Wander	
Mean wheel location (mm)	460.0
Traffic wander standard deviation (mm)	254.0
Design lane width (m)	3.7

Axle Configuration	
Average axle width (m)	2.6
Dual tire spacing (mm)	305.0
Tire pressure (kPa)	827.4

Average Axle Spacing	
Tandem axle spacing (m)	1.3
Tridem axle spacing (m)	1.3
Quad axle spacing (m)	1.3

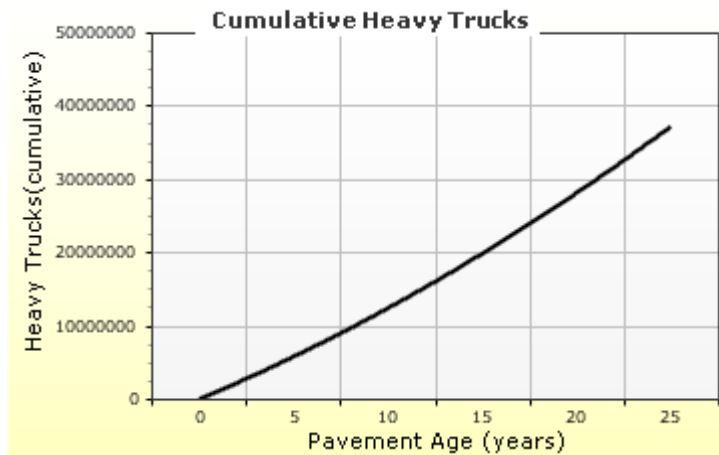
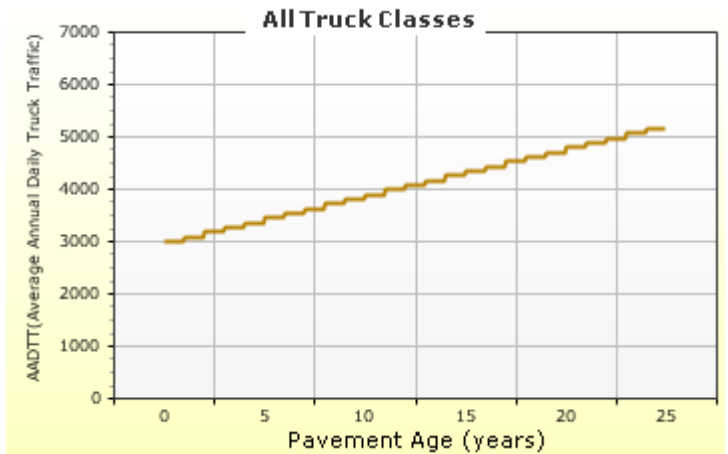
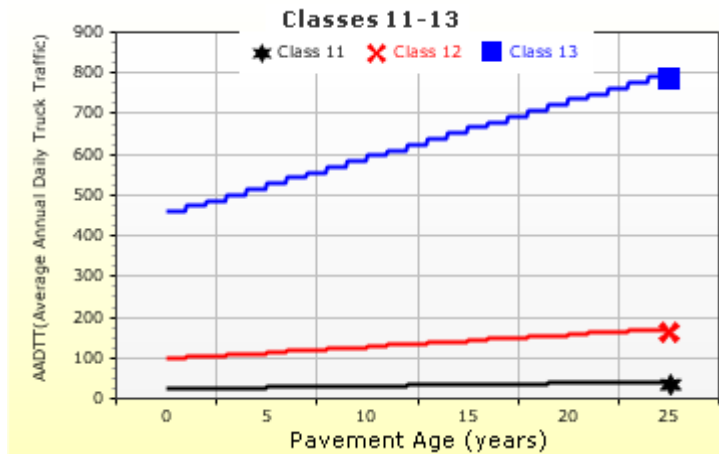
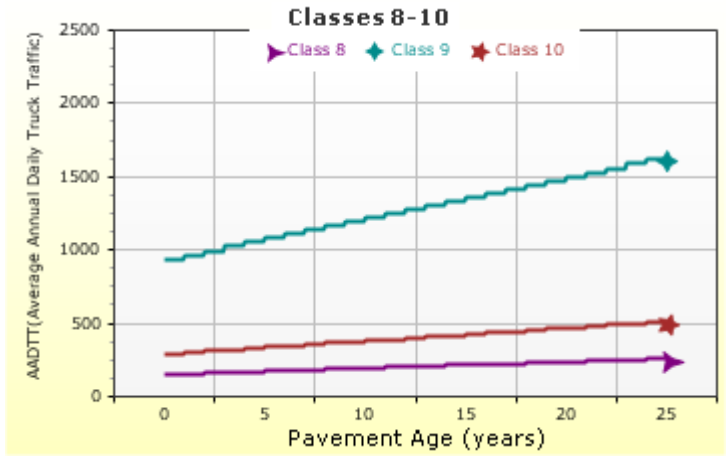
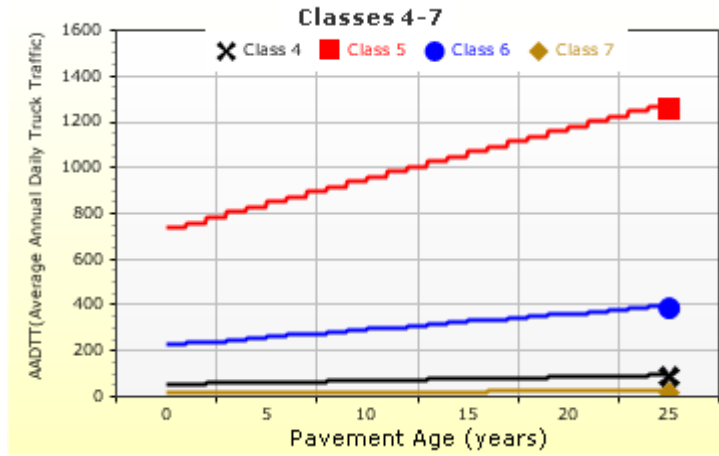
Wheelbase does not apply

Number of Axles per Truck

Vehicle Class	Single Axle	Tandem Axle	Tridem Axle	Quad Axle
Class 4	1.62	0.39	0	0
Class 5	2	0	0	0
Class 6	1.02	0.99	0	0
Class 7	1	0.26	0.83	0
Class 8	2.38	0.67	0	0
Class 9	1.13	1.93	0	0
Class 10	1.19	1.09	0.89	0
Class 11	4.29	0.26	0.06	0
Class 12	3.52	1.14	0.06	0
Class 13	2.15	2.13	0.35	0

AADTT (Average Annual Daily Truck Traffic) Growth

* Traffic cap is not enforced





GB Section Major Arterial 7500AADTT

File Name: C:\Users\admin\Desktop\Frank Ni\Major Arterial\7500 AADTT\GB Section Major Arterial 7500AADTT.dgpx



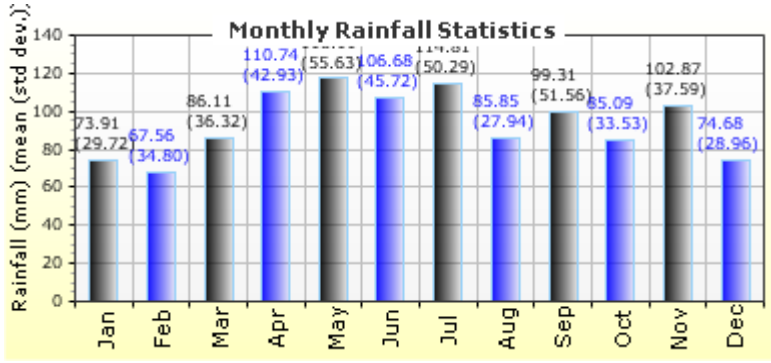
Climate Inputs

Climate Data Sources:

Climate Station Cities: Location (lat lon elevation(m))
 CA, ON 43.50000 -80.62500 369

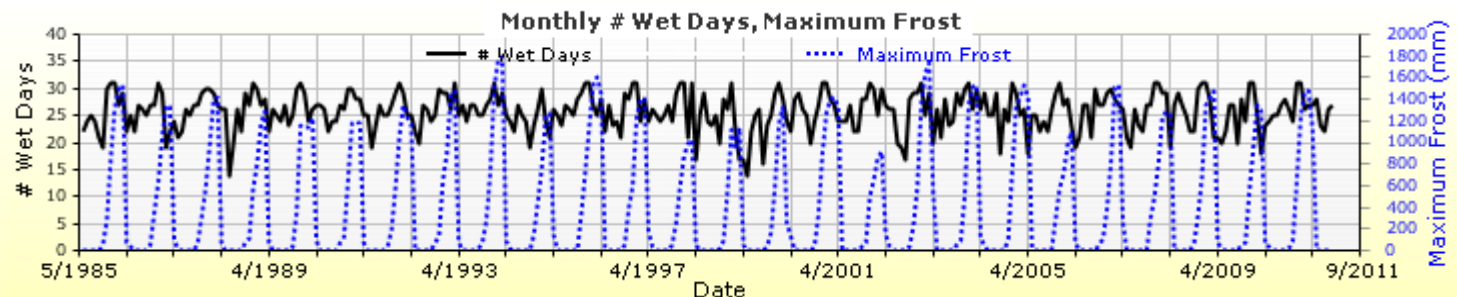
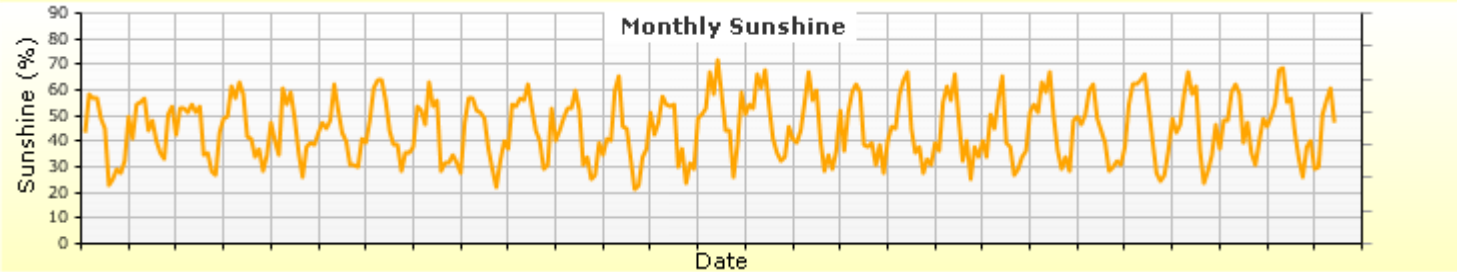
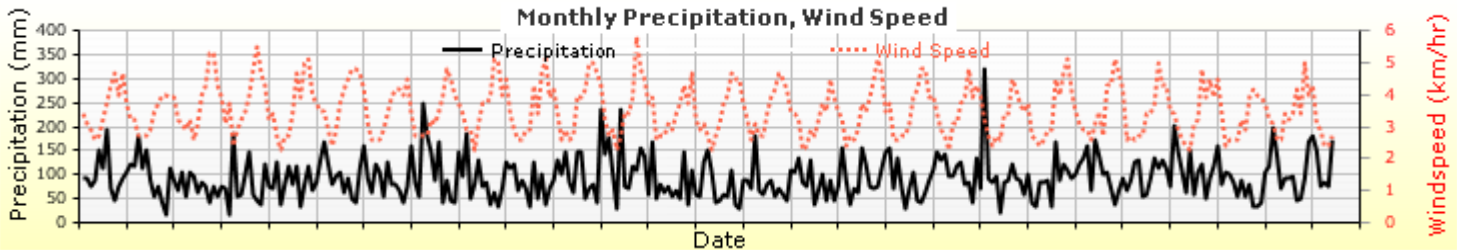
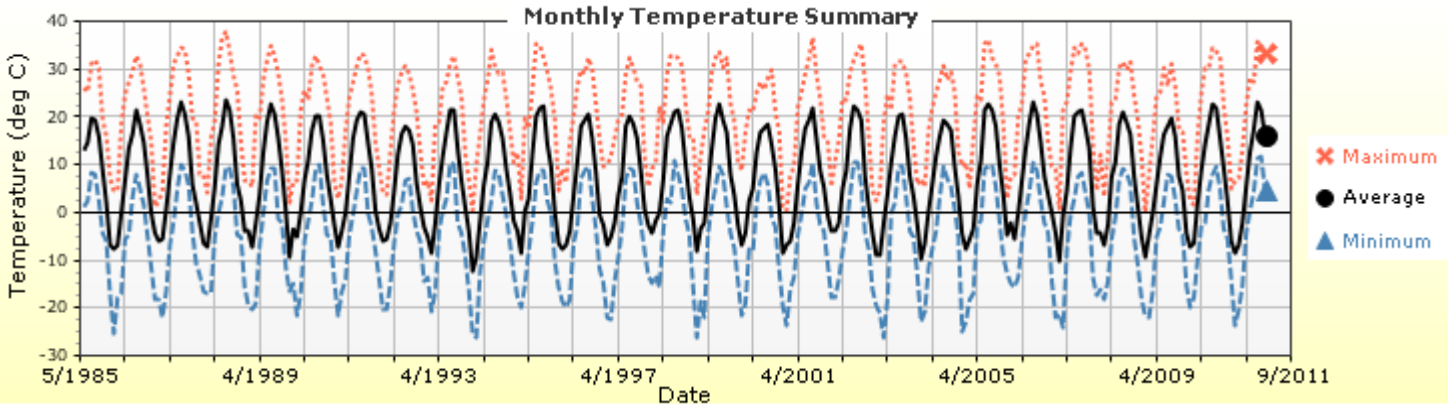
Annual Statistics:

Mean annual air temperature (°C) 7.46
 Mean annual precipitation (mm) 1127.76
 Freezing index (°C - days) 627.54
 Average annual number of freeze/thaw cycles: 87.25



Water table depth (m) 10.00

Monthly Climate Summary:



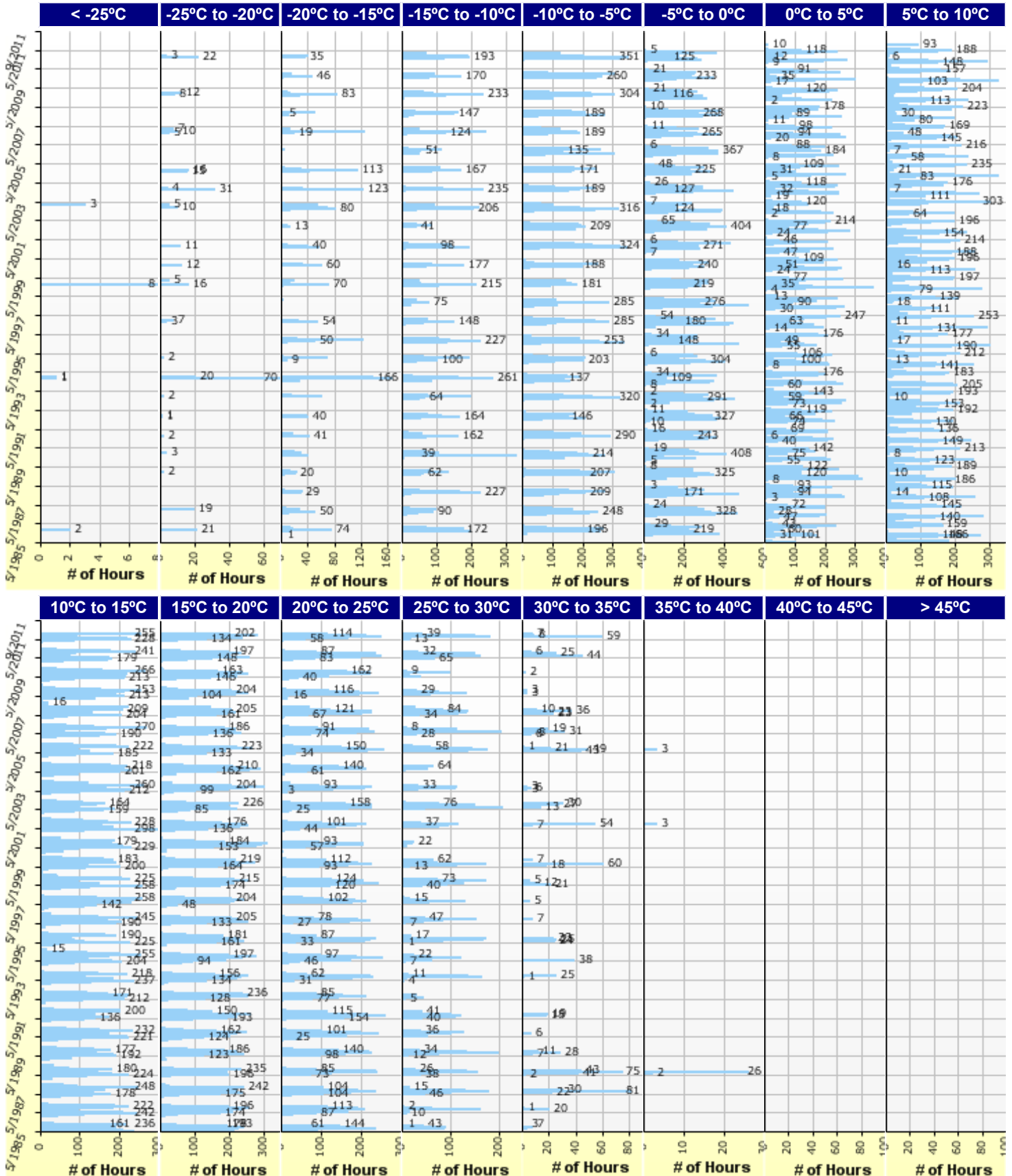


GB Section Major Arterial 7500AADTT

File Name: C:\Users\admin\Desktop\Frank Ni\Major Arterial\7500 AADTT\GB Section Major Arterial 7500AADTT.dgp



Hourly Air Temperature Distribution by Month:





GB Section Major Arterial 7500AADTT

File Name: C:\Users\admin\Desktop\Frank Ni\Major Arterial\7500 AADTT\GB Section Major Arterial 7500AADTT.dgpx



Design Properties

HMA Design Properties

Use Multilayer Rutting Model	False
Using G* based model (not nationally calibrated)	False
Is NCHRP 1-37A HMA Rutting Model Coefficients	True
Endurance Limit	-
Use Reflective Cracking	True

Structure - ICM Properties	
AC surface shortwave absorptivity	0.85

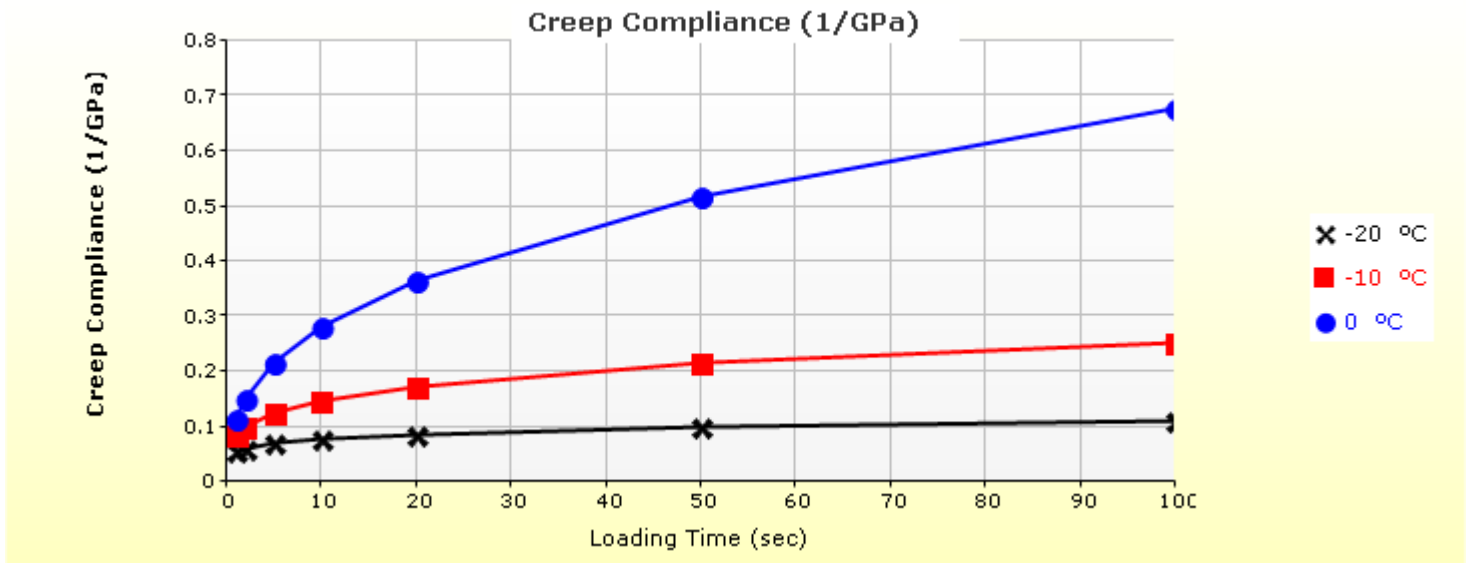
Layer Name	Layer Type	Interface Friction
Layer 1 Flexible : Default asphalt concrete	Flexible (1)	1.00
Layer 2 Flexible : Default asphalt concrete	Flexible (1)	1.00
Layer 3 Non-stabilized Base : A-1-a	Non-stabilized Base (4)	1.00
Layer 4 Non-stabilized Base : A-1-b	Non-stabilized Base (4)	1.00
Layer 5 Subgrade : A-1-a	Subgrade (5)	-

Thermal Cracking

Thermal Contraction	
Is thermal contraction calculated?	True
Mix coefficient of thermal contraction (mm/mm/°C)	-
Aggregate coefficient of thermal contraction (mm/mm/°C)	9.0e-006
Voids in Mineral Aggregate (%)	18.8

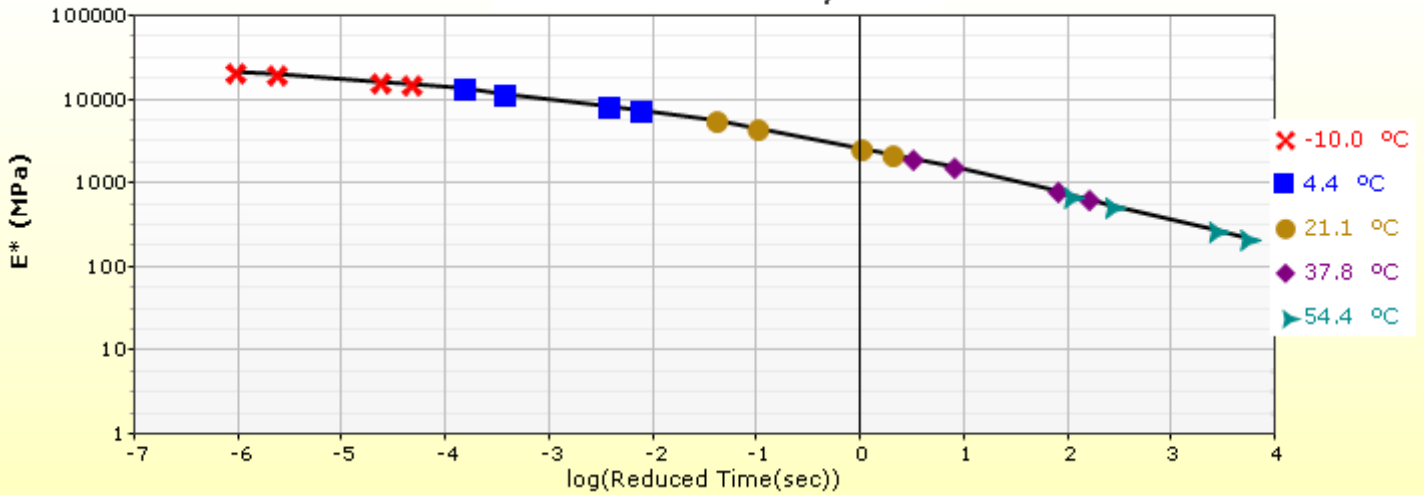
Indirect Tensile Strength (Input Level: 3)	
Test Temperature (°C)	Indirect Tensile Strength (Mpa)
-10.0	2.79

Creep Compliance (1/GPa) (Input Level: 3)			
Loading time (sec)	-20 °C	-10 °C	0 °C
1	5.57e-002	8.57e-002	1.16e-001
2	6.17e-002	1.01e-001	1.51e-001
5	7.07e-002	1.25e-001	2.15e-001
10	7.83e-002	1.48e-001	2.80e-001
20	8.68e-002	1.74e-001	3.65e-001
50	9.94e-002	2.16e-001	5.19e-001
100	1.10e-001	2.55e-001	6.77e-001

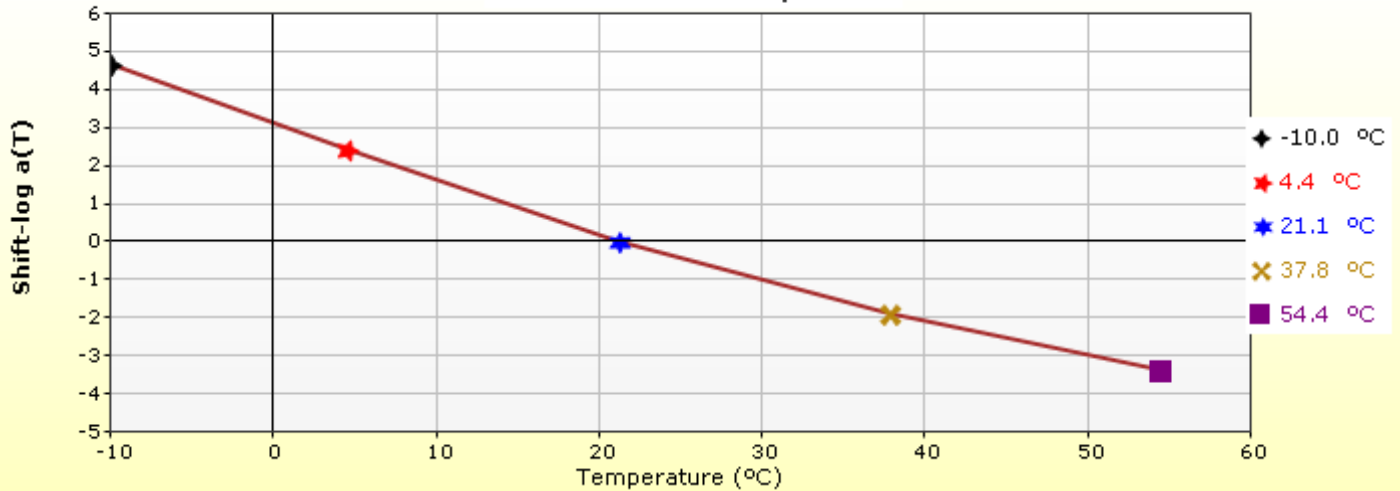


HMA Layer 1: Layer 1 Flexible : Default asphalt concrete

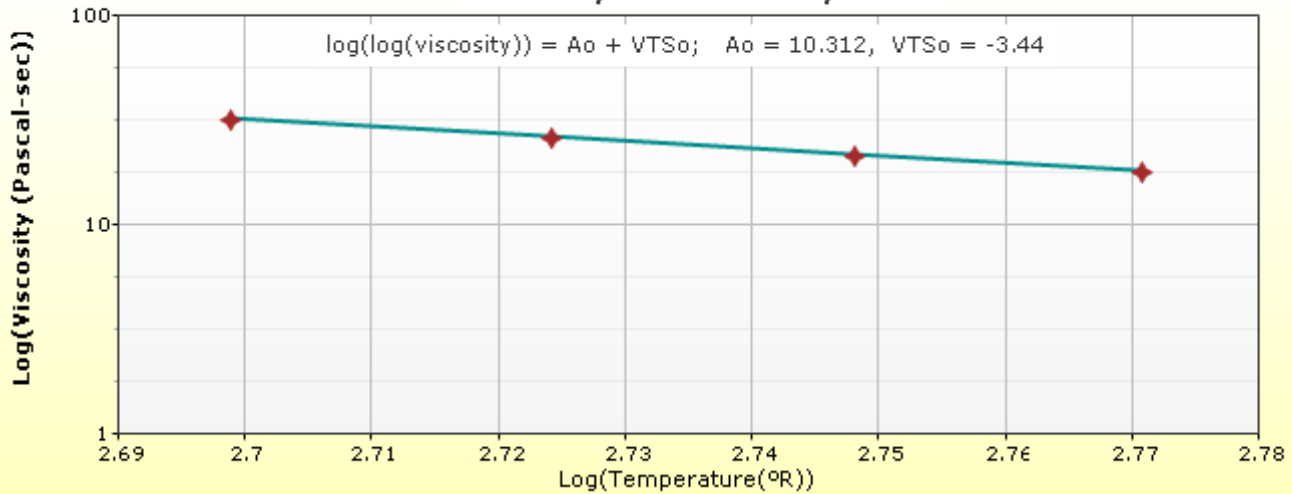
Master Curve HMA Layer 1



Shift Curve HMA Layer 1

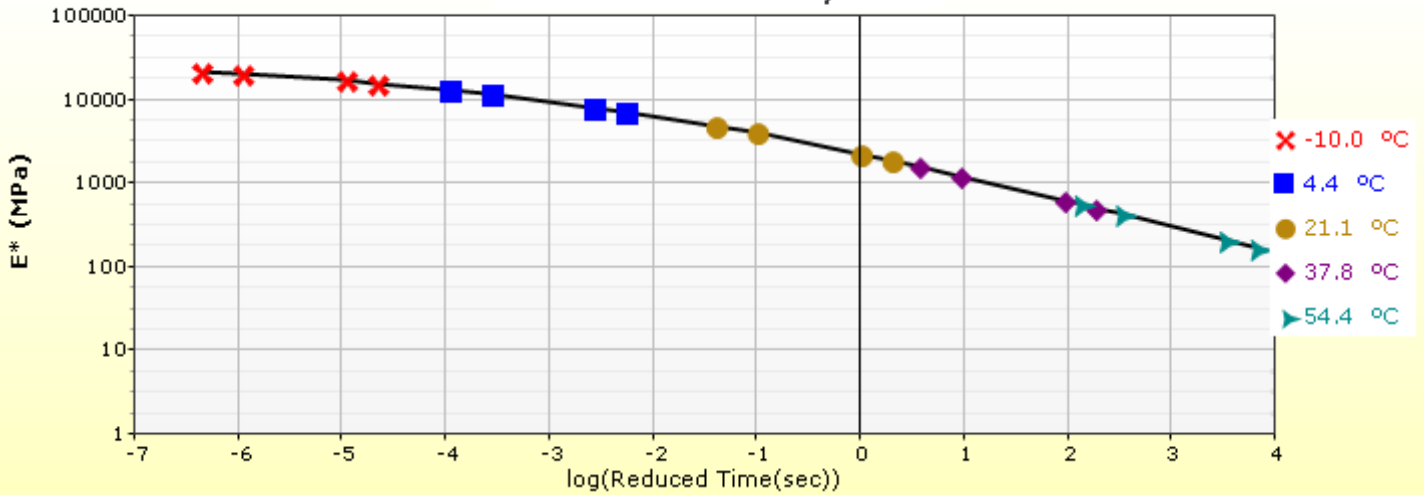


Viscosity Curve HMA Layer 1

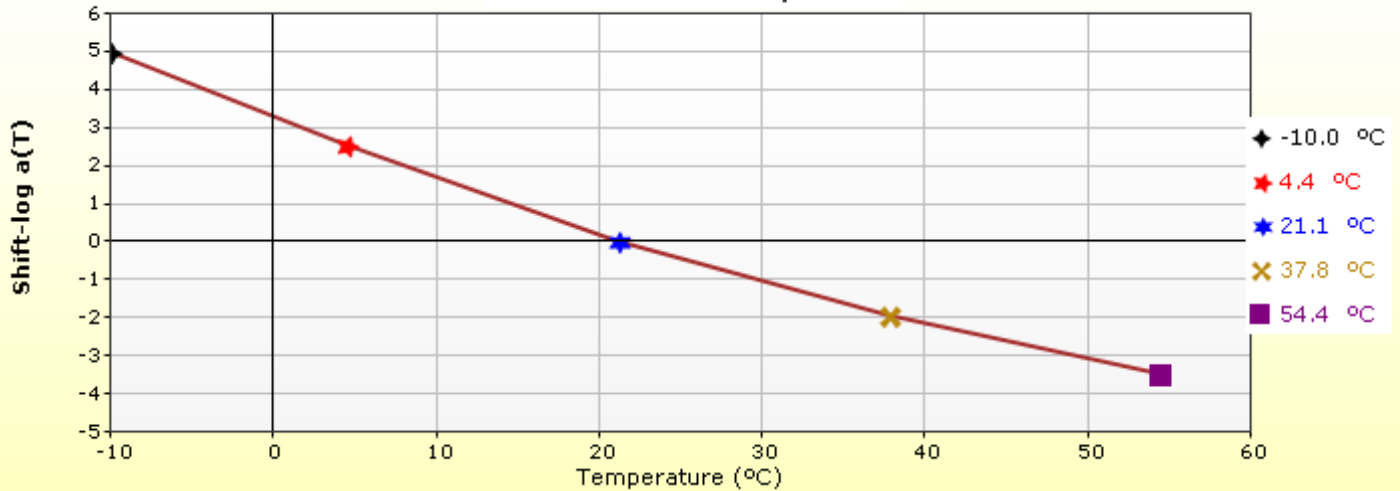


HMA Layer 2: Layer 2 Flexible : Default asphalt concrete

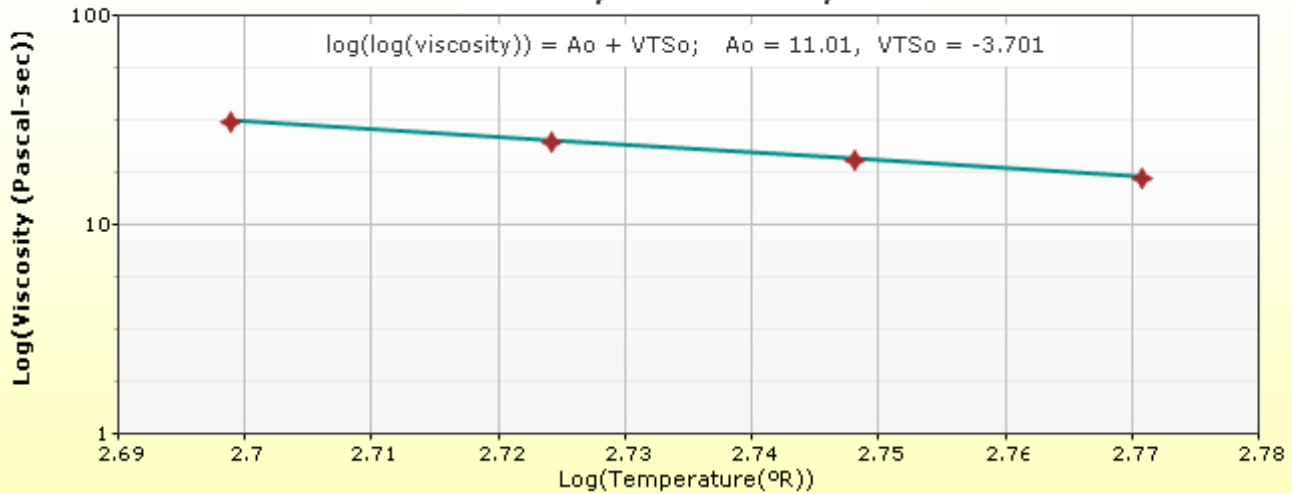
Master Curve HMA Layer 2



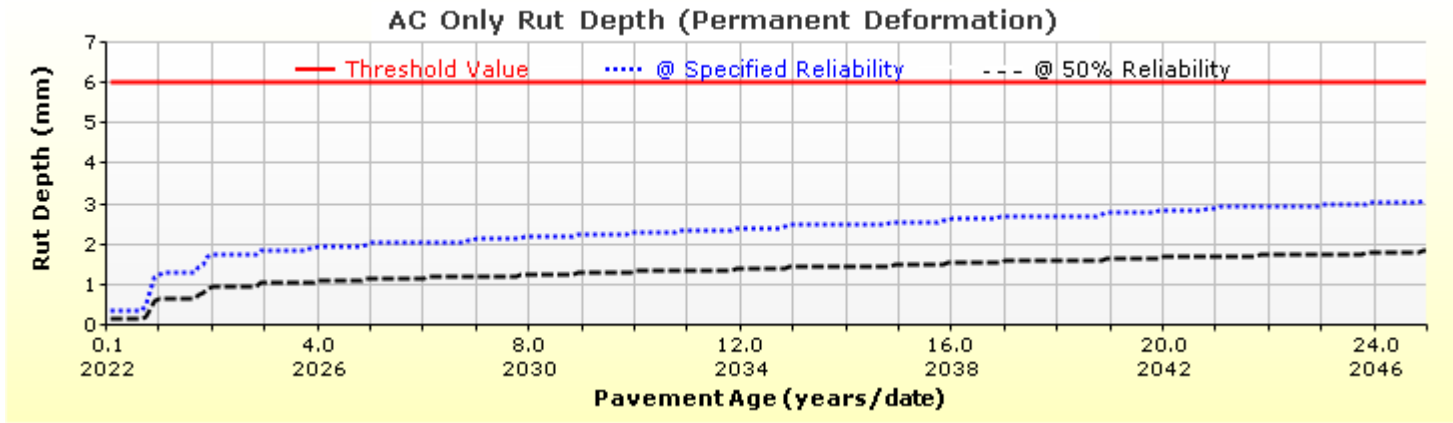
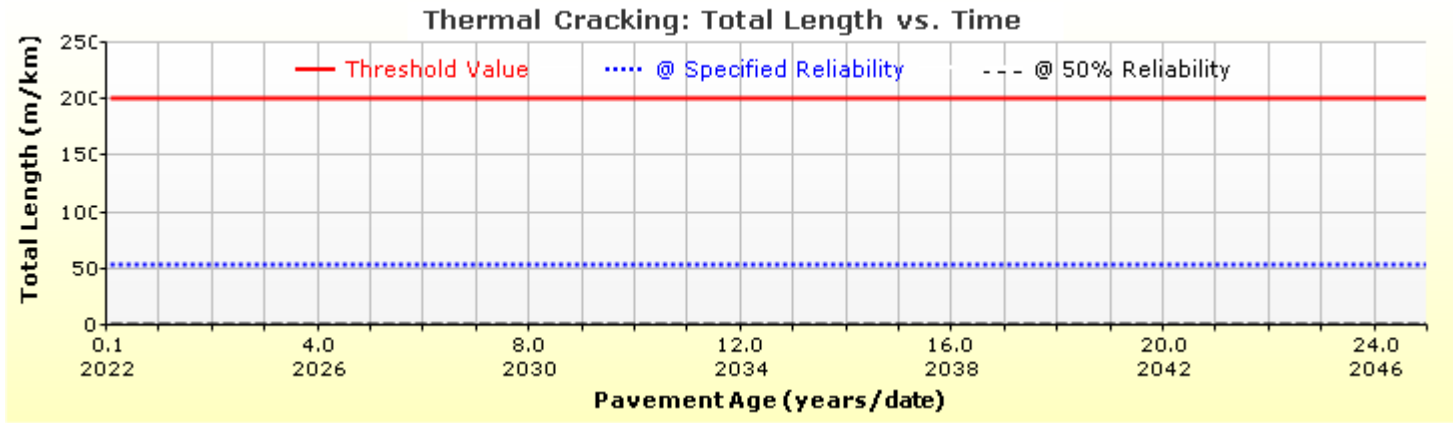
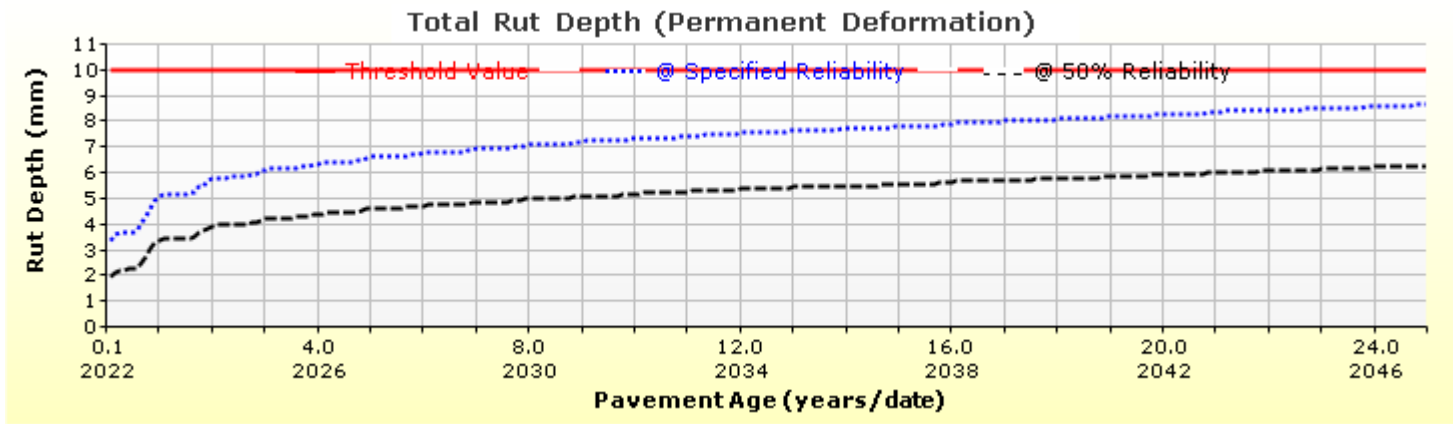
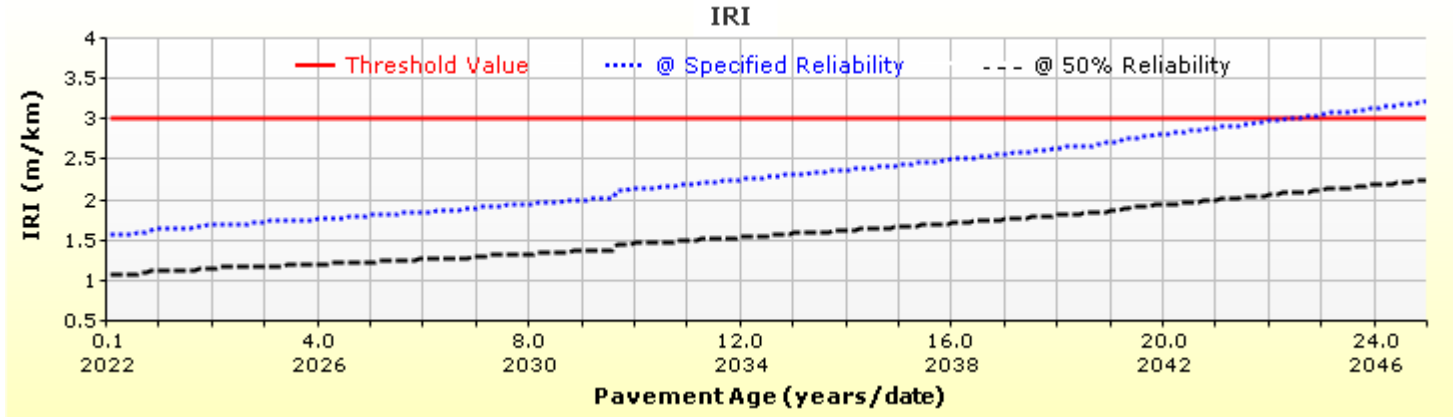
Shift Curve HMA Layer 2

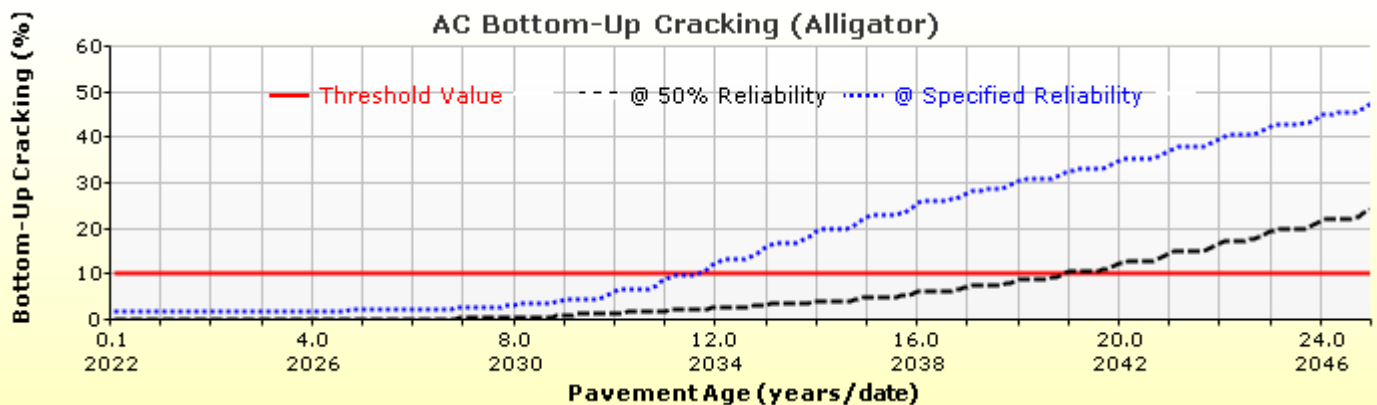
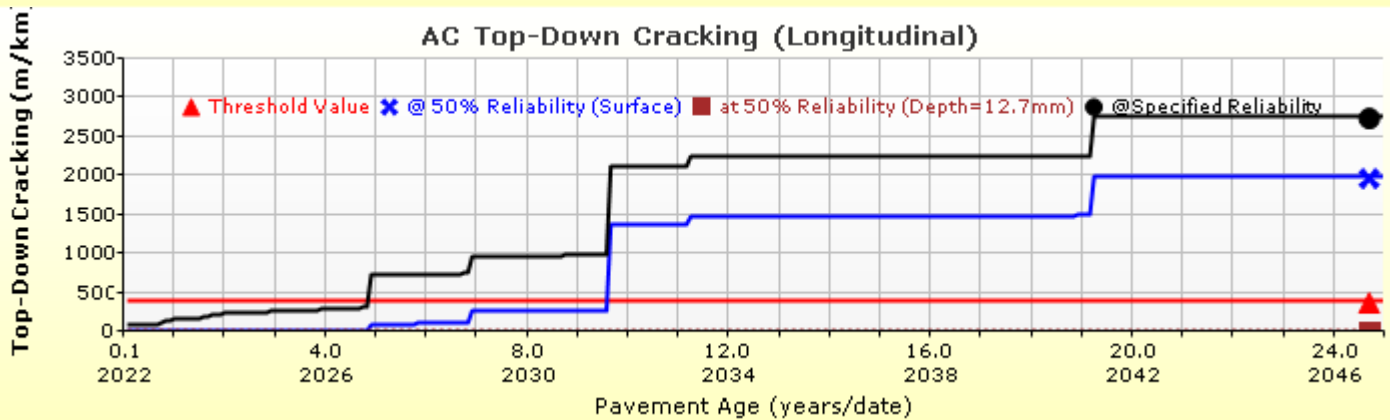
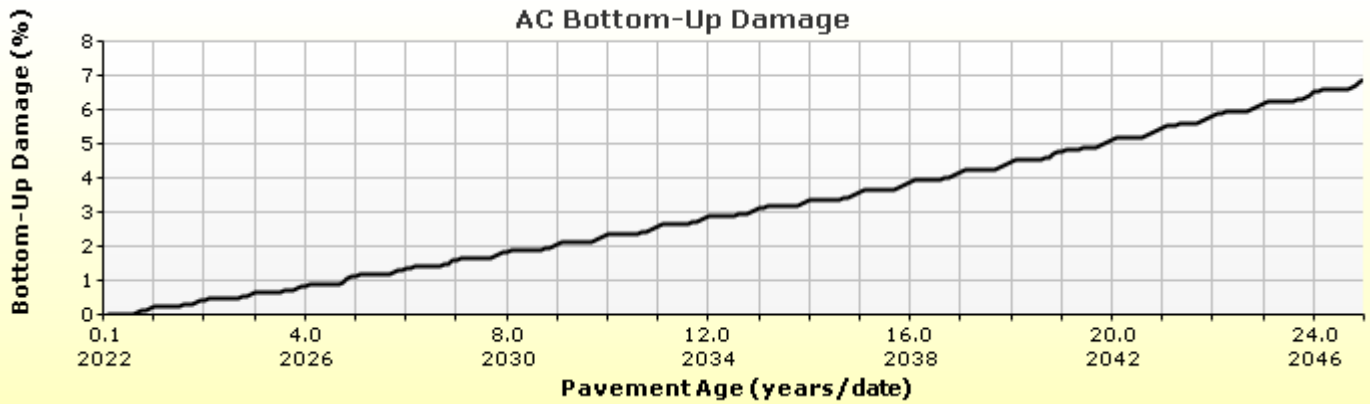
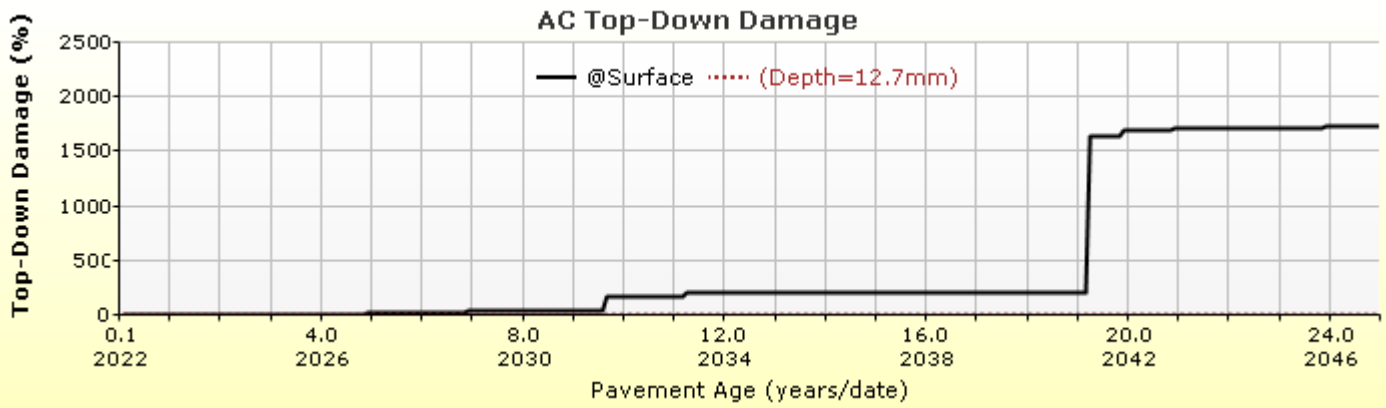


Viscosity Curve HMA Layer 2

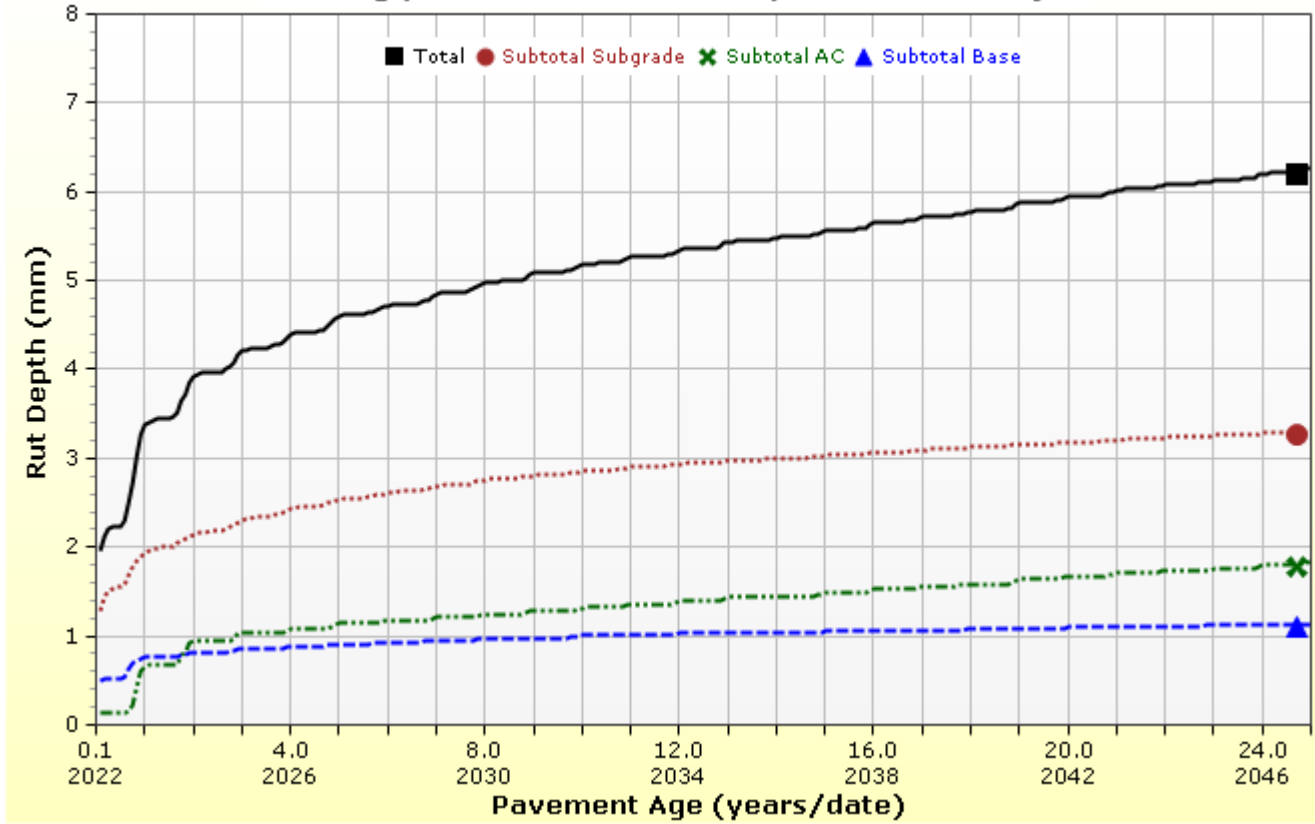


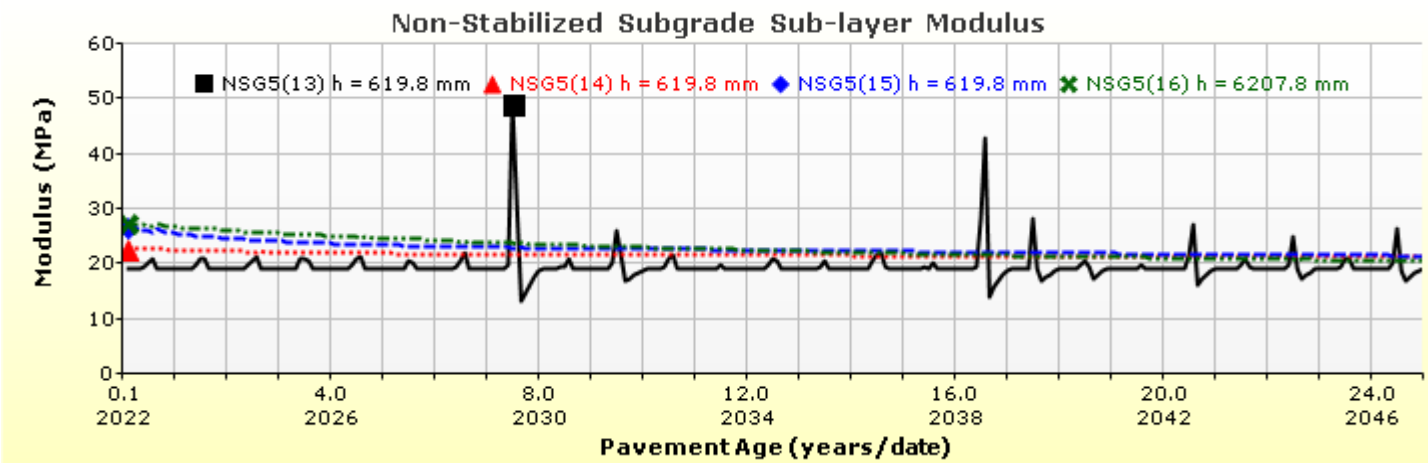
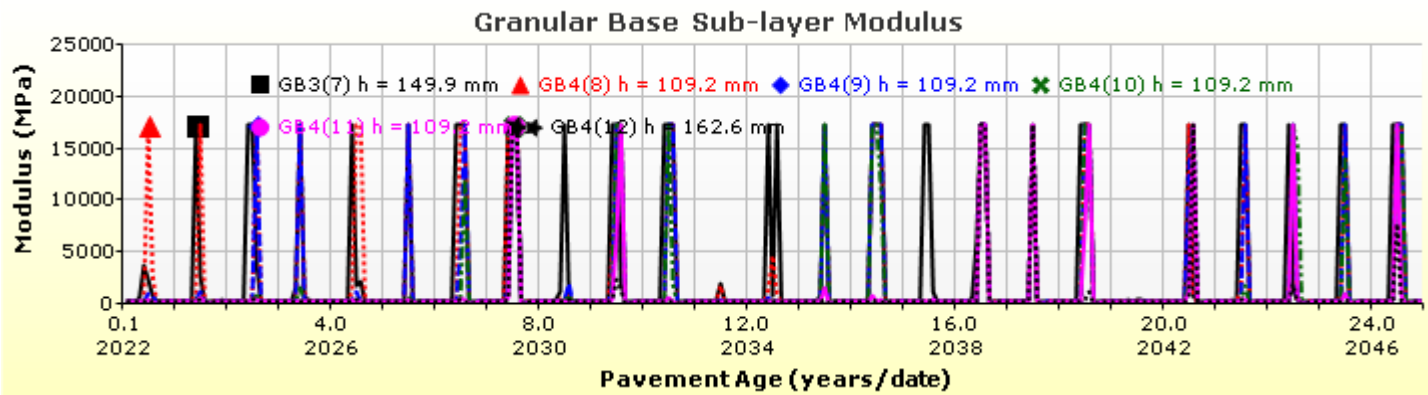
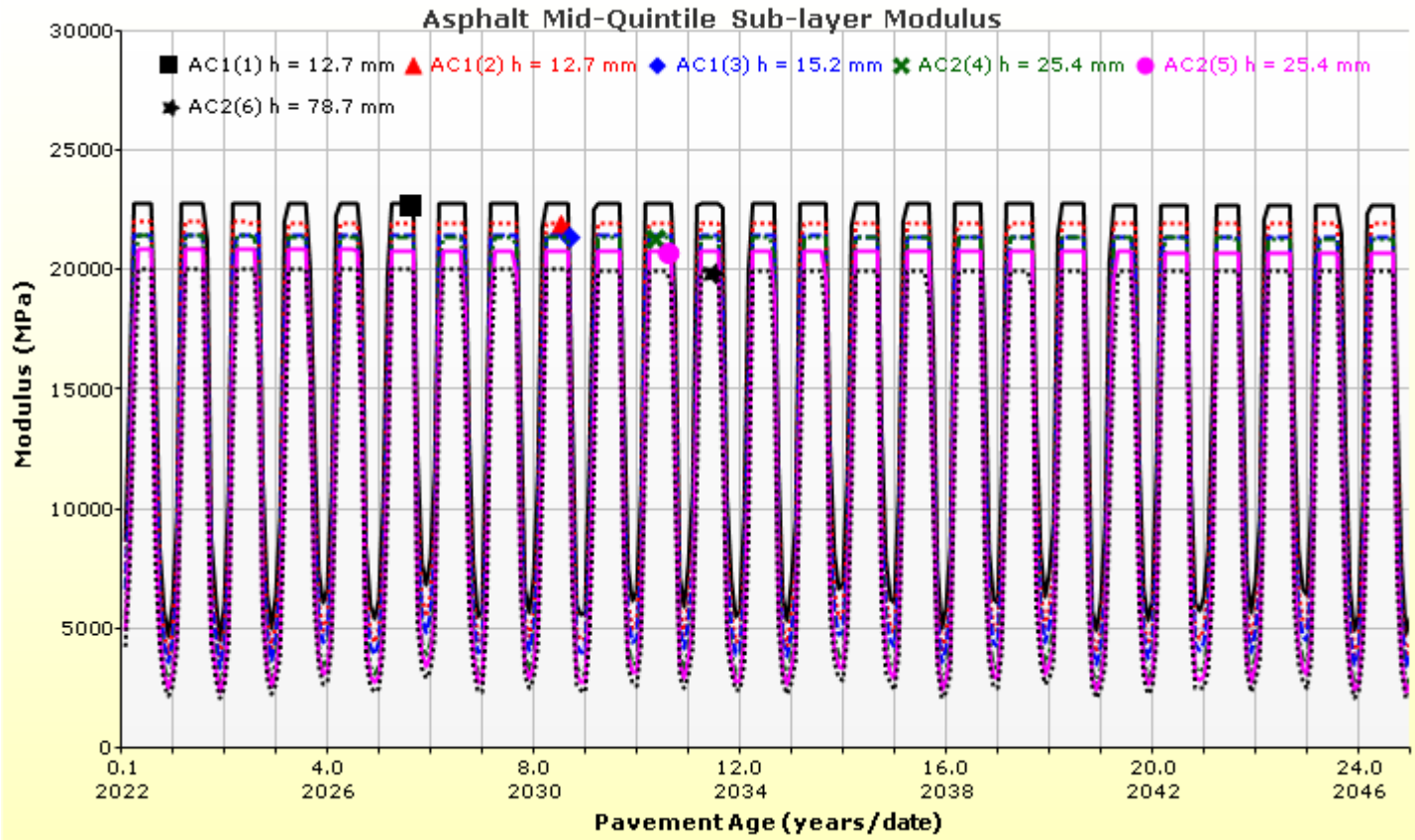
Analysis Output Charts





Rutting (Permanent Deformation) at 50% Reliability





Layer Information

Layer 1 Flexible : Default asphalt concrete

Asphalt		
Thickness (mm)	40.0	
Unit weight (kgf/m ³)	2390.0	
Poisson's ratio	Is Calculated?	False
	Ratio	0.35
	Parameter A	-
	Parameter B	-

Asphalt Dynamic Modulus (Input Level: 3)

Gradation	Percent Passing
19 mm sieve	100
9.5 mm sieve	77
4.75 mm sieve	60
0.075mm sieve	6

Asphalt Binder

Parameter	Value
Grade	Superpave Performance Grade
Binder Type	64-28
A	10.312
VTS	-3.44

General Info

Name	Value
Reference temperature (°C)	21.1
Effective binder content (%)	11.8
Air voids (%)	7
Thermal conductivity (watt/meter-kelvin)	1.16
Heat capacity (joule/kg-kelvin)	963

Identifiers

Field	Value
Display name/identifier	Default asphalt concrete
Description of object	
Author	
Date Created	9/16/2010 1:00:00 AM
Approver	
Date approved	9/16/2010 1:00:00 AM
State	
District	
County	
Highway	
Direction of Travel	
From station (km)	
To station (km)	
Province	
User defined field 1	
User defined field 2	
User defined field 3	
Revision Number	0



GB Section Major Arterial 7500AADTT

File Name: C:\Users\admin\Desktop\Frank Ni\Major Arterial\7500 AADTT\GB Section Major Arterial 7500AADTT.dgpx



Layer 2 Flexible : Default asphalt concrete

Asphalt		
Thickness (mm)	130.0	
Unit weight (kgf/m ³)	2460.0	
Poisson's ratio	Is Calculated?	False
	Ratio	0.35
	Parameter A	-
	Parameter B	-

Asphalt Dynamic Modulus (Input Level: 3)

Gradation	Percent Passing
19 mm sieve	100
9.5 mm sieve	77
4.75 mm sieve	60
0.075mm sieve	6

Asphalt Binder

Parameter	Value
Grade	Superpave Performance Grade
Binder Type	58-28
A	11.01
VTS	-3.701

General Info

Name	Value
Reference temperature (°C)	21.1
Effective binder content (%)	11.2
Air voids (%)	7
Thermal conductivity (watt/meter-kelvin)	1.16
Heat capacity (joule/kg-kelvin)	963

Identifiers

Field	Value
Display name/identifier	Default asphalt concrete
Description of object	
Author	
Date Created	9/16/2010 1:00:00 AM
Approver	
Date approved	9/16/2010 1:00:00 AM
State	
District	
County	
Highway	
Direction of Travel	
From station (km)	
To station (km)	
Province	
User defined field 1	
User defined field 2	
User defined field 3	
Revision Number	0

Layer 3 Non-stabilized Base : A-1-a

Unbound

Layer thickness (mm)	150.0
Poisson's ratio	0.35
Coefficient of lateral earth pressure (k0)	0.5

Modulus (Input Level: 3)

Analysis Type:	Modify input values by temperature/moisture
Method:	Resilient Modulus (MPa)

Resilient Modulus (MPa)

250.0

Use Correction factor for NDT modulus?	-
NDT Correction Factor:	-

Identifiers

Field	Value
Display name/identifier	A-1-a
Description of object	Default material
Author	AASHTO
Date Created	1/1/2011 12:00:00 AM
Approver	
Date approved	1/1/2011 12:00:00 AM
State	
District	
County	
Highway	
Direction of Travel	
From station (km)	
To station (km)	
Province	
User defined field 1	
User defined field 2	
User defined field 3	
Revision Number	0

Sieve

Liquid Limit	6.0
Plasticity Index	0.0
Is layer compacted?	True

	Is User Defined?	Value
Maximum dry unit weight (kgf/m ³)	False	2038.2
Saturated hydraulic conductivity (m/hr)	False	2.376e-02
Specific gravity of solids	False	2.7
Water Content (%)	False	5.7

User-defined Soil Water Characteristic Curve (SWCC)

Is User Defined?	False
af	3.0201
bf	2.5984
cf	0.7539
hr	100.0000

Sieve Size	% Passing
0.001mm	
0.002mm	
0.020mm	
0.075mm	5.0
0.150mm	
0.180mm	
0.250mm	
0.300mm	13.5
0.425mm	
0.600mm	
0.850mm	
1.18mm	27.5
2.0mm	
2.36mm	
4.75mm	45.0
9.5mm	61.5
12.5mm	77.5
19.0mm	92.5
25.0mm	100.0
37.5mm	
50.0mm	
63.0mm	
75.0mm	
90.0mm	

Layer 4 Non-stabilized Base : A-1-b

Unbound	
Layer thickness (mm)	600.0
Poisson's ratio	0.35
Coefficient of lateral earth pressure (k0)	0.5

Modulus (Input Level: 3)

Analysis Type:	Modify input values by temperature/moisture
Method:	Resilient Modulus (MPa)

Resilient Modulus (MPa)
200.0

Use Correction factor for NDT modulus?	-
NDT Correction Factor:	-

Identifiers

Field	Value
Display name/identifier	A-1-b
Description of object	Default material
Author	AASHTO
Date Created	1/1/2011 12:00:00 AM
Approver	
Date approved	1/1/2011 12:00:00 AM
State	
District	
County	
Highway	
Direction of Travel	
From station (km)	
To station (km)	
Province	
User defined field 1	
User defined field 2	
User defined field 3	
Revision Number	0

Sieve

Liquid Limit	11.0
Plasticity Index	0.0
Is layer compacted?	True

	Is User Defined?	Value
Maximum dry unit weight (kgf/m ³)	False	2022.2
Saturated hydraulic conductivity (m/hr)	False	6.073e-02
Specific gravity of solids	False	2.7
Water Content (%)	False	7.3

User-defined Soil Water Characteristic Curve (SWCC)

Is User Defined?	False
af	6.8181
bf	1.6200
cf	0.8174
hr	100.0000

Sieve Size	% Passing
0.001mm	
0.002mm	
0.020mm	
0.075mm	5.0
0.150mm	
0.180mm	
0.250mm	
0.300mm	13.5
0.425mm	
0.600mm	
0.850mm	
1.18mm	25.0
2.0mm	
2.36mm	
4.75mm	37.5
9.5mm	
12.5mm	
19.0mm	
25.0mm	75.0
37.5mm	
50.0mm	
63.0mm	
75.0mm	
90.0mm	100.0

Layer 5 Subgrade : A-1-a

Unbound	
Layer thickness (mm)	Semi-infinite
Poisson's ratio	0.45
Coefficient of lateral earth pressure (k0)	0.5

Modulus (Input Level: 3)

Analysis Type:	Modify input values by temperature/moisture
Method:	Resilient Modulus (MPa)

Resilient Modulus (MPa)
30.0

Use Correction factor for NDT modulus?	-
NDT Correction Factor:	-

Identifiers

Field	Value
Display name/identifier	A-1-a
Description of object	Default Material
Author	AASHTO
Date Created	1/1/2011 12:00:00 AM
Approver	
Date approved	1/1/2011 12:00:00 AM
State	
District	
County	
Highway	
Direction of Travel	
From station (km)	
To station (km)	
Province	
User defined field 1	
User defined field 2	
User defined field 3	
Revision Number	0

Sieve

Liquid Limit	26.0
Plasticity Index	12.0
Is layer compacted?	True

	Is User Defined?	Value
Maximum dry unit weight (kgf/m ³)	False	1748.5
Saturated hydraulic conductivity (m/hr)	False	8.129e-06
Specific gravity of solids	False	2.7
Water Content (%)	False	16.8

User-defined Soil Water Characteristic Curve (SWCC)

Is User Defined?	False
af	106.7030
bf	0.6914
cf	0.2273
hr	500.0000

Sieve Size	% Passing
0.001mm	
0.002mm	30.0
0.020mm	
0.075mm	80.0
0.150mm	
0.180mm	84.0
0.250mm	
0.300mm	
0.425mm	91.0
0.600mm	
0.850mm	
1.18mm	
2.0mm	95.0
2.36mm	
4.75mm	97.0
9.5mm	99.0
12.5mm	100.0
19.0mm	100.0
25.0mm	100.0
37.5mm	
50.0mm	
63.0mm	
75.0mm	
90.0mm	

Calibration Coefficients

AC Fatigue

$N_f = 0.00432 * C * \beta_{f1} k_1 \left(\frac{1}{\epsilon_1}\right)^{k_2 \beta_{f2}} \left(\frac{1}{E}\right)^{k_3 \beta_{f3}}$	k1: 3.75
$C = 10^M$	k2: 2.87
$M = 4.84 \left(\frac{V_b}{V_a + V_b} - 0.69\right)$	k3: 1.46
	Bf1: (5.014 * Pow(hac,-3.416)) * 1 + 0
	Bf2: 1.38
	Bf3: 0.88

AC Rutting

$\frac{\epsilon_p}{\epsilon_r} = k_z \beta_{r1} 10^{k_1 T} k_2 \beta_{r2} N^{k_3 B_{r3}}$ $k_z = (C_1 + C_2 * depth) * 0.328196^{depth}$ $C_1 = -0.1039 * H_\alpha^2 + 2.4868 * H_\alpha - 17.342$ $C_2 = 0.0172 * H_\alpha^2 - 1.7331 * H_\alpha + 27.428$ <p style="margin-top: 10px;"><i>Where:</i> H_{ac} = total AC thickness(in)</p>	ϵ_p = plastic strain(in/in) ϵ_r = resilient strain(in/in) T = layer temperature(°F) N = number of load repetitions
AC Rutting Standard Deviation	0.24 * Pow(RUT,0.8026) + 0.001
AC Layer 1	K1:-2.45 K2:3.01 K3:0.22 Br1:0.128 Br2:0.52 Br3:1.36
AC Layer 2	K1:-2.45 K2:3.01 K3:0.22 Br1:0.4 Br2:0.52 Br3:1.36

Thermal Fracture

$C_f = 400 * N \left(\frac{\log C / h_{ac}}{\sigma} \right)$ $\Delta C = (k * \beta t)^{n+1} * A * \Delta K^n$ $A = 10^{(4.389 - 2.52 * \log(E * \sigma_m * n))}$	C_f = observed amount of thermal cracking(ft/500ft) k = refression coefficient determined through field calibration $N()$ = standard normal distribution evaluated at() σ = standard deviation of the log of the depth of cracks in the pavments C = crack depth(in) h_{ac} = thickness of asphalt layer(in) ΔC = Change in the crack depth due to a cooling cycle ΔK = Change in the stress intensity factor due to a cooling cycle A, n = Fracture parameters for the asphalt mixture E = mixture stiffness σ_m = Undamaged mixture tensile strength β_t = Calibration parameter
Level 1 K: ((3 * Pow(10,-7)) * Pow(MAAT,4.0319)) * 1 + 0	Level 1 Standard Deviation: 0.14 * THERMAL + 168
Level 2 K: ((3 * Pow(10,-7)) * Pow(MAAT,4.0319)) * 1 + 0	Level 2 Standard Deviation: 0.20 * THERMAL + 168
Level 3 K: ((3 * Pow(10,-7)) * Pow(MAAT,4.0319)) * 1 + 0	Level 3 Standard Deviation: 0.289 * THERMAL + 168

CSM Fatigue

$N_f = 10^{\left(\frac{k_1 \beta_{c1} \left(\frac{\sigma_s}{M_r}\right)}{k_2 \beta_{c2}} \right)}$	N_f = number of repetitions to fatigue cracking σ_s = Tensile stress(psi) M_r = modulus of rupture(psi)
k1: 0.972	k2: 0.0825
Bc1: 1	Bc2: 1

Unbound Layer Rutting			
$\delta_a(N) = \beta_{s_1} k_1 \varepsilon_v h \left(\frac{\varepsilon_0}{\varepsilon_r} \right) \left e^{-\left(\frac{\rho}{N}\right)^\beta} \right $		δ_a = permanent deformation for the layer N = number of repetitions ε_v = average vertical strain(in/in) $\varepsilon_0, \beta, \rho$ = material properties ε_r = resilient strain(in/in)	
Base Rutting		Subgrade Rutting	
k1: 0.965	Bs1: 0.322	k1: 0.965	Bs1: 0.322
Standard Deviation (BASERUT) 0.1477 * Pow(BASERUT,0.6711) + 0.001		Standard Deviation (BASERUT) 0.1235 * Pow(SUBRUT,0.5012) + 0.001	

AC Cracking					
AC Top Down Cracking			AC Bottom Up Cracking		
$FC_{top} = \left(\frac{C_4}{1 + e^{(C_1 - C_2 * \log_{10}(Damage))}} \right) * 10.56$			$FC = \left(\frac{6000}{1 + e^{(C_1 * C'_1 + C_2 * C'_2 * \log_{10}(D * 100))}} \right) * \left(\frac{1}{60} \right)$		
			$C'_2 = -2.40874 - 39.748 * (1 + h_{ac})^{-2.856}$		
			$C'_1 = -2 * C'_2$		
c1: 7	c2: 3.5	c3: 0	c4: 1000	c1: 1.31	c2: (0.867 + 0.2583 * hac) * 1 + 0
c3: 6000					
Top down AC Cracking Standard Deviation			Bottom up AC Cracking Standard Deviation		
200 + 2300/(1+exp(1.072-2.1654*LOG10(TOP+0.0001)))			1.13 + 13/(1+exp(7.57-15.5*LOG10(BOTTOM+0.0001)))		

CSM Cracking				IRI Flexible Pavements			
$FC_{ctb} = C_1 + \frac{C_2}{1 + e^{C_3 - C_4 * \log_{10}(Damage)}}$				C1 - Rutting C3 - Transverse Crack C2 - Fatigue Crack C4 - Site Factors			
C1: 0	C2: 75	C3: 2	C4: 2	C1: 55	C2: 0.4	C3: 0.008	C4: 0.015
CSM Standard Deviation							
CTB*1							



LCC 400 Section Major Arterial 7500AADTT

File Name: C:\Users\admin\Desktop\Frank Ni\Major Arterial\7500 AADTT\combined average E\LCC 400 Section Major Arterial 7500AADTT.dgp



Design Inputs

Design Life: **25 years** Base construction: **May, 2021** Climate Data: **43.5, -80.625**
 Design Type: **FLEXIBLE** Pavement construction: **June, 2022** Sources (Lat/Lon)
 Traffic opening: **September, 2022**

Design Structure

Layer type	Material Type	Thickness(mm)
Flexible	Default asphalt concrete	40.0
Flexible	Default asphalt concrete	130.0
NonStabilized	A-1-a	150.0
NonStabilized	A-1-b	600.0
Subgrade	A-1-a	Semi-infinite

Volumetric at Construction:

Effective binder content (%)	11.8
Air voids (%)	7.0

Traffic

Age (year)	Heavy Trucks (cumulative)
2022 (initial)	7,500
2034 (12 years)	16,063,700
2047 (25 years)	37,255,500

Design Outputs

Distress Prediction Summary

Distress Type	Distress @ Specified Reliability		Reliability (%)		Criterion Satisfied?
	Target	Predicted	Target	Achieved	
Terminal IRI (m/km)	3.00	2.99	95.00	95.12	Pass
Permanent deformation - total pavement (mm)	10.00	7.35	95.00	99.99	Pass
AC bottom-up fatigue cracking (percent)	10.00	17.60	95.00	77.47	Fail
AC thermal cracking (m/km)	200.00	52.53	95.00	100.00	Pass
AC top-down fatigue cracking (m/km)	378.80	2766.41	95.00	0.03	Fail
Permanent deformation - AC only (mm)	6.00	3.35	95.00	100.00	Pass

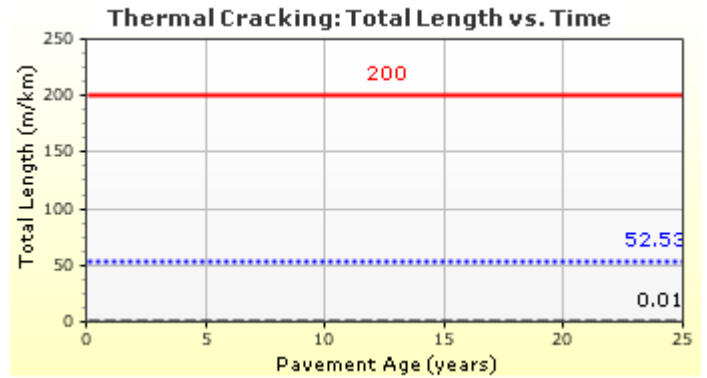
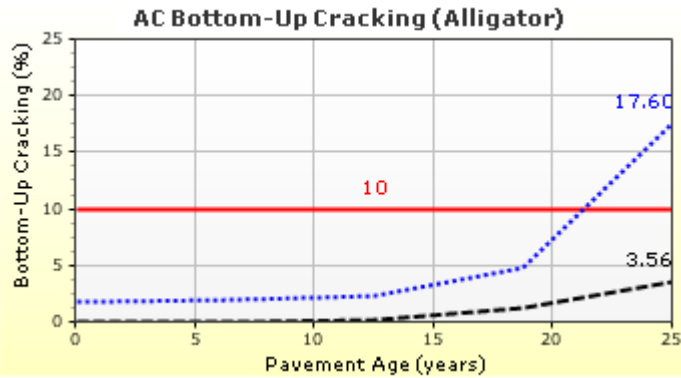
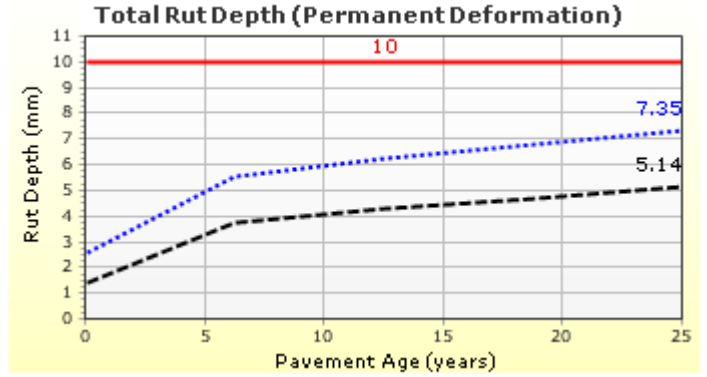
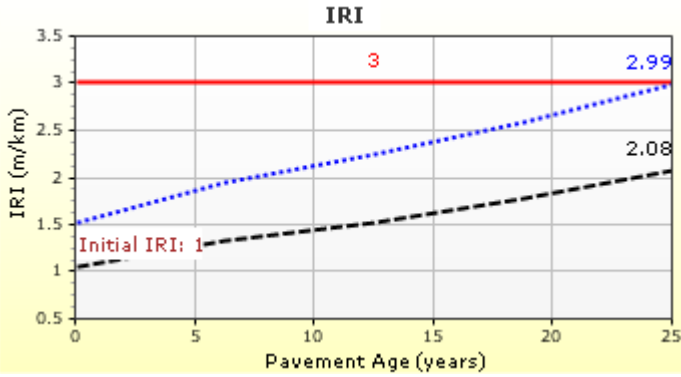


LCC 400 Section Major Arterial 7500AADTT

File Name: C:\Users\admin\Desktop\Frank Ni\Major Arterial\7500 AADTT\combined average E\LCC 400 Section Major Arterial 7500AADTT.dgpx



Distress Charts

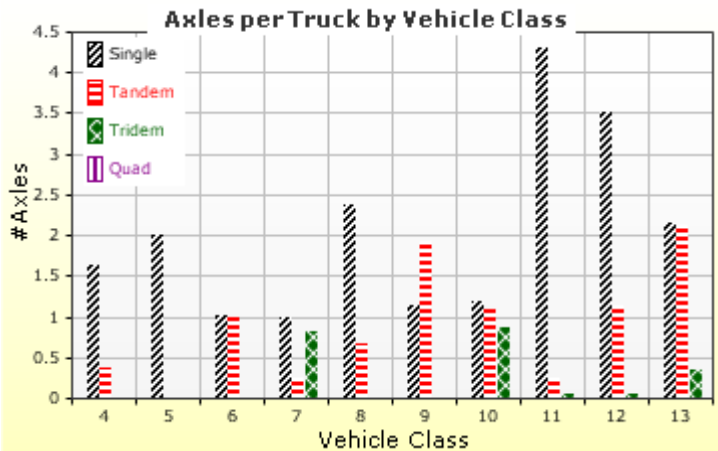
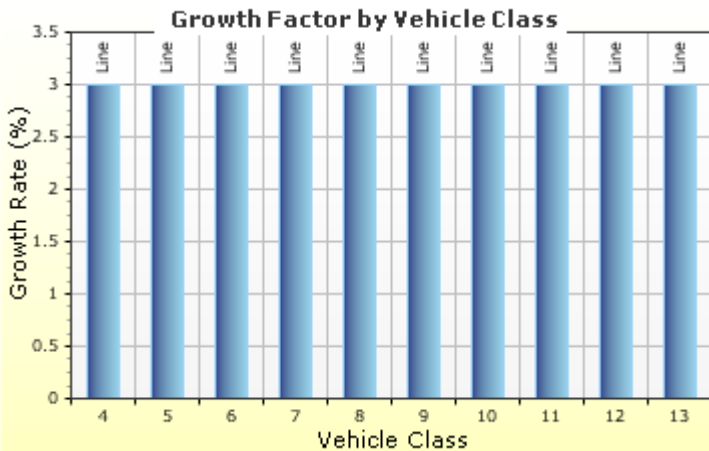
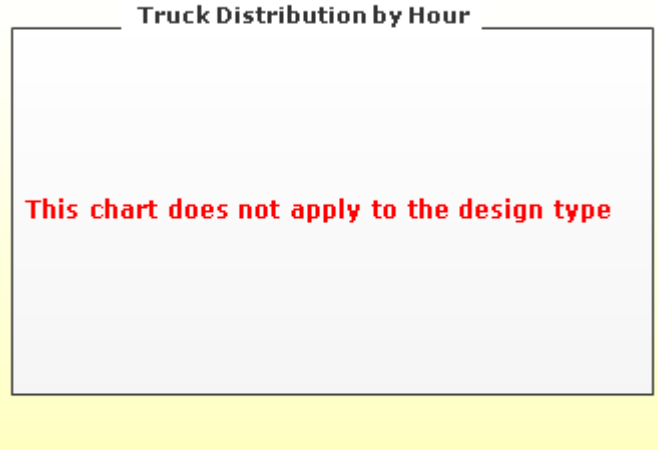
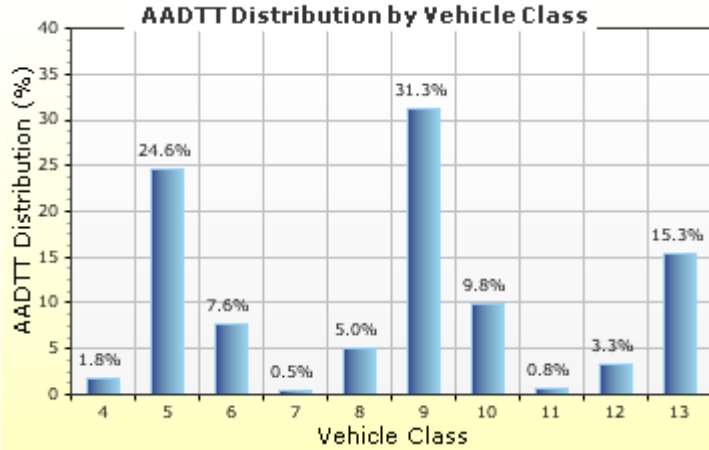


Traffic Inputs

Graphical Representation of Traffic Inputs

Initial two-way AADTT: **7,500**
 Number of lanes in design direction: **2**

Percent of trucks in design direction (%): **50.0**
 Percent of trucks in design lane (%): **80.0**
 Operational speed (kph): **100.0**



Traffic Volume Monthly Adjustment Factors





LCC 400 Section Major Arterial 7500AADTT

File Name: C:\Users\admin\Desktop\Frank Ni\Major Arterial\7500 AADTT\combined average E\LCC 400 Section Major Arterial 7500AADTT.dgp



Tabular Representation of Traffic Inputs

Volume Monthly Adjustment Factors

Level 3: Default MAF

Month	Vehicle Class									
	4	5	6	7	8	9	10	11	12	13
January	1.0	1.0	1.0	1.0	1.0	1.0	1.0	1.0	1.0	1.0
February	1.0	1.0	1.0	1.0	1.0	1.0	1.0	1.0	1.0	1.0
March	1.0	1.0	1.0	1.0	1.0	1.0	1.0	1.0	1.0	1.0
April	1.0	1.0	1.0	1.0	1.0	1.0	1.0	1.0	1.0	1.0
May	1.0	1.0	1.0	1.0	1.0	1.0	1.0	1.0	1.0	1.0
June	1.0	1.0	1.0	1.0	1.0	1.0	1.0	1.0	1.0	1.0
July	1.0	1.0	1.0	1.0	1.0	1.0	1.0	1.0	1.0	1.0
August	1.0	1.0	1.0	1.0	1.0	1.0	1.0	1.0	1.0	1.0
September	1.0	1.0	1.0	1.0	1.0	1.0	1.0	1.0	1.0	1.0
October	1.0	1.0	1.0	1.0	1.0	1.0	1.0	1.0	1.0	1.0
November	1.0	1.0	1.0	1.0	1.0	1.0	1.0	1.0	1.0	1.0
December	1.0	1.0	1.0	1.0	1.0	1.0	1.0	1.0	1.0	1.0

Distributions by Vehicle Class

Vehicle Class	AADTT Distribution (%) (Level 3)	Growth Factor	
		Rate (%)	Function
Class 4	1.8%	3%	Linear
Class 5	24.6%	3%	Linear
Class 6	7.6%	3%	Linear
Class 7	0.5%	3%	Linear
Class 8	5%	3%	Linear
Class 9	31.3%	3%	Linear
Class 10	9.8%	3%	Linear
Class 11	0.8%	3%	Linear
Class 12	3.3%	3%	Linear
Class 13	15.3%	3%	Linear

Truck Distribution by Hour does not apply

Axle Configuration

Traffic Wander	
Mean wheel location (mm)	460.0
Traffic wander standard deviation (mm)	254.0
Design lane width (m)	3.7

Axle Configuration	
Average axle width (m)	2.6
Dual tire spacing (mm)	305.0
Tire pressure (kPa)	827.4

Average Axle Spacing	
Tandem axle spacing (m)	1.3
Tridem axle spacing (m)	1.3
Quad axle spacing (m)	1.3

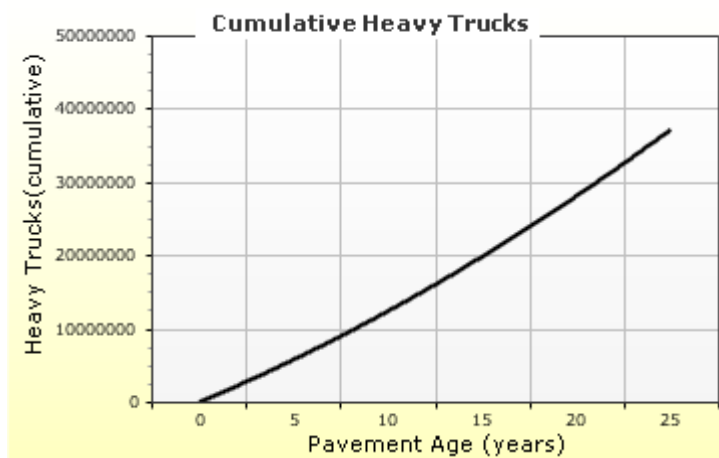
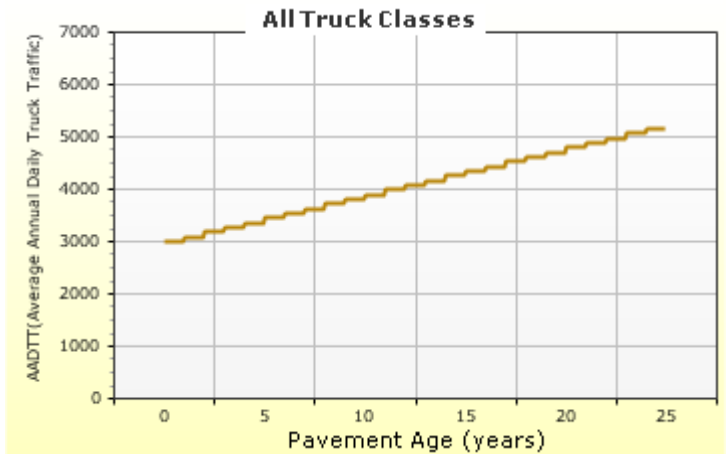
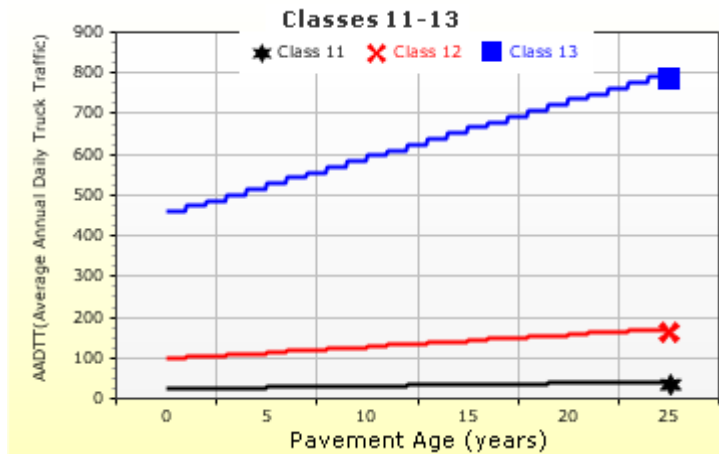
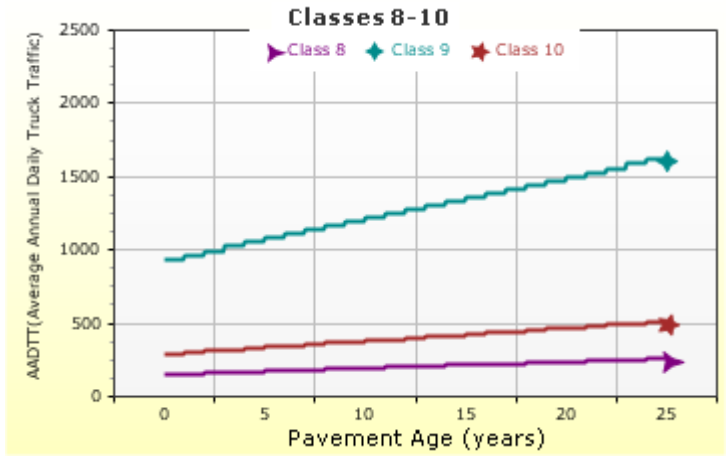
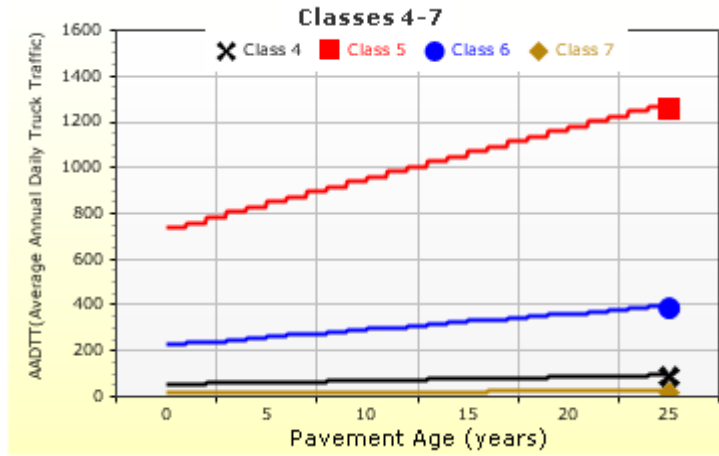
Wheelbase does not apply

Number of Axles per Truck

Vehicle Class	Single Axle	Tandem Axle	Tridem Axle	Quad Axle
Class 4	1.62	0.39	0	0
Class 5	2	0	0	0
Class 6	1.02	0.99	0	0
Class 7	1	0.26	0.83	0
Class 8	2.38	0.67	0	0
Class 9	1.13	1.93	0	0
Class 10	1.19	1.09	0.89	0
Class 11	4.29	0.26	0.06	0
Class 12	3.52	1.14	0.06	0
Class 13	2.15	2.13	0.35	0

AADTT (Average Annual Daily Truck Traffic) Growth

* Traffic cap is not enforced





LCC 400 Section Major Arterial 7500AADTT

File Name: C:\Users\admin\Desktop\Frank Ni\Major Arterial\7500 AADTT\combined average E\LCC 400 Section Major Arterial 7500AADTT.dgp



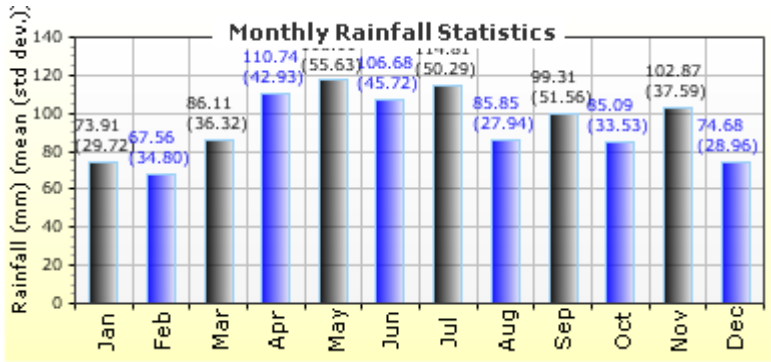
Climate Inputs

Climate Data Sources:

Climate Station Cities: Location (lat lon elevation(m))
 CA, ON 43.50000 -80.62500 369

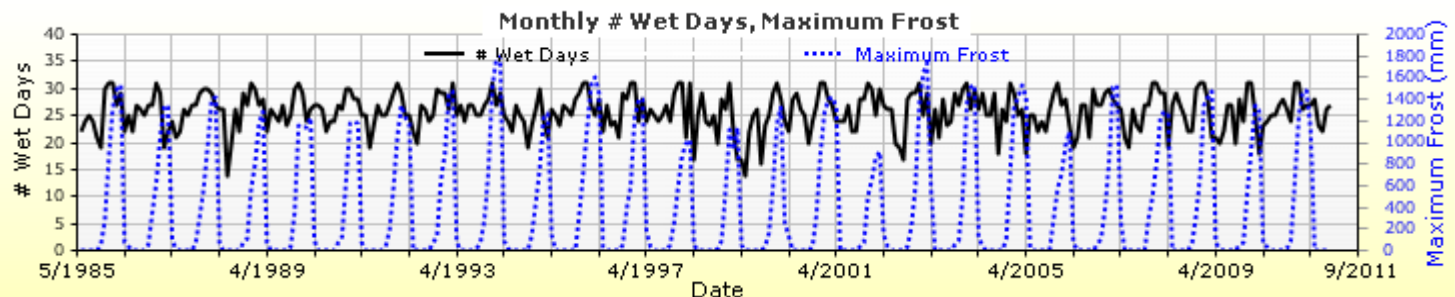
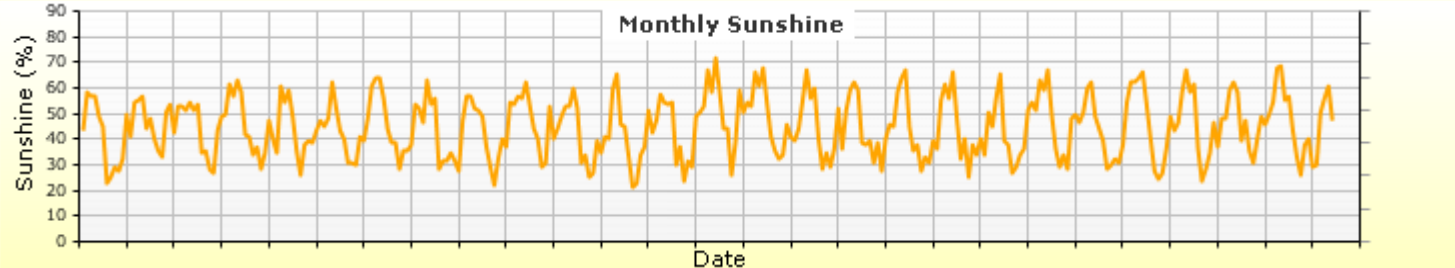
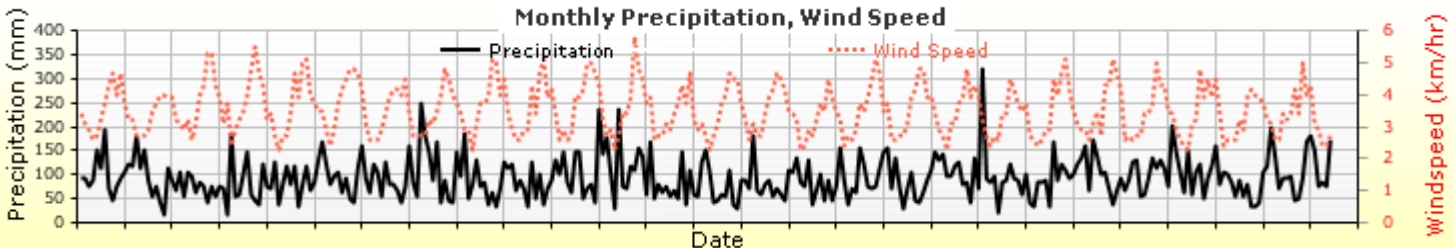
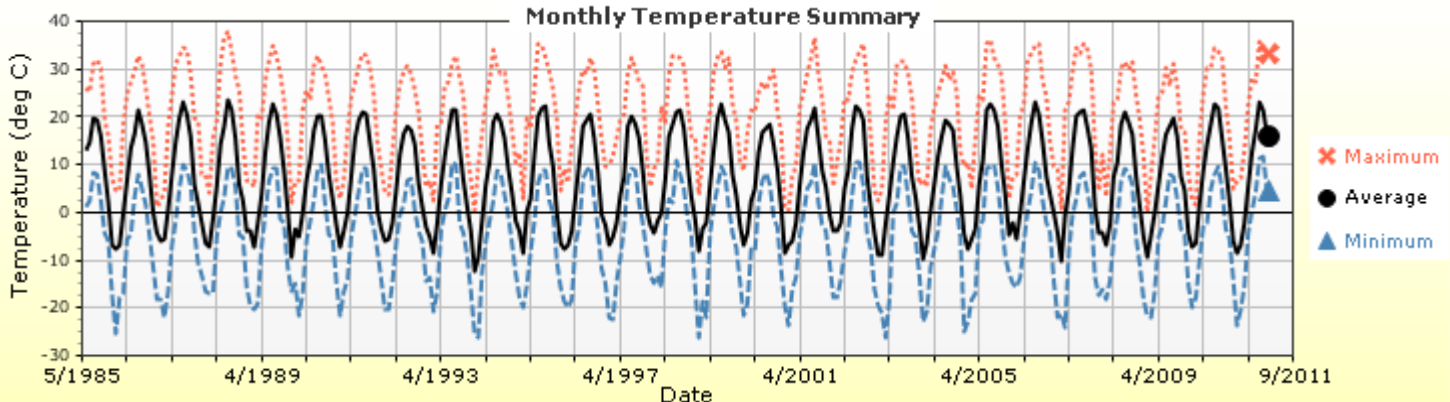
Annual Statistics:

Mean annual air temperature (°C) 7.46
 Mean annual precipitation (mm) 1127.76
 Freezing index (°C - days) 627.54
 Average annual number of freeze/thaw cycles: 87.25



Water table depth (m) 10.00

Monthly Climate Summary:



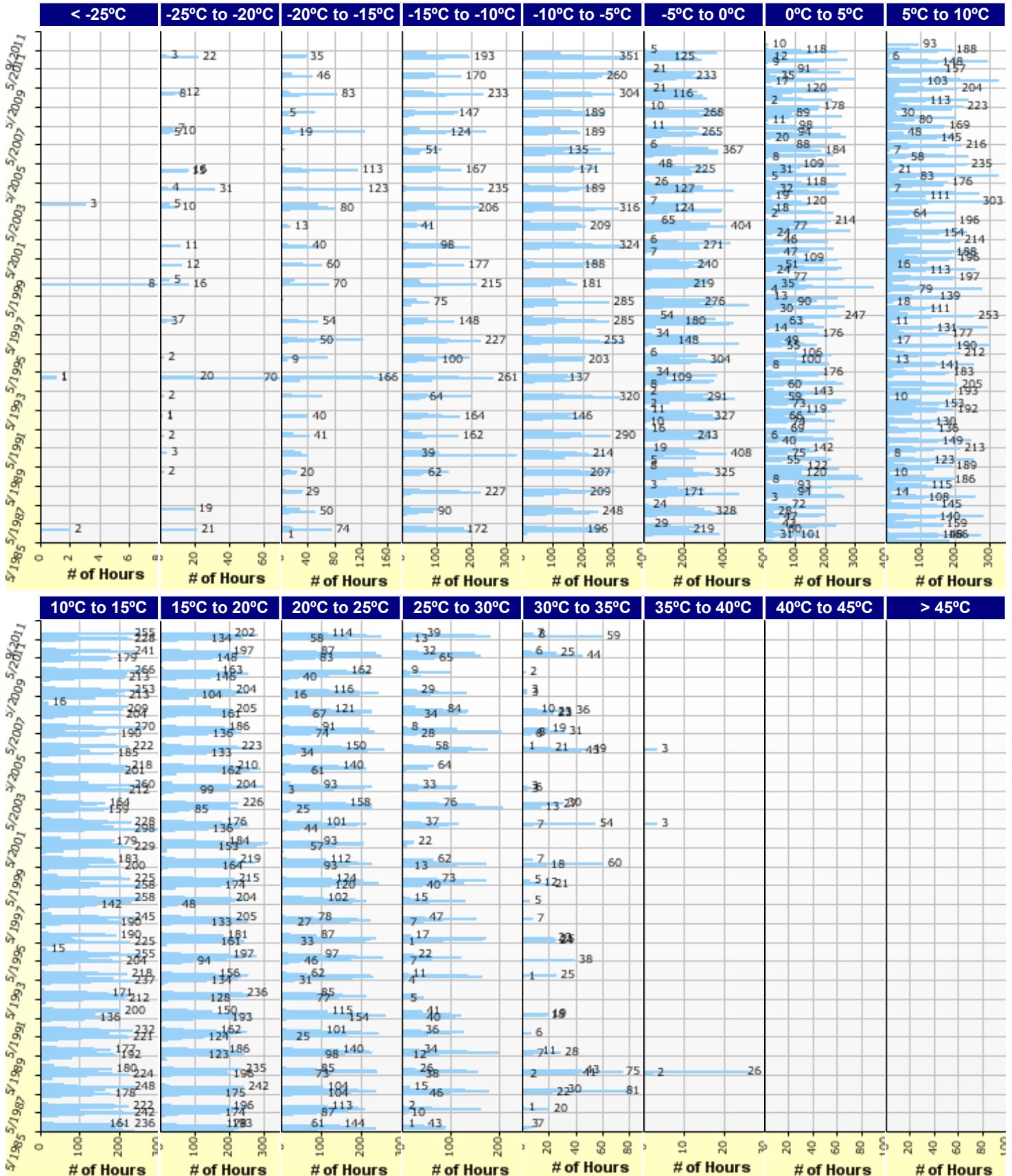


LCC 400 Section Major Arterial 7500AADTT

File Name: C:\Users\admin\Desktop\Frank Ni\Major Arterial\7500 AADTT\combined average E\LCC 400 Section Major Arterial 7500AADTT.dgp



Hourly Air Temperature Distribution by Month:





LCC 400 Section Major Arterial 7500AADTT

File Name: C:\Users\admin\Desktop\Frank Ni\Major Arterial\7500 AADTT\combined average E\LCC 400 Section Major Arterial 7500AADTT.dgpx



Design Properties

HMA Design Properties

Use Multilayer Rutting Model	False
Using G* based model (not nationally calibrated)	False
Is NCHRP 1-37A HMA Rutting Model Coefficients	True
Endurance Limit	-
Use Reflective Cracking	True

Structure - ICM Properties	
AC surface shortwave absorptivity	0.85

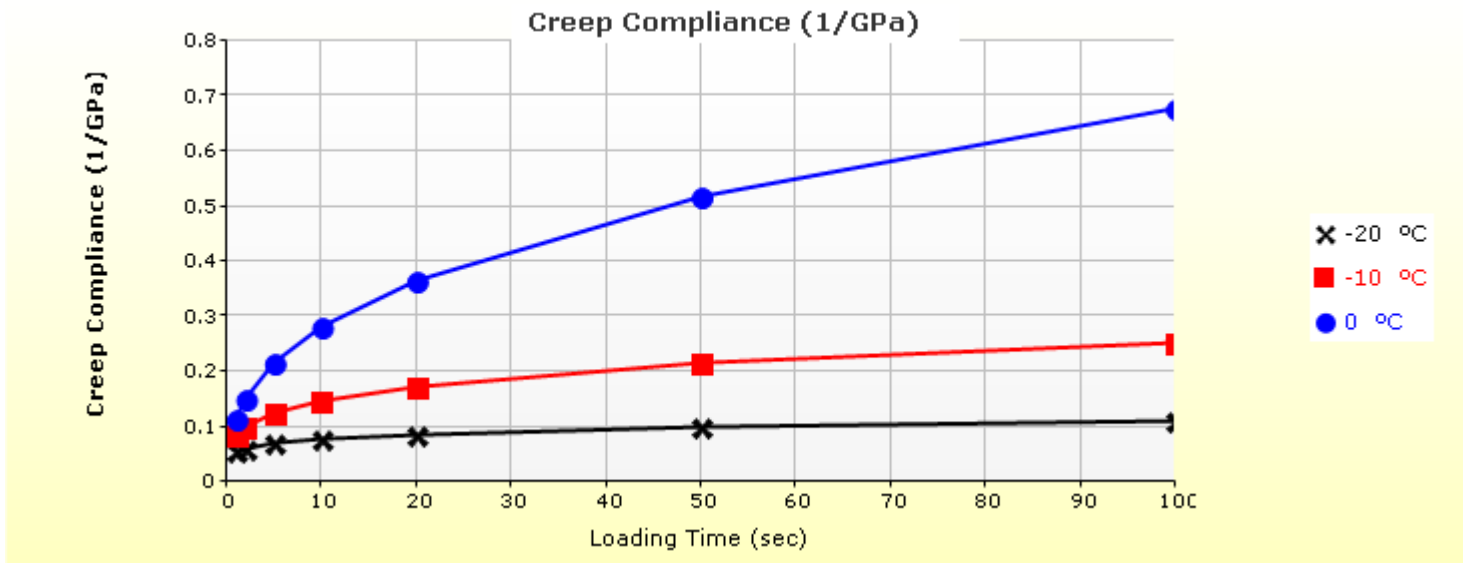
Layer Name	Layer Type	Interface Friction
Layer 1 Flexible : Default asphalt concrete	Flexible (1)	1.00
Layer 2 Flexible : Default asphalt concrete	Flexible (1)	1.00
Layer 3 Non-stabilized Base : A-1-a	Non-stabilized Base (4)	1.00
Layer 4 Non-stabilized Base : A-1-b	Non-stabilized Base (4)	1.00
Layer 5 Subgrade : A-1-a	Subgrade (5)	-

Thermal Cracking

Thermal Contraction	
Is thermal contraction calculated?	True
Mix coefficient of thermal contraction (mm/mm/°C)	-
Aggregate coefficient of thermal contraction (mm/mm/°C)	9.0e-006
Voids in Mineral Aggregate (%)	18.8

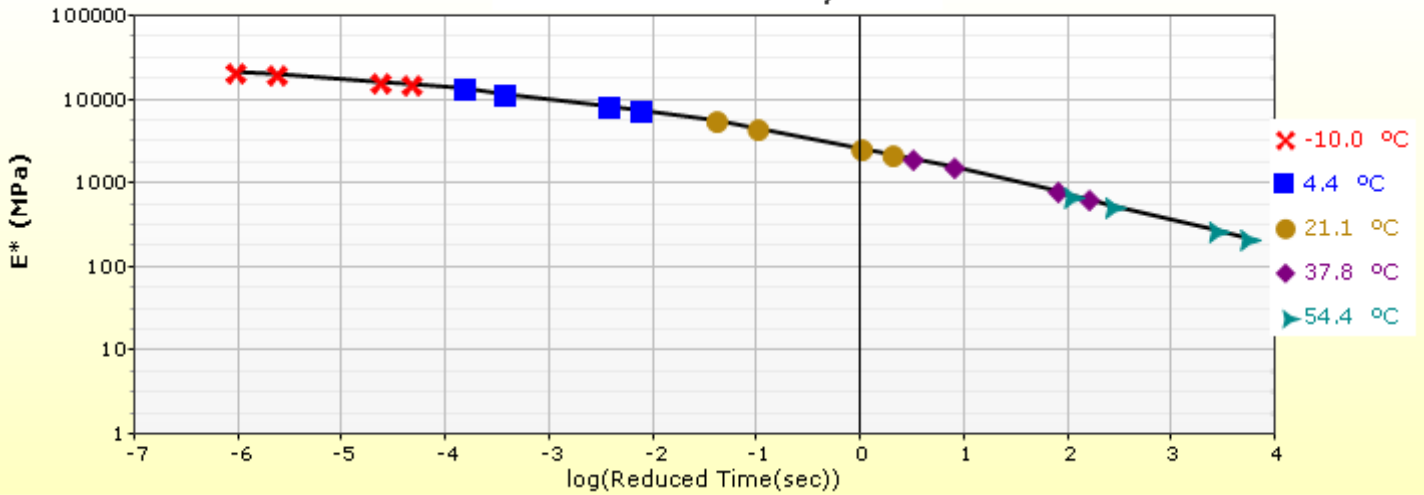
Indirect Tensile Strength (Input Level: 3)	
Test Temperature (°C)	Indirect Tensile Strength (Mpa)
-10.0	2.79

Creep Compliance (1/GPa) (Input Level: 3)			
Loading time (sec)	-20 °C	-10 °C	0 °C
1	5.57e-002	8.57e-002	1.16e-001
2	6.17e-002	1.01e-001	1.51e-001
5	7.07e-002	1.25e-001	2.15e-001
10	7.83e-002	1.48e-001	2.80e-001
20	8.68e-002	1.74e-001	3.65e-001
50	9.94e-002	2.16e-001	5.19e-001
100	1.10e-001	2.55e-001	6.77e-001

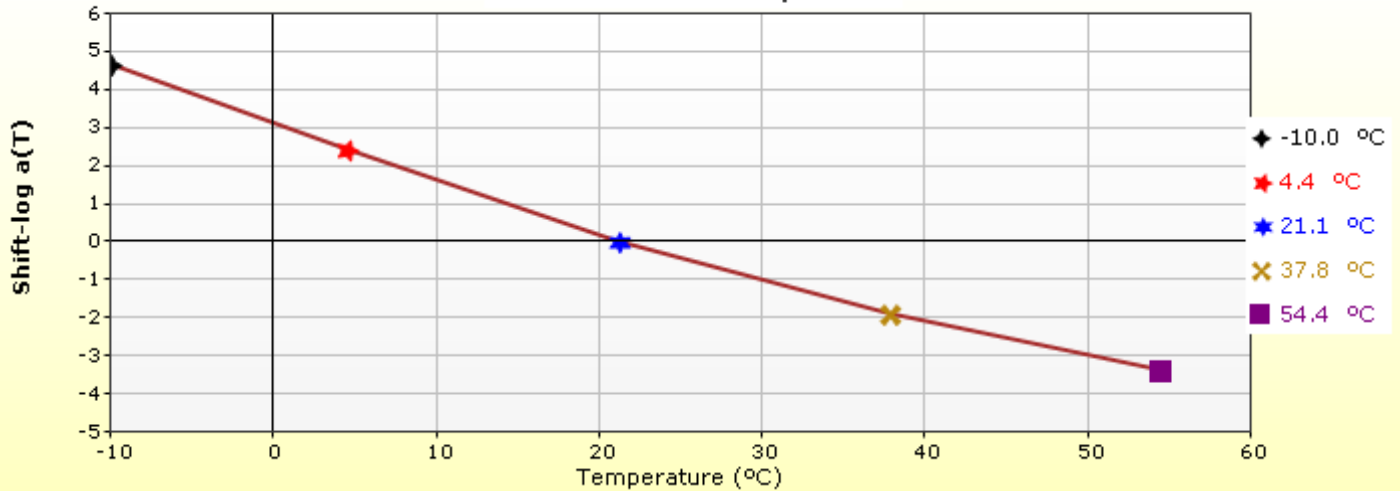


HMA Layer 1: Layer 1 Flexible : Default asphalt concrete

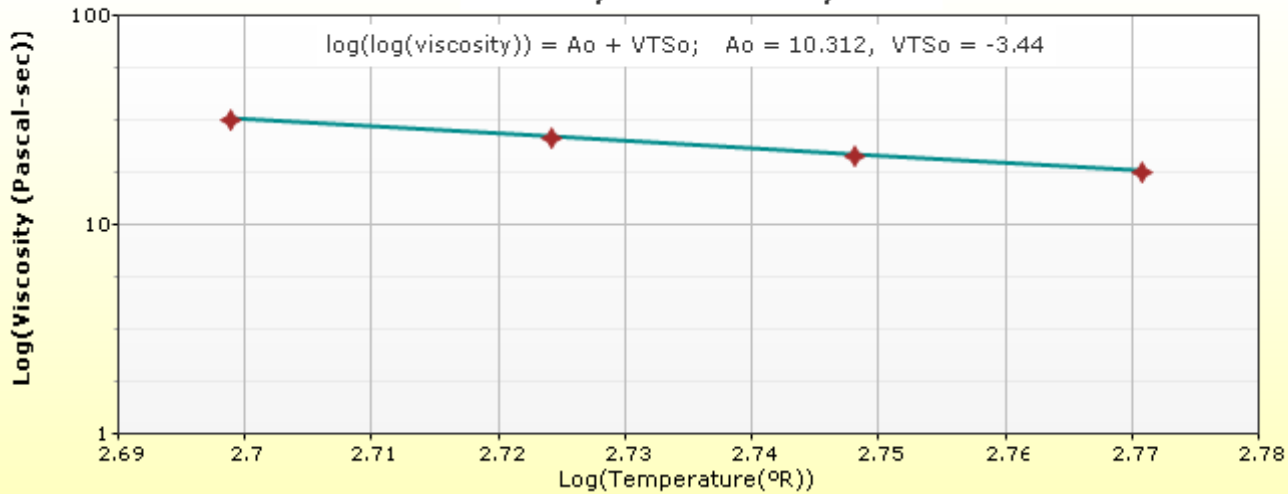
Master Curve HMA Layer 1



Shift Curve HMA Layer 1

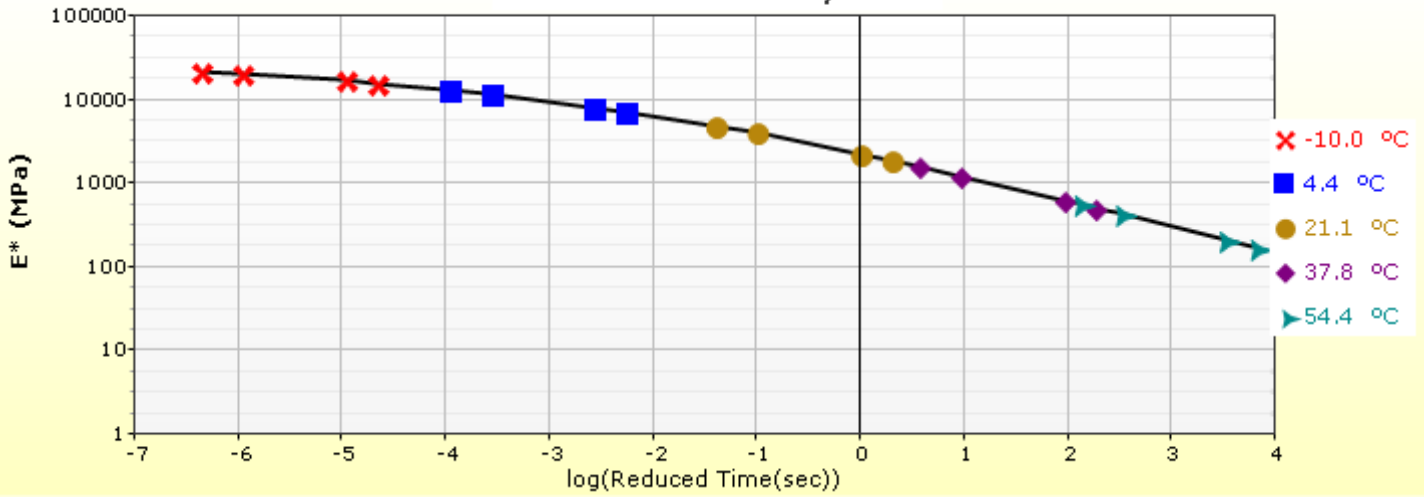


Viscosity Curve HMA Layer 1

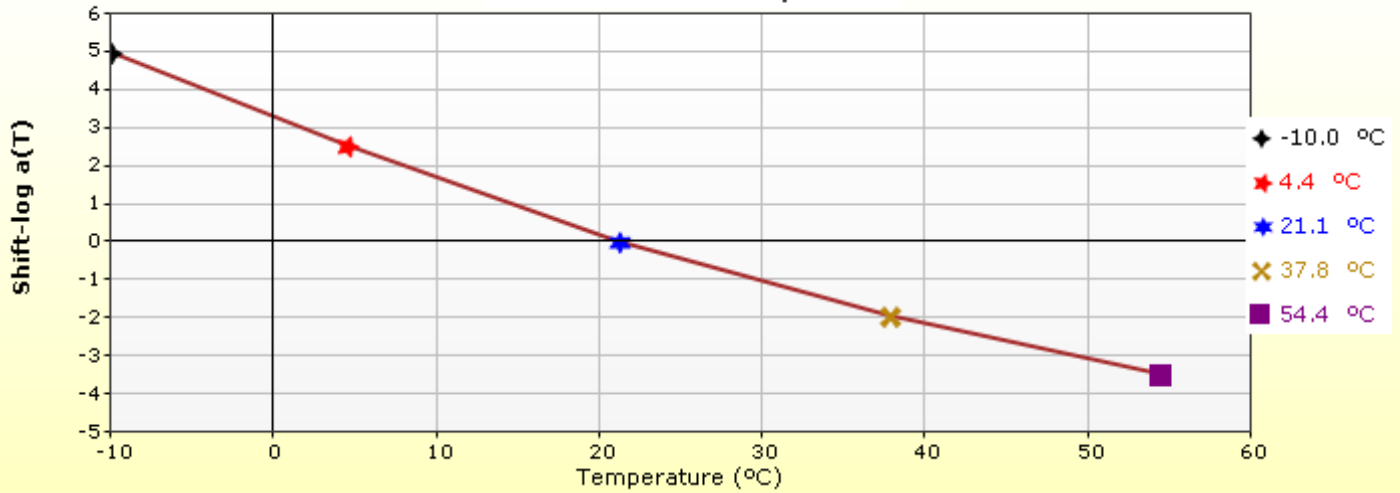


HMA Layer 2: Layer 2 Flexible : Default asphalt concrete

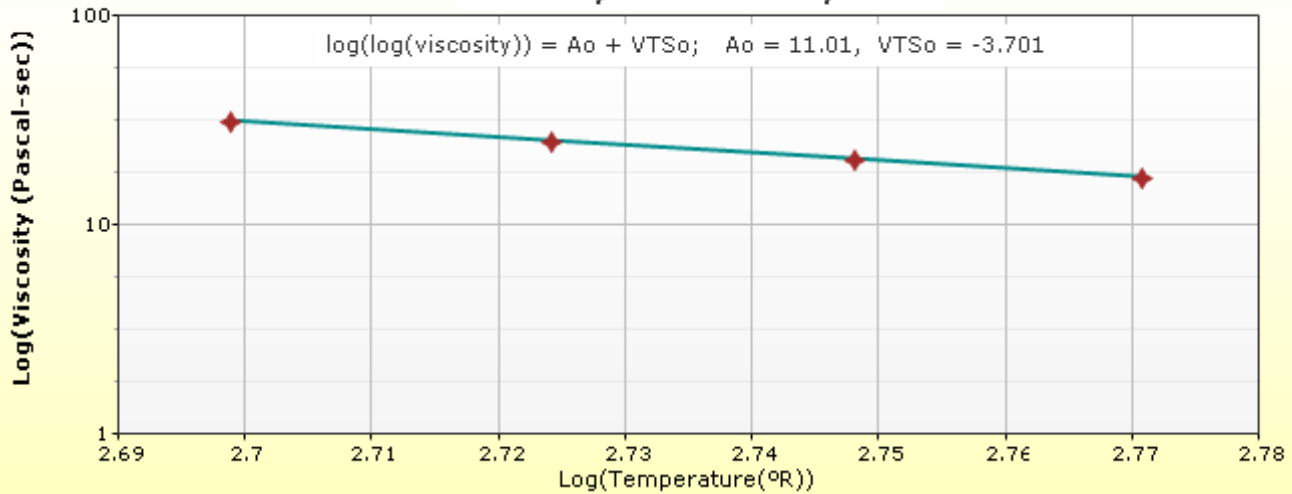
Master Curve HMA Layer 2



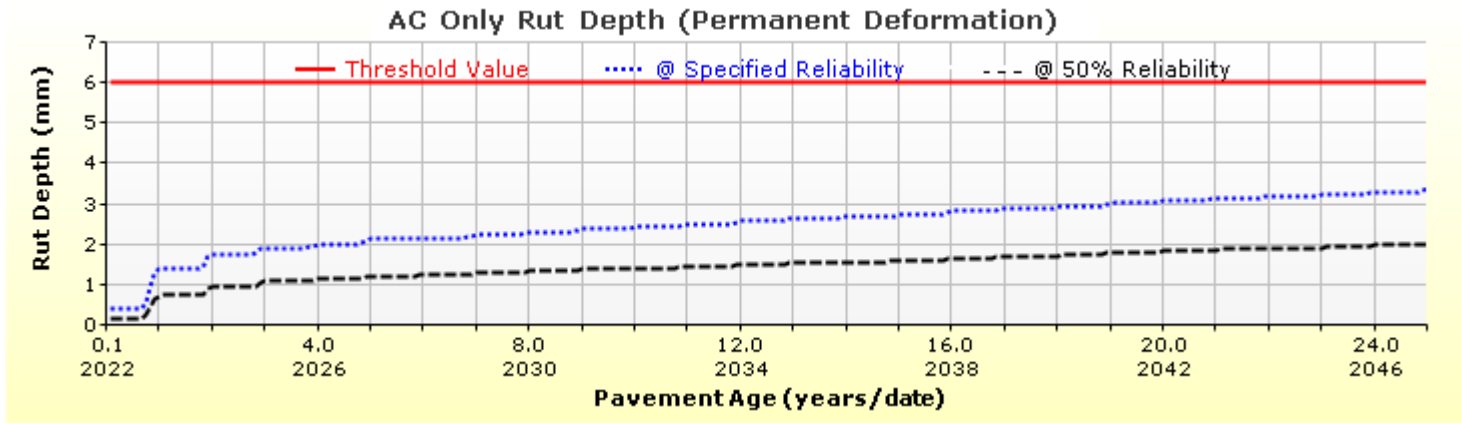
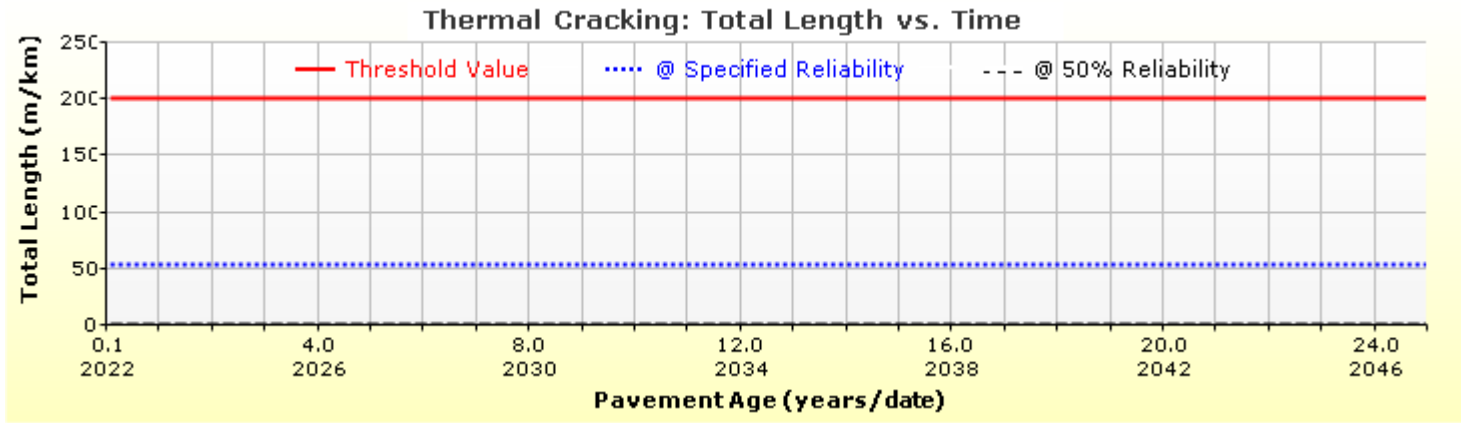
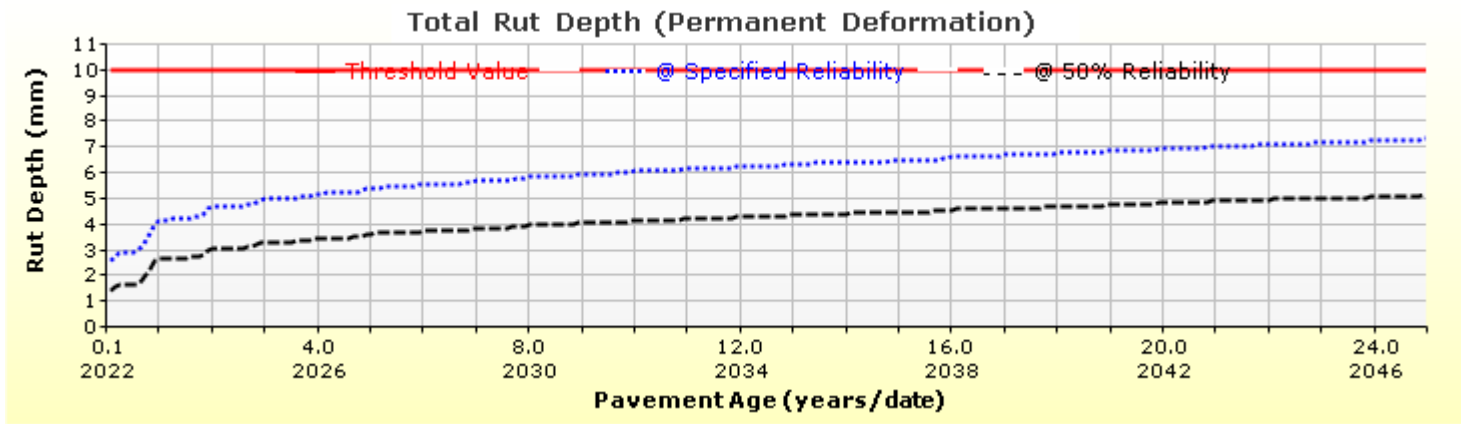
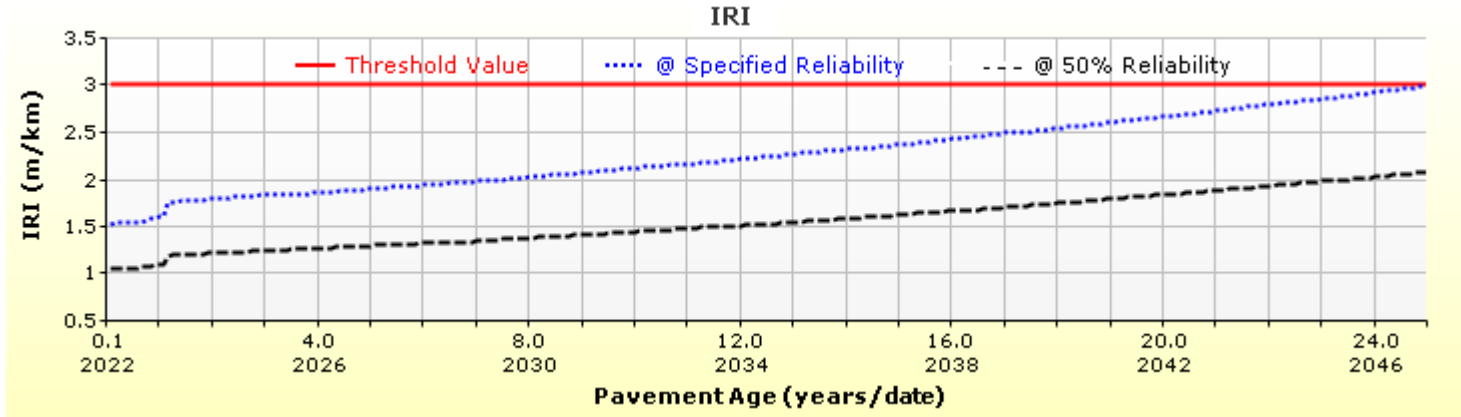
Shift Curve HMA Layer 2

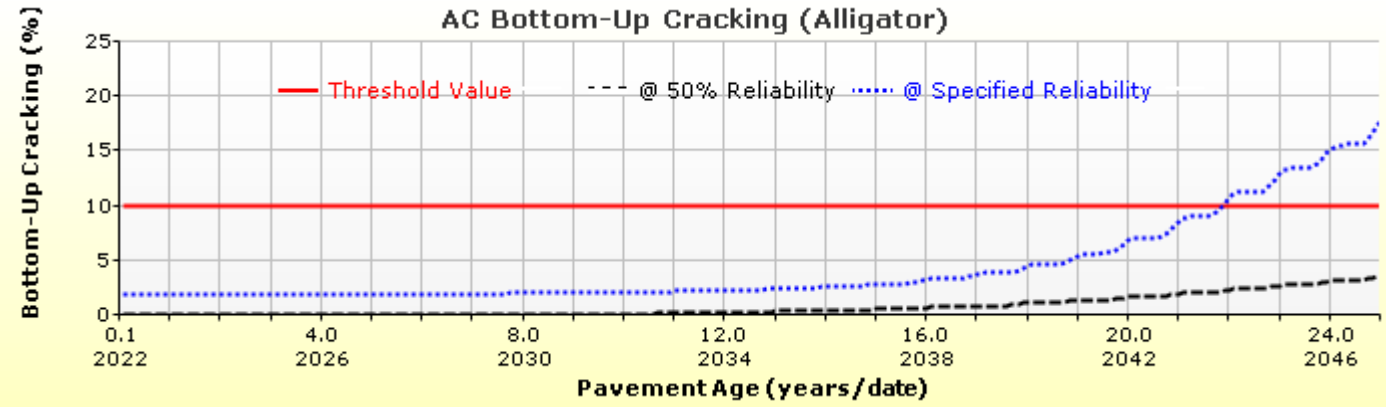
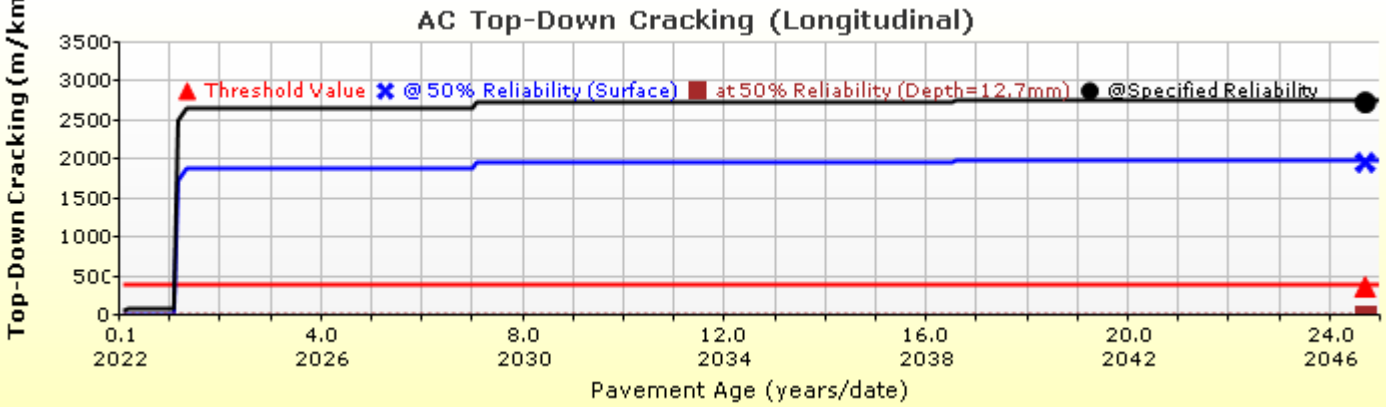
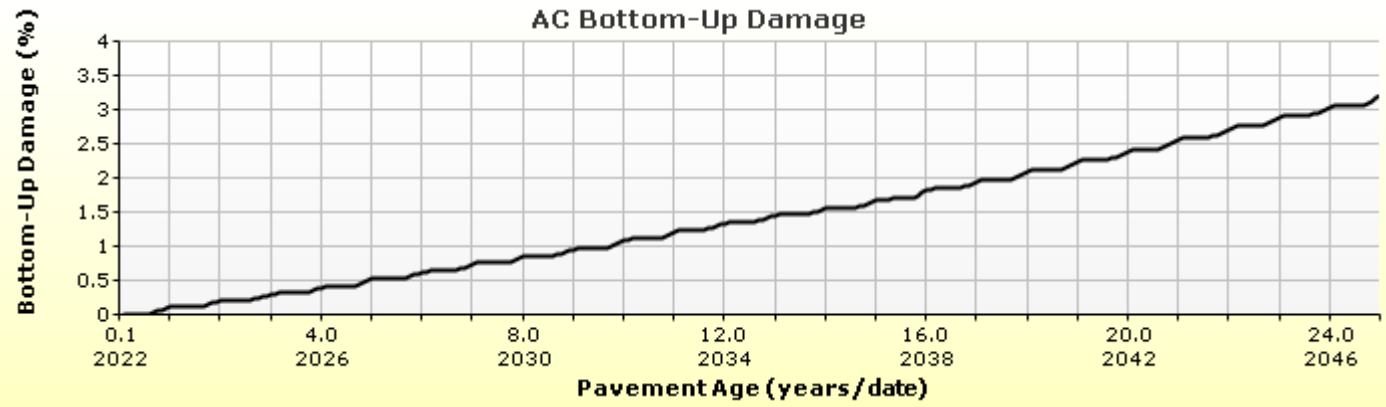
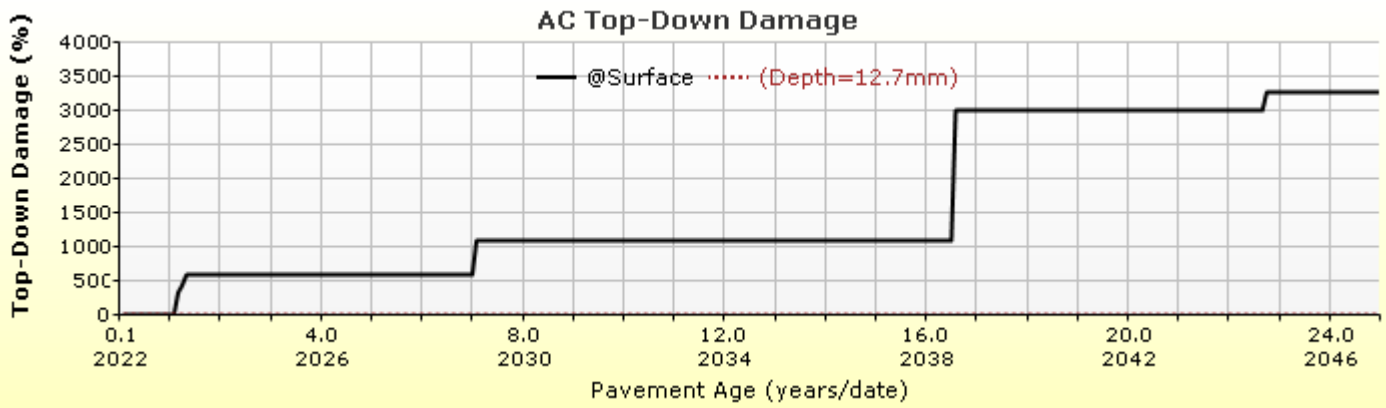


Viscosity Curve HMA Layer 2

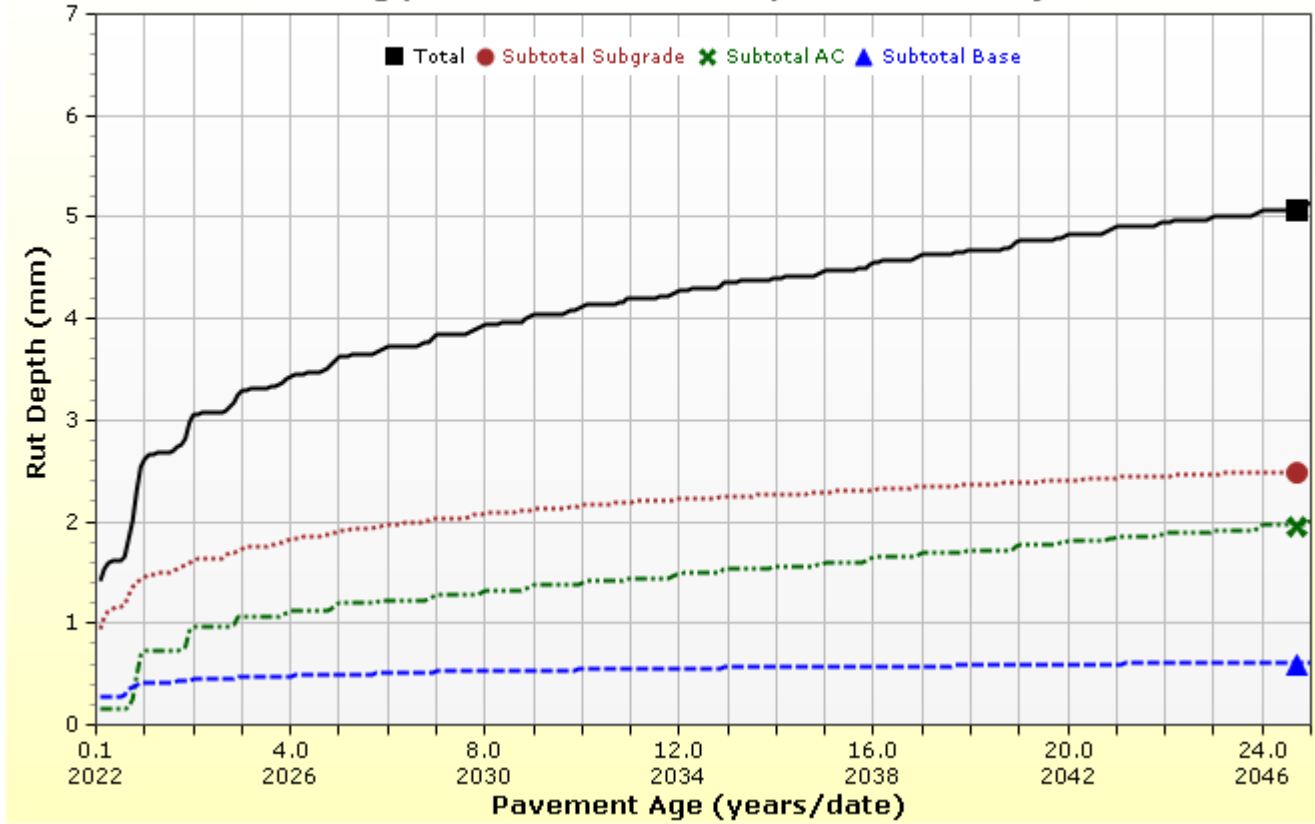


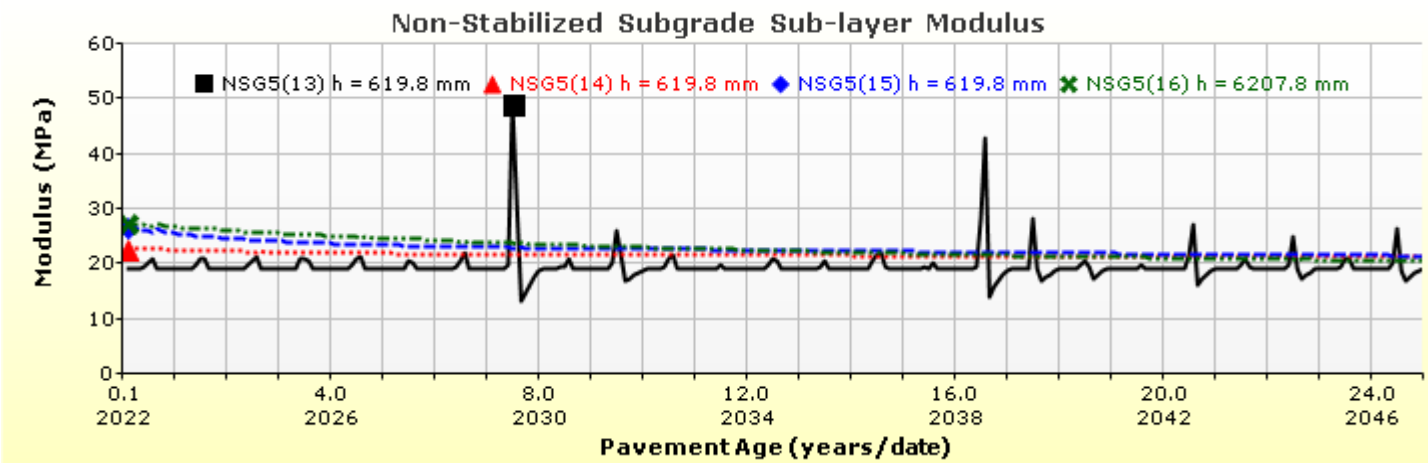
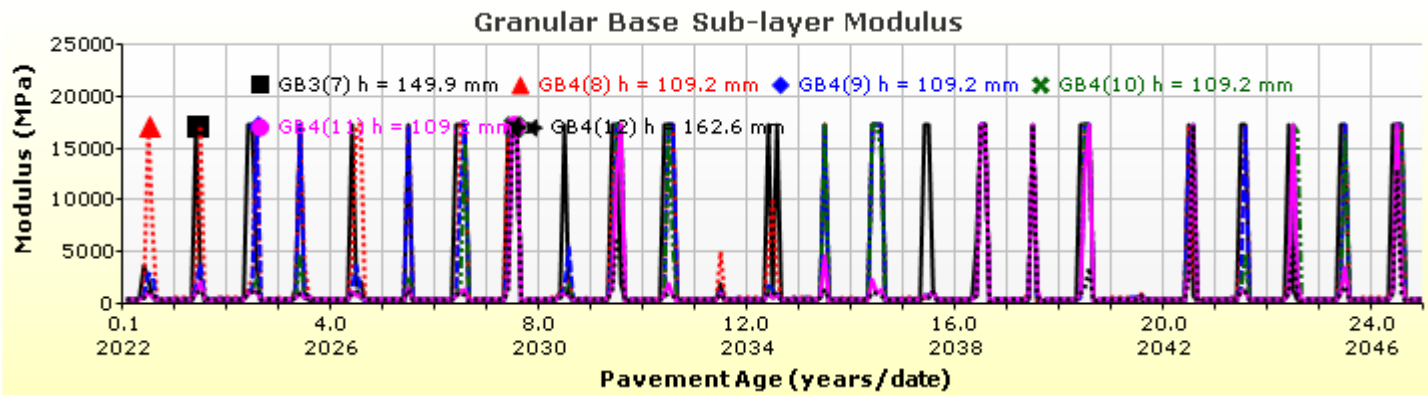
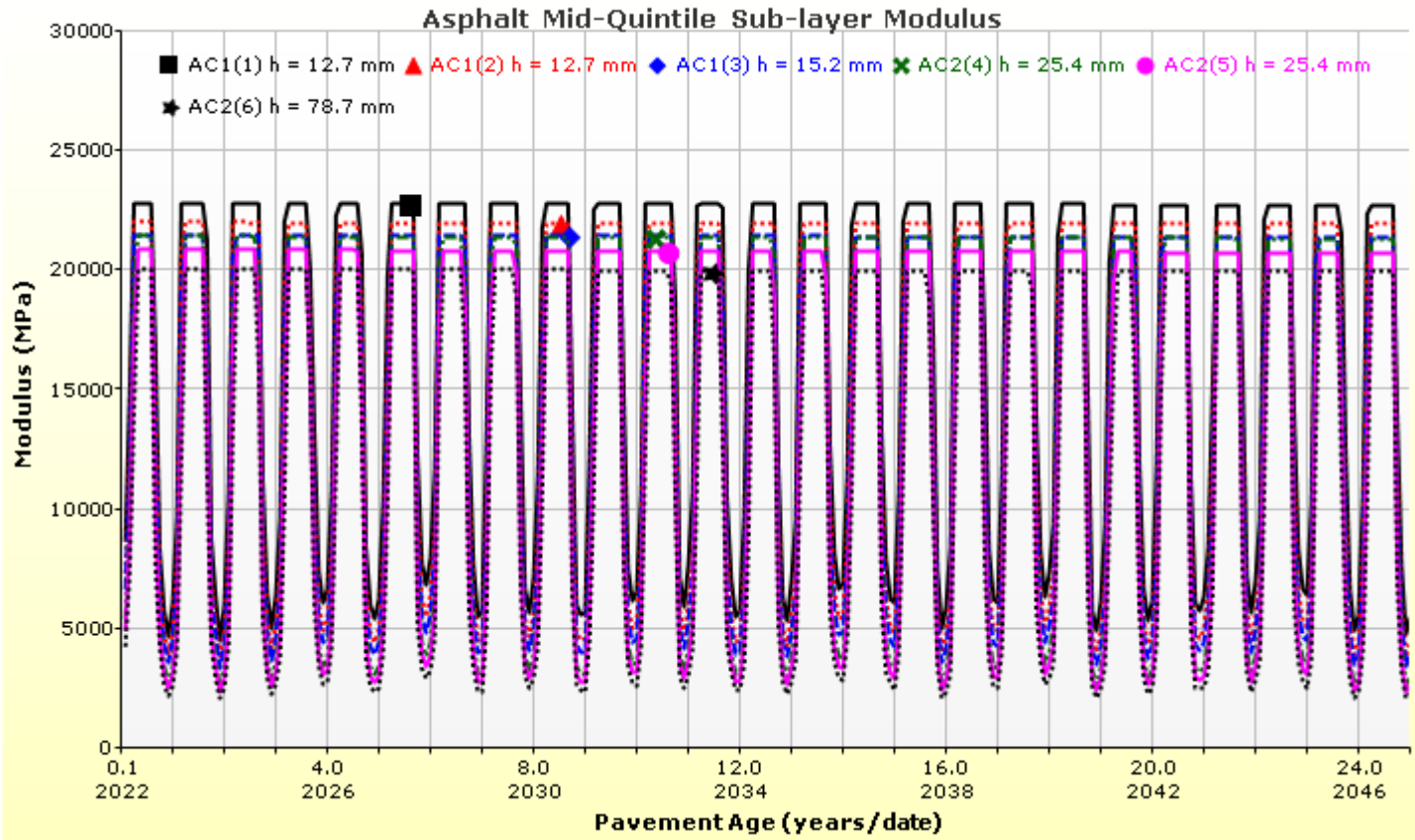
Analysis Output Charts





Rutting (Permanent Deformation) at 50% Reliability







LCC 400 Section Major Arterial 7500AADTT

File Name: C:\Users\admin\Desktop\Frank Ni\Major Arterial\7500 AADTT\combined average E\LCC 400 Section Major Arterial 7500AADTT.dgpx



Layer Information

Layer 1 Flexible : Default asphalt concrete

Asphalt		
Thickness (mm)	40.0	
Unit weight (kgf/m ³)	2390.0	
Poisson's ratio	Is Calculated?	False
	Ratio	0.35
	Parameter A	-
	Parameter B	-

Asphalt Dynamic Modulus (Input Level: 3)

Gradation	Percent Passing
19 mm sieve	100
9.5 mm sieve	77
4.75 mm sieve	60
0.075mm sieve	6

Asphalt Binder

Parameter	Value
Grade	Superpave Performance Grade
Binder Type	64-28
A	10.312
VTS	-3.44

General Info

Name	Value
Reference temperature (°C)	21.1
Effective binder content (%)	11.8
Air voids (%)	7
Thermal conductivity (watt/meter-kelvin)	1.16
Heat capacity (joule/kg-kelvin)	963

Identifiers

Field	Value
Display name/identifier	Default asphalt concrete
Description of object	
Author	
Date Created	9/16/2010 1:00:00 AM
Approver	
Date approved	9/16/2010 1:00:00 AM
State	
District	
County	
Highway	
Direction of Travel	
From station (km)	
To station (km)	
Province	
User defined field 1	
User defined field 2	
User defined field 3	
Revision Number	0



LCC 400 Section Major Arterial 7500AADTT

File Name: C:\Users\admin\Desktop\Frank Ni\Major Arterial\7500 AADTT\combined average E\LCC 400 Section Major Arterial 7500AADTT.dgpx



Layer 2 Flexible : Default asphalt concrete

Asphalt		
Thickness (mm)	130.0	
Unit weight (kg/m ³)	2460.0	
Poisson's ratio	Is Calculated?	False
	Ratio	0.35
	Parameter A	-
	Parameter B	-

Asphalt Dynamic Modulus (Input Level: 3)

Gradation	Percent Passing
19 mm sieve	100
9.5 mm sieve	77
4.75 mm sieve	60
0.075mm sieve	6

Asphalt Binder

Parameter	Value
Grade	Superpave Performance Grade
Binder Type	58-28
A	11.01
VTS	-3.701

General Info

Name	Value
Reference temperature (°C)	21.1
Effective binder content (%)	11.2
Air voids (%)	7
Thermal conductivity (watt/meter-kelvin)	1.16
Heat capacity (joule/kg-kelvin)	963

Identifiers

Field	Value
Display name/identifier	Default asphalt concrete
Description of object	
Author	
Date Created	9/16/2010 1:00:00 AM
Approver	
Date approved	9/16/2010 1:00:00 AM
State	
District	
County	
Highway	
Direction of Travel	
From station (km)	
To station (km)	
Province	
User defined field 1	
User defined field 2	
User defined field 3	
Revision Number	0

Layer 3 Non-stabilized Base : A-1-a

Unbound	
Layer thickness (mm)	150.0
Poisson's ratio	0.35
Coefficient of lateral earth pressure (k0)	0.5

Modulus (Input Level: 3)

Analysis Type:	Modify input values by temperature/moisture
Method:	Resilient Modulus (MPa)

Resilient Modulus (MPa)
250.0

Use Correction factor for NDT modulus?	-
NDT Correction Factor:	-

Identifiers

Field	Value
Display name/identifier	A-1-a
Description of object	Default material
Author	AASHTO
Date Created	1/1/2011 12:00:00 AM
Approver	
Date approved	1/1/2011 12:00:00 AM
State	
District	
County	
Highway	
Direction of Travel	
From station (km)	
To station (km)	
Province	
User defined field 1	
User defined field 2	
User defined field 3	
Revision Number	0

Sieve

Liquid Limit	6.0
Plasticity Index	0.0
Is layer compacted?	True

	Is User Defined?	Value
Maximum dry unit weight (kgf/m ³)	False	2038.2
Saturated hydraulic conductivity (m/hr)	False	2.376e-02
Specific gravity of solids	False	2.7
Water Content (%)	False	5.7

User-defined Soil Water Characteristic Curve (SWCC)

Is User Defined?	False
af	3.0201
bf	2.5984
cf	0.7539
hr	100.0000

Sieve Size	% Passing
0.001mm	
0.002mm	
0.020mm	
0.075mm	5.0
0.150mm	
0.180mm	
0.250mm	
0.300mm	13.5
0.425mm	
0.600mm	
0.850mm	
1.18mm	27.5
2.0mm	
2.36mm	
4.75mm	45.0
9.5mm	61.5
12.5mm	77.5
19.0mm	92.5
25.0mm	100.0
37.5mm	
50.0mm	
63.0mm	
75.0mm	
90.0mm	



LCC 400 Section Major Arterial 7500AADTT

File Name: C:\Users\admin\Desktop\Frank Ni\Major Arterial\7500 AADTT\combined average E\LCC 400 Section Major Arterial 7500AADTT.dgpx



Layer 4 Non-stabilized Base : A-1-b

Unbound	
Layer thickness (mm)	600.0
Poisson's ratio	0.25
Coefficient of lateral earth pressure (k0)	0.5

Modulus (Input Level: 3)

Analysis Type:	Modify input values by temperature/moisture
Method:	Resilient Modulus (MPa)

Resilient Modulus (MPa)
728.0

Use Correction factor for NDT modulus?	-
NDT Correction Factor:	-

Identifiers

Field	Value
Display name/identifier	A-1-b
Description of object	Default material
Author	AASHTO
Date Created	1/1/2011 12:00:00 AM
Approver	
Date approved	1/1/2011 12:00:00 AM
State	
District	
County	
Highway	
Direction of Travel	
From station (km)	
To station (km)	
Province	
User defined field 1	
User defined field 2	
User defined field 3	
Revision Number	0

Sieve

Liquid Limit	11.0
Plasticity Index	0.0
Is layer compacted?	True

	Is User Defined?	Value
Maximum dry unit weight (kgf/m ³)	False	2022.2
Saturated hydraulic conductivity (m/hr)	False	6.073e-02
Specific gravity of solids	False	2.7
Water Content (%)	False	7.3

User-defined Soil Water Characteristic Curve (SWCC)

Is User Defined?	False
af	6.8181
bf	1.6200
cf	0.8174
hr	100.0000

Sieve Size	% Passing
0.001mm	
0.002mm	
0.020mm	
0.075mm	5.0
0.150mm	
0.180mm	
0.250mm	
0.300mm	13.5
0.425mm	
0.600mm	
0.850mm	
1.18mm	25.0
2.0mm	
2.36mm	
4.75mm	37.5
9.5mm	
12.5mm	
19.0mm	
25.0mm	75.0
37.5mm	
50.0mm	
63.0mm	
75.0mm	
90.0mm	100.0



LCC 400 Section Major Arterial 7500AADTT

File Name: C:\Users\admin\Desktop\Frank Ni\Major Arterial\7500 AADTT\combined average E\LCC 400 Section Major Arterial 7500AADTT.dgpx



Layer 5 Subgrade : A-1-a

Unbound	
Layer thickness (mm)	Semi-infinite
Poisson's ratio	0.45
Coefficient of lateral earth pressure (k0)	0.5

Modulus (Input Level: 3)

Analysis Type:	Modify input values by temperature/moisture
Method:	Resilient Modulus (MPa)

Resilient Modulus (MPa)
30.0

Use Correction factor for NDT modulus?	-
NDT Correction Factor:	-

Identifiers

Field	Value
Display name/identifier	A-1-a
Description of object	Default Material
Author	AASHTO
Date Created	1/1/2011 12:00:00 AM
Approver	
Date approved	1/1/2011 12:00:00 AM
State	
District	
County	
Highway	
Direction of Travel	
From station (km)	
To station (km)	
Province	
User defined field 1	
User defined field 2	
User defined field 3	
Revision Number	0

Sieve

Liquid Limit	26.0
Plasticity Index	12.0
Is layer compacted?	True

	Is User Defined?	Value
Maximum dry unit weight (kgf/m ³)	False	1748.5
Saturated hydraulic conductivity (m/hr)	False	8.129e-06
Specific gravity of solids	False	2.7
Water Content (%)	False	16.8

User-defined Soil Water Characteristic Curve (SWCC)

Is User Defined?	False
af	106.7030
bf	0.6914
cf	0.2273
hr	500.0000

Sieve Size	% Passing
0.001mm	
0.002mm	30.0
0.020mm	
0.075mm	80.0
0.150mm	
0.180mm	84.0
0.250mm	
0.300mm	
0.425mm	91.0
0.600mm	
0.850mm	
1.18mm	
2.0mm	95.0
2.36mm	
4.75mm	97.0
9.5mm	99.0
12.5mm	100.0
19.0mm	100.0
25.0mm	100.0
37.5mm	
50.0mm	
63.0mm	
75.0mm	
90.0mm	

Calibration Coefficients

AC Fatigue

$N_f = 0.00432 * C * \beta_{f1} k_1 \left(\frac{1}{\epsilon_1}\right)^{k_2 \beta_{f2}} \left(\frac{1}{E}\right)^{k_3 \beta_{f3}}$ $C = 10^M$ $M = 4.84 \left(\frac{V_b}{V_a + V_b} - 0.69\right)$	k1: 3.75
	k2: 2.87
	k3: 1.46
	Bf1: (5.014 * Pow(hac,-3.416)) * 1 + 0
	Bf2: 1.38
	Bf3: 0.88

AC Rutting

$\frac{\epsilon_p}{\epsilon_r} = k_z \beta_{r1} 10^{k_1 T} k_2 \beta_{r2} N^{k_3 B_{r3}}$ $k_z = (C_1 + C_2 * depth) * 0.328196^{depth}$ $C_1 = -0.1039 * H_\alpha^2 + 2.4868 * H_\alpha - 17.342$ $C_2 = 0.0172 * H_\alpha^2 - 1.7331 * H_\alpha + 27.428$ <p>Where: H_{ac} = total AC thickness(in)</p>	ϵ_p = plastic strain(in/in) ϵ_r = resilient strain(in/in) T = layer temperature(°F) N = number of load repetitions
AC Rutting Standard Deviation	0.24 * Pow(RUT,0.8026) + 0.001
AC Layer 1	K1:-2.45 K2:3.01 K3:0.22 Br1:0.128 Br2:0.52 Br3:1.36
AC Layer 2	K1:-2.45 K2:3.01 K3:0.22 Br1:0.4 Br2:0.52 Br3:1.36

Thermal Fracture

$C_f = 400 * N \left(\frac{\log C / h_{ac}}{\sigma}\right)$ $\Delta C = (k * \beta t)^{n+1} * A * \Delta K^{-n}$ $A = 10^{(4.389 - 2.52 * \log(E * \sigma_m * n))}$	C_f = observed amount of thermal cracking(ft/500ft) k = refression coefficient determined through field calibration $N()$ = standard normal distribution evaluated at() σ = standard deviation of the log of the depth of cracks in the pavments C = crack depth(in) h_{ac} = thickness of asphalt layer(in) ΔC = Change in the crack depth due to a cooling cycle ΔK = Change in the stress intensity factor due to a cooling cycle A, n = Fracture parameters for the asphalt mixture E = mixture stiffness σ_m = Undamaged mixture tensile strength β_t = Calibration parameter
Level 1 K: ((3 * Pow(10,-7)) * Pow(MAAT,4.0319)) * 1 + 0	Level 1 Standard Deviation: 0.14 * THERMAL + 168
Level 2 K: ((3 * Pow(10,-7)) * Pow(MAAT,4.0319)) * 1 + 0	Level 2 Standard Deviation: 0.20 * THERMAL + 168
Level 3 K: ((3 * Pow(10,-7)) * Pow(MAAT,4.0319)) * 1 + 0	Level 3 Standard Deviation: 0.289 * THERMAL + 168

CSM Fatigue

$N_f = 10^{\left(\frac{k_1 \beta_{c1} \left(\frac{\sigma_s}{M_r}\right)}{k_2 \beta_{c2}}\right)}$	N_f = number of repetitions to fatigue cracking σ_s = Tensile stress(psi) M_r = modulus of rupture(psi)		
k1: 0.972	k2: 0.0825	Bc1: 1	Bc2: 1

Unbound Layer Rutting			
$\delta_a(N) = \beta_{s_1} k_1 \varepsilon_v h \left(\frac{\varepsilon_0}{\varepsilon_r} \right) \left e^{-\left(\frac{\rho}{N}\right)^\beta} \right $		$\delta_a =$ permanent deformation for the layer $N =$ number of repetitions $\varepsilon_v =$ average vertical strain(in/in) $\varepsilon_0, \beta, \rho =$ material properties $\varepsilon_r =$ resilient strain(in/in)	
Base Rutting		Subgrade Rutting	
k1: 0.965	Bs1: 0.322	k1: 0.965	Bs1: 0.322
Standard Deviation (BASERUT) 0.1477 * Pow(BASERUT,0.6711) + 0.001		Standard Deviation (BASERUT) 0.1235 * Pow(SUBRUT,0.5012) + 0.001	

AC Cracking			
AC Top Down Cracking		AC Bottom Up Cracking	
$FC_{top} = \left(\frac{C_4}{1 + e^{(C_1 - C_2 * \log_{10}(Damage))}} \right) * 10.56$		$FC = \left(\frac{6000}{1 + e^{(C_1 * C'_1 + C_2 * C'_2 * \log_{10}(D * 100))}} \right) * \left(\frac{1}{60} \right)$ $C'_2 = -2.40874 - 39.748 * (1 + h_{ac})^{-2.856}$ $C'_1 = -2 * C'_2$	
c1: 7	c2: 3.5	c3: 0	c4: 1000
c1: 1.31	c2: (0.867 + 0.2583 * hac) * 1 + 0	c3: 6000	
Top down AC Cracking Standard Deviation		Bottom up AC Cracking Standard Deviation	
200 + 2300/(1+exp(1.072-2.1654*LOG10(TOP+0.0001)))		1.13 + 13/(1+exp(7.57-15.5*LOG10(BOTTOM+0.0001)))	

CSM Cracking				IRI Flexible Pavements			
$FC_{ctb} = C_1 + \frac{C_2}{1 + e^{C_3 - C_4 * \log_{10}(Damage)}}$				C1 - Rutting		C3 - Transverse Crack	
				C2 - Fatigue Crack		C4 - Site Factors	
C1: 0	C2: 75	C3: 2	C4: 2	C1: 55	C2: 0.4	C3: 0.008	C4: 0.015
CSM Standard Deviation							
CTB*1							



LCC 475 Section Major Arterial 7500AADTT

File Name: C:\Users\admin\Desktop\Frank Ni\Major Arterial\7500 AADTT\combined average E\LCC 475 Section Major Arterial 7500AADTT.dgpx



Design Inputs

Design Life: **25 years** Base construction: **May, 2021** Climate Data: **43.5, -80.625**
 Design Type: **FLEXIBLE** Pavement construction: **June, 2022** Sources (Lat/Lon)
 Traffic opening: **September, 2022**

Design Structure

Layer type	Material Type	Thickness(mm)
Flexible	Default asphalt concrete	40.0
Flexible	Default asphalt concrete	130.0
NonStabilized	A-1-a	150.0
NonStabilized	A-1-b	600.0
Subgrade	A-1-a	Semi-infinite

Volumetric at Construction:	
Effective binder content (%)	11.8
Air voids (%)	7.0

Traffic

Age (year)	Heavy Trucks (cumulative)
2022 (initial)	7,500
2034 (12 years)	16,063,700
2047 (25 years)	37,255,500

Design Outputs

Distress Prediction Summary

Distress Type	Distress @ Specified Reliability		Reliability (%)		Criterion Satisfied?
	Target	Predicted	Target	Achieved	
Terminal IRI (m/km)	3.00	2.97	95.00	95.50	Pass
Permanent deformation - total pavement (mm)	10.00	7.10	95.00	99.99	Pass
AC bottom-up fatigue cracking (percent)	10.00	11.00	95.00	92.71	Fail
AC thermal cracking (m/km)	200.00	52.53	95.00	100.00	Pass
AC top-down fatigue cracking (m/km)	378.80	2766.75	95.00	0.03	Fail
Permanent deformation - AC only (mm)	6.00	3.41	95.00	100.00	Pass

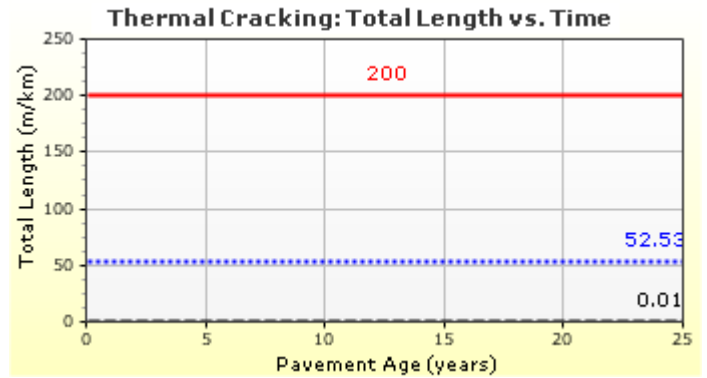
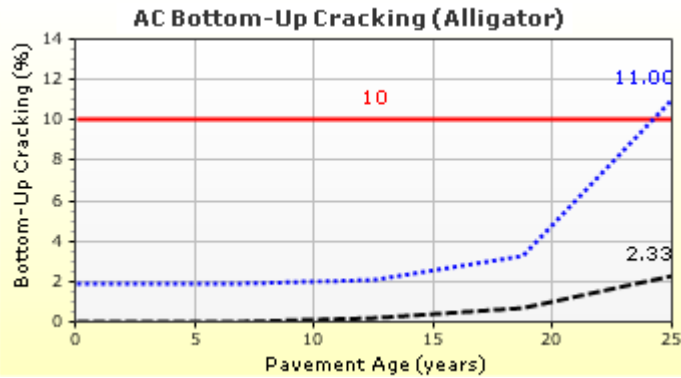
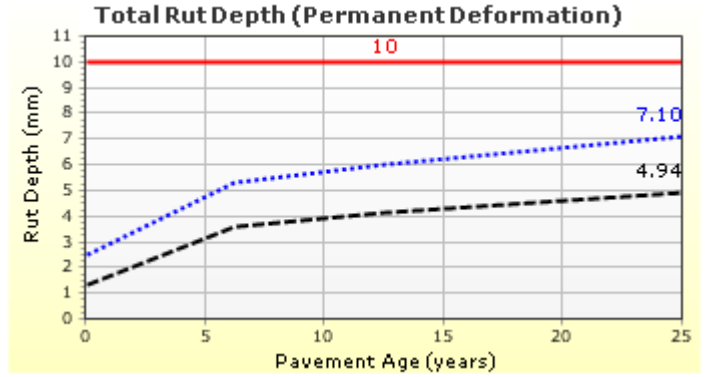
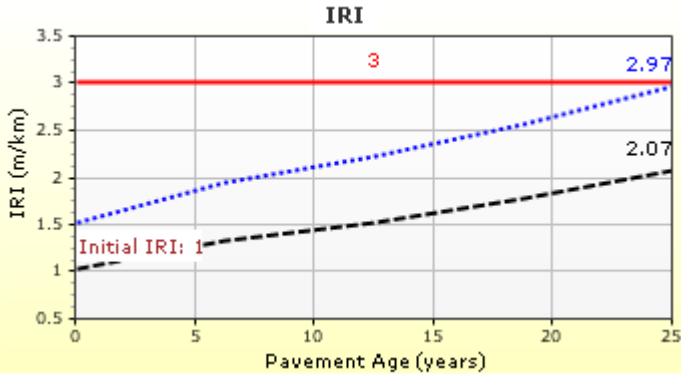


LCC 475 Section Major Arterial 7500AADTT

File Name: C:\Users\admin\Desktop\Frank Ni\Major Arterial\7500 AADTT\combined average E\LCC 475 Section Major Arterial 7500AADTT.dgpx



Distress Charts

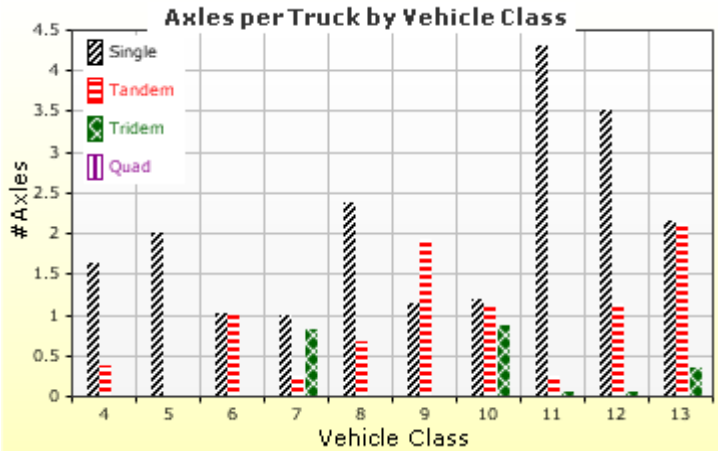
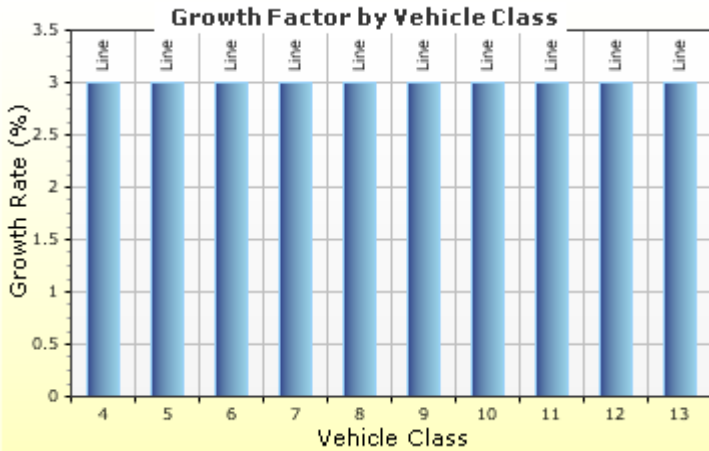
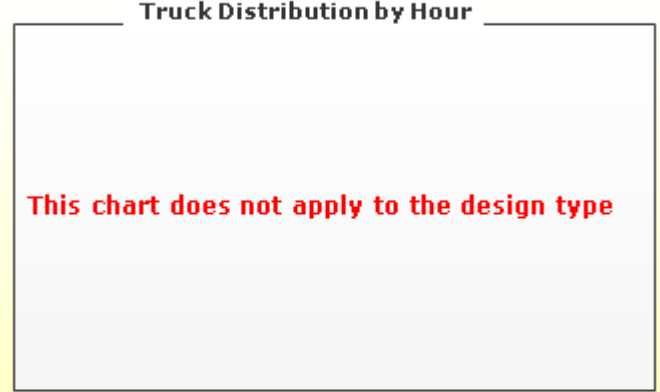
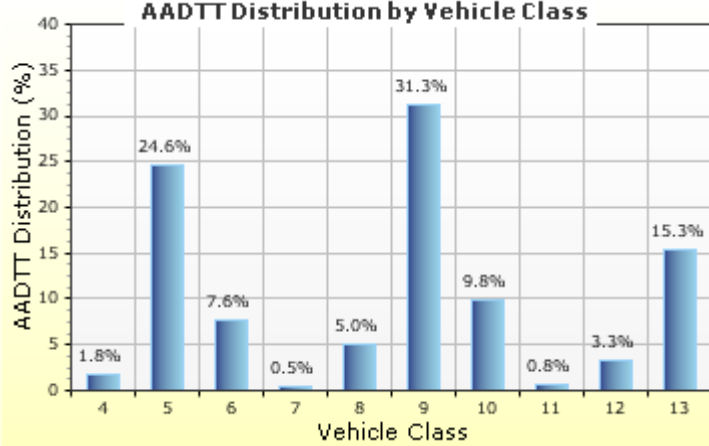


Traffic Inputs

Graphical Representation of Traffic Inputs

Initial two-way AADTT: **7,500**
 Number of lanes in design direction: **2**

Percent of trucks in design direction (%): **50.0**
 Percent of trucks in design lane (%): **80.0**
 Operational speed (kph): **100.0**



Traffic Volume Monthly Adjustment Factors





LCC 475 Section Major Arterial 7500AADTT

File Name: C:\Users\admin\Desktop\Frank Ni\Major Arterial\7500 AADTT\combined average E\LCC 475 Section Major Arterial 7500AADTT.dgp



Tabular Representation of Traffic Inputs

Volume Monthly Adjustment Factors

Level 3: Default MAF

Month	Vehicle Class									
	4	5	6	7	8	9	10	11	12	13
January	1.0	1.0	1.0	1.0	1.0	1.0	1.0	1.0	1.0	1.0
February	1.0	1.0	1.0	1.0	1.0	1.0	1.0	1.0	1.0	1.0
March	1.0	1.0	1.0	1.0	1.0	1.0	1.0	1.0	1.0	1.0
April	1.0	1.0	1.0	1.0	1.0	1.0	1.0	1.0	1.0	1.0
May	1.0	1.0	1.0	1.0	1.0	1.0	1.0	1.0	1.0	1.0
June	1.0	1.0	1.0	1.0	1.0	1.0	1.0	1.0	1.0	1.0
July	1.0	1.0	1.0	1.0	1.0	1.0	1.0	1.0	1.0	1.0
August	1.0	1.0	1.0	1.0	1.0	1.0	1.0	1.0	1.0	1.0
September	1.0	1.0	1.0	1.0	1.0	1.0	1.0	1.0	1.0	1.0
October	1.0	1.0	1.0	1.0	1.0	1.0	1.0	1.0	1.0	1.0
November	1.0	1.0	1.0	1.0	1.0	1.0	1.0	1.0	1.0	1.0
December	1.0	1.0	1.0	1.0	1.0	1.0	1.0	1.0	1.0	1.0

Distributions by Vehicle Class

Vehicle Class	AADTT Distribution (%) (Level 3)	Growth Factor	
		Rate (%)	Function
Class 4	1.8%	3%	Linear
Class 5	24.6%	3%	Linear
Class 6	7.6%	3%	Linear
Class 7	0.5%	3%	Linear
Class 8	5%	3%	Linear
Class 9	31.3%	3%	Linear
Class 10	9.8%	3%	Linear
Class 11	0.8%	3%	Linear
Class 12	3.3%	3%	Linear
Class 13	15.3%	3%	Linear

Truck Distribution by Hour does not apply

Axle Configuration

Traffic Wander	
Mean wheel location (mm)	460.0
Traffic wander standard deviation (mm)	254.0
Design lane width (m)	3.7

Axle Configuration	
Average axle width (m)	2.6
Dual tire spacing (mm)	305.0
Tire pressure (kPa)	827.4

Average Axle Spacing	
Tandem axle spacing (m)	1.3
Tridem axle spacing (m)	1.3
Quad axle spacing (m)	1.3

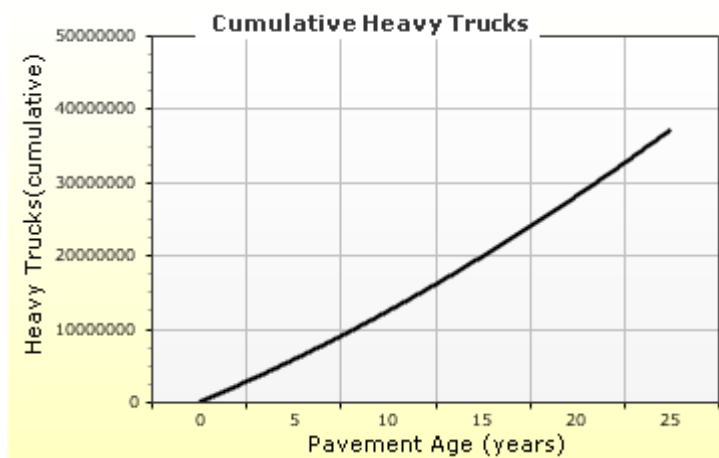
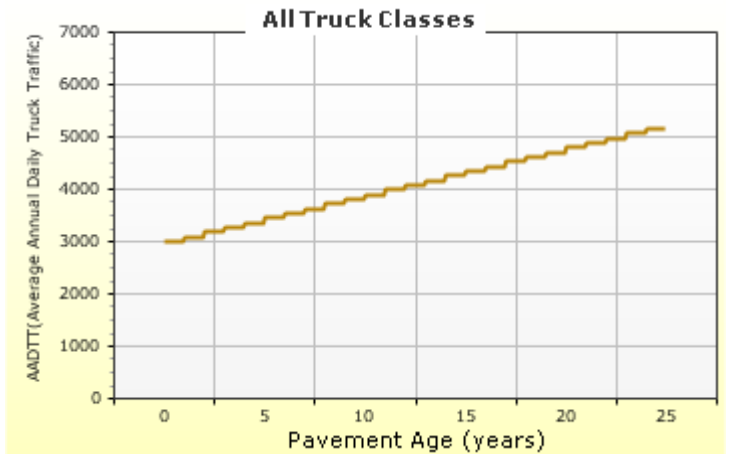
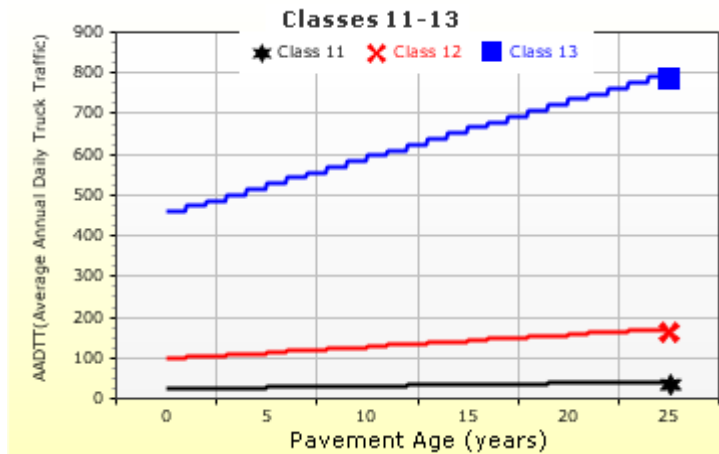
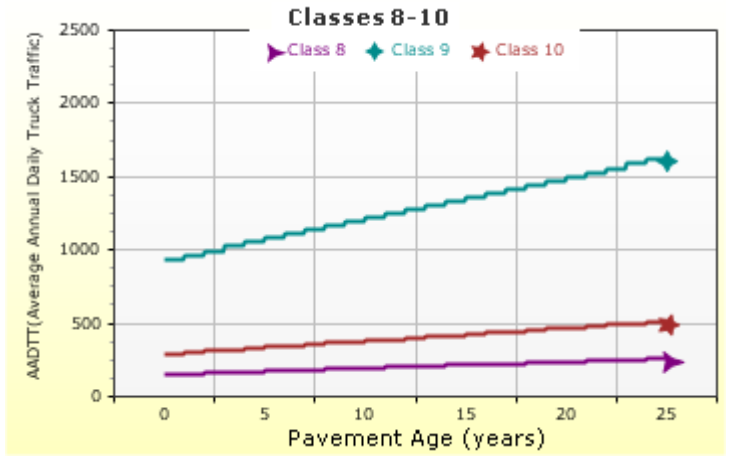
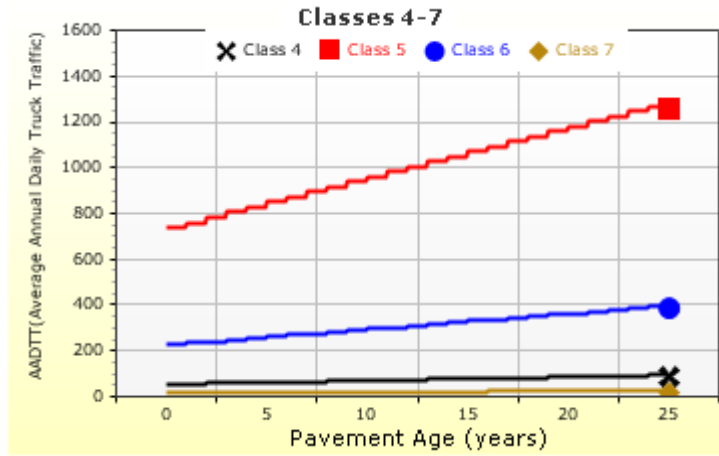
Wheelbase does not apply

Number of Axles per Truck

Vehicle Class	Single Axle	Tandem Axle	Tridem Axle	Quad Axle
Class 4	1.62	0.39	0	0
Class 5	2	0	0	0
Class 6	1.02	0.99	0	0
Class 7	1	0.26	0.83	0
Class 8	2.38	0.67	0	0
Class 9	1.13	1.93	0	0
Class 10	1.19	1.09	0.89	0
Class 11	4.29	0.26	0.06	0
Class 12	3.52	1.14	0.06	0
Class 13	2.15	2.13	0.35	0

AADTT (Average Annual Daily Truck Traffic) Growth

* Traffic cap is not enforced





LCC 475 Section Major Arterial 7500AADTT

File Name: C:\Users\admin\Desktop\Frank Ni\Major Arterial\7500 AADTT\combined average E\LCC 475 Section Major Arterial 7500AADTT.dgp



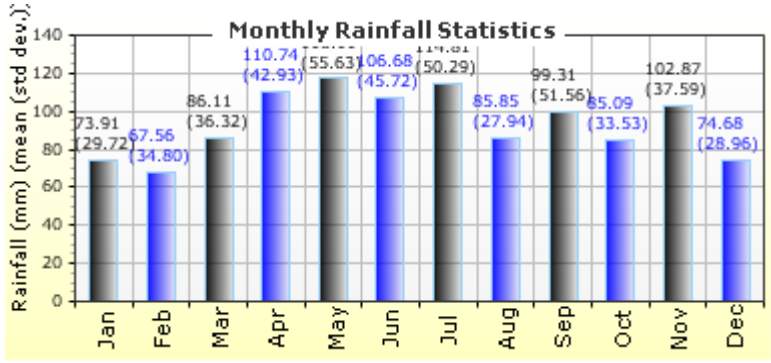
Climate Inputs

Climate Data Sources:

Climate Station Cities: Location (lat lon elevation(m))
 CA, ON 43.50000 -80.62500 369

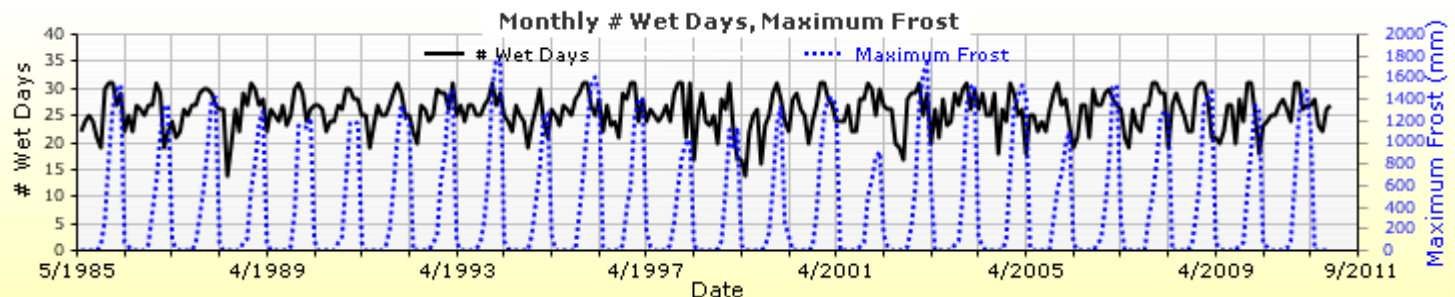
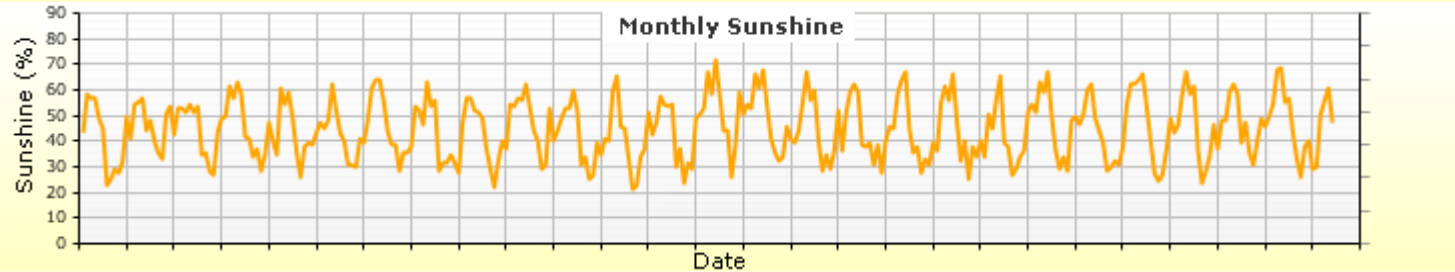
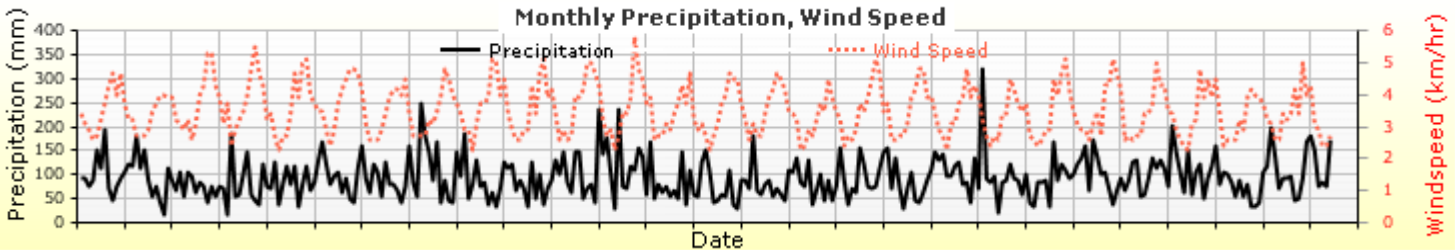
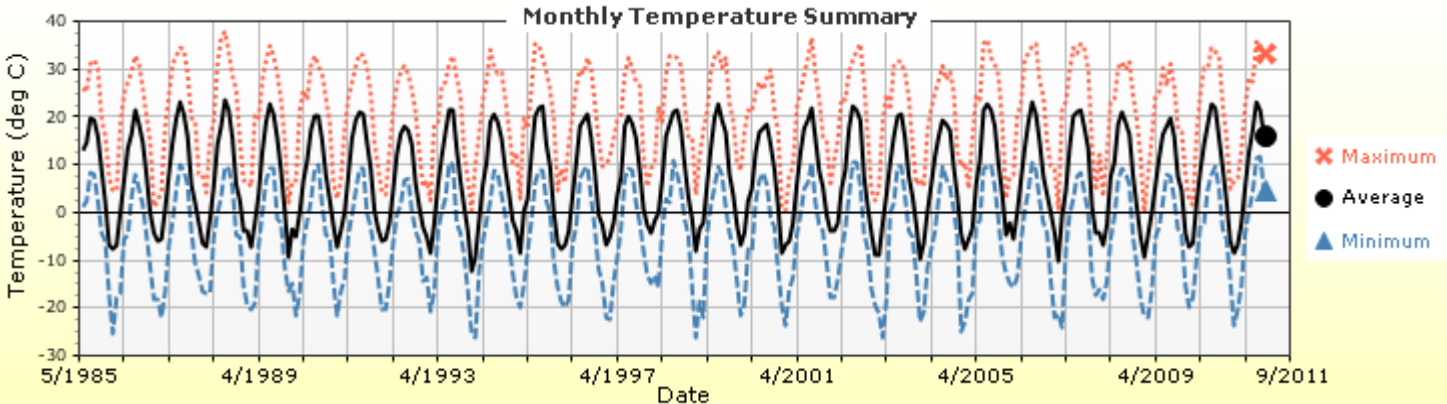
Annual Statistics:

Mean annual air temperature (°C) 7.46
 Mean annual precipitation (mm) 1127.76
 Freezing index (°C - days) 627.54
 Average annual number of freeze/thaw cycles: 87.25



Water table depth (m) 10.00

Monthly Climate Summary:



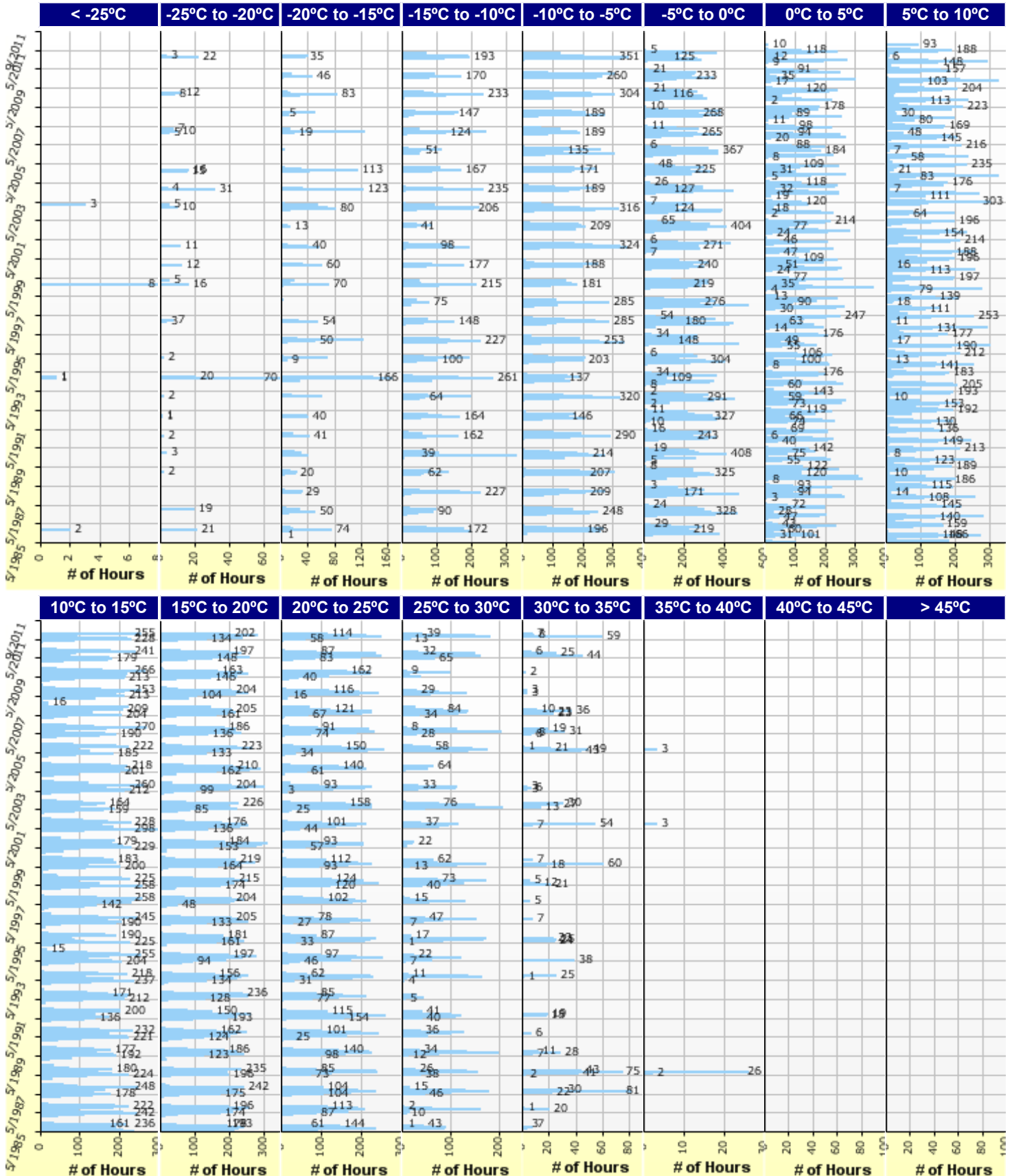


LCC 475 Section Major Arterial 7500AADTT

File Name: C:\Users\admin\Desktop\Frank Ni\Major Arterial\7500 AADTT\combined average E\LCC 475 Section Major Arterial 7500AADTT.dgp



Hourly Air Temperature Distribution by Month:





LCC 475 Section Major Arterial 7500AADTT

File Name: C:\Users\admin\Desktop\Frank Ni\Major Arterial\7500 AADTT\combined average E\LCC 475 Section Major Arterial 7500AADTT.dgpx



Design Properties

HMA Design Properties

Use Multilayer Rutting Model	False
Using G* based model (not nationally calibrated)	False
Is NCHRP 1-37A HMA Rutting Model Coefficients	True
Endurance Limit	-
Use Reflective Cracking	True

Structure - ICM Properties	
AC surface shortwave absorptivity	0.85

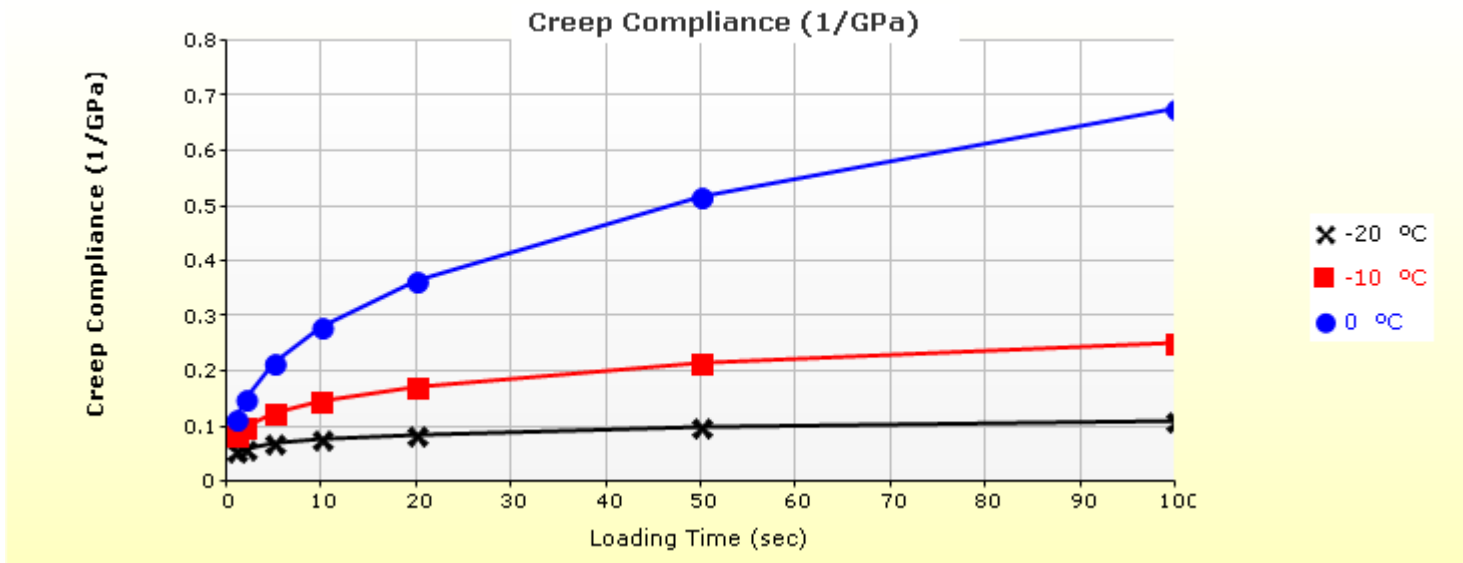
Layer Name	Layer Type	Interface Friction
Layer 1 Flexible : Default asphalt concrete	Flexible (1)	1.00
Layer 2 Flexible : Default asphalt concrete	Flexible (1)	1.00
Layer 3 Non-stabilized Base : A-1-a	Non-stabilized Base (4)	1.00
Layer 4 Non-stabilized Base : A-1-b	Non-stabilized Base (4)	1.00
Layer 5 Subgrade : A-1-a	Subgrade (5)	-

Thermal Cracking

Thermal Contraction	
Is thermal contraction calculated?	True
Mix coefficient of thermal contraction (mm/mm/°C)	-
Aggregate coefficient of thermal contraction (mm/mm/°C)	9.0e-006
Voids in Mineral Aggregate (%)	18.8

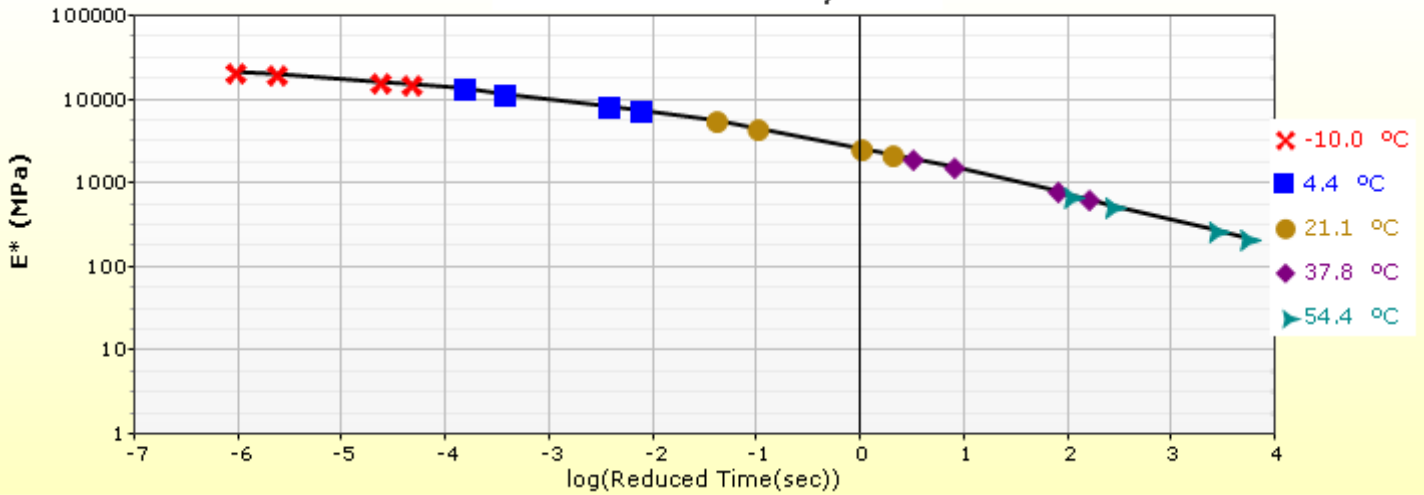
Indirect Tensile Strength (Input Level: 3)	
Test Temperature (°C)	Indirect Tensile Strength (Mpa)
-10.0	2.79

Creep Compliance (1/GPa) (Input Level: 3)			
Loading time (sec)	-20 °C	-10 °C	0 °C
1	5.57e-002	8.57e-002	1.16e-001
2	6.17e-002	1.01e-001	1.51e-001
5	7.07e-002	1.25e-001	2.15e-001
10	7.83e-002	1.48e-001	2.80e-001
20	8.68e-002	1.74e-001	3.65e-001
50	9.94e-002	2.16e-001	5.19e-001
100	1.10e-001	2.55e-001	6.77e-001

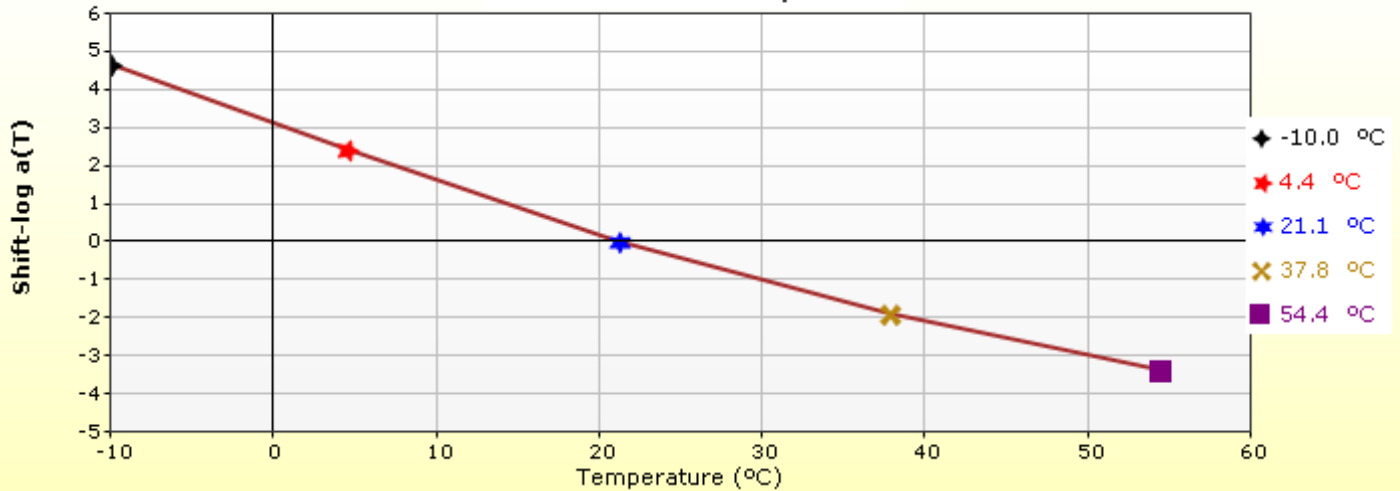


HMA Layer 1: Layer 1 Flexible : Default asphalt concrete

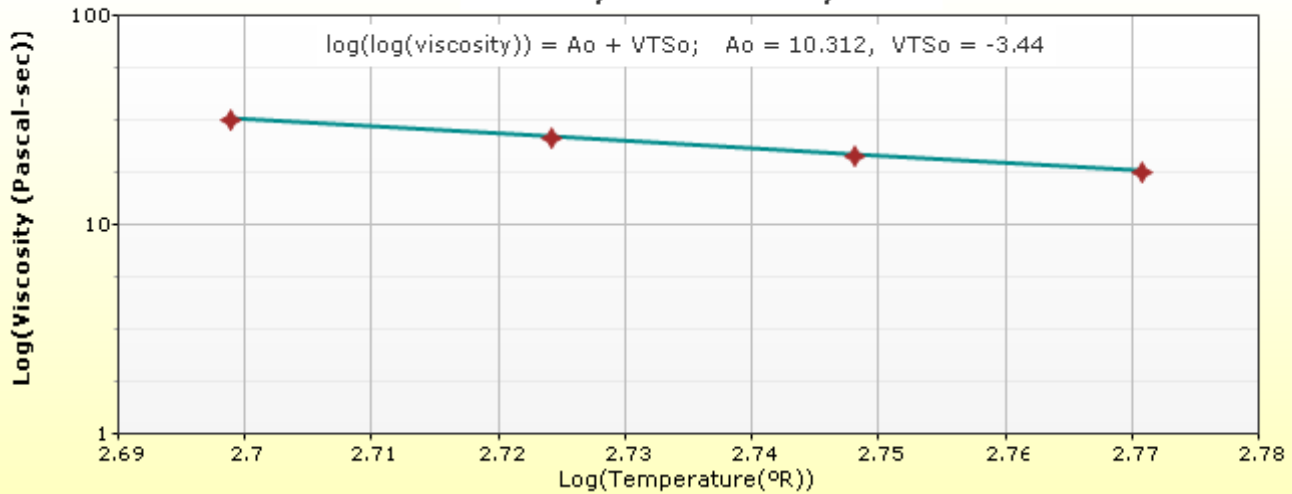
Master Curve HMA Layer 1



Shift Curve HMA Layer 1

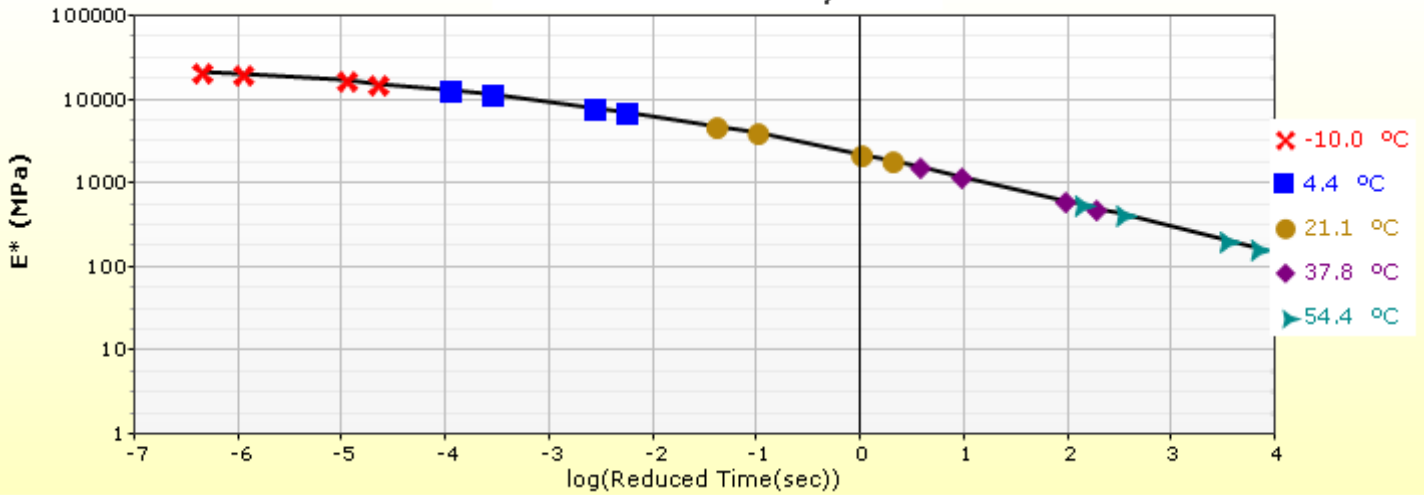


Viscosity Curve HMA Layer 1

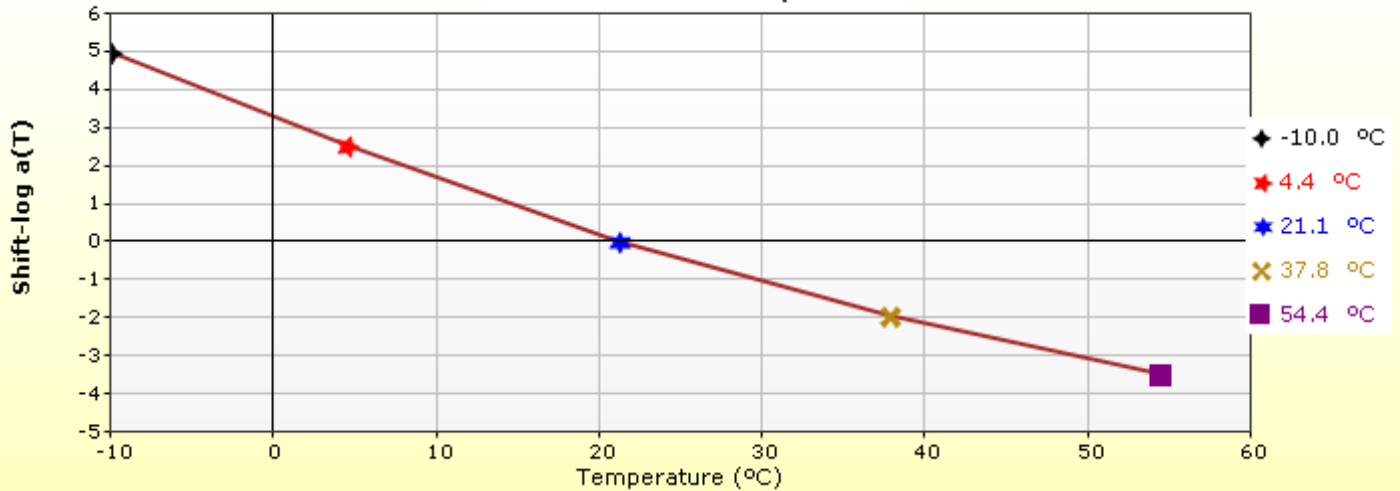


HMA Layer 2: Layer 2 Flexible : Default asphalt concrete

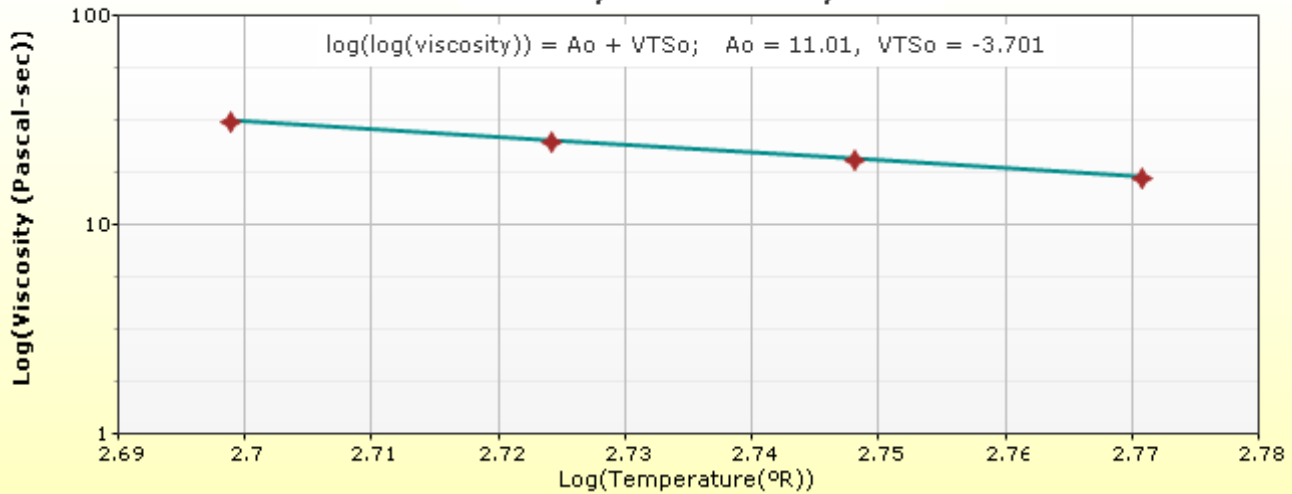
Master Curve HMA Layer 2



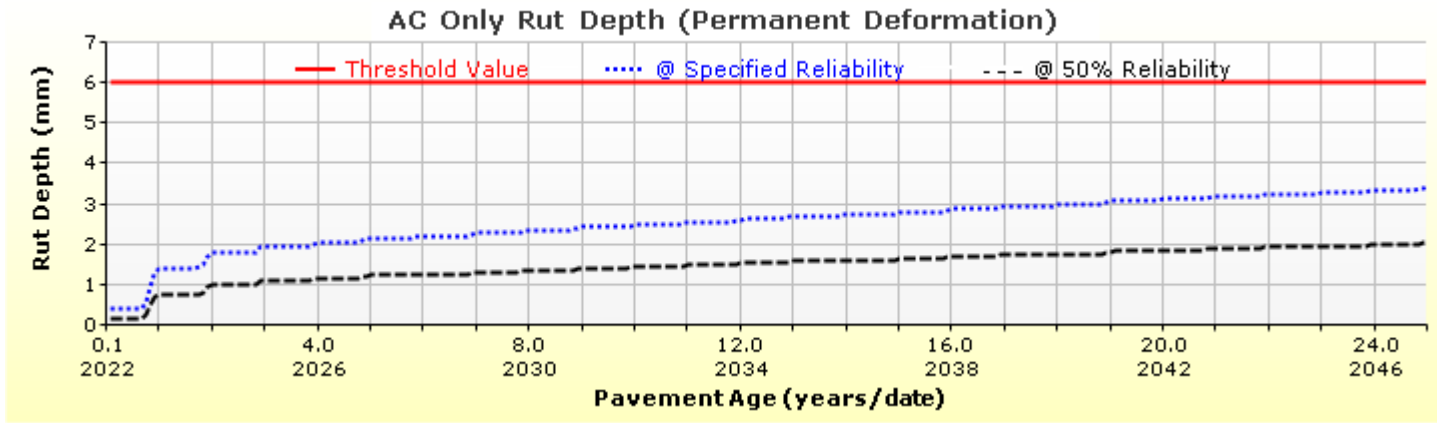
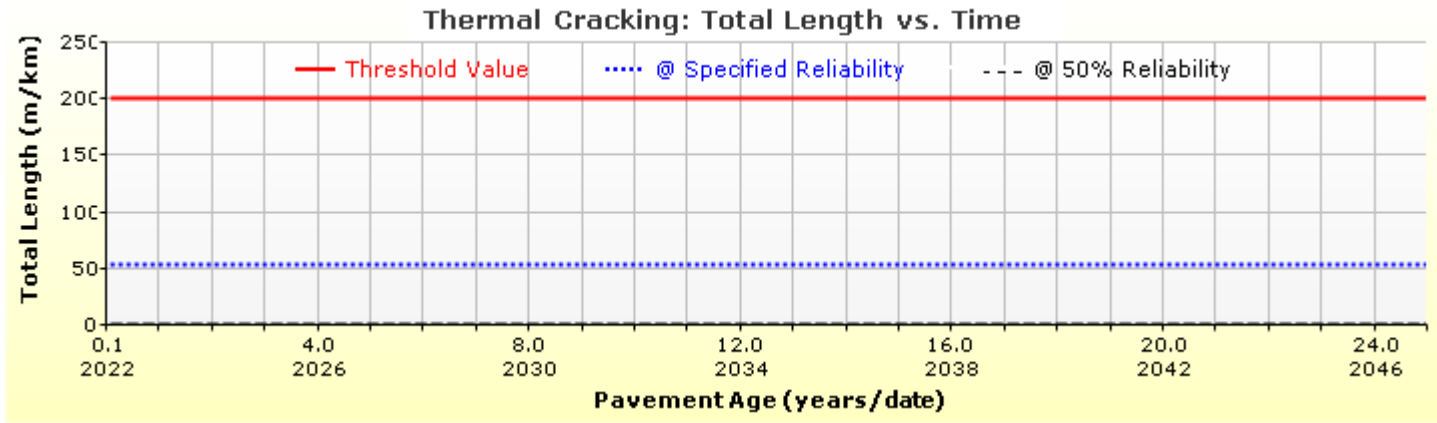
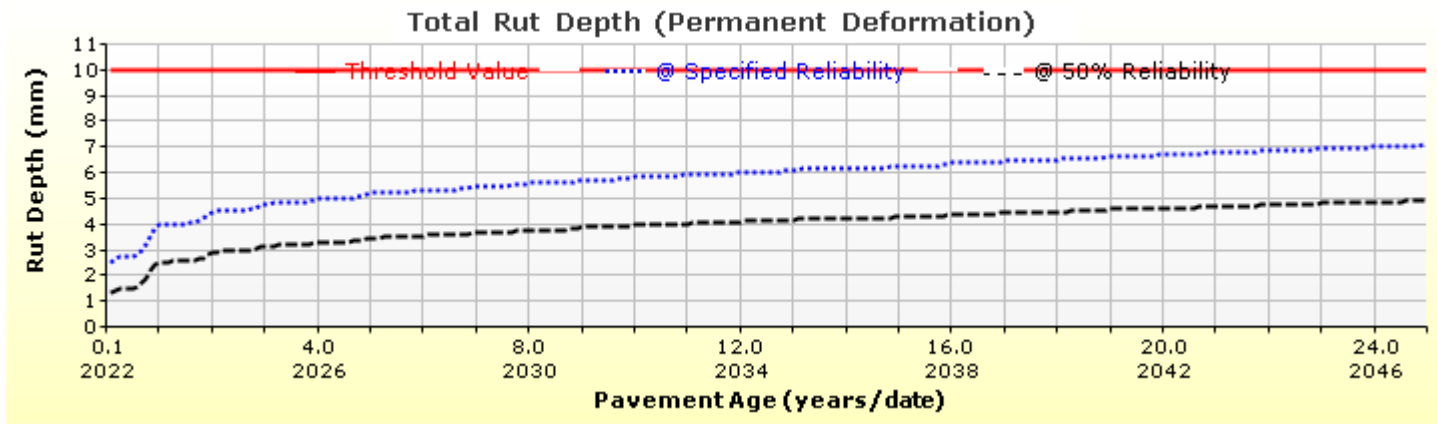
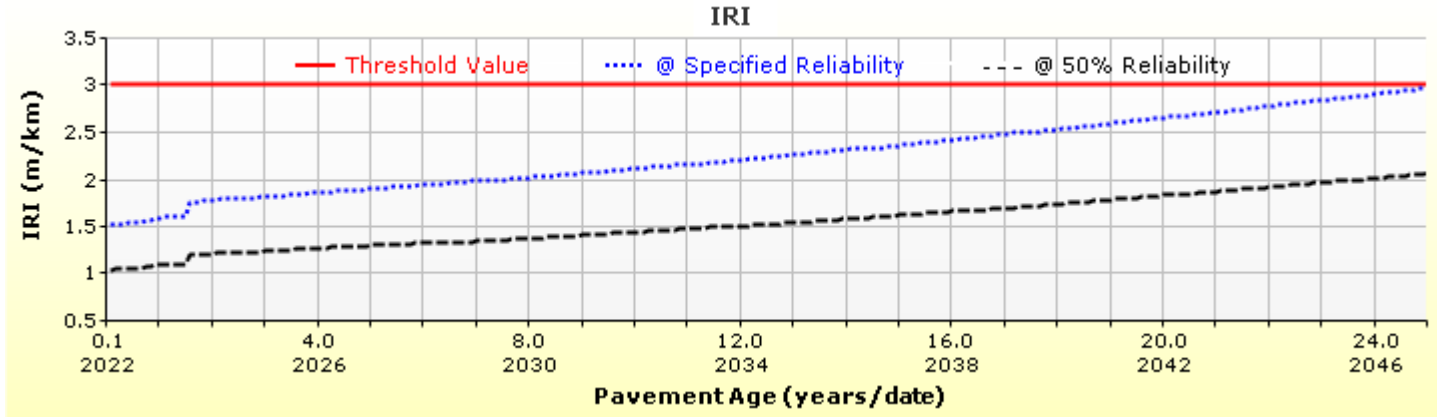
Shift Curve HMA Layer 2

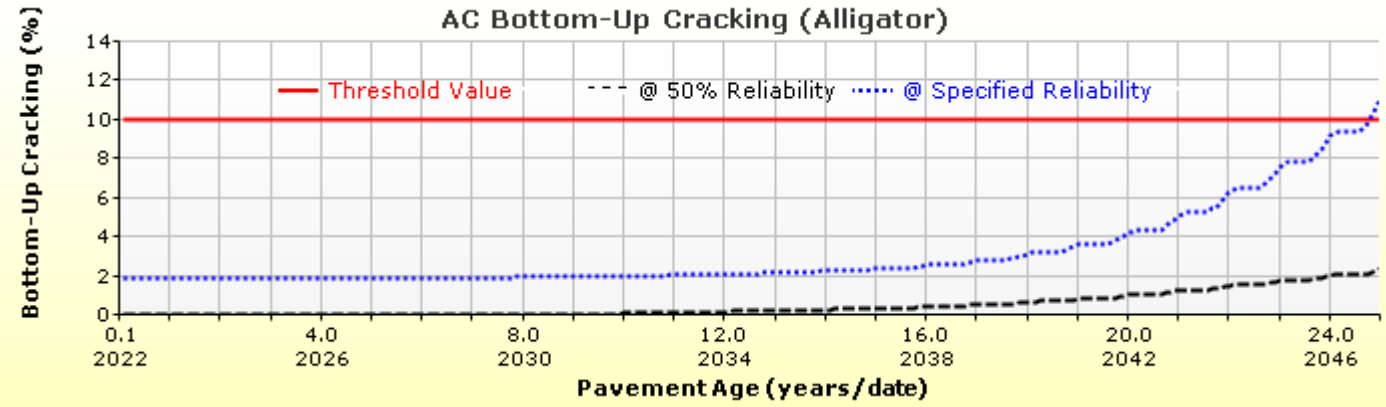
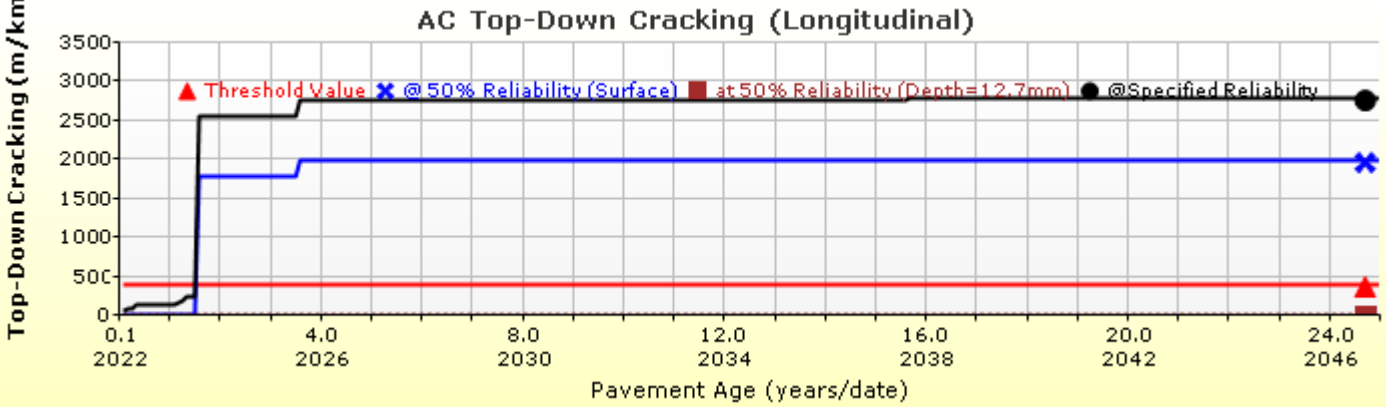
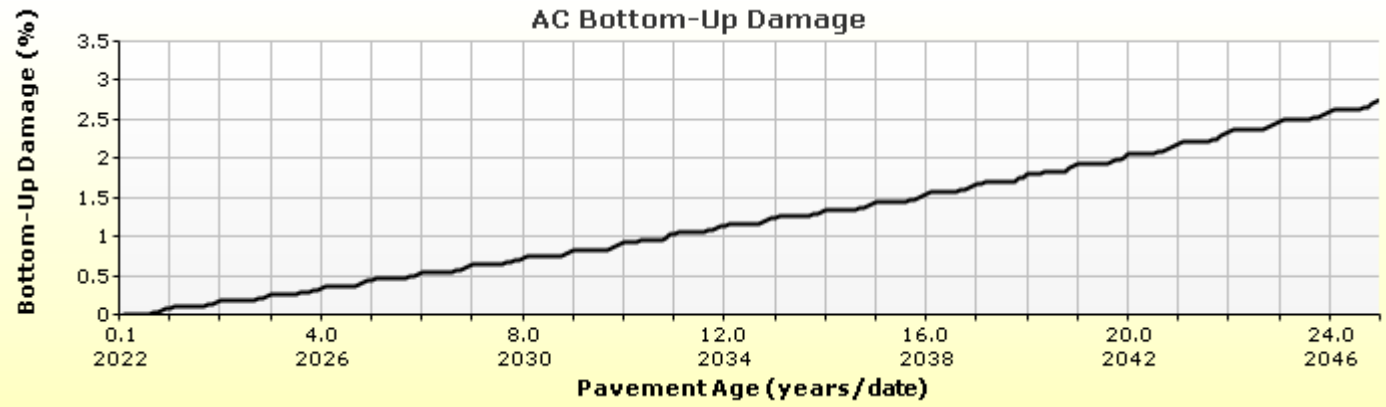
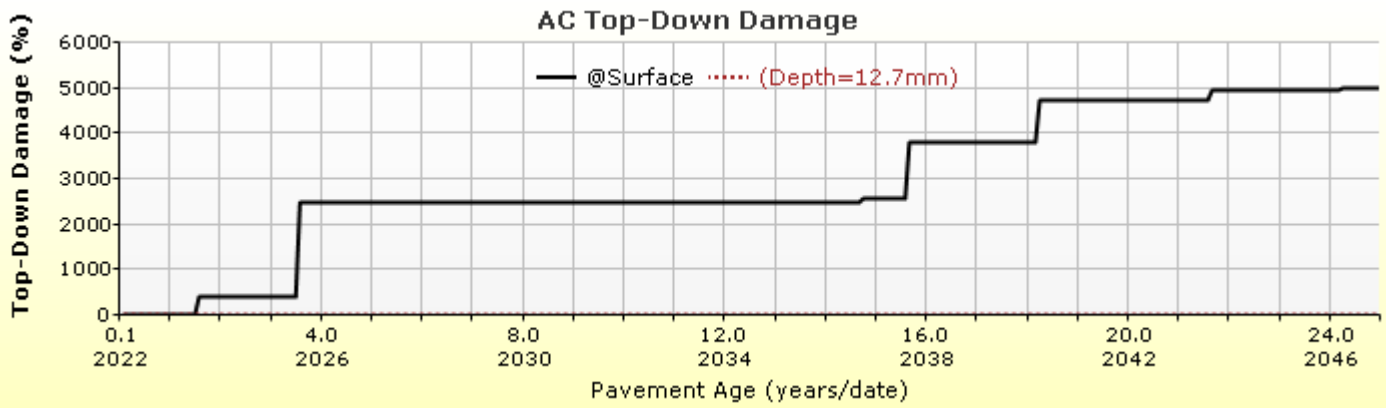


Viscosity Curve HMA Layer 2

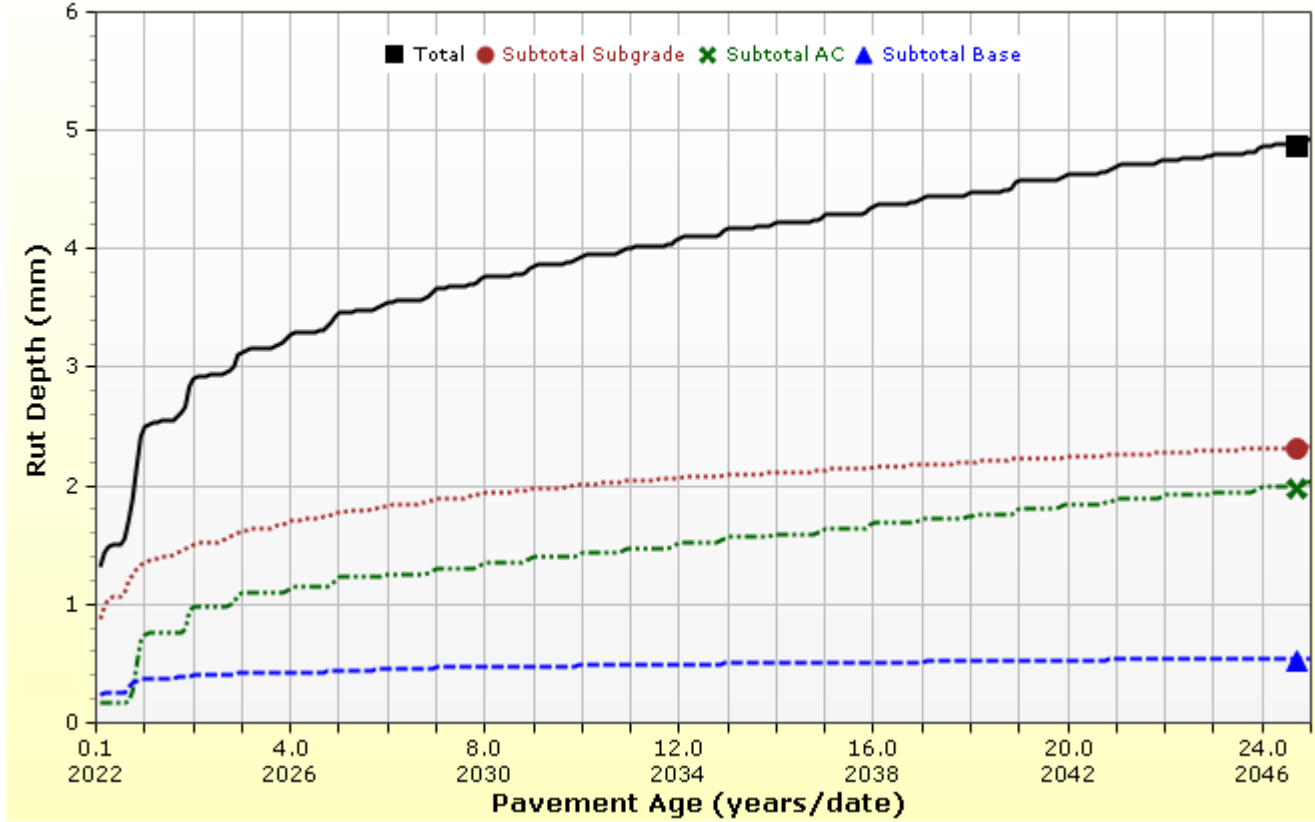


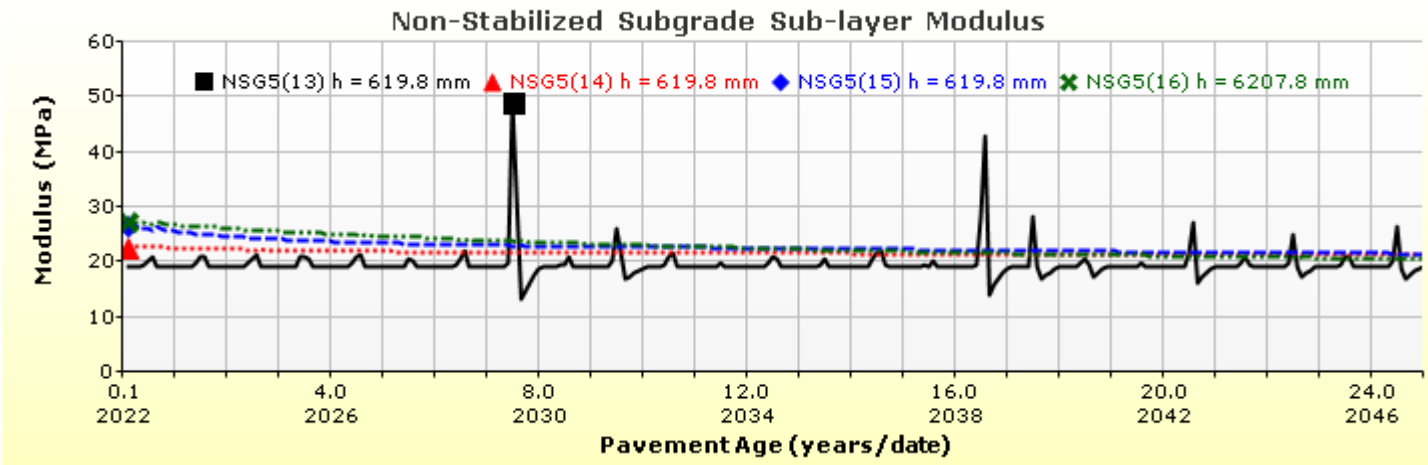
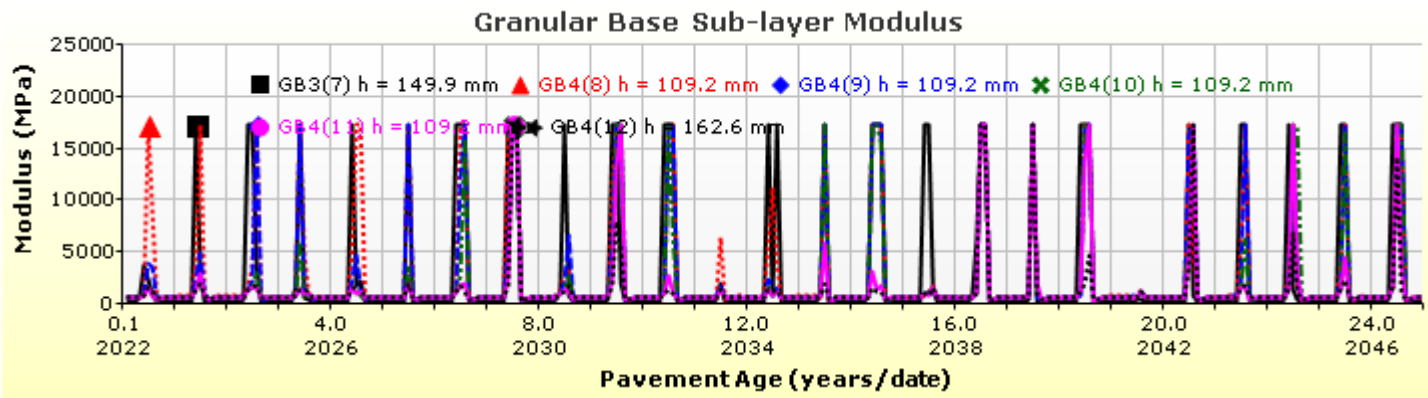
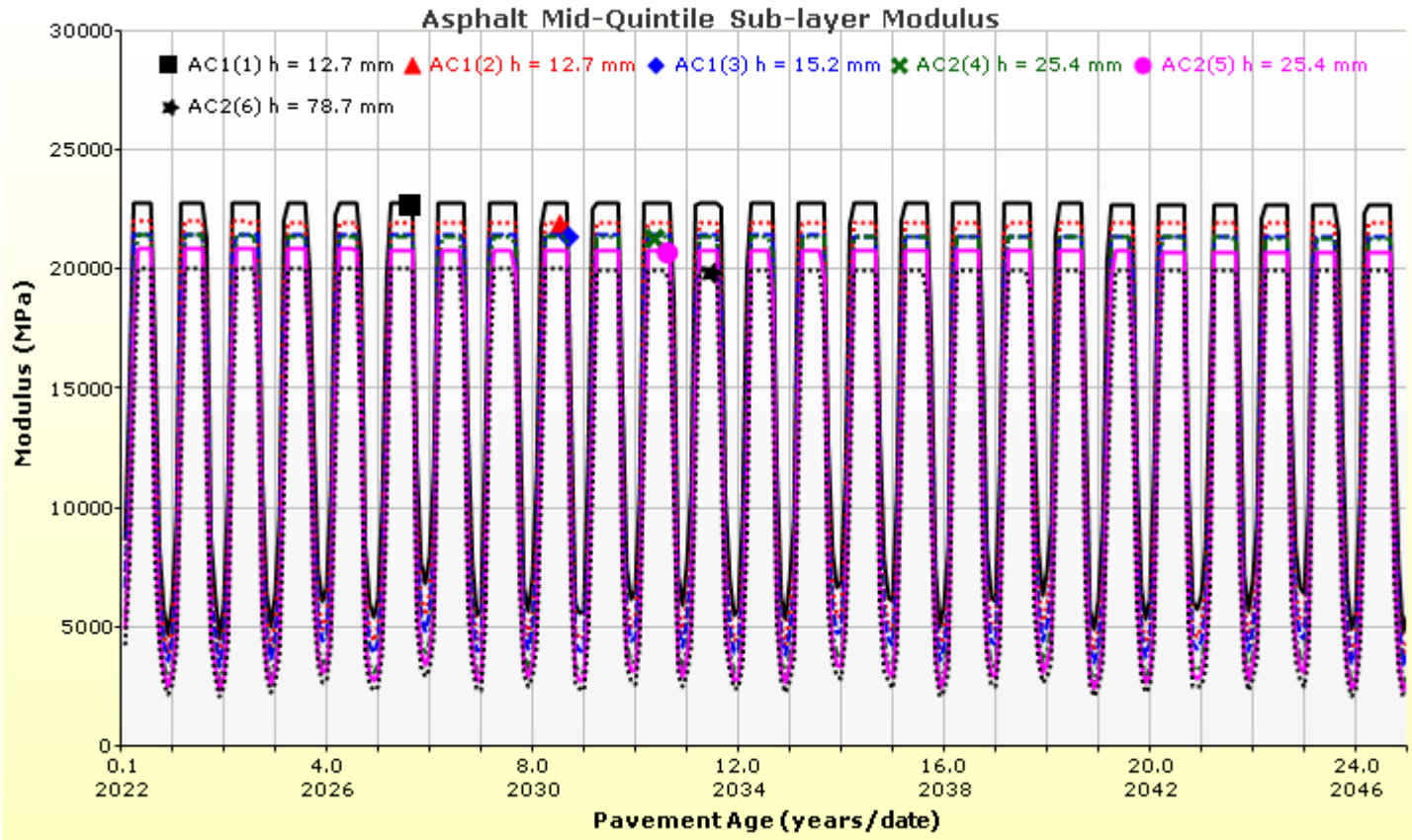
Analysis Output Charts





Rutting (Permanent Deformation) at 50% Reliability







LCC 475 Section Major Arterial 7500AADTT

File Name: C:\Users\admin\Desktop\Frank Ni\Major Arterial\7500 AADTT\combined average E\LCC 475 Section Major Arterial 7500AADTT.dgpx



Layer Information

Layer 1 Flexible : Default asphalt concrete

Asphalt		
Thickness (mm)	40.0	
Unit weight (kgf/m ³)	2390.0	
Poisson's ratio	Is Calculated?	False
	Ratio	0.35
	Parameter A	-
	Parameter B	-

Asphalt Dynamic Modulus (Input Level: 3)

Gradation	Percent Passing
19 mm sieve	100
9.5 mm sieve	77
4.75 mm sieve	60
0.075mm sieve	6

Asphalt Binder

Parameter	Value
Grade	Superpave Performance Grade
Binder Type	64-28
A	10.312
VTS	-3.44

General Info

Name	Value
Reference temperature (°C)	21.1
Effective binder content (%)	11.8
Air voids (%)	7
Thermal conductivity (watt/meter-kelvin)	1.16
Heat capacity (joule/kg-kelvin)	963

Identifiers

Field	Value
Display name/identifier	Default asphalt concrete
Description of object	
Author	
Date Created	9/16/2010 1:00:00 AM
Approver	
Date approved	9/16/2010 1:00:00 AM
State	
District	
County	
Highway	
Direction of Travel	
From station (km)	
To station (km)	
Province	
User defined field 1	
User defined field 2	
User defined field 3	
Revision Number	0



LCC 475 Section Major Arterial 7500AADTT

File Name: C:\Users\admin\Desktop\Frank Ni\Major Arterial\7500 AADTT\combined average E\LCC 475 Section Major Arterial 7500AADTT.dgpx



Layer 2 Flexible : Default asphalt concrete

Asphalt		
Thickness (mm)	130.0	
Unit weight (kg/m ³)	2460.0	
Poisson's ratio	Is Calculated?	False
	Ratio	0.35
	Parameter A	-
	Parameter B	-

Asphalt Dynamic Modulus (Input Level: 3)

Gradation	Percent Passing
19 mm sieve	100
9.5 mm sieve	77
4.75 mm sieve	60
0.075mm sieve	6

Asphalt Binder

Parameter	Value
Grade	Superpave Performance Grade
Binder Type	58-28
A	11.01
VTS	-3.701

General Info

Name	Value
Reference temperature (°C)	21.1
Effective binder content (%)	11.2
Air voids (%)	7
Thermal conductivity (watt/meter-kelvin)	1.16
Heat capacity (joule/kg-kelvin)	963

Identifiers

Field	Value
Display name/identifier	Default asphalt concrete
Description of object	
Author	
Date Created	9/16/2010 1:00:00 AM
Approver	
Date approved	9/16/2010 1:00:00 AM
State	
District	
County	
Highway	
Direction of Travel	
From station (km)	
To station (km)	
Province	
User defined field 1	
User defined field 2	
User defined field 3	
Revision Number	0



LCC 475 Section Major Arterial 7500AADTT

File Name: C:\Users\admin\Desktop\Frank Ni\Major Arterial\7500 AADTT\combined average E\LCC 475 Section Major Arterial 7500AADTT.dgpx



Layer 3 Non-stabilized Base : A-1-a

Unbound

Layer thickness (mm)	150.0
Poisson's ratio	0.35
Coefficient of lateral earth pressure (k0)	0.5

Modulus (Input Level: 3)

Analysis Type:	Modify input values by temperature/moisture
Method:	Resilient Modulus (MPa)

Resilient Modulus (MPa)

250.0

Use Correction factor for NDT modulus?	-
NDT Correction Factor:	-

Identifiers

Field	Value
Display name/identifier	A-1-a
Description of object	Default material
Author	AASHTO
Date Created	1/1/2011 12:00:00 AM
Approver	
Date approved	1/1/2011 12:00:00 AM
State	
District	
County	
Highway	
Direction of Travel	
From station (km)	
To station (km)	
Province	
User defined field 1	
User defined field 2	
User defined field 3	
Revision Number	0

Sieve

Liquid Limit	6.0
Plasticity Index	0.0
Is layer compacted?	True

	Is User Defined?	Value
Maximum dry unit weight (kgf/m ³)	False	2038.2
Saturated hydraulic conductivity (m/hr)	False	2.376e-02
Specific gravity of solids	False	2.7
Water Content (%)	False	5.7

User-defined Soil Water Characteristic Curve (SWCC)

Is User Defined?	False
af	3.0201
bf	2.5984
cf	0.7539
hr	100.0000

Sieve Size	% Passing
0.001mm	
0.002mm	
0.020mm	
0.075mm	5.0
0.150mm	
0.180mm	
0.250mm	
0.300mm	13.5
0.425mm	
0.600mm	
0.850mm	
1.18mm	27.5
2.0mm	
2.36mm	
4.75mm	45.0
9.5mm	61.5
12.5mm	77.5
19.0mm	92.5
25.0mm	100.0
37.5mm	
50.0mm	
63.0mm	
75.0mm	
90.0mm	



LCC 475 Section Major Arterial 7500AADTT

File Name: C:\Users\admin\Desktop\Frank Ni\Major Arterial\7500 AADTT\combined average E\LCC 475 Section Major Arterial 7500AADTT.dgpx



Layer 4 Non-stabilized Base : A-1-b

Unbound	
Layer thickness (mm)	600.0
Poisson's ratio	0.21
Coefficient of lateral earth pressure (k0)	0.5

Modulus (Input Level: 3)

Analysis Type:	Modify input values by temperature/moisture
Method:	Resilient Modulus (MPa)

Resilient Modulus (MPa)
1001.0

Use Correction factor for NDT modulus?	-
NDT Correction Factor:	-

Identifiers

Field	Value
Display name/identifier	A-1-b
Description of object	Default material
Author	AASHTO
Date Created	1/1/2011 12:00:00 AM
Approver	
Date approved	1/1/2011 12:00:00 AM
State	
District	
County	
Highway	
Direction of Travel	
From station (km)	
To station (km)	
Province	
User defined field 1	
User defined field 2	
User defined field 3	
Revision Number	0

Sieve

Liquid Limit	11.0
Plasticity Index	0.0
Is layer compacted?	True

	Is User Defined?	Value
Maximum dry unit weight (kgf/m ³)	False	2022.2
Saturated hydraulic conductivity (m/hr)	False	6.073e-02
Specific gravity of solids	False	2.7
Water Content (%)	False	7.3

User-defined Soil Water Characteristic Curve (SWCC)

Is User Defined?	False
af	6.8181
bf	1.6200
cf	0.8174
hr	100.0000

Sieve Size	% Passing
0.001mm	
0.002mm	
0.020mm	
0.075mm	5.0
0.150mm	
0.180mm	
0.250mm	
0.300mm	13.5
0.425mm	
0.600mm	
0.850mm	
1.18mm	25.0
2.0mm	
2.36mm	
4.75mm	37.5
9.5mm	
12.5mm	
19.0mm	
25.0mm	75.0
37.5mm	
50.0mm	
63.0mm	
75.0mm	
90.0mm	100.0



LCC 475 Section Major Arterial 7500AADTT

File Name: C:\Users\admin\Desktop\Frank Ni\Major Arterial\7500 AADTT\combined average E\LCC 475 Section Major Arterial 7500AADTT.dgp



Layer 5 Subgrade : A-1-a

Unbound	
Layer thickness (mm)	Semi-infinite
Poisson's ratio	0.45
Coefficient of lateral earth pressure (k0)	0.5

Modulus (Input Level: 3)

Analysis Type:	Modify input values by temperature/moisture
Method:	Resilient Modulus (MPa)

Resilient Modulus (MPa)
30.0

Use Correction factor for NDT modulus?	-
NDT Correction Factor:	-

Identifiers

Field	Value
Display name/identifier	A-1-a
Description of object	Default Material
Author	AASHTO
Date Created	1/1/2011 12:00:00 AM
Approver	
Date approved	1/1/2011 12:00:00 AM
State	
District	
County	
Highway	
Direction of Travel	
From station (km)	
To station (km)	
Province	
User defined field 1	
User defined field 2	
User defined field 3	
Revision Number	0

Sieve

Liquid Limit	26.0
Plasticity Index	12.0
Is layer compacted?	True

	Is User Defined?	Value
Maximum dry unit weight (kgf/m ³)	False	1748.5
Saturated hydraulic conductivity (m/hr)	False	8.129e-06
Specific gravity of solids	False	2.7
Water Content (%)	False	16.8

User-defined Soil Water Characteristic Curve (SWCC)

Is User Defined?	False
af	106.7030
bf	0.6914
cf	0.2273
hr	500.0000

Sieve Size	% Passing
0.001mm	
0.002mm	30.0
0.020mm	
0.075mm	80.0
0.150mm	
0.180mm	84.0
0.250mm	
0.300mm	
0.425mm	91.0
0.600mm	
0.850mm	
1.18mm	
2.0mm	95.0
2.36mm	
4.75mm	97.0
9.5mm	99.0
12.5mm	100.0
19.0mm	100.0
25.0mm	100.0
37.5mm	
50.0mm	
63.0mm	
75.0mm	
90.0mm	

Calibration Coefficients

AC Fatigue

$N_f = 0.00432 * C * \beta_{f1} k_1 \left(\frac{1}{\epsilon_1}\right)^{k_2 \beta_{f2}} \left(\frac{1}{E}\right)^{k_3 \beta_{f3}}$ $C = 10^M$ $M = 4.84 \left(\frac{V_b}{V_a + V_b} - 0.69\right)$	k1: 3.75
	k2: 2.87
	k3: 1.46
	Bf1: (5.014 * Pow(hac,-3.416)) * 1 + 0
	Bf2: 1.38
	Bf3: 0.88

AC Rutting

$\frac{\epsilon_p}{\epsilon_r} = k_z \beta_{r1} 10^{k_1 T} k_2 \beta_{r2} N^{k_3 B_{r3}}$ $k_z = (C_1 + C_2 * depth) * 0.328196^{depth}$ $C_1 = -0.1039 * H_a^2 + 2.4868 * H_a - 17.342$ $C_2 = 0.0172 * H_a^2 - 1.7331 * H_a + 27.428$ <p>Where: H_{ac} = total AC thickness(in)</p>	ϵ_p = plastic strain(in/in) ϵ_r = resilient strain(in/in) T = layer temperature(°F) N = number of load repetitions
AC Rutting Standard Deviation	0.24 * Pow(RUT,0.8026) + 0.001
AC Layer 1	K1:-2.45 K2:3.01 K3:0.22 Br1:0.128 Br2:0.52 Br3:1.36
AC Layer 2	K1:-2.45 K2:3.01 K3:0.22 Br1:0.4 Br2:0.52 Br3:1.36

Thermal Fracture

$C_f = 400 * N \left(\frac{\log C / h_{ac}}{\sigma}\right)$ $\Delta C = (k * \beta t)^{n+1} * A * \Delta K^{-n}$ $A = 10^{(4.389 - 2.52 * \log(E * \sigma_m * n))}$	C_f = observed amount of thermal cracking(ft/500ft) k = refression coefficient determined through field calibration $N()$ = standard normal distribution evaluated at() σ = standard deviation of the log of the depth of cracks in the pavments C = crack depth(in) h_{ac} = thickness of asphalt layer(in) ΔC = Change in the crack depth due to a cooling cycle ΔK = Change in the stress intensity factor due to a cooling cycle A, n = Fracture parameters for the asphalt mixture E = mixture stiffness σ_m = Undamaged mixture tensile strength β_t = Calibration parameter
Level 1 K: ((3 * Pow(10,-7)) * Pow(MAAT,4.0319)) * 1 + 0	Level 1 Standard Deviation: 0.14 * THERMAL + 168
Level 2 K: ((3 * Pow(10,-7)) * Pow(MAAT,4.0319)) * 1 + 0	Level 2 Standard Deviation: 0.20 * THERMAL + 168
Level 3 K: ((3 * Pow(10,-7)) * Pow(MAAT,4.0319)) * 1 + 0	Level 3 Standard Deviation: 0.289 * THERMAL + 168

CSM Fatigue

$N_f = 10^{\left(\frac{k_1 \beta_{c1} \left(\frac{\sigma_s}{M_r}\right)}{k_2 \beta_{c2}}\right)}$	N_f = number of repetitions to fatigue cracking σ_s = Tensile stress(psi) M_r = modulus of rupture(psi)		
k1: 0.972	k2: 0.0825	Bc1: 1	Bc2: 1

Unbound Layer Rutting			
$\delta_a(N) = \beta_{s_1} k_1 \varepsilon_v h \left(\frac{\varepsilon_0}{\varepsilon_r} \right) \left e^{-\left(\frac{\rho}{N}\right)^\beta} \right $		δ_a = permanent deformation for the layer N = number of repetitions ε_v = average vertical strain(in/in) $\varepsilon_0, \beta, \rho$ = material properties ε_r = resilient strain(in/in)	
Base Rutting		Subgrade Rutting	
k1: 0.965	Bs1: 0.322	k1: 0.965	Bs1: 0.322
Standard Deviation (BASERUT) 0.1477 * Pow(BASERUT,0.6711) + 0.001		Standard Deviation (BASERUT) 0.1235 * Pow(SUBRUT,0.5012) + 0.001	

AC Cracking					
AC Top Down Cracking			AC Bottom Up Cracking		
$FC_{top} = \left(\frac{C_4}{1 + e^{(C_1 - C_2 * \log_{10}(Damage))}} \right) * 10.56$			$FC = \left(\frac{6000}{1 + e^{(C_1 * C'_1 + C_2 * C'_2 * \log_{10}(D * 100))}} \right) * \left(\frac{1}{60} \right)$		
			$C'_2 = -2.40874 - 39.748 * (1 + h_{ac})^{-2.856}$		
			$C'_1 = -2 * C'_2$		
c1: 7	c2: 3.5	c3: 0	c4: 1000	c1: 1.31	c2: (0.867 + 0.2583 * hac) * 1 + 0
c3: 6000					
Top down AC Cracking Standard Deviation			Bottom up AC Cracking Standard Deviation		
200 + 2300/(1+exp(1.072-2.1654*LOG10(TOP+0.0001)))			1.13 + 13/(1+exp(7.57-15.5*LOG10(BOTTOM+0.0001)))		

CSM Cracking				IRI Flexible Pavements			
$FC_{ctb} = C_1 + \frac{C_2}{1 + e^{C_3 - C_4 * \log_{10}(Damage)}}$				C1 - Rutting C3 - Transverse Crack C2 - Fatigue Crack C4 - Site Factors			
C1: 0	C2: 75	C3: 2	C4: 2	C1: 55	C2: 0.4	C3: 0.008	C4: 0.015
CSM Standard Deviation							
CTB*1							



LCC 600 Section Major Arterial 7500AADTT

File Name: C:\Users\admin\Desktop\Frank Ni\Major Arterial\7500 AADTT\combined average E\LCC 600 Section Major Arterial 7500AADTT.dgpx



Design Inputs

Design Life: **25 years** Base construction: **May, 2021** Climate Data: **43.5, -80.625**
 Design Type: **FLEXIBLE** Pavement construction: **June, 2022** Sources (Lat/Lon)
 Traffic opening: **September, 2022**

Design Structure

Layer type	Material Type	Thickness(mm)
Flexible	Default asphalt concrete	40.0
Flexible	Default asphalt concrete	130.0
NonStabilized	A-1-a	150.0
NonStabilized	A-1-b	600.0
Subgrade	A-1-a	Semi-infinite

Volumetric at Construction:	
Effective binder content (%)	11.8
Air voids (%)	7.0

Traffic

Age (year)	Heavy Trucks (cumulative)
2022 (initial)	7,500
2034 (12 years)	16,063,700
2047 (25 years)	37,255,500

Design Outputs

Distress Prediction Summary

Distress Type	Distress @ Specified Reliability		Reliability (%)		Criterion Satisfied?
	Target	Predicted	Target	Achieved	
Terminal IRI (m/km)	3.00	2.96	95.00	95.77	Pass
Permanent deformation - total pavement (mm)	10.00	6.85	95.00	100.00	Pass
AC bottom-up fatigue cracking (percent)	10.00	6.52	95.00	99.74	Pass
AC thermal cracking (m/km)	200.00	52.53	95.00	100.00	Pass
AC top-down fatigue cracking (m/km)	378.80	2786.39	95.00	0.03	Fail
Permanent deformation - AC only (mm)	6.00	3.48	95.00	100.00	Pass

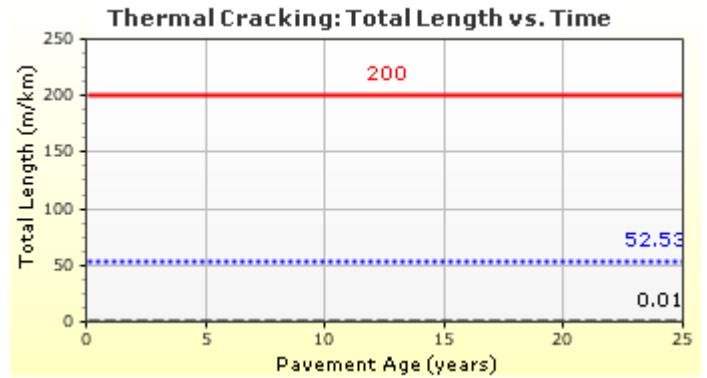
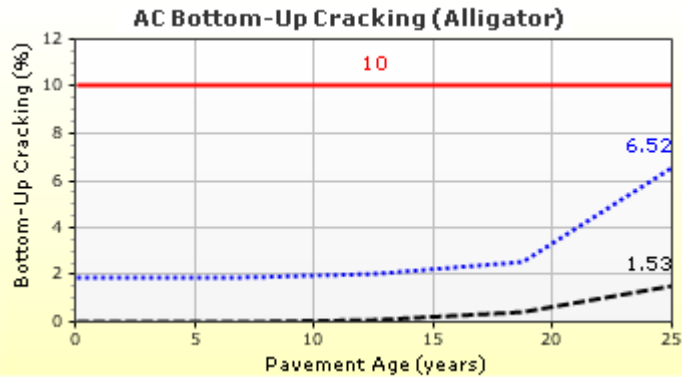
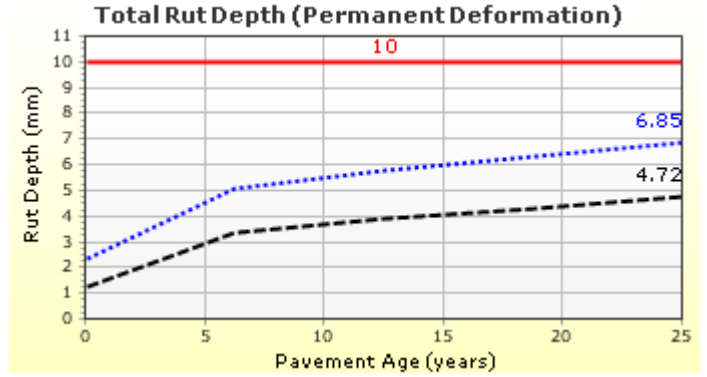
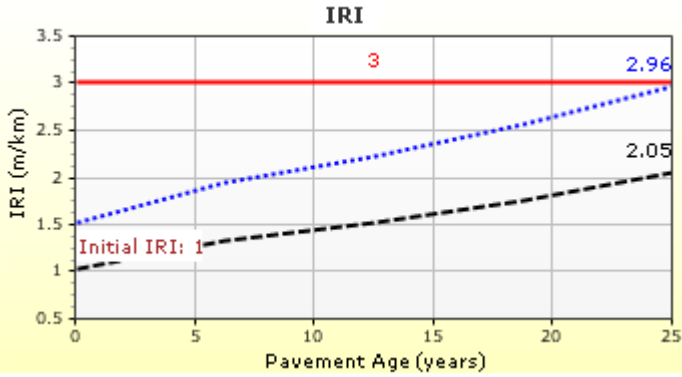


LCC 600 Section Major Arterial 7500AADTT

File Name: C:\Users\admin\Desktop\Frank Ni\Major Arterial\7500 AADTT\combined average E\LCC 600 Section Major Arterial 7500AADTT.dgpx



Distress Charts

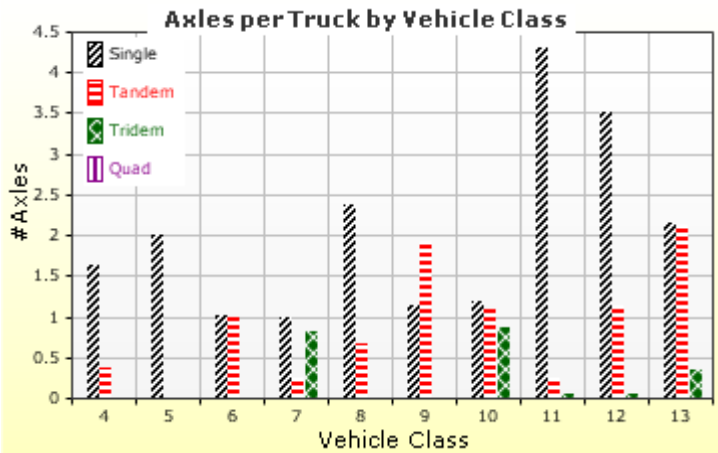
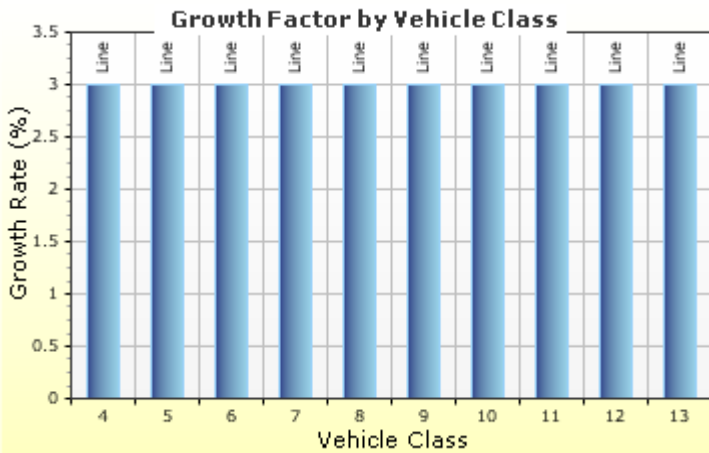
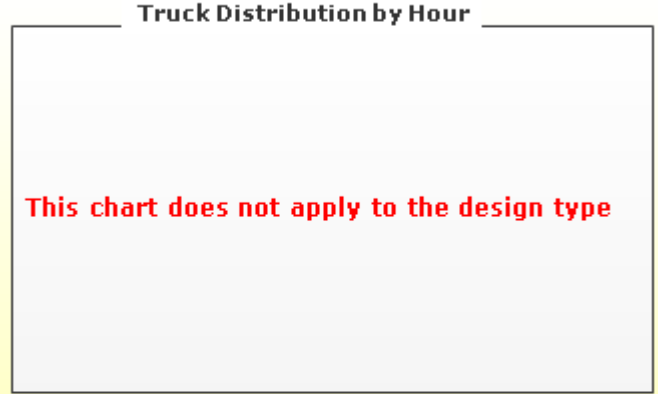
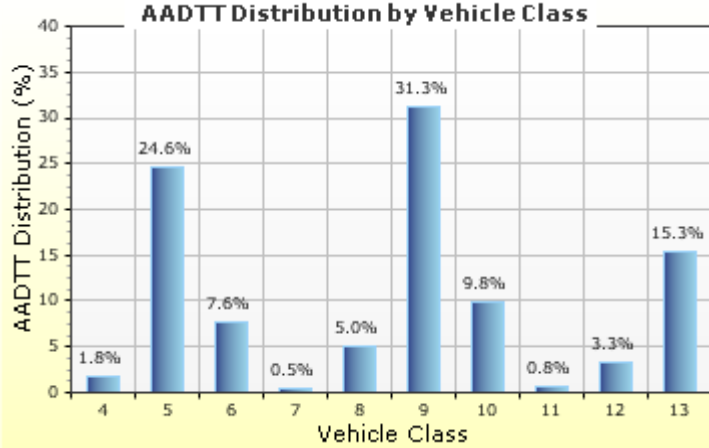


Traffic Inputs

Graphical Representation of Traffic Inputs

Initial two-way AADTT: **7,500**
 Number of lanes in design direction: **2**

Percent of trucks in design direction (%): **50.0**
 Percent of trucks in design lane (%): **80.0**
 Operational speed (kph): **100.0**



Traffic Volume Monthly Adjustment Factors





LCC 600 Section Major Arterial 7500AADTT

File Name: C:\Users\admin\Desktop\Frank Ni\Major Arterial\7500 AADTT\combined average E\LCC 600 Section Major Arterial 7500AADTT.dgp



Tabular Representation of Traffic Inputs

Volume Monthly Adjustment Factors Level 3: Default MAF

Month	Vehicle Class									
	4	5	6	7	8	9	10	11	12	13
January	1.0	1.0	1.0	1.0	1.0	1.0	1.0	1.0	1.0	1.0
February	1.0	1.0	1.0	1.0	1.0	1.0	1.0	1.0	1.0	1.0
March	1.0	1.0	1.0	1.0	1.0	1.0	1.0	1.0	1.0	1.0
April	1.0	1.0	1.0	1.0	1.0	1.0	1.0	1.0	1.0	1.0
May	1.0	1.0	1.0	1.0	1.0	1.0	1.0	1.0	1.0	1.0
June	1.0	1.0	1.0	1.0	1.0	1.0	1.0	1.0	1.0	1.0
July	1.0	1.0	1.0	1.0	1.0	1.0	1.0	1.0	1.0	1.0
August	1.0	1.0	1.0	1.0	1.0	1.0	1.0	1.0	1.0	1.0
September	1.0	1.0	1.0	1.0	1.0	1.0	1.0	1.0	1.0	1.0
October	1.0	1.0	1.0	1.0	1.0	1.0	1.0	1.0	1.0	1.0
November	1.0	1.0	1.0	1.0	1.0	1.0	1.0	1.0	1.0	1.0
December	1.0	1.0	1.0	1.0	1.0	1.0	1.0	1.0	1.0	1.0

Distributions by Vehicle Class

Vehicle Class	AADTT Distribution (%) (Level 3)	Growth Factor	
		Rate (%)	Function
Class 4	1.8%	3%	Linear
Class 5	24.6%	3%	Linear
Class 6	7.6%	3%	Linear
Class 7	0.5%	3%	Linear
Class 8	5%	3%	Linear
Class 9	31.3%	3%	Linear
Class 10	9.8%	3%	Linear
Class 11	0.8%	3%	Linear
Class 12	3.3%	3%	Linear
Class 13	15.3%	3%	Linear

Truck Distribution by Hour does not apply

Axle Configuration

Traffic Wander	
Mean wheel location (mm)	460.0
Traffic wander standard deviation (mm)	254.0
Design lane width (m)	3.7

Axle Configuration	
Average axle width (m)	2.6
Dual tire spacing (mm)	305.0
Tire pressure (kPa)	827.4

Average Axle Spacing	
Tandem axle spacing (m)	1.3
Tridem axle spacing (m)	1.3
Quad axle spacing (m)	1.3

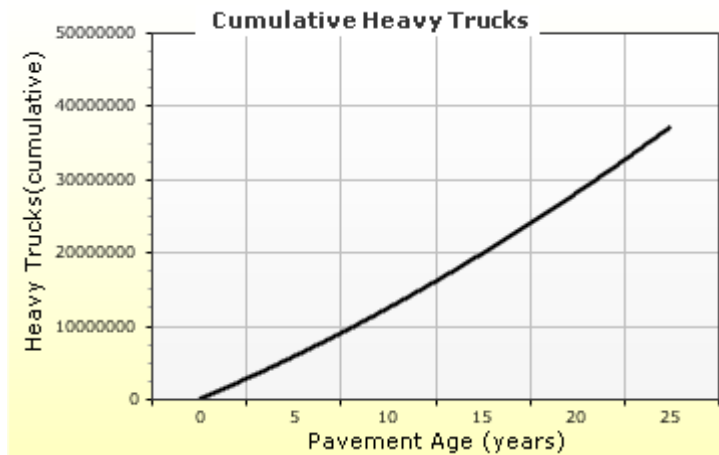
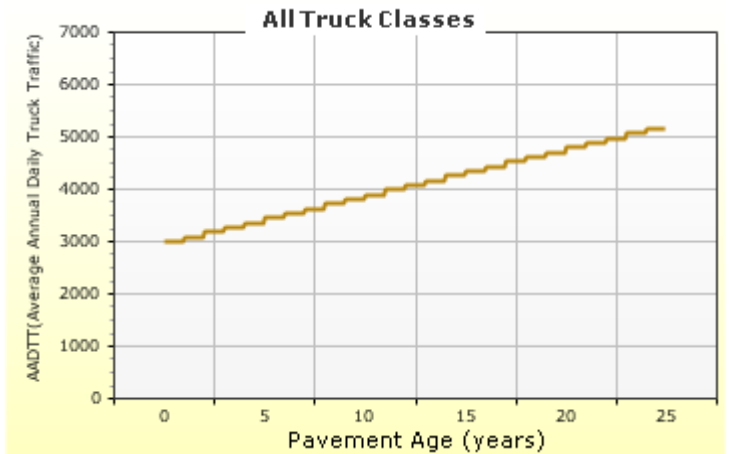
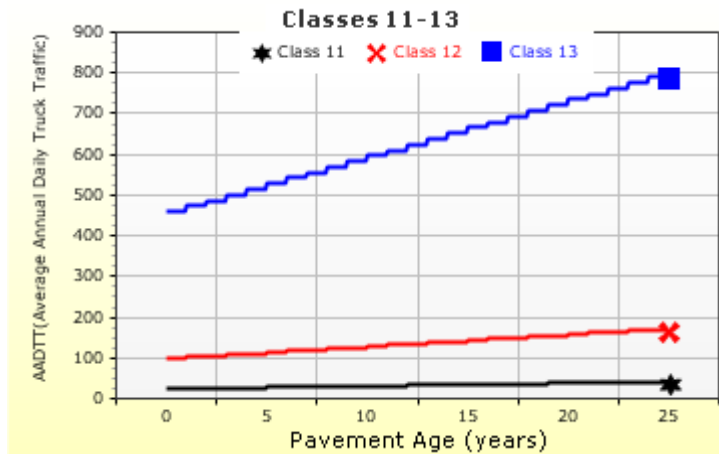
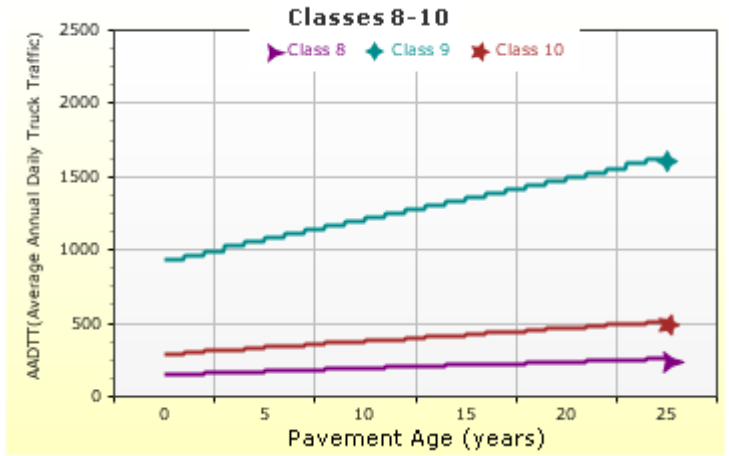
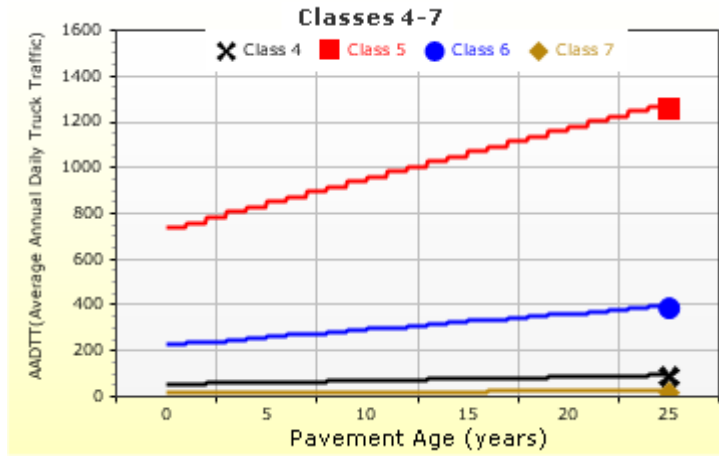
Wheelbase does not apply

Number of Axles per Truck

Vehicle Class	Single Axle	Tandem Axle	Tridem Axle	Quad Axle
Class 4	1.62	0.39	0	0
Class 5	2	0	0	0
Class 6	1.02	0.99	0	0
Class 7	1	0.26	0.83	0
Class 8	2.38	0.67	0	0
Class 9	1.13	1.93	0	0
Class 10	1.19	1.09	0.89	0
Class 11	4.29	0.26	0.06	0
Class 12	3.52	1.14	0.06	0
Class 13	2.15	2.13	0.35	0

AADTT (Average Annual Daily Truck Traffic) Growth

* Traffic cap is not enforced





LCC 600 Section Major Arterial 7500AADTT

File Name: C:\Users\admin\Desktop\Frank Ni\Major Arterial\7500 AADTT\combined average E\LCC 600 Section Major Arterial 7500AADTT.dgp



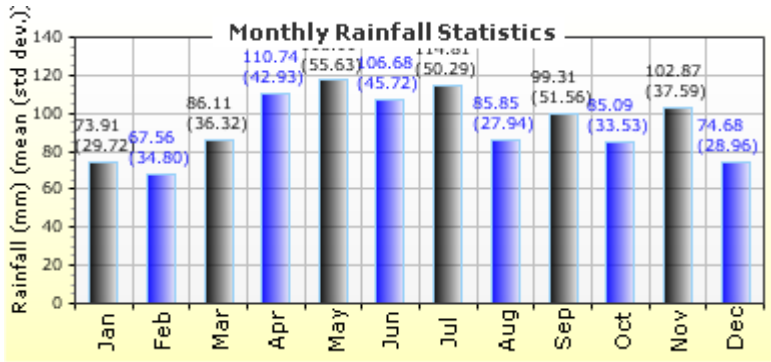
Climate Inputs

Climate Data Sources:

Climate Station Cities: Location (lat lon elevation(m))
 CA, ON 43.50000 -80.62500 369

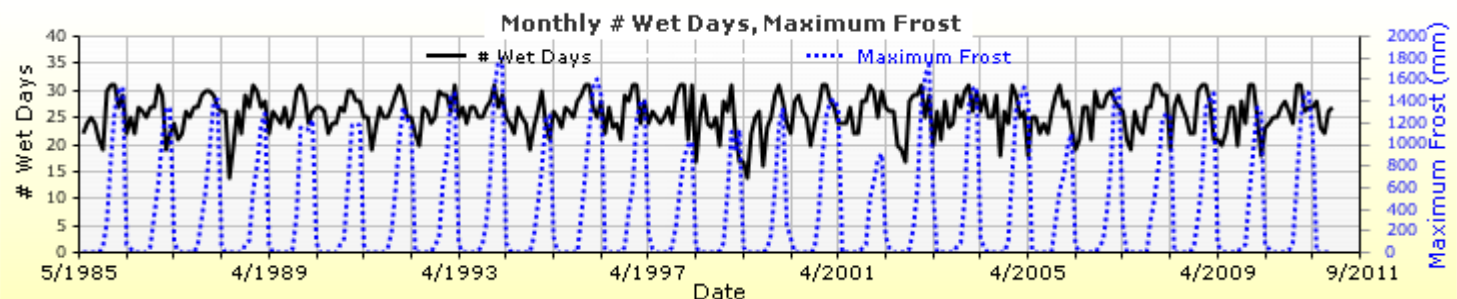
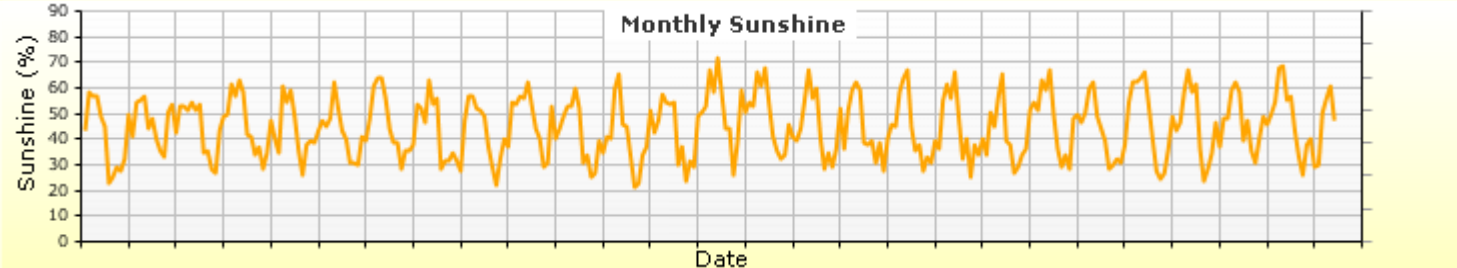
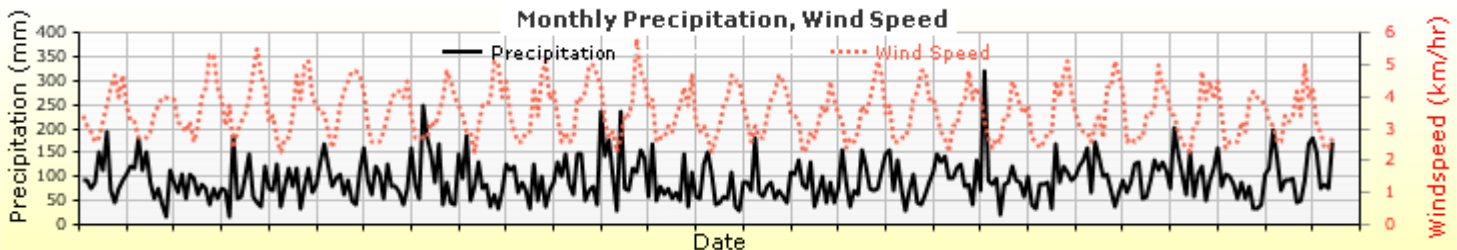
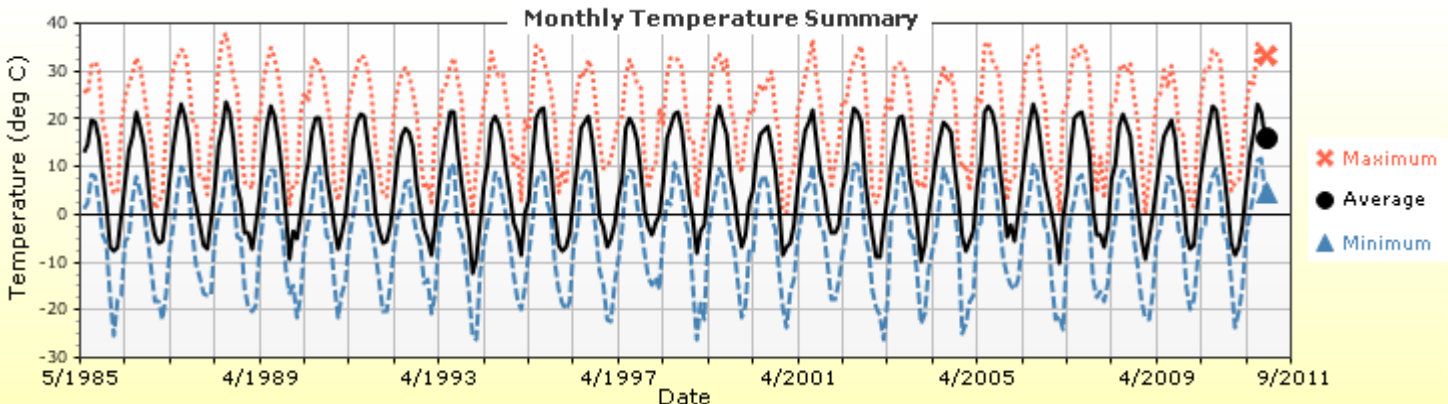
Annual Statistics:

Mean annual air temperature (°C) 7.46
 Mean annual precipitation (mm) 1127.76
 Freezing index (°C - days) 627.54
 Average annual number of freeze/thaw cycles: 87.25



Water table depth (m) 10.00

Monthly Climate Summary:



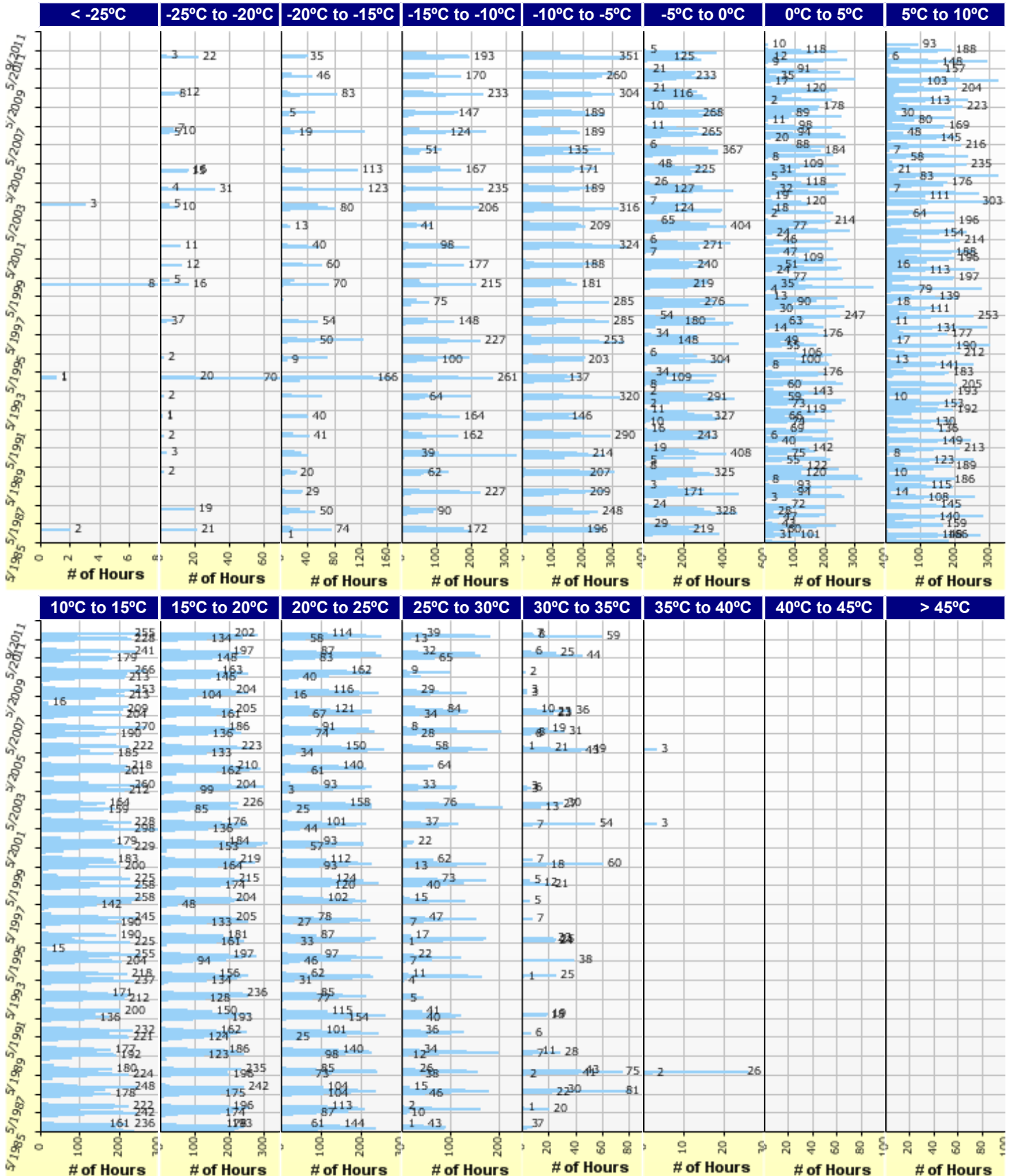


LCC 600 Section Major Arterial 7500AADTT

File Name: C:\Users\admin\Desktop\Frank Ni\Major Arterial\7500 AADTT\combined average E\LCC 600 Section Major Arterial 7500AADTT.dgp



Hourly Air Temperature Distribution by Month:





LCC 600 Section Major Arterial 7500AADTT

File Name: C:\Users\admin\Desktop\Frank Ni\Major Arterial\7500 AADTT\combined average E\LCC 600 Section Major Arterial 7500AADTT.dgpx



Design Properties

HMA Design Properties

Use Multilayer Rutting Model	False
Using G* based model (not nationally calibrated)	False
Is NCHRP 1-37A HMA Rutting Model Coefficients	True
Endurance Limit	-
Use Reflective Cracking	True

Structure - ICM Properties	
AC surface shortwave absorptivity	0.85

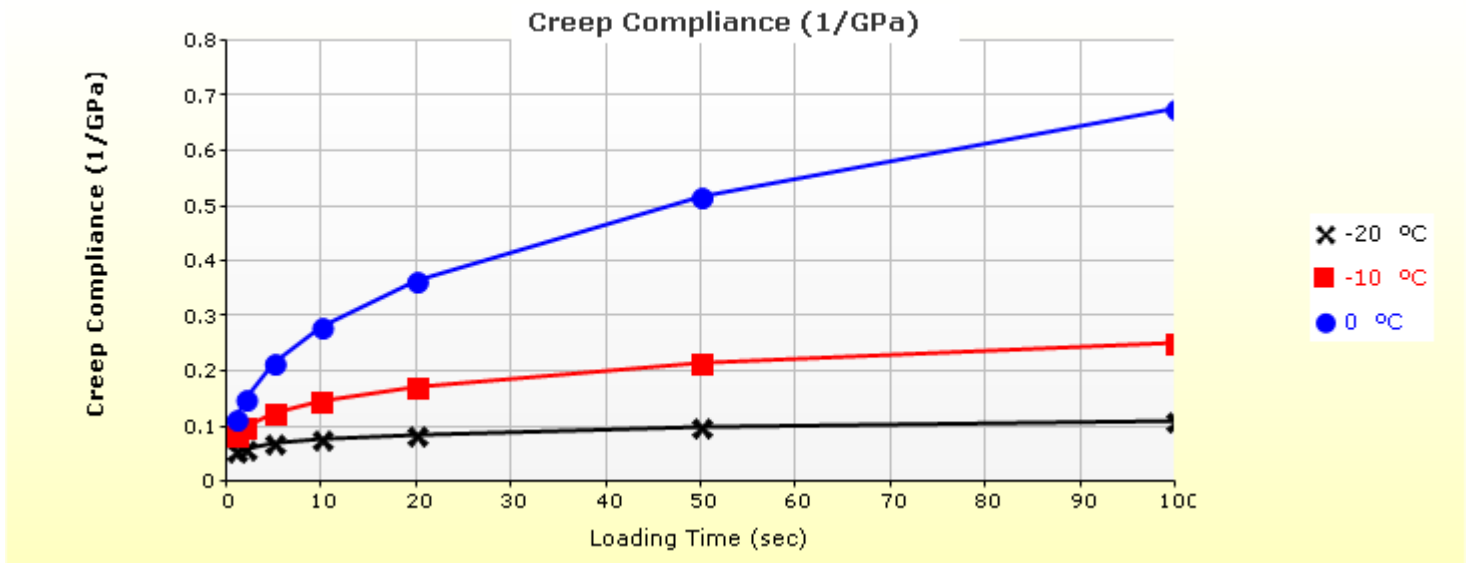
Layer Name	Layer Type	Interface Friction
Layer 1 Flexible : Default asphalt concrete	Flexible (1)	1.00
Layer 2 Flexible : Default asphalt concrete	Flexible (1)	1.00
Layer 3 Non-stabilized Base : A-1-a	Non-stabilized Base (4)	1.00
Layer 4 Non-stabilized Base : A-1-b	Non-stabilized Base (4)	1.00
Layer 5 Subgrade : A-1-a	Subgrade (5)	-

Thermal Cracking

Thermal Contraction	
Is thermal contraction calculated?	True
Mix coefficient of thermal contraction (mm/mm/°C)	-
Aggregate coefficient of thermal contraction (mm/mm/°C)	9.0e-006
Voids in Mineral Aggregate (%)	18.8

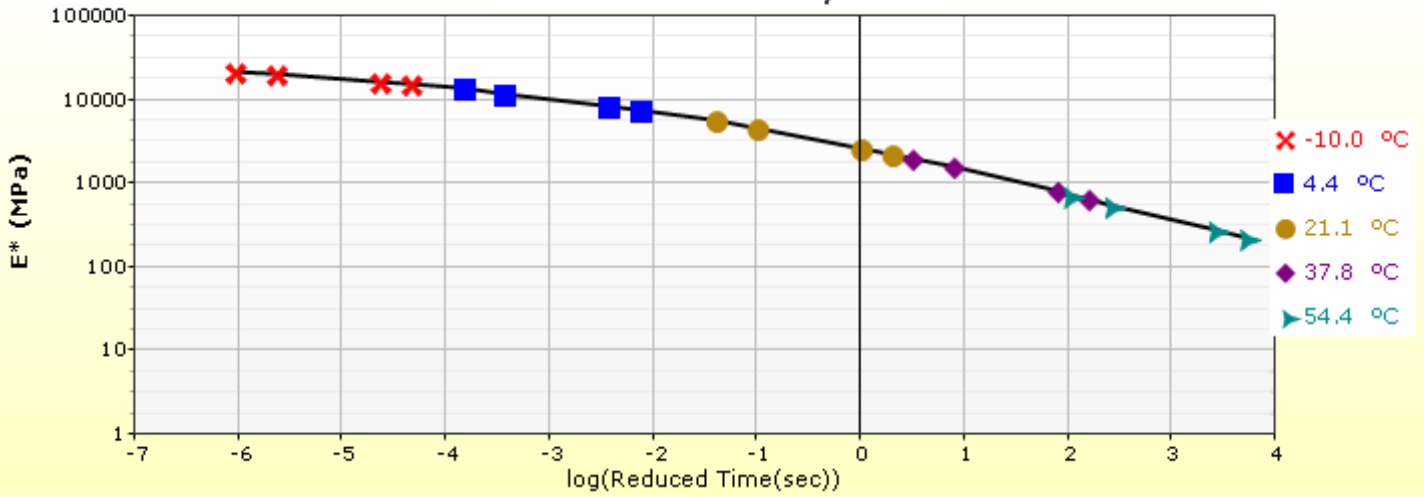
Indirect Tensile Strength (Input Level: 3)	
Test Temperature (°C)	Indirect Tensile Strength (Mpa)
-10.0	2.79

Creep Compliance (1/GPa) (Input Level: 3)			
Loading time (sec)	-20 °C	-10 °C	0 °C
1	5.57e-002	8.57e-002	1.16e-001
2	6.17e-002	1.01e-001	1.51e-001
5	7.07e-002	1.25e-001	2.15e-001
10	7.83e-002	1.48e-001	2.80e-001
20	8.68e-002	1.74e-001	3.65e-001
50	9.94e-002	2.16e-001	5.19e-001
100	1.10e-001	2.55e-001	6.77e-001

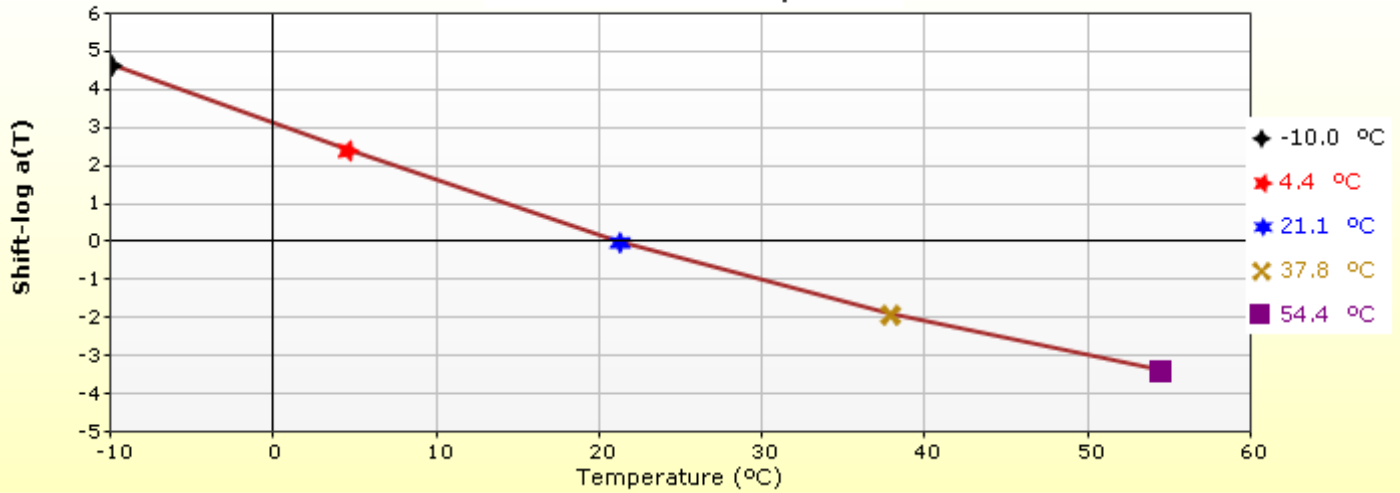


HMA Layer 1: Layer 1 Flexible : Default asphalt concrete

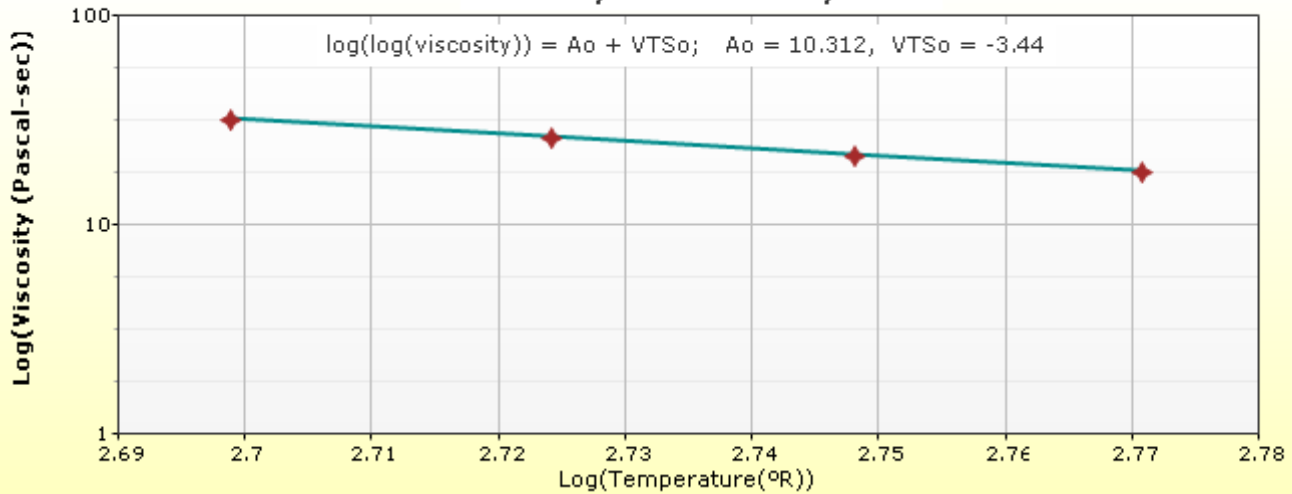
Master Curve HMA Layer 1



Shift Curve HMA Layer 1

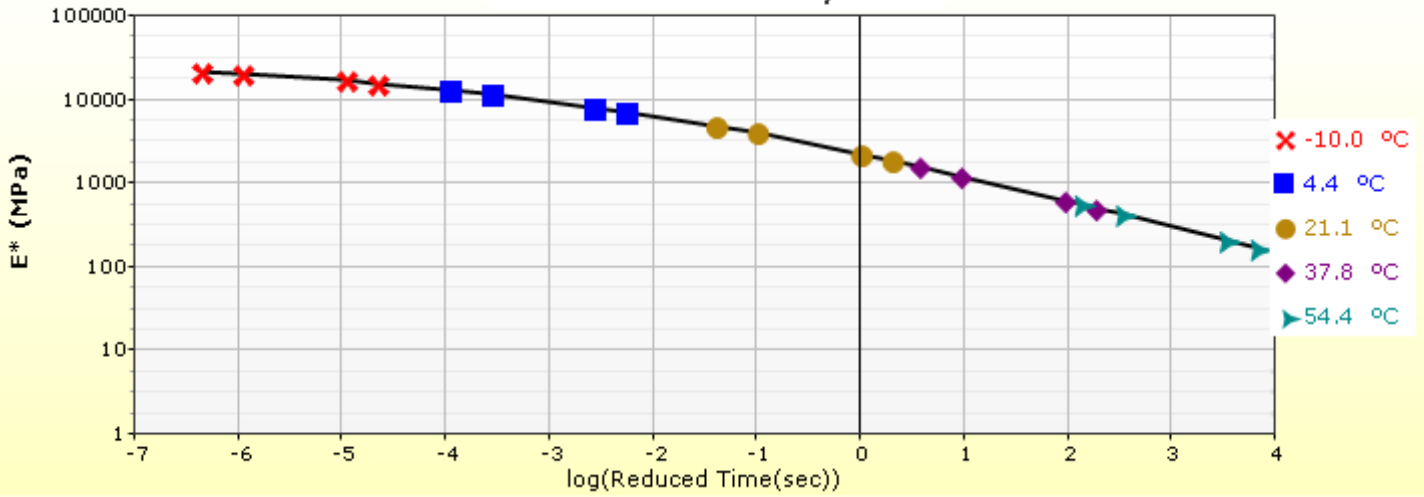


Viscosity Curve HMA Layer 1

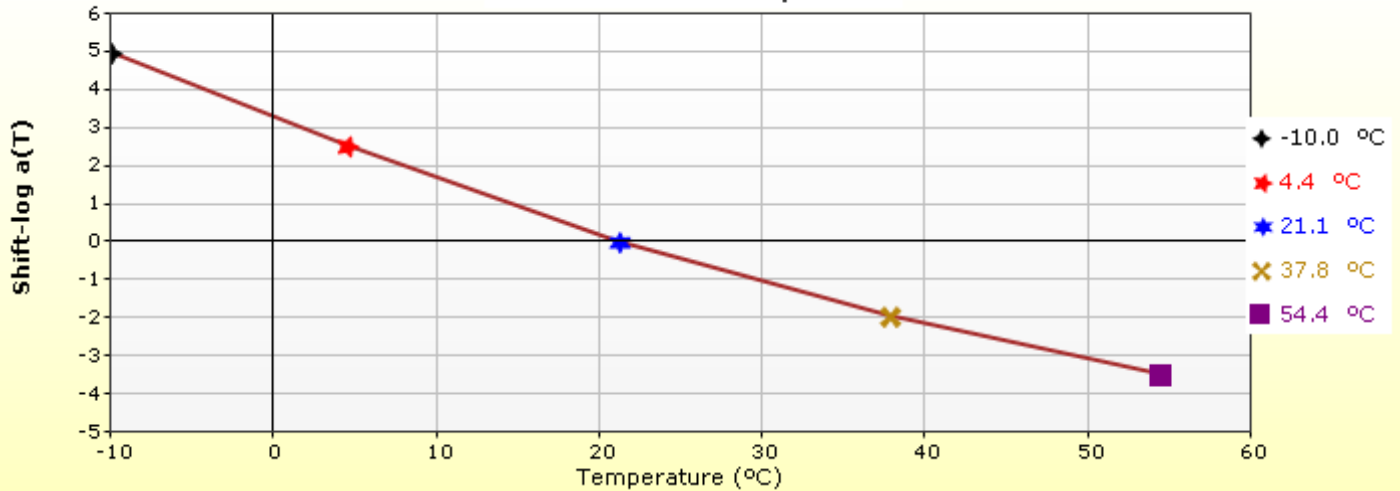


HMA Layer 2: Layer 2 Flexible : Default asphalt concrete

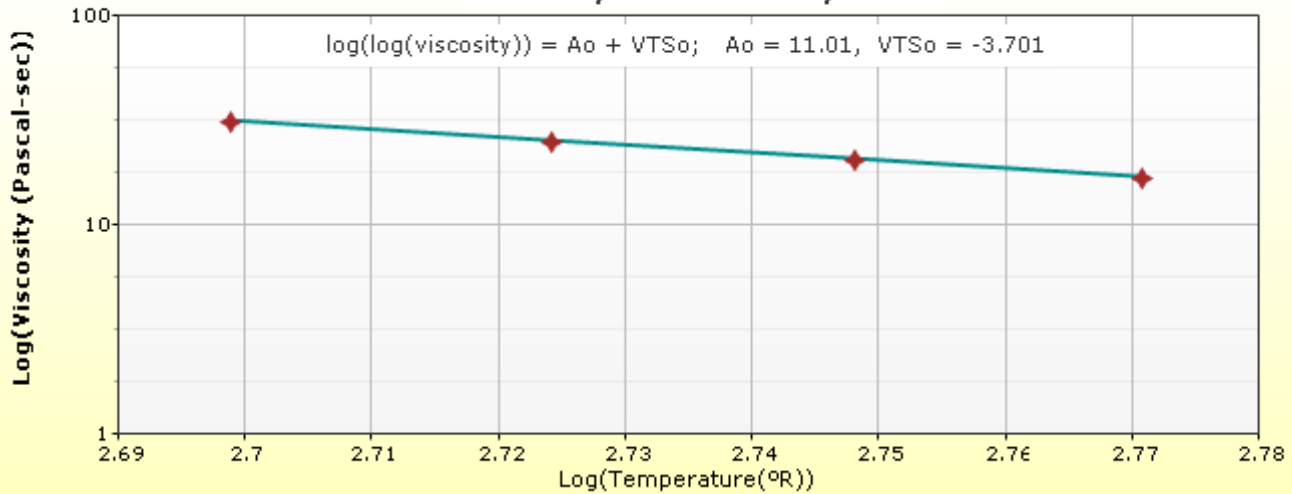
Master Curve HMA Layer 2



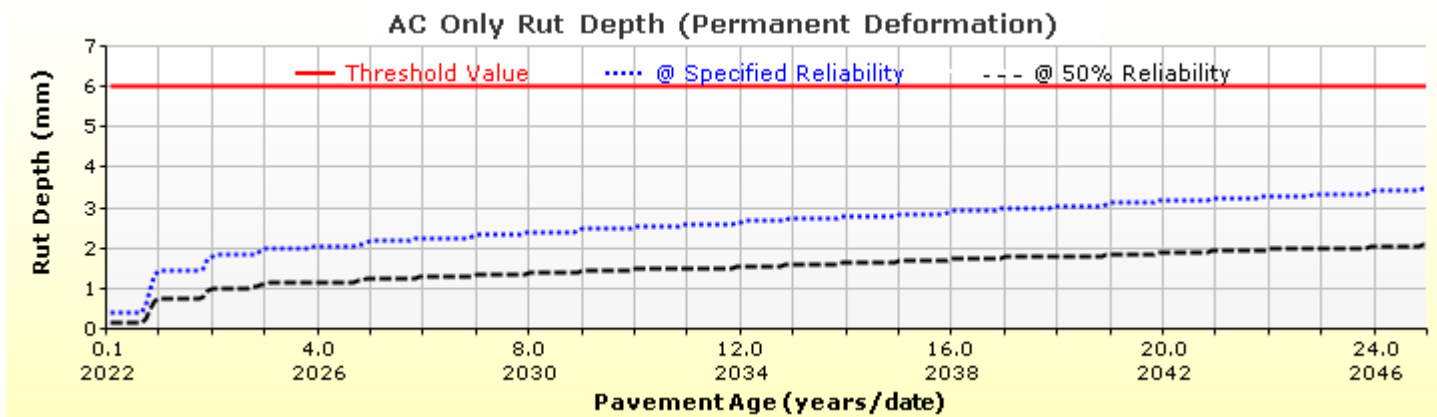
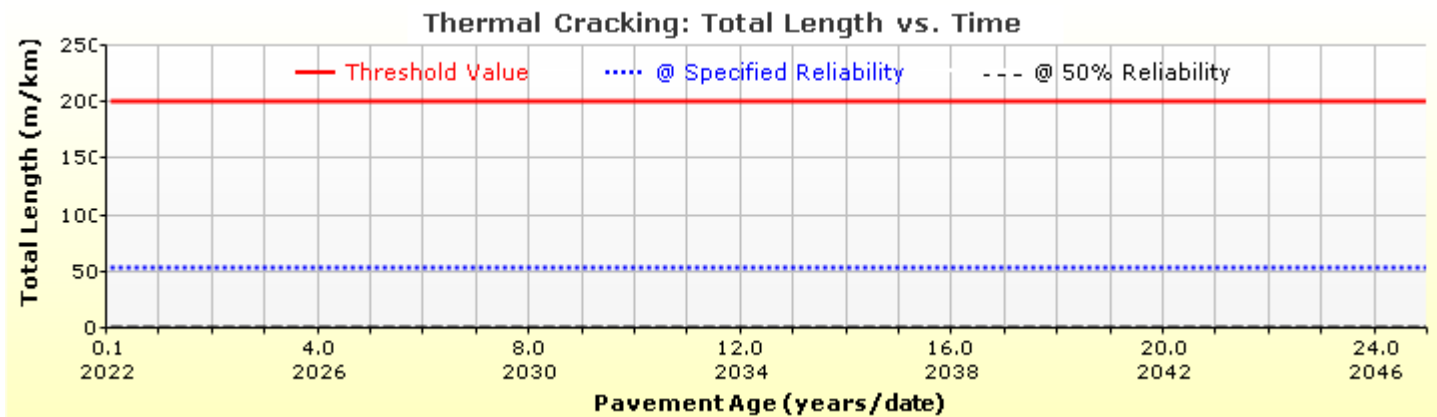
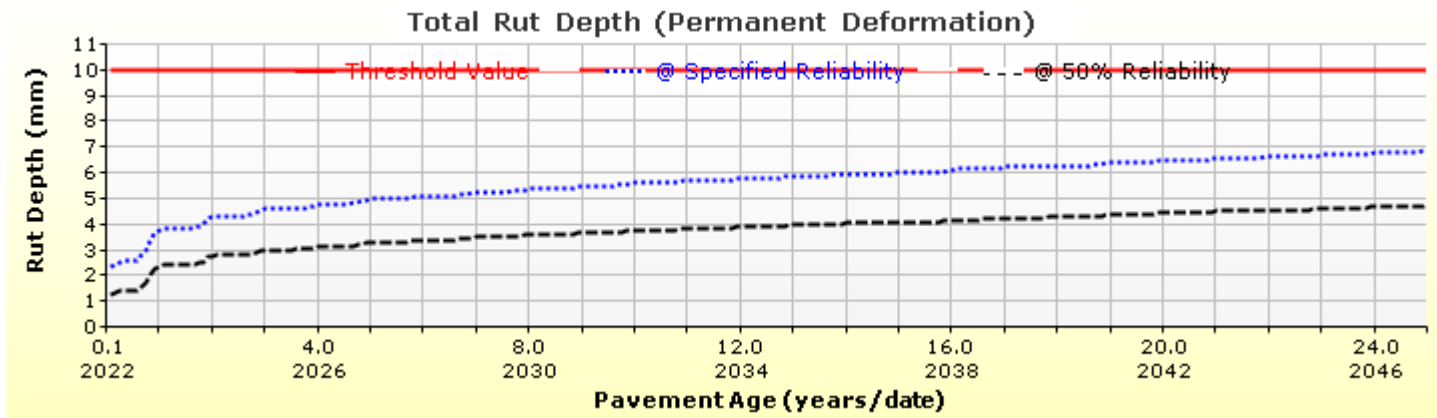
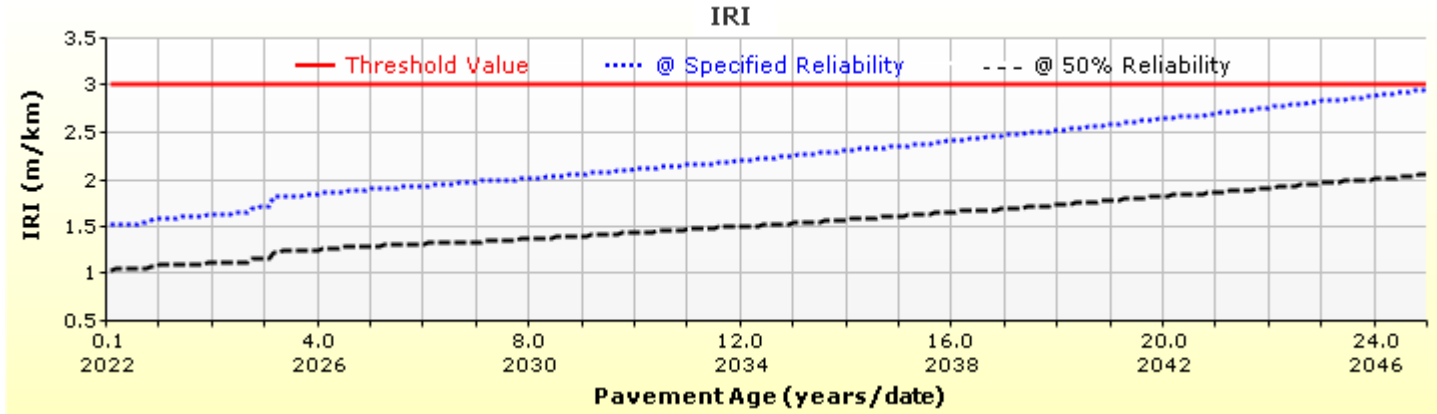
Shift Curve HMA Layer 2

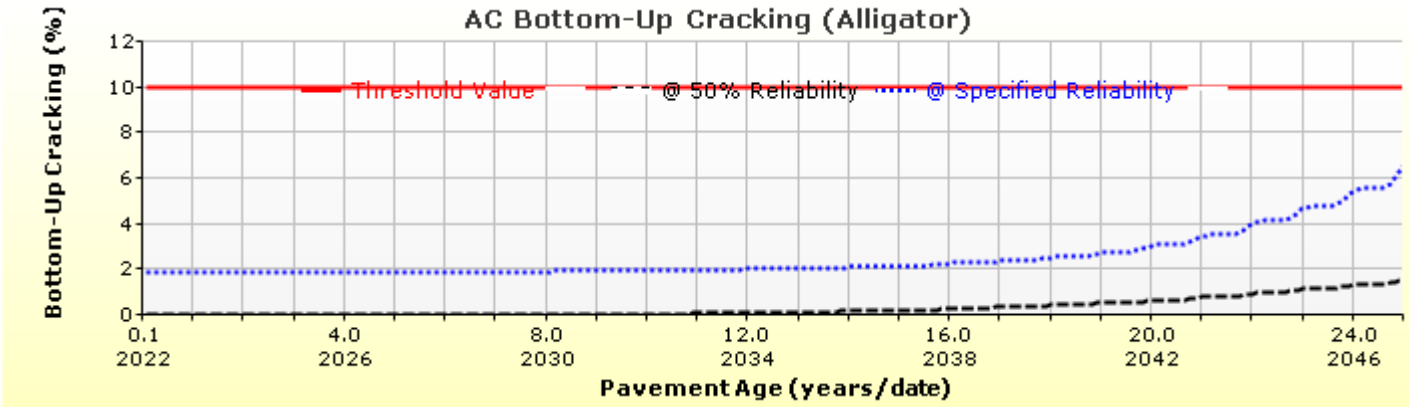
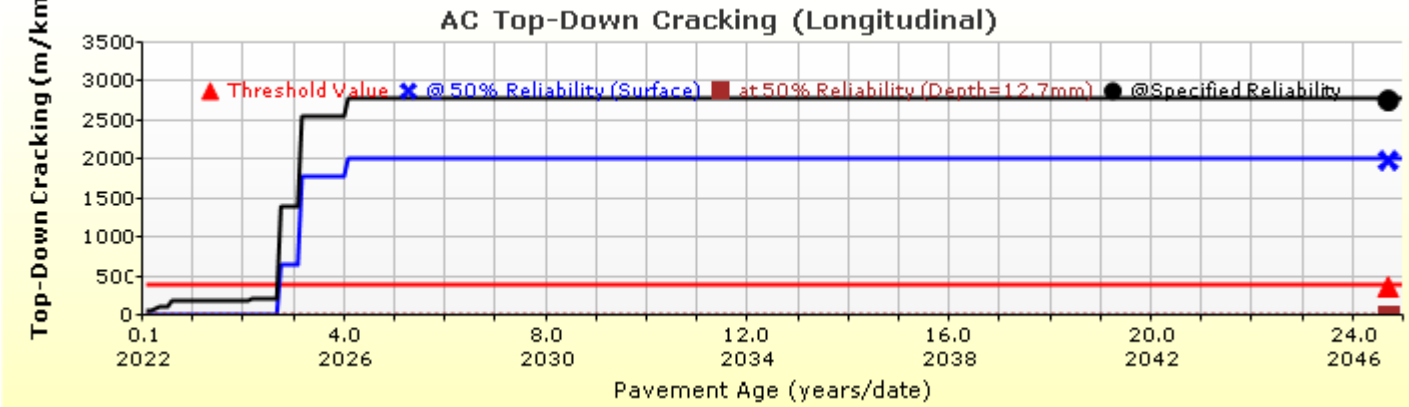
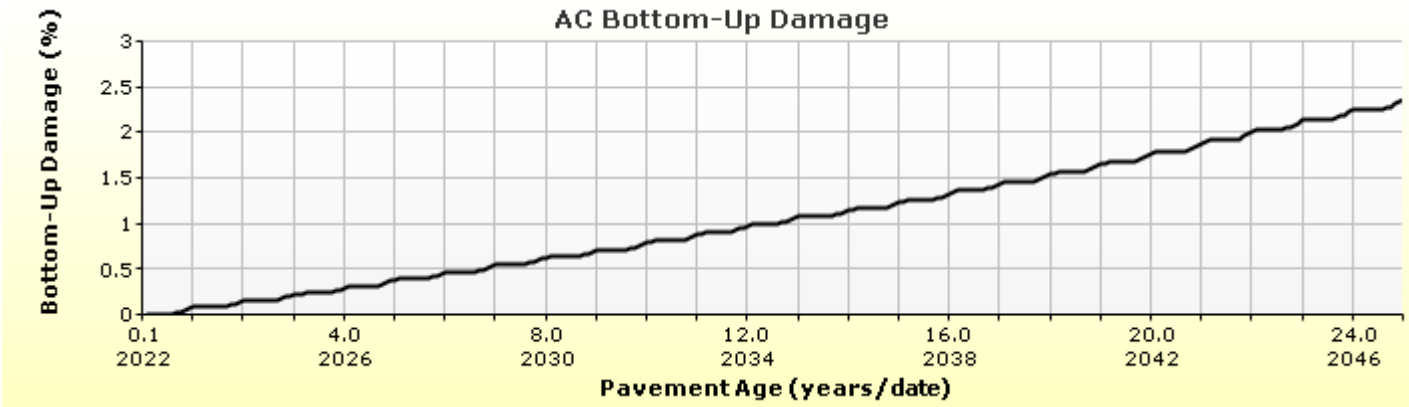
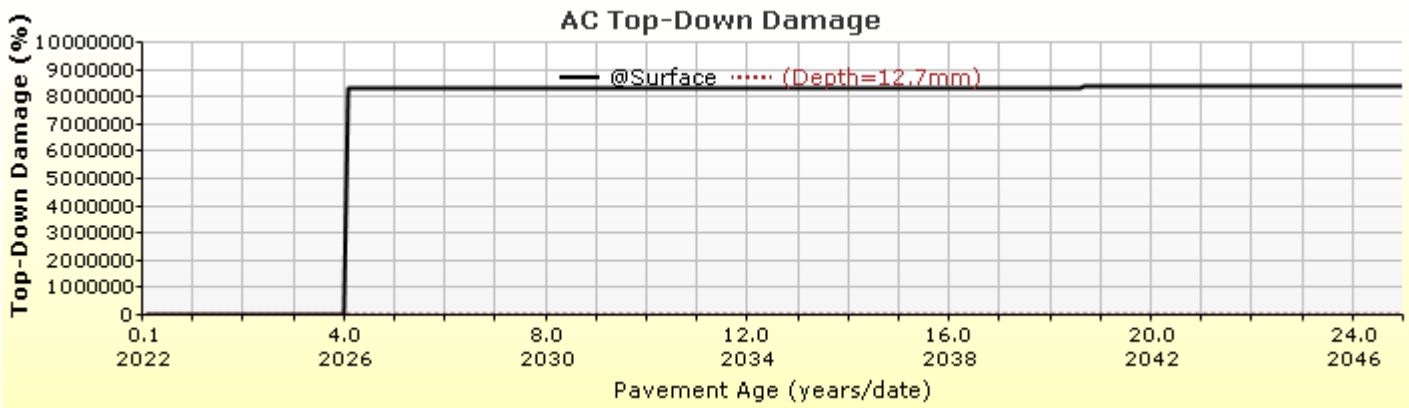


Viscosity Curve HMA Layer 2



Analysis Output Charts





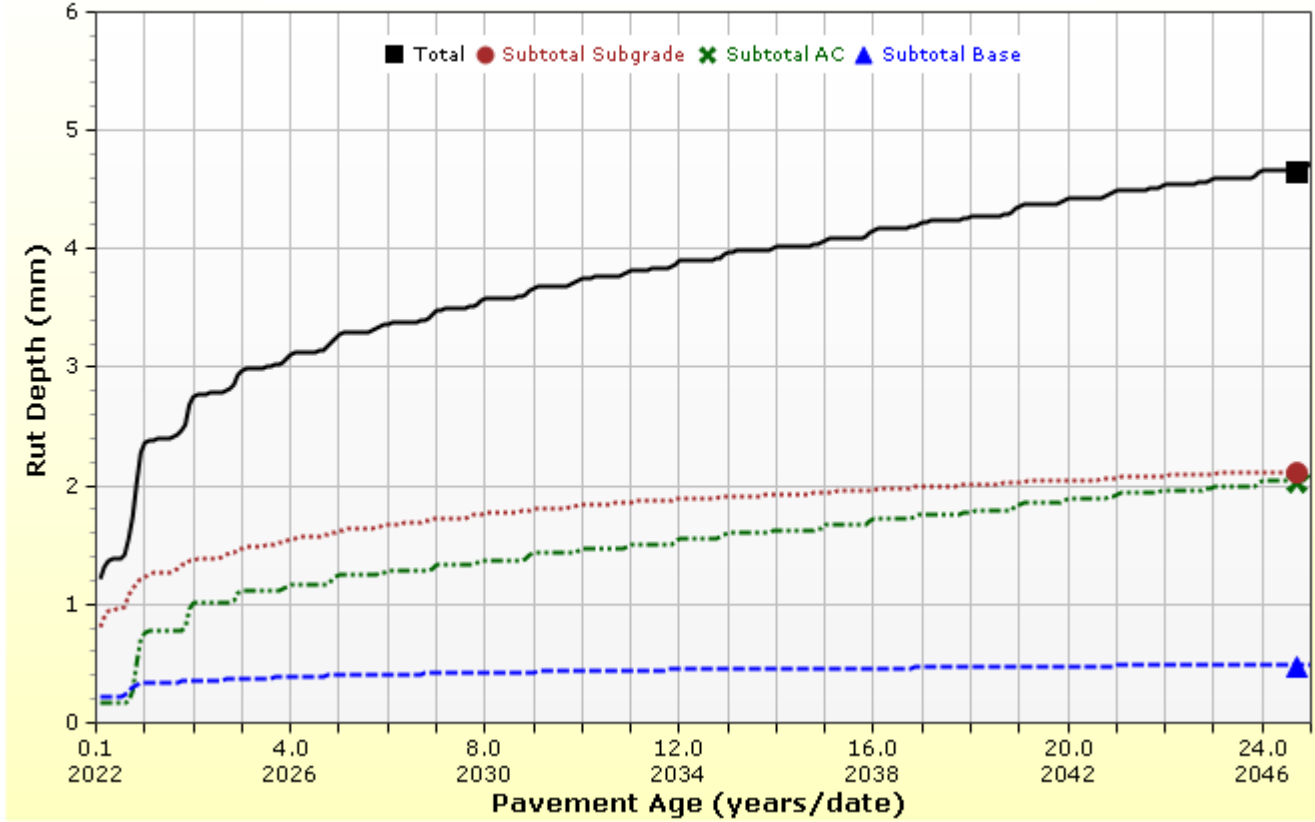


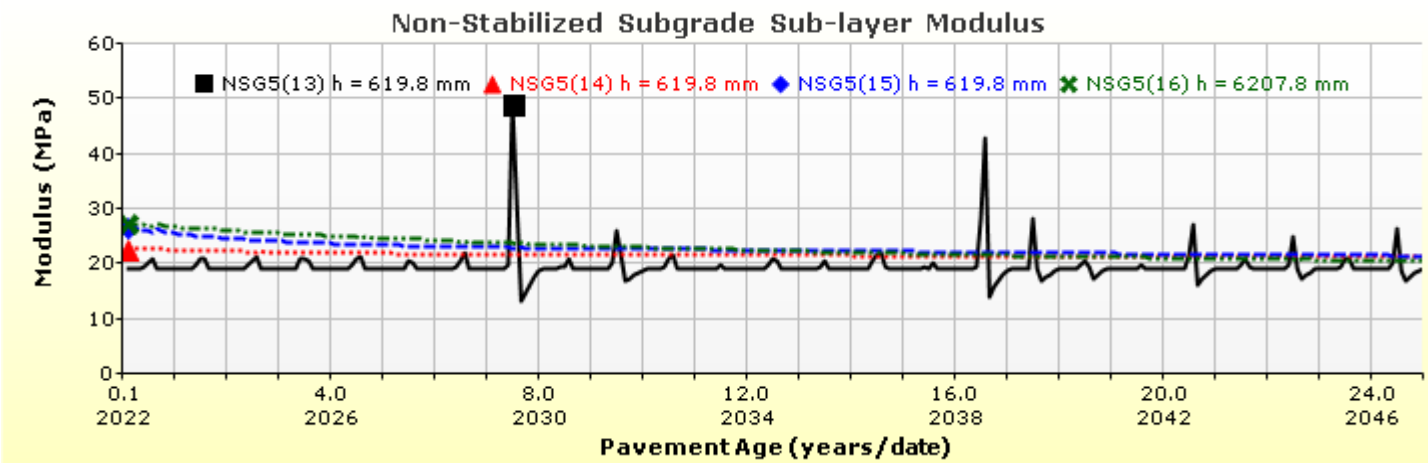
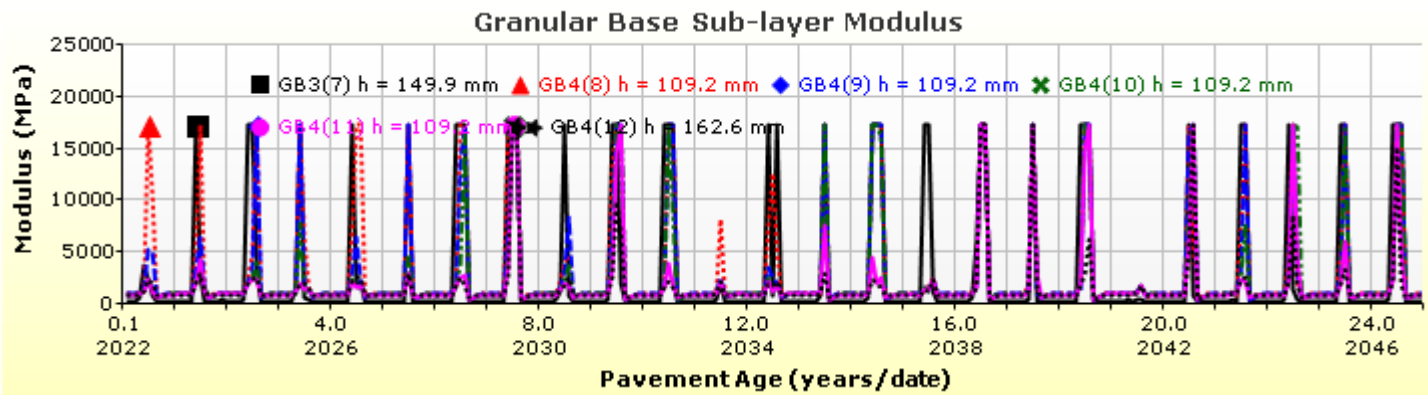
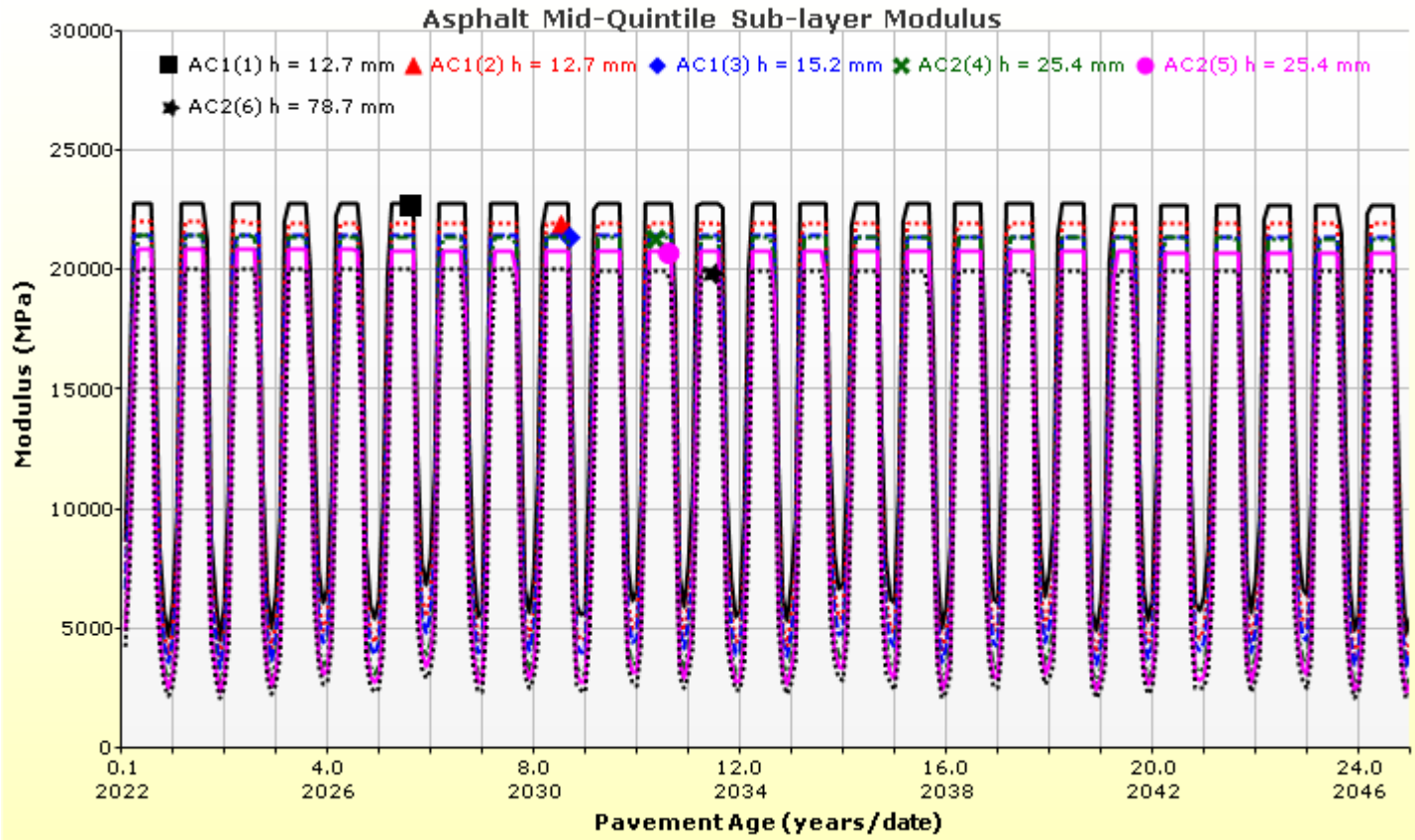
LCC 600 Section Major Arterial 7500AADTT

File Name: C:\Users\admin\Desktop\Frank Ni\Major Arterial\7500 AADTT\combined average E\LCC 600 Section Major Arterial 7500AADTT.dgpx



Rutting (Permanent Deformation) at 50% Reliability







LCC 600 Section Major Arterial 7500AADTT

File Name: C:\Users\admin\Desktop\Frank Ni\Major Arterial\7500 AADTT\combined average E\LCC 600 Section Major Arterial 7500AADTT.dgpx



Layer Information

Layer 1 Flexible : Default asphalt concrete

Asphalt		
Thickness (mm)	40.0	
Unit weight (kgf/m ³)	2390.0	
Poisson's ratio	Is Calculated?	False
	Ratio	0.35
	Parameter A	-
	Parameter B	-

Asphalt Dynamic Modulus (Input Level: 3)

Gradation	Percent Passing
19 mm sieve	100
9.5 mm sieve	77
4.75 mm sieve	60
0.075mm sieve	6

Asphalt Binder

Parameter	Value
Grade	Superpave Performance Grade
Binder Type	64-28
A	10.312
VTS	-3.44

General Info

Name	Value
Reference temperature (°C)	21.1
Effective binder content (%)	11.8
Air voids (%)	7
Thermal conductivity (watt/meter-kelvin)	1.16
Heat capacity (joule/kg-kelvin)	963

Identifiers

Field	Value
Display name/identifier	Default asphalt concrete
Description of object	
Author	
Date Created	9/16/2010 1:00:00 AM
Approver	
Date approved	9/16/2010 1:00:00 AM
State	
District	
County	
Highway	
Direction of Travel	
From station (km)	
To station (km)	
Province	
User defined field 1	
User defined field 2	
User defined field 3	
Revision Number	0



LCC 600 Section Major Arterial 7500AADTT

File Name: C:\Users\admin\Desktop\Frank Ni\Major Arterial\7500 AADTT\combined average E\LCC 600 Section Major Arterial 7500AADTT.dgpx



Layer 2 Flexible : Default asphalt concrete

Asphalt		
Thickness (mm)	130.0	
Unit weight (kg/m ³)	2460.0	
Poisson's ratio	Is Calculated?	False
	Ratio	0.35
	Parameter A	-
	Parameter B	-

Asphalt Dynamic Modulus (Input Level: 3)

Gradation	Percent Passing
19 mm sieve	100
9.5 mm sieve	77
4.75 mm sieve	60
0.075mm sieve	6

Asphalt Binder

Parameter	Value
Grade	Superpave Performance Grade
Binder Type	58-28
A	11.01
VTS	-3.701

General Info

Name	Value
Reference temperature (°C)	21.1
Effective binder content (%)	11.2
Air voids (%)	7
Thermal conductivity (watt/meter-kelvin)	1.16
Heat capacity (joule/kg-kelvin)	963

Identifiers

Field	Value
Display name/identifier	Default asphalt concrete
Description of object	
Author	
Date Created	9/16/2010 1:00:00 AM
Approver	
Date approved	9/16/2010 1:00:00 AM
State	
District	
County	
Highway	
Direction of Travel	
From station (km)	
To station (km)	
Province	
User defined field 1	
User defined field 2	
User defined field 3	
Revision Number	0



LCC 600 Section Major Arterial 7500AADTT

File Name: C:\Users\admin\Desktop\Frank Ni\Major Arterial\7500 AADTT\combined average E\LCC 600 Section Major Arterial 7500AADTT.dgpx



Layer 3 Non-stabilized Base : A-1-a

Unbound	
Layer thickness (mm)	150.0
Poisson's ratio	0.35
Coefficient of lateral earth pressure (k0)	0.5

Modulus (Input Level: 3)

Analysis Type:	Modify input values by temperature/moisture
Method:	Resilient Modulus (MPa)

Resilient Modulus (MPa)
250.0

Use Correction factor for NDT modulus?	-
NDT Correction Factor:	-

Identifiers

Field	Value
Display name/identifier	A-1-a
Description of object	Default material
Author	AASHTO
Date Created	1/1/2011 12:00:00 AM
Approver	
Date approved	1/1/2011 12:00:00 AM
State	
District	
County	
Highway	
Direction of Travel	
From station (km)	
To station (km)	
Province	
User defined field 1	
User defined field 2	
User defined field 3	
Revision Number	0

Sieve

Liquid Limit	6.0
Plasticity Index	0.0
Is layer compacted?	True

	Is User Defined?	Value
Maximum dry unit weight (kgf/m ³)	False	2038.2
Saturated hydraulic conductivity (m/hr)	False	2.376e-02
Specific gravity of solids	False	2.7
Water Content (%)	False	5.7

User-defined Soil Water Characteristic Curve (SWCC)

Is User Defined?	False
af	3.0201
bf	2.5984
cf	0.7539
hr	100.0000

Sieve Size	% Passing
0.001mm	
0.002mm	
0.020mm	
0.075mm	5.0
0.150mm	
0.180mm	
0.250mm	
0.300mm	13.5
0.425mm	
0.600mm	
0.850mm	
1.18mm	27.5
2.0mm	
2.36mm	
4.75mm	45.0
9.5mm	61.5
12.5mm	77.5
19.0mm	92.5
25.0mm	100.0
37.5mm	
50.0mm	
63.0mm	
75.0mm	
90.0mm	



LCC 600 Section Major Arterial 7500AADTT

File Name: C:\Users\admin\Desktop\Frank Ni\Major Arterial\7500 AADTT\combined average E\LCC 600 Section Major Arterial 7500AADTT.dgp



Layer 4 Non-stabilized Base : A-1-b

Unbound	
Layer thickness (mm)	600.0
Poisson's ratio	0.2
Coefficient of lateral earth pressure (k0)	0.5

Modulus (Input Level: 3)

Analysis Type:	Modify input values by temperature/moisture
Method:	Resilient Modulus (MPa)

Resilient Modulus (MPa)
1490.0

Use Correction factor for NDT modulus?	-
NDT Correction Factor:	-

Identifiers

Field	Value
Display name/identifier	A-1-b
Description of object	Default material
Author	AASHTO
Date Created	1/1/2011 12:00:00 AM
Approver	
Date approved	1/1/2011 12:00:00 AM
State	
District	
County	
Highway	
Direction of Travel	
From station (km)	
To station (km)	
Province	
User defined field 1	
User defined field 2	
User defined field 3	
Revision Number	0

Sieve

Liquid Limit	11.0
Plasticity Index	0.0
Is layer compacted?	True

	Is User Defined?	Value
Maximum dry unit weight (kgf/m ³)	False	2022.2
Saturated hydraulic conductivity (m/hr)	False	6.073e-02
Specific gravity of solids	False	2.7
Water Content (%)	False	7.3

User-defined Soil Water Characteristic Curve (SWCC)

Is User Defined?	False
af	6.8181
bf	1.6200
cf	0.8174
hr	100.0000

Sieve Size	% Passing
0.001mm	
0.002mm	
0.020mm	
0.075mm	5.0
0.150mm	
0.180mm	
0.250mm	
0.300mm	13.5
0.425mm	
0.600mm	
0.850mm	
1.18mm	25.0
2.0mm	
2.36mm	
4.75mm	37.5
9.5mm	
12.5mm	
19.0mm	
25.0mm	75.0
37.5mm	
50.0mm	
63.0mm	
75.0mm	
90.0mm	100.0



LCC 600 Section Major Arterial 7500AADTT

File Name: C:\Users\admin\Desktop\Frank Ni\Major Arterial\7500 AADTT\combined average E\LCC 600 Section Major Arterial 7500AADTT.dgpx



Layer 5 Subgrade : A-1-a

Unbound	
Layer thickness (mm)	Semi-infinite
Poisson's ratio	0.45
Coefficient of lateral earth pressure (k0)	0.5

Modulus (Input Level: 3)

Analysis Type:	Modify input values by temperature/moisture
Method:	Resilient Modulus (MPa)

Resilient Modulus (MPa)
30.0

Use Correction factor for NDT modulus?	-
NDT Correction Factor:	-

Identifiers

Field	Value
Display name/identifier	A-1-a
Description of object	Default Material
Author	AASHTO
Date Created	1/1/2011 12:00:00 AM
Approver	
Date approved	1/1/2011 12:00:00 AM
State	
District	
County	
Highway	
Direction of Travel	
From station (km)	
To station (km)	
Province	
User defined field 1	
User defined field 2	
User defined field 3	
Revision Number	0

Sieve

Liquid Limit	26.0
Plasticity Index	12.0
Is layer compacted?	True

	Is User Defined?	Value
Maximum dry unit weight (kgf/m ³)	False	1748.5
Saturated hydraulic conductivity (m/hr)	False	8.129e-06
Specific gravity of solids	False	2.7
Water Content (%)	False	16.8

User-defined Soil Water Characteristic Curve (SWCC)

Is User Defined?	False
af	106.7030
bf	0.6914
cf	0.2273
hr	500.0000

Sieve Size	% Passing
0.001mm	
0.002mm	30.0
0.020mm	
0.075mm	80.0
0.150mm	
0.180mm	84.0
0.250mm	
0.300mm	
0.425mm	91.0
0.600mm	
0.850mm	
1.18mm	
2.0mm	95.0
2.36mm	
4.75mm	97.0
9.5mm	99.0
12.5mm	100.0
19.0mm	100.0
25.0mm	100.0
37.5mm	
50.0mm	
63.0mm	
75.0mm	
90.0mm	

Calibration Coefficients

AC Fatigue

$N_f = 0.00432 * C * \beta_{f1} k_1 \left(\frac{1}{\epsilon_1}\right)^{k_2 \beta_{f2}} \left(\frac{1}{E}\right)^{k_3 \beta_{f3}}$ $C = 10^M$ $M = 4.84 \left(\frac{V_b}{V_a + V_b} - 0.69\right)$	k1: 3.75
	k2: 2.87
	k3: 1.46
	Bf1: (5.014 * Pow(hac,-3.416)) * 1 + 0
	Bf2: 1.38
	Bf3: 0.88

AC Rutting

$\frac{\epsilon_p}{\epsilon_r} = k_z \beta_{r1} 10^{k_1 T} k_2 \beta_{r2} N^{k_3 B_{r3}}$ $k_z = (C_1 + C_2 * depth) * 0.328196^{depth}$ $C_1 = -0.1039 * H_a^2 + 2.4868 * H_a - 17.342$ $C_2 = 0.0172 * H_a^2 - 1.7331 * H_a + 27.428$ <p>Where: H_{ac} = total AC thickness(in)</p>	ϵ_p = plastic strain(in/in) ϵ_r = resilient strain(in/in) T = layer temperature(°F) N = number of load repetitions
AC Rutting Standard Deviation	0.24 * Pow(RUT,0.8026) + 0.001
AC Layer 1	K1:-2.45 K2:3.01 K3:0.22 Br1:0.128 Br2:0.52 Br3:1.36
AC Layer 2	K1:-2.45 K2:3.01 K3:0.22 Br1:0.4 Br2:0.52 Br3:1.36

Thermal Fracture

$C_f = 400 * N \left(\frac{\log C / h_{ac}}{\sigma}\right)$ $\Delta C = (k * \beta t)^{n+1} * A * \Delta K^{-n}$ $A = 10^{(4.389 - 2.52 * \log(E * \sigma_m * n))}$	C_f = observed amount of thermal cracking(ft/500ft) k = refression coefficient determined through field calibration $N()$ = standard normal distribution evaluated at() σ = standard deviation of the log of the depth of cracks in the pavments C = crack depth(in) h_{ac} = thickness of asphalt layer(in) ΔC = Change in the crack depth due to a cooling cycle ΔK = Change in the stress intensity factor due to a cooling cycle A, n = Fracture parameters for the asphalt mixture E = mixture stiffness σ_m = Undamaged mixture tensile strength β_t = Calibration parameter
Level 1 K: ((3 * Pow(10,-7)) * Pow(MAAT,4.0319)) * 1 + 0	Level 1 Standard Deviation: 0.14 * THERMAL + 168
Level 2 K: ((3 * Pow(10,-7)) * Pow(MAAT,4.0319)) * 1 + 0	Level 2 Standard Deviation: 0.20 * THERMAL + 168
Level 3 K: ((3 * Pow(10,-7)) * Pow(MAAT,4.0319)) * 1 + 0	Level 3 Standard Deviation: 0.289 * THERMAL + 168

CSM Fatigue

$N_f = 10^{\left(\frac{k_1 \beta_{c1} \left(\frac{\sigma_s}{M_r}\right)}{k_2 \beta_{c2}}\right)}$	N_f = number of repetitions to fatigue cracking σ_s = Tensile stress(psi) M_r = modulus of rupture(psi)		
k1: 0.972	k2: 0.0825	Bc1: 1	Bc2: 1

Unbound Layer Rutting			
$\delta_a(N) = \beta_{s_1} k_1 \varepsilon_v h \left(\frac{\varepsilon_0}{\varepsilon_r} \right) \left e^{-\left(\frac{\rho}{N}\right)^\beta} \right $		$\delta_a = \text{permanent deformation for the layer}$ $N = \text{number of repetitions}$ $\varepsilon_v = \text{average vertical strain(in/in)}$ $\varepsilon_0, \beta, \rho = \text{material properties}$ $\varepsilon_r = \text{resilient strain(in/in)}$	
Base Rutting		Subgrade Rutting	
k1: 0.965	Bs1: 0.322	k1: 0.965	Bs1: 0.322
Standard Deviation (BASERUT) 0.1477 * Pow(BASERUT,0.6711) + 0.001		Standard Deviation (BASERUT) 0.1235 * Pow(SUBRUT,0.5012) + 0.001	

AC Cracking			
AC Top Down Cracking		AC Bottom Up Cracking	
$FC_{top} = \left(\frac{C_4}{1 + e^{(C_1 - C_2 * \log_{10}(Damage))}} \right) * 10.56$		$FC = \left(\frac{6000}{1 + e^{(C_1 * C'_1 + C_2 * C'_2 * \log_{10}(D * 100))}} \right) * \left(\frac{1}{60} \right)$ $C'_2 = -2.40874 - 39.748 * (1 + h_{ac})^{-2.856}$ $C'_1 = -2 * C'_2$	
c1: 7	c2: 3.5	c3: 0	c4: 1000
c1: 1.31	c2: (0.867 + 0.2583 * hac) * 1 + 0	c3: 6000	
Top down AC Cracking Standard Deviation		Bottom up AC Cracking Standard Deviation	
200 + 2300/(1+exp(1.072-2.1654*LOG10(TOP+0.0001)))		1.13 + 13/(1+exp(7.57-15.5*LOG10(BOTTOM+0.0001)))	

CSM Cracking				IRI Flexible Pavements			
$FC_{ctb} = C_1 + \frac{C_2}{1 + e^{C_3 - C_4 * \log_{10}(Damage)}}$				C1 - Rutting		C3 - Transverse Crack	
				C2 - Fatigue Crack		C4 - Site Factors	
C1: 0	C2: 75	C3: 2	C4: 2	C1: 55	C2: 0.4	C3: 0.008	C4: 0.015
CSM Standard Deviation							
CTB*1							